UNICA

UNIVERSITÀ
DEGLI STUDI
DI CAGLIARI

Ph.D. DEGREE IN
Earth and Environmental Sciences and Technologies

Cycle XXXVIII

TITLE OF THE Ph.D. THESIS

Sardinia's Mineral Resources Database Update: New Exploration Guides for Identifying Critical and Strategic Raw Materials for Decarbonization and Ecological Transition

Scientific Disciplinary Sector

GEO/09

Ph.D. Student: Antonio Attardi

Supervisor Prof. Stefano Naitza

Co-Supervisor Prof. Fabrizio Cocco, Prof. Antonio Funedda

Final exam. Academic Year 2024/2025
Thesis defence session: July 2026

Table of Contents

Abstract

The European Union's strategic agenda for a decarbonised and self-sufficient economy culminated in the Critical Raw Materials Act (CRMA, 2024), which defined Critical and Strategic Raw Materials (CRMs and SRMs) essential for technological development and economic resilience, while being subject to high supply risk. Within this framework, the PNRR Geosciences IR project of ISPRA (Italian Institute for Environmental Protection and Research) is developing a series of thematic databases. This thesis presents the new Metallogenic Database of Sardinia, the foremost mining region of Italy, designed to support the exploration of CRMs fundamental to the energetic transition.

A comprehensive, relational geodatabase was built using PostgreSQL-PostGIS and QGIS, integrating over 630 mineral occurrences, deposits, and active mines. The schema combines descriptive, compositional, structural, and technical data, with a dedicated focus on CRMs. The work valorised legacy information from the historical Metallogenic Maps of Sardinia (1978, 2008) and the reports of the former Sardinian Mining Agency (EMSA, 1980s), integrating them with recent scientific literature, targeted field campaigns, and new laboratory analyses.

The database structure is inherently designed to schematise mineralisation models and facilitate predictivity models. The iterative, data-driven methodology is illustrated through representative case studies, each investigated with specific techniques based on the dominant ore control: the structures of mixed-sulphides skarn and fluorite-barite hydrothermal veins of the Rosas-Orbai district (SW Sardinia) and the Fluminese district (W Sardinia); the geochemistry and geochronology of Mo-W-LREE greisen and fluorite veins of the Su Laccheddu-Giacone system (N Sardinia); the vertically-zoned fluorite-barite veins of the Silius deposit (SE Sardinia). These studies provided new mineralogical and structural data, which were iteratively fed back into the database to refine the genetic models.

Finally, the database was applied to regional-scale Mineral Prospectivity Modelling (MPM) for skarn-type deposits in central and southern Sardinia. A fuzzy logic-based approach, integrating proximity to intrusions, reactive lithologies, and faults, generated a prospectivity map validated by ROC analysis (AUC = 0.845). This demonstrates the database's predictive power, successfully distinguishing skarn-bearing from barren cells and identifying high-priority exploration targets. The work establishes a robust, transferable framework for modern mineral resource assessment, directly supporting Europe's strategic autonomy goals.

1. Introduction

The Strategic and Critical Raw Materials Act

The European Union's geopolitical stance to move towards a carbon-free and sustainable development constituted the base for lawmakers, academia and the private sector to build upon a technical, scientific, social and political framework that is best represented in the European Union's Critical Raw Materials Act (CRMA, 2023) and the Green Deal Industrial Plan (Appendix A). These initiatives aim to secure a sustainable domestic supply of Critical Raw Materials, deemed vital for EU resilience, and to ensure strategic autonomy during the clean energy transition. Faster access to funding and professional formation are at the base of the strategy. The EU classifies the raw materials based on their economic importance and supply risk (Table 1.1): Critical Raw Materials are both highly valuable and vulnerable to supply disruptions, and Strategic Raw Materials are essential for key technologies. The last report on Critical Raw Materials classification was drafted in 2023 (Grohol et al., 2023). They included materials such as lithium (Li) for batteries; cobalt (Co) and rare earth elements (REEs) for permanent magnets in electric vehicles and wind turbines; tungsten (W) and tin (Sn) for electronics; copper (Cu) for all electrification; and fluorite as a critical source of fluorine. The CRMA sets binding 2030 benchmarks for domestic extraction, processing, and recycling.

2023 Critical Raw Materials (*new CRMs in italics*)			
aluminium/bauxite ★	coking coal	lithium ★	phosphorus ★
antimony ★	*feldspar* ★	LREE ★	scandium
arsenic ★	fluorspar ★	magnesium	silicon metal
baryte ★	gallium	*manganese* ★	strontium
beryllium	germanium ★	natural graphite	tantalum
bismuth ★	hafnium	niobium ★	titanium metal ★
boron/borate	*helium*	PGM	tungsten ★
cobalt ★	HREE	phosphate rock	vanadium ★
		copper* ★	_nickel*_ ★

2023 Critical Raw Materials (*Strategic Raw Materials in italics*)			
aluminium/bauxite	coking coal	*lithium*	phosphorus
antimony	feldspar	*LREE*	scandium
arsenic	fluorspar	*magnesium*	*silicon metal*
baryte	*gallium*	*manganese*	strontium
beryllium	*germanium*	*natural graphite*	tantalum
bismuth	hafnium	niobium	*titanium metal*
boron/borate	helium	*PGM*	*tungsten*
cobalt	*HREE*	phosphate rock	vanadium
		copper*	_nickel*_

Table 1.1: Critical and Strategic Raw Materials list from (Grohol et al., 2023). The star in the first table denotes the presence in Sardinian territory.

The metallogenic databases: mapping and modelling ore deposits

Several raw materials digital databases on local, national and European levels resume the mineral occurrences and spatial distribution (e.g., MINTELL4EU, EuroLithos, REESERVE, Minerals4EU, SCREEN), each one of which has a particular focus.

However, the sustainable management and exploration of raw materials require a deep understanding of their geological context and genesis. That is achieved through comprehensive, mineralisation-focused geological mapping, critical for environmental and prospecting planning, underpinning the creation of robust metallogenic models and prospectivity maps.

The traditional knowledge approach of metallogenic representation relies on cataloguing ore deposits and binding them to the geological history of the area on metallogenic maps (McCuaig and Hronsky, 2014; Hronsky and Kreuzer, 2019; Pohl, 2022), providing the foundational framework for:

- identifying mineralised areas.
- illustrating the kinematic and dynamic evolution of ore-forming processes.
- revealing the critical controls of structures and geochemistry on fluid flow and mineral deposition.

Geographic Information Systems (GIS) are pivotal in the modernisation of these studies, enabling the creation of integrated databases that combine geology, structures, and metallogenesis with precise geographical positioning (Knox-Robinson and Wyborn, 1997). The flexibility of GIS allows for the generation of multi-scale maps that illustrate the distribution of structures and mineralisations, thereby illuminating the geological and geochemical mechanisms that drive metallogenesis and minerogenesis (Billa et al., 2004; Lang, 1961; McCuaig and Hronsky, 2014).

The metallogenic database of Sardinia

This work directly contributes to all the objectives mentioned by providing a modern, data-driven foundational database for re-evaluating and guiding the future exploration of mineral potential of Sardinia, a region with a long, rich history of mining.

Two metallogenic maps of Sardinia were drafted in 1978 and 2008 (Marcello et al., 1978; Tocco et al., 2008), representing the pillars of ore-related knowledge in the region for almost 40 years. They illustrate over 600 mineralizations of different types, some of which are notable for their CRM content, reflecting Sardinia's great metallogenic diversity: Cambrian-age MVT and SEDEX Pb-Zn deposits; Ordovician REE paleoplacers and oolitic Fe deposits; Carboniferous-Permian orogenic-gold-type Au-As-Sb-W mineralizations; Permian granite-related Pb-Zn-Cu skarns, As-Sn-W hydrothermal veins, Mo-W-Sn-REE greisen, and feldspar pegmatites; post-Variscan hydrothermal veins of Pb-Zn, F-Ba-Pb-Ag, and Ni-Co-As-Bi-Sb; bauxites in Cretaceous carbonate successions; and Miocene volcanic-associated epithermal Au-Cu-Te and Au-Ag deposits, manganese, bentonites, kaolinite, and zeolites.

The plan to update the metallogenic database of Sardinia is a collaborative project between ISPRA (Italian Institute for Environmental Protection and Research) and the University of Cagliari (UniCa), Italy. It aims to modernise the legacy data from the previous Metallogenic Maps and the former Sardinian Mining Agency (Ente Minerario Sardo - EMSA), integrate new data to meet the 2023 economic and geopolitical demands, and to elaborate data-driven methodologies to study and discover ore deposits. The project is hierarchically structured within the Geosciences Infrastructure Research initiative, part of the National Recovery and Resilience Plan (PNRR), Mission 4, Component 2, Investment 3.1, under the title "Sardinia's Mineral Resources Database Update: New Exploration Guides for Identifying Critical and Strategic Raw Materials for Decarbonization and the Ecological Transition".

For the mentioned purposes, we synthesised Sardinia's multifaceted geological information through the construction of a robust relational database of the mineralisation of Sardinia. The relational nature of the geodatabase makes it a dynamic tool that facilitates complex queries, spatial analysis, and integration with diverse datasets within a Geographic Information System (GIS) environment. Detailed studies easily sustain the integration of data into this infrastructure. For instance, in this work, we propose two case studies which we used to implement the database. They are elected as representatives of the complex interplay of different types of mineralisation and, for their characteristics, a different approach to study:

- The Rosas – Orbai sulfides skarn deposits and later fluorite-barite hydrothermal veins are strongly controlled by the structural evolution of the area, which offered a good field of application of the database implementation and metallogenic representation on a map at a detailed scale.
- The Su Laccheddu Mo-W-LREE greisen system is a great example of a more geochemically controlled system, with a complex mineral assemblage requiring petrological analyses and where new geochronological analyses were possible.

Moreover, the application of such an integrated database allows for the transition from descriptive models to predictive ones. The natural data schematisation allows to easily extrapolate genetic model for the ore deposit types. Crossing these models with our knowledge on the regional mineralisations allows us to choose parameters and weights on their distinctive characteristics, which are necessary for the Mineral Prospectivity Modelling (MPM). We applied it to some of the most common CRM-bearing ore deposits in Sardinia, skarn and hydrothermal veins, using mathematical and statistical methods to identify areas with high potential for hosting mineral deposits by combining multiple predictive maps (e.g., fault density, lithological contacts, geochemical anomalies). The Sardinia metallogenic database was then used as a spatial control guide for the Mineral Prospectivity Model validation.

2. Geological framework

Sardinia is a composite crustal segment of the Variscan orogenic chain, whose present-day architecture results from the superposition of multiple Palaeozoic to Cenozoic stratigraphic and volcanic sequences, along with magmatic intrusions (Figure 2.1). This complex evolution has been instrumental in generating a remarkable diversity of ore deposit types, making Sardinia one of the most historically important mining regions of the Mediterranean.

2.1. Lithostratigraphic evolution of Sardinia

The pre-Variscan basement of Sardinia consists of a thick succession of sedimentary and minor volcanic rocks deposited along the northern margin of Gondwana from the Early Cambrian to the Early Devonian. Although broadly correlatable across the island, the lithostratigraphic record varies considerably between regions, reflecting differences in paleogeographic setting, subsidence history, and the degree of subsequent tectonic reworking.

In southwestern Sardinia (Sulcis-Iglesiente), the Paleozoic stratigraphic succession is particularly well preserved and comprises, from base to top: the lower Cambrian Nebida Formation (Pillola et al., 1995), consisting of siliciclastic and carbonate deposits marking the onset of platform sedimentation; the lower Cambrian Gonnesa Formation (Pillola et al., 2002), composed of massive to stratified platform limestones representing the primary reactive carbonate host for later mineralising processes; the middle Cambrian Campo Pisano Formation (Pillola et al., 2002), characterised by layered, marly, and nodular limestones; and the upper Cambrian – lower Ordovician Cabitza Formation (Pillola et al., 2002; Loi et al., 2023), composed of phylladic siltstones and clays. The top of this succession is marked by the Sardic Unconformity (Stille, 1939), a major tectonic and stratigraphic discontinuity related to the Ordovician geodynamic reorganisation of the Gondwana margin (Carmignani et al., 1982, 1994), which separates the Cambrian-lower Ordovician sequences from the overlying siliciclastic successions.

Above the unconformity, the Middle-to-Upper Ordovician Monte Argentu, Monte Orri, Portixeddu, Domusnovas and Rio San Marco Formations consist of siliciclastic deposits, conglomerates, and phyllites, followed by Silurian to Lower Devonian shales and limestones. Glacio-eustatic deposits and overlying Silurian black shales mark a shift to deeper marine conditions at the end of the Ordovician (Loi et al., 2023).

Devonian-to-Carboniferous sedimentation was strongly influenced by the progressive onset of the Variscan orogeny. Siliciclastic basins developed synchronously with deformation and metamorphism and were ultimately involved in large-scale nappe stacking and crustal thickening (Carmignani et al., 1994). These successions are variably preserved due to later tectonic reworking.

In central and southeastern Sardinia the pre-Sardic phase is mainly represented by the San Vito Formation (Calvino, 1963) and the Solanas Formation (Minzoni, 1975), a primarily terrigenous platform marine siliciclastic sequence (Loi et al., 2023) made of well-stratified sandstones and siltstones with carbonate layers.

The Cambrian-Lower Ordovician succession is cut by the Sarrabese unconformity (Calvino, 1959), over which lie the Middle-Upper Ordovician volcano-sedimentary succession consisting of conglomerates of the "Metaconglomerati" di Muravera Formation at the base and volcanic rocks with calc-alkaline affinity (e.g., Santa Vittoria, "Porfiroidi" Auct., "Porfidi grigi" Formations) (Carmignani et al., 1994)., The occurrence of volcanic rocks marks the main lithostratigraphic difference with the southwestern sequence. The volcanic lithologies are overlaid by Upper Ordovician transgressive siliciclastic succession characterized by conglomerates, arkoses, greywackes and siltstones (Punta Serpeddì, "Metarcose" di Genna Mesa, "Argilloscisti" di Rio Canoni formations), calcarenites and silicified limestones ("Quarziti del Sarrabus", Tuviois formation), and interlayered alkaline metabasalt (Carmignani et al., 2001). The post-Sarrabese succession continues with Silurian-Lower Devonian marine carbonaceous black shales and limestones ("Scisti a graptoliti", Naud, 1979; Corradini et al., 2001), Middle Devonian-Lower Carboniferous limestones ("Calcari di Villasalto" Formation) and by scattered Lower Carboniferous syn-tectonic siliciclastic deposits (Pala Manna Formation - Barca et al., 2003). Finally, the Variscan metamorphic basement was intruded during the late Carboniferous-Permian by the plutonic complex (the so-called Sardinia-Corsica batholith) and related dike complex.

The most notably sedimentary deposits during the Mesozoic are the limestone platform formations outcropping in eastern (Monte Albo, Siniscola; Ogliastra) and northwestern Sardinia (Nurra - Anglona).

The Cenozoic Era is characterised by two main magmatic events: the calc-alkaline Oligo-Miocene suite outcropping as dacite and rhyodacites in western Sardinia (Lustrino et al., 2007); the Plio-Pleistocene anorogenic cycle with OIB affinity, represented by basalts, trachytes and hawaiites (Petteruti Lieberknecht et al., 2003; Peccerillo, 2017).

The complex, multi-phase magmatic history of the Palaeozoic and Cenozoic, closely linked respectively to the late and post Variscan phases and the geodynamic evolution of the western Mediterranean, are described in detail in the next paragraphs.

2.2. The late-Variscan intrusive suites

Sardinia records a complex, multi-phase magmatic history spanning from the Palaeozoic to the Quaternary, closely linked to the geodynamic evolution of the western Mediterranean.

The most volumetrically significant intrusive event corresponds to the late- to post-Variscan magmatic pulse (ca. 340–280 Ma), which produced the Sardinia–Corsica Batholith. Plutonic bodies are particularly well exposed in northern and central Sardinia, including the Gallura, Logudoro, and Barbagia regions, where they occupy the axial zone of the Variscan belt, and in the Sarrabus region, in southeastern Sardinia. Smaller volumes but notable intrusions are spread across southwestern Sardinia, Sulcis and Iglesiente regions.

The sequence is characterized by a calc-alkaline affinity, predominantly peraluminous to metaluminous granitoids, ranging in composition from gabbro-diorite to monzogranite and leucogranite, and reflects a prolonged magmatic evolution from early, syn-tectonic peraluminous monzogranites and granodiorites to late, post-tectonic suballuminous, F-bearing, ferroan compositions (Carmignani et al., 2001; Conte et al., 2017).

The ages of these granitoids cluster between 305-300 Ma and 290-285 Ma, namely the Old Magmatic Peak (OMP) and the Young Magmatic Peak (YMP) (Naitza et al., 2017).

The OMP is represented by granodiorites, monzogranites and tonalites in the Arbus and Sarrabus southern regions. A significant mantle contribution is evidenced by the gabbroid terms of the lithologies and by the magnesian to ferroan-alkaline composition. These were emplaced as large, shallow-dipping sheets, with magmatic foliations and lineations indicating a N120–140 stretching direction (Gattacceca et al., 2004).

The younger leucocratic intrusions (295–285 Ma) were emplaced within tensional fractures (Gattacceca et al., 2004; Cuccuru et al., 2016), and the later emplacement of Permian dyke swarms confirms a sustained period of crustal extension. They were formed by F-bearing, reduced ilmenite-series, and water-undersaturated magmas, generating ferroan granites with a granophile-type metallogenic signature with Sn-W-Mo and U-Th-Nb-Ta associated skarn, greisen and hydrothermal veins. These includes monzogranites, granodiorites and leucogranites of Quirra, Monte Linas, Monte Genis and Sulcis granites in southern Sardinia (Conte et al., 2017).

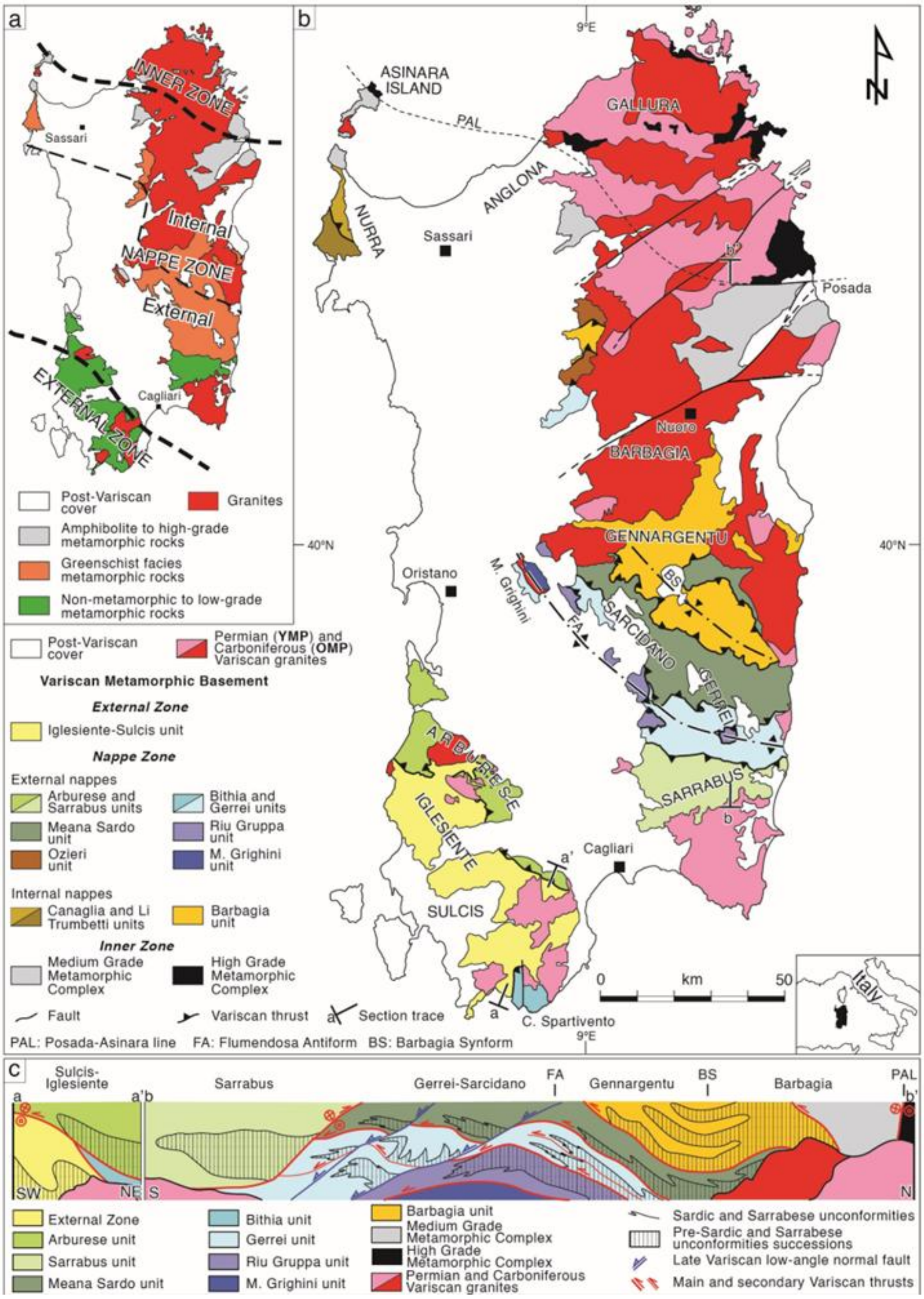

Figure 2.1: Geological sketch map of the Variscan basement of Sardinia. Modified by (Cocco and Funedda, 2019) after Oggiano et al. 2010.

2.3. The Cenozoic magmatism

During the Oligo-Miocene (ca. 32–15 Ma), Sardinia occupied an active position along the southern European continental margin above the subducting Apulian–Adriatic plate, generating calc-alkaline to high-K calc-alkaline and locally shoshonitic magmatism (Lustrino et al., 2007). This magmatic episode consists of arc volcanism and associated shallow-level intrusions, comprising predominantly andesitic to dacitic porphyries and microgranodiorites. Cenozoic intrusions and volcanic centres are particularly widespread in western Sardinia (Sulcis, Campidano margins) and in Logudoro, Planargia and Anglona regions (Figure 2.2). Within-plate basaltic volcanism occurred in Plio-Quaternary times in central-western Sardinia (Montiferru, Meilogu, and northern Campidano areas).

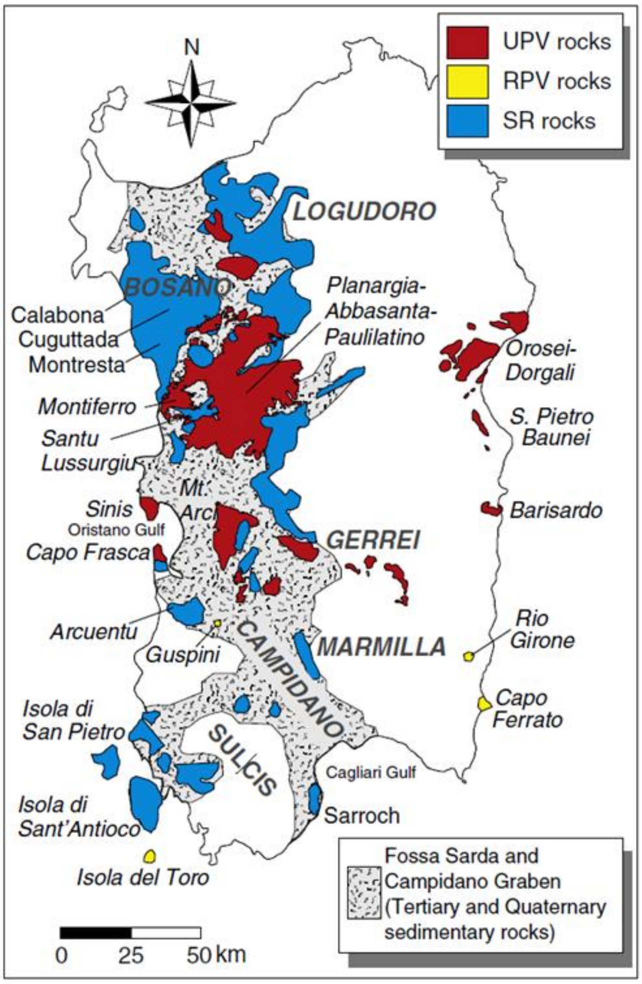

Figure 2.2: Cenozoic volcanics of Sardinia. Blue - calc-alkaline suites; yellow and red – alkaline suites (Lustrino et al., 2013).

2.4. Structural and geodynamic evolution

The structural framework of Sardinia is the result of a polyphase tectonic history in which Ordovician, Variscan, and Cenozoic deformation events have successively overprinted and exploited pre-existing crustal anisotropies. Ordovician deformation (Sardic phase) produced significant folding and uplift of the Cambrian–Lower Ordovician strata, generating angular unconformities and establishing long-lived structural fabrics that would later influence fluid pathways and ore localisation (Calvino, 1959; Cocco and Funedda, 2019).

The Variscan Orogeny (Late Devonian–Carboniferous, ca. 360–320 Ma) is by far the dominant tectonic event recorded across the island. Continental collision between Gondwana and Laurussia resulted in the development of a fold-and-thrust belt characterised by nappe stacking, tight to isoclinal recumbent folds, and a pervasive tectonic fabric. The orogenic transport direction was initially top-to-the-SSW, later rotating clockwise to a top-to-the-W direction (Funedda, 2009). Associated crustal thickening drove high-temperature, high-pressure (HT-HP) metamorphism whose grade varies systematically across the island: eclogitic and granulitic facies, with local anatexis and migmatite formation, are documented in northeastern Sardinia (Gallura region), while amphibolite facies conditions characterise the central sector, and greenschist to very low-grade facies prevail in the central-southern regions, including the Sulcis-Iglesiente and Barbagia areas (Carmignani et al., 1982; Franceschelli et al., 2005).

In the Sulcis-Iglesiente region, the most significant structure is the Arburese Thrust (AT), along which the Variscan Nappe Zone (Arburese Unit) was emplaced over the Variscan External Zone (Conti et al., 2001; Funedda, 2009). This thrusting event imposed high strain in the footwall, generating widespread ductile-to-brittle shear zones (e.g., the Rosas Shear Zone of Sulcis - RSZ), fold-thrust complexes, and the tectonic dismemberment of competent lithologies such as Cambrian limestones (Funedda, 2009; Attardi et al., 2020). In the Arburese and Iglesiente sectors, these shear zones are concentrated in the footwalls of major thrusts and are associated with the formation of mylonites and cataclasites. In northeastern Sardinia, the deeper structural levels exposed in the Gallura and Ogliastra areas document the axial zone of the Variscan belt, with pervasive migmatisation and large-scale ductile shear zones indicative of mid-to-lower crustal deformation (Oggiano et al., 2007; Casini et al., 2012).

Late and post-Variscan phases (ca. 320–280 Ma) were characterised by progressive relaxation of the compressional regime, post-orogenic extension, and the intrusion of voluminous calc-alkaline granites that formed the Sardinia–Corsica Batholith. The exhumation of the Variscan chain was accompanied by the emplacement of mafic and acidic dykes, as well as hydrothermal veins, along NE-SW and NW-SE trending normal and strike-slip faults. Permian–Triassic extension further promoted lithospheric thinning, emplacement of mafic to felsic magmas, and the formation of continental basins (Carmignani et al., 1994). These post-orogenic extensional structures were subsequently reactivated during the Alpine orogeny (Mesozoic) and, most significantly, during the Oligo-Miocene rotation of the Sardinia–Corsica block. This latter event, associated with the opening of the Ligurian–Provençal basin, involved a counter-clockwise rotation of approximately 45° (Gattacceca et al., 2007) and was accompanied by renewed NE-SW extension, the formation of the NW-SE trending western Sardinia tectonically-controlled sedimentary basins, and widespread calc-alkaline to shoshonitic volcanism concentrated in western Sardinia (Carmignani et al., 2001). Although younger than the main metallogenic events, Cenozoic tectonic and magmatic activity locally reactivated pre-existing structures and facilitated the remobilisation of earlier mineralisation (Funedda et al., 2018; Cocco et al., 2022a; Naitza et al., 2024).

2.5. Metallogenic evolution

Sardinia hosts one of the most diverse and historically productive metallogenic provinces in the Mediterranean, with different ore deposit types spanning from Palaeozoic to Cenozoic in age. The island's metallogeny is spatially and genetically linked to the polyphase tectonic, magmatic, and hydrothermal history, and is particularly concentrated in the Sulcis-Iglesiente and Arburese districts of southwestern Sardinia, as well as in the central and northeastern sectors.

The geological history of Sardinia is characterised by distinct metallogenic periods (Naitza et al., 2024), each linked to major geodynamic events spanning from the Early Cambrian through the Cenozoic (Table 2.1).

In the early Paleozoic two different provinces, southwestern and eastern Sardinia, may be delineated, each with a different geological and metallogenic.evolution. The two provinces started to share a common metallogenic history from the onset of late Variscan large-scale shear zones (Edel et al., 2014) and the emplacement of late Carboniferous-early Permian post-collisional granites (Secchi et al., 2022).

Following the regional metallogenic synthesis of Naitza et al. (2024), three main metallogenic peaks are recognised based on the Variscan orogeny.

- The pre-Variscan Peak (Cambrian to Carboniferous) produced large mineral deposits and proto-ores in syn-sedimentary, diagenetic and hydrothermal systems, particularly concentrated in southwestern Sardinia.
- The Variscan Peak (Carboniferous to Early Permian) encompasses a broad spectrum of orogenic and intrusion-related ore types intimately associated with post-collisional extensional tectonics, which facilitated large-scale fluid circulation driven by the thermal anomaly generated by the emplacement of granitoid intrusions.
- The first post-Variscan Period (Permian to Triassic) is characterised by the remobilisation of older ore deposits by low-temperature hydrothermal fluids, leading to the formation of new ore deposits at shallow depth.

Pre-Variscan Metallogeny

In southwestern Sardinia metallogenic province, the Cambrian – Devonian passive-margin setting laid the basis for crustal metal sources by favouring large-scale sedimentary and diagenetic concentration processes, whereas in eastern Sardinia province the onset of the Middle-Upper Ordovician volcanic arc corresponded to a relevant phase of crustal fertilization, although the only significant deposits are related to sedimentary, post-arc mineral systems. In detail:

i. During the pre-Sardic phase (Early Cambrian-early Ordovician), sedimentary-exhalative (SEDEX) to Mississippi Valley-Type (MVT) Pb-Zn deposits formed in the Iglesiente-Sulcis district (SW Sardinia) within platform successions as a result of syn-sedimentary to early diagenetic processes and basin-scale fluid circulation (Boni et al., 1996; Santoro et al., 2023).
ii. In southwestern Sardinia, the middle Ordovician Sardic tectonic phase (Loi et al., 2023) is characterised by basin reconfiguration following regional uplift and erosion, generating unconformity-related and karst Ba-Pb and Zn-Pb deposits (Padalino et al., 1972; Bechstädt and Boni, 1994; Boni et al., 2003).
iii. In eastern Sardinia, the early-middle Ordovician Sarrabese tectonic phase (Loi et al., 2023) resulted from convergence and subduction, with a volcanic arc calc-alkaline magmatism to which volcanic-exhalative base metal proto-ores are referred (Garbarino et al., 1989). The post-Sarrabese phase (late Ordovician-late Devonian) was characterized by widespread erosion of the volcanic arc and development of sedimentary mineral systems: Ti-Zr-REE-rich placers (Pistis et al., 2016), oolitic iron deposits (Oggiano and Mameli, 2006) and

protores linked to concentrations of U, V, and Ni-Co-As in carbonaceous black shales (Naitza et al., 2024; Boni et al., 2025).

Variscan Metallogenic Peak

During the Carboniferous – Early Permian period, the Southern Variscan orogenesis (ca. 320–290 Ma) shaped the structural and compositional features of the Sardinian metamorphic basement and the later Sardinia-Corsica batholith. Recent syntheses conceptualise this evolution as the Sardinian Variscan Mineral System (SVMS), a crustal-scale system driven almost entirely by crustal reworking, with negligible direct mantle metal input (Naitza et al., 2024).

Two main ore types define this metallogenic peak:

iv. Orogenic-Type Deposits reported only in eastern Sardinia, comprise mesothermal to epithermal As-Sb-W-Au ± (Pb-Zn-Cu, Ag) vein systems (e.g., Baccu Locci, SE Sardinia) (Garbarino et al., 2003). They are structurally controlled by regional shear zones and folds, with mineralising fluids derived from crustal metamorphic dehydration. These mineralisations occurred during late- to post-collisional extension and are spatially unrelated to exposed granitoids (Funedda et al., 2011, 2018).

v. Intrusion-Related Deposits found in both southwestern and eastern Sardinia, comprise diverse types associated with the emplacement of the Sardinian Batholith. The highest reactivity is inferred to the highly evolved, F-bearing, ilmenite-serie granites (GS1 suite) of the Younger Magmatic Peak (YMP, ~291–286 Ma), products of low-degree partial melting of a metal-rich lower crust (Naitza et al., 2017). They include:
   - Sn-W-Mo-Bi-F mineralisation (e.g., Monte Linas, Monte Limbara districts) and hosted by greisen, pegmatites, skarn, and high-temperature hydrothermal systems.
   - Pb-Zn-Cu-Ag-Fe ± LREE skarn and hydrothermal vein deposits are related to more oxidised granitoid suites (e.g., Funtana Raminosa district), or possibly involving remobilisation of base metals from Cambrian ores (e.g., Rosas-Orbai district).

Post-Variscan Metallogeny

vi. During the Permian-Jurassic period, extensional tectonics spanning Permian to Jurassic, mainly caused localised hydrothermal remobilisation and supergene enrichment of pre-existing deposits. It generated low-temperature polymetallic Pb-Zn ± Ag ± Ga-Ge-In (Moroni et al., 2019; Scano et al., 2023) and Bi-Ni-Co-As-Fe (five-element type) veins (Scano et al., 2023) (e.g., Arburese district - Montevecchio, Pira Inferida), F-Ba veins (e.g., Silius, Asuni, Gerrei district) (Boni et al., 2009; Castorina et al., 2020; Bakos, 1972a) and Ba ± Zn-Pb karsts.

vii. Bauxite deposits formed during the Cretaceous pedogenesis (Mameli et al., 2007) in the Nurra district (NW Sardinia).

viii. The Cenozoic Metallogenic Peak (Oligocene-Miocene) is characterised by mineral deposits expression of the volcanism associated with subduction-related magmatism in western Sardinia: Au-Cu-Mo porphyry systems, Au-As-Te high sulfidation (HS) and Au-Ag-Sb low-sulfidation (LS) epithermal deposits (Lattanzi, 1999; Fiori and Grillo, 2001; Fadda et al., 2017), as well as small volcano-sedimentary Mn deposits.

Metallogenic peak	***Geological Age***	***Ore Deposits & Characteristics***	***Tectonic Setting & Key Processes***
Pre-Sardic/Sarrabese Phase	Early Cambrian – Early Ordovician	SEDEX and MVT/Irish Type systems Pb-Zn – (Fe) mineralisations	Passive margin, evolution from siliciclastic to carbonate basins promoted metal concentration.
Sardic/Sarrabese Phase	Middle – Late Ordovician	Karst-hosted Ba-Zn-Pb deposits Sedimentary & volcanic-exhalative base metal protores	Compressive tectonic, unconformities and folding Metal pre-concentration and fluid circulation in a conducive tectonic environment.
Post-Sardic/Sarrabese Phase	Late Ordovician – Late Devonian	Ti-Zr-LREE marine placers Fe-rich oolitic deposits U-V-base metals deposits	Marine conditions with anoxic environments. Sedimentary concentration of heavy elements.
Variscan Peak	Carboniferous – Early Permian	Intrusion-related As-Sb, W-Sn-Mo-Bi, F-Pb-Zn-Cu greisens, skarns and hydrothermal veins	Post-collisional extensional tectonics. Large-scale HT fluid circulation and emplacement of granitoid intrusions.
Post-Variscan Period I	Permian – Triassic	Pb-Zn (Ag, Ga-Ge-In) veins F-Ba-Pb-Ag-LREE veins Ba, Zn-Pb supergene	Low-temperature hydrothermal fluid circulation. Remobilisation and alteration of pre-existing ore deposits.
Post-Variscan Period II	Cretaceous-Miocene	Bauxite-LREE paleosoils Epithermal Au-Ag-Te-Cu HS and LS Mn deposits	Sedimentary and volcano-sedimentary promoted concentration and alteration.

Table 2.1: Scheme of the Sardinian Metallogenic Peaks.

3. Materials and Methods

3.1. Relational Database Architecture and Development

The creation of a relational database follows a structured workflow (Figure 3.1) to ensure data integrity, efficiency, and scalability. It begins with a requirements analysis, where we gather and document what data needs to be stored and how it will be used. This leads to conceptual design, which defines the high-level entities and their relationships. The next phase is logical design, which organises these entities and relations into a detailed schema of tables, columns, primary keys, and foreign keys (Figure 4.1). To eliminate redundancy and avoid anomalies, the schema undergoes a normalisation process, organizing data to reduce dependency and applying controlled vocabularies to avoid redundancy. Finally, physical implementation brings the design to life, where the database is implemented and queried using SQL statements to populate and retrieve data, indexes are set up for performance, and the tool can be deployed to the target environment.

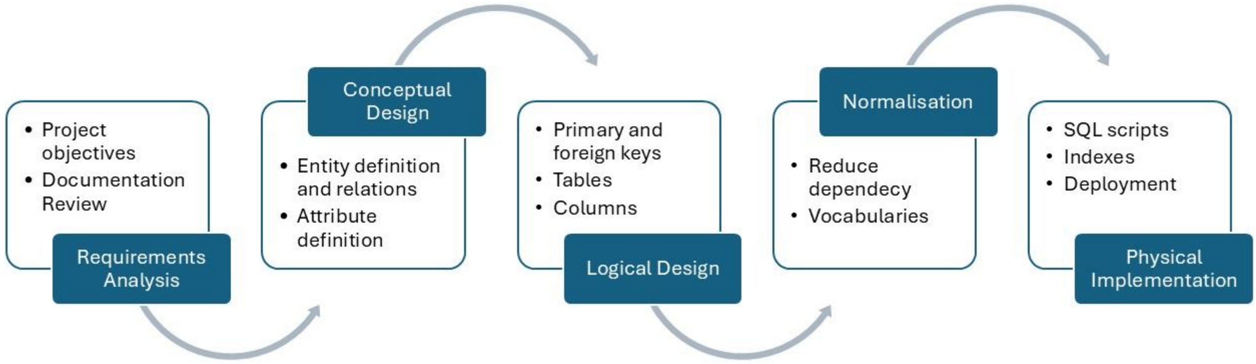

Figure 3.1: Relational Database development workflow.

The database was built using PostgreSQL 17+ as the database management system, with the PostGIS 3+ extension for geographic object support (Zhang and Yi, 2010; Chaudhry and Yousaf, 2019). These ensure:

- Data relationships: complex relationships between entities are efficiently managed (e.g., a site can have multiple minerals and a complex mining history).
- Spatial Querying: queries based on parameters, location, and spatial relationships are natively possible.
- GIS integration: the database interfaces with GIS environments, making it an ideal backend for mapping and spatial analysis.
- Scalability and interoperability: the database is designed to be continuously updated and integrated with new data and other regional, national, and European databases.

The development involved: 1) a complete revision of 563 pre-existing points; 2) integration of recent ore deposit studies, focusing on Critical and Strategic Raw Materials (CRM, SRM); 3) insertion of new mineralised points; and 4) review of historical archives of the Sardinian Mining Agency (*Ente Minerario Sardo* - EMSA).

This resulted in a comprehensive inventory of over 630 points related to mineral occurrences, deposits, and active mines.

The schema was designed to reflect the logical relationships between geological entities (Sites, Commodities, Structures, etc.). Data compilation involved:

- Data Sources: Digitising and validating legacy data from EMSA reports, the 1978 and 2008 Metallogenic Maps of Sardinia, geological features from the geoportalesardegna, scientific literature.
- Spatial Referencing: All site locations were meticulously revised using orthophotos, Regional Technical Maps, and geological maps from the RAS geoportal. Coordinates are stored in the EPSG:3003 (Monte Mario / Italy zone 1) reference system within the PostGIS geometry fields.
- GIS Workflow: QGIS was used as the primary GIS clients to connect to the PostgreSQL/PostGIS database, allowing for simultaneous editing, visualisation, and spatial analysis.

3.2. Field and Laboratory

Structural Geology

Detailed structural mapping was conducted at key sites and disitricts (e.g., Rosas – Orbai district, Su Laccheddu site, Fluminese district, Muscadroxiu mine – Silius) to characterise ore-controlling structures.

Methodology for EMP analyses

Mineral chemistry for white mica, feldspar, carbonates, apatite, and monazite was determined using wavelength-dispersive spectrometry (WDS) with a Jeol JXA8530F Hyperprobe Field Emission EPMA at the Department of Earth Sciences, Uppsala University, Sweden. All analyses were performed using an accelerating voltage of 15 kV.

For white mica, Si, Al, Fe, Mg, Na, K, Ca, Ba, Mn, Ti, Ni, Cr, and Cl were acquired using a probe diameter of 10 µm and a beam current of 10 nA.

For feldspar, Si, Al, Na, K, Ca, Ba, Sr, Fe, Mg, Mn, Ti, Ni, Cr, Cl, and F were acquired using a probe diameter of 10 µm and a beam current of 10 nA.

For carbonate, Ca, Mg, Fe, Mn, Sr, Ba, S, La, Ce, Pr, Nd, Sm, Eu, Gd, Tb, Dy, Ho, Er, Tm, Yb, Lu, and F were acquired using a probe diameter of 5 µm and a beam current of 20 nA.

For apatite, Ca, P, F, Cl, S, Na, Sr, Ba, Y, Pb, Th, U, La, Ce, Pr, Nd, Sm, Eu, Fe, Mn, Si, and Al were acquired using a probe diameter of 15 µm and a beam current of 20 nA.

For monazite, P, Si, Al, Y, Pb, Th, U, Ca, La, Ce, Pr, Nd, Sm, Eu, Gd, Tb, Dy, Ho, Er, Tm, Yb, Lu, and Fe were acquired using a probe diameter of 1 µm and a beam current of 60 nA.

Methodology for Rb/Sr Geochronology

Geochronological and chemical analysis of biotite was performed at the Fipke Laboratory for Trace Element Research (University of British Columbia Okanagan, Kelowna, Canada). Data was gathered during one analytical session using an ESL NWR 193 excimer laser ablation (LA) apparatus with a TwoVol3 ablation cell connected to an Agilent 8900 inductively coupled plasma reaction-cell mass spectrometer (ICP-MS/MS). The Rb/Sr geochronology setup follows the protocol of Larson et al. (2023) that is based from Zack and Hogmalm (2016) and Redaa et al. (2021).

Laser ablation was performed on the minerals *in situ* using standard thin sections (30 µm thickness) with a 60 µm beam diameter, a 5 Hz repetition rate, and fluence of ~3.5 J/cm^3.

The geochronological ratios from the raw measured data are calculated with Iolite software (v. 4.10; Paton et al., 2011) using an in-house data reduction scheme for Rb/Sr (Larson et al., 2023; 2024). The data reduction scheme includes background-subtraction, and correction for both instrument drift and downhole fractionation of the raw data (Paton et al., 2010). The isochron date was calculated using IsoplotR (Vermeesch, 2018).

3.3. Mineral Prospectivity Modelling

A Mineral Prospectivity Modelling (MPM) workflow was implemented using Fuzzy Set Theory (Zadeh, 1965) to demonstrate the database's application for predictive modelling. This statistical methods is widely applied to mineral prospectiveness evaluation (Carranza and Hale, 2001; Porwal et al., 2003; Luo and Dimitrakopoulos, 2003; Nykänen et al., 2008; Carranza, 2012; Ford and Blenkinsop, 2008).

The process involves:

1. defining a genetic model for a target deposit type to identify critical spatial criteria.
2. processing geospatial data into fuzzy membership maps (0–1 value) representing these criteria.
3. integrating maps using a Fuzzy Gamma operator to generate a prospectivity map.
4. validating the model by quantifying the spatial correlation between high-prospectivity zones and known deposits.

While applying a more data-driven possible fuzzy scores attribution, a percentage of uncertainty was covered by experience-based attribution, which is expected to balance this kind of models (Zimmermann and Zysno, 1980). The validation is exclusively evidence-based, considering the true and false positives and negatives.

4. The Database architecture

The vast amount of historical exploration and exploitation data for Sardinia's mineral occurrences and ore deposits needed a systematic reorganisation and synthesis into the Metallogenic Database of Sardinia. Designed to describe, classify, and spatially locate mineral sites, this resource serves as a foundation for predictive modelling and assessing mineral deposits across the region (Table 4.1).

It is inherently a relational geospatial database developed within a GIS environment, implemented through QGIS and PostGIS (via PostgreSQL and PgAdmin). The database is structured as a dynamic and flexible tool for both research and exploration, and its parameters are chosen to describe the mineralisations. Its architecture is designed for continuous expansion, allowing it to incorporate new data and remain current. Data are stored in separate, thematic tables (e.g., sites, materials, minerals, type) related to each other by a unique "id" for each geographically placed site (Figure 4.1). This prevents duplication, ensures information consistency, allows new data entry and complex queries for checking and updating data (e.g., "*find all mineralisation within 1km of a major fault that contains certain elements and has been mined*"). The schema design anticipates the addition of new data types by simply adding a new table and using the corresponding "*id*".

What marks the transition of this database from a repository to a predictive tool is the possibility of easily finding patterns through:

- Queries: to generate derivative maps and conduct quantitative and statistical analyses (e.g., "map every skarn mineralisation in a 2km radius from a main overthrust and list their mineralogical composition").
- Data coupling and visualisation: to analyse data as different layers and features on GIS (e.g., "couple the previous map with systematically gathered geochemical data").

Feature	*For Research*	*For Exploration*
Comprehensive Data	Metallogenic models	May have potential or not
Relational and Spatial	Analysing geological controls on the mineralisations	Hierarchisation of targets
Dynamic and Flexible	Allows integration of new research (e.g., geochronology, geochemistry)	Incorporates new exploration data (e.g., geophysics surveys) to refine targets
Coupled with Other Data	Creating holistic models	Core of the GIS-based prospectivity analysis.

Table 4.1: Scopes and utilities for the structure of the Metallogenic Database of Sardinia.

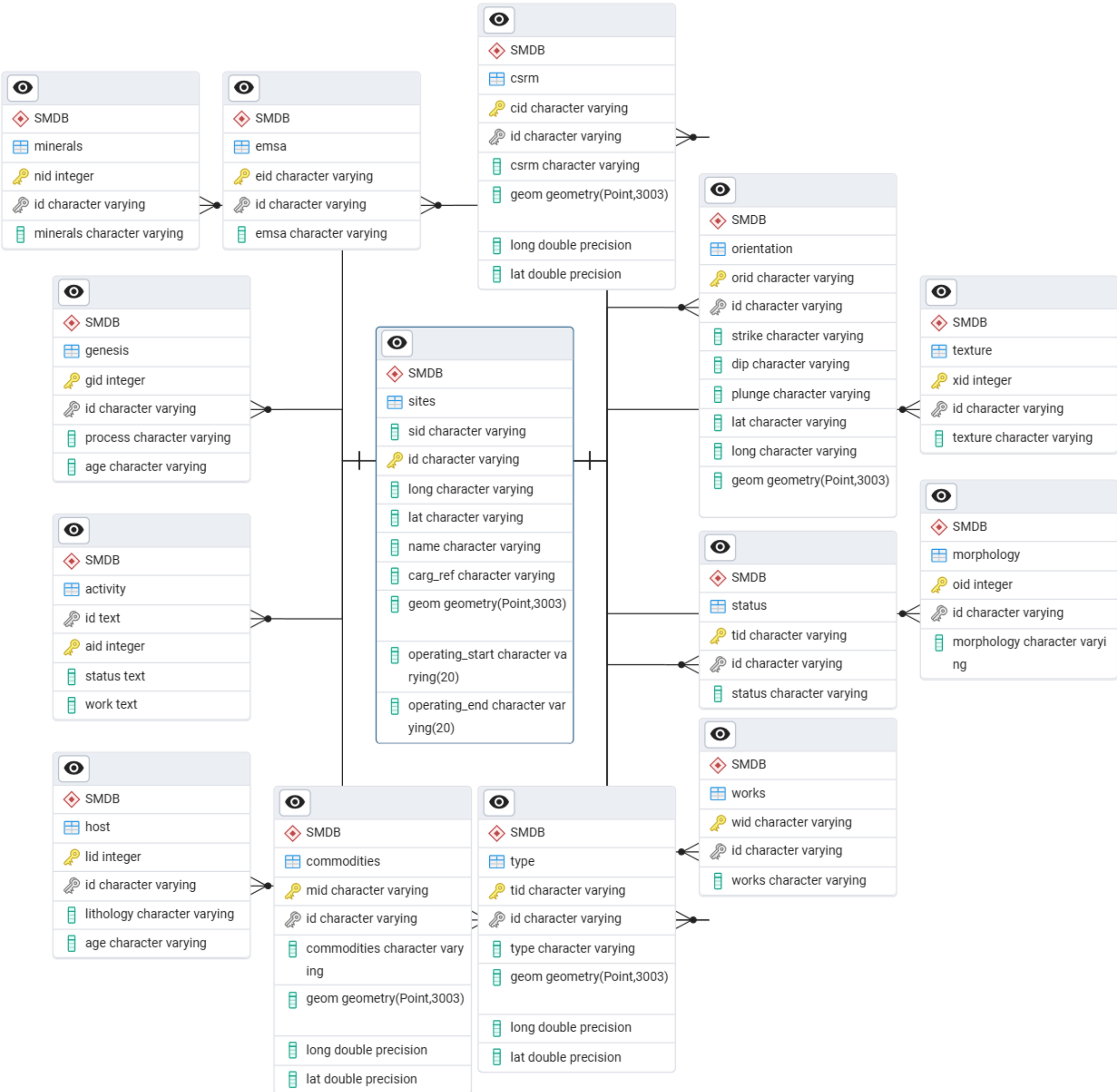

Figure 4.1: Entity Relationship Diagram (ER) of the Metallogenic Database of Sardinia

4.1. Relational tables

The relational geodatabase was constructed using PostGIS v3+ for PostgreSQL v17+ to manage the comprehensive geological, mineralogical, and structural attributes for each deposit designated as points. We adopted the local EPSG:3003 (Monte Mario / Italy zone 1) coordinate system.

The database schema comprises 12 tables, with relationships defined by a foreign key ("*id*"). The "*sites*" table stores the general information of the mineralisation (name, coordinates, etc.) and the foreign key to which all the other tables refer.

***sites*:** The primary table containing the deposit *id*, *name*, geographic coordinates, and the period of mining or exploration activity. The *sid* field contains the primary key for this table. The *id* field serves as the foreign key for all subordinate tables.

- *sid*: The primary identification key for the table entities.
- *id*: A unique numerical code assigned with a north-to-south progression, generally respecting the convention established in the 2008 Metallogenic Map. It's the foreign key for the other entities.
- *name*: The primary identifying name of the point. This can refer to an existing mining title (permit or concession), the locality, or the nearest prominent toponym. For practicality and accessibility, this version prioritises locality names easily found on the web or on recent Regional Technical Maps (CTR). Where present, the denomination from the previous metallogenic map is retained as a second name, separated by a hyphen.
- *lat, long*: Define the location of the point, expressed with kilometre coordinates in the EPSG:3003 – Monte Mario / Italy zone 1 reference system, stored as a geometry type in PostGIS. All points were meticulously revisited using orthophotos, geological maps, and technical reports to locate mineralised outcrops or representative mining sites precisely.
- *carg_ref*: The identification number of the official geological cartography (CARG) sheet in which the area falls.
- *operating_start, operating_end*: The historical period of mining activity and/or exploration.

***emsa*:** Contains the identification code linking each site to its corresponding record in the former Sardinian Mining Agency (EMSA) archive.

- *eid*: The primary identification key for the table entities.
- *id*: The foreign key relating to the *sites* table.
- *emsa*: The original identification number from the Ente Minerario Sardo (EMSA) reports related to the exploration and/or mining permit.

***activity*:** synthesise the kind of activities that were carried out in terms of exploration or exploitation.

- *aid*: The primary identification key for the table entities.
- *id*: The foreign key relating to the *sites* table.
- *status*: Classifies as: i) *hint* the known but unevaluated occurrences which could serve as guides for prospection, ii) *ore deposits*, the ones that have been subject to economic evaluation and/or extraction.

- *works*: identify active and inactive mines and quarries, exploration-only sites, mining wastes and inaccessible areas (anthropised, recovered).

***type*:** Defines the primary ore deposit class according to the most common international terms. For each point (same "*id*" and same coordinates), multiple types of ore deposits with different characteristics may be present, and the following attributes may refer to one type or another, to all of them or to part of them. To avoid redundancies and complications, we didn't assign each feature univocally to each type (which is possible at more detailed scales, e.g., the Rosas-Orbai database), but the simple terms can be applied to the right type by reading the general models for each type.

- *tid*: The primary identification key for the table entities.
- *id*: The foreign key relating to the *sites* table.
- *type*: It is assigned based on mineralogical composition, genesis, morphology, and geological context. Examples include greisen, skarn, low/high-sulfidation epithermal vein, porphyry, MVT (Mississippi Valley-Type), SEDEX, pegmatite, among others.

csrm: highlight the Critical and Strategic Raw materials found in the mineralisation.

- *cid*: The primary identification key for the table entities.
- *id*: The foreign key relating to the *sites* table.
- *c-srm*: Indicates the Critical and/or Strategic Raw Materials (CRMs/SRMs) present in the mineralisation. They include occurrences to permit prospect evaluation and ore modelling.

commodities: catalogues the economic raw materials (e.g., silver, barite, copper) present in the mineralisation.

- *mid*: The primary identification key for the table entities.
- *id*: The foreign key relating to the *sites* table.
- *commodities*: A comprehensive list of all raw materials present, including both critical/non-critical and strategic/non-strategic ones. This table expands upon the csrm table.

***minerals*:** explicate the most common mineralogical phases in which the economic materials can be found (e.g., galena, sphalerite, fluorite, chalcopyrite).

- *nid*: The primary identification key for the table entities.
- *id*: The foreign key relating to the *sites* table.
- *minerals*: The primary and secondary mineral species composing the mineralisation, including the hosts for CRMs and native metals (e.g., gold, silver).

morphology: describes the geometric form of the mineralised body (e.g., stratiform, tabular, lentiform).

- *oid*: The primary identification key for the table entities.
- *id*: The foreign key relating to the *sites* table.
- *morphology*: the geometric shape of the mineralisation.

texture: Describes the internal fabric of the mineralisations (e.g., brecciated, disseminated)

- *xid*: The primary identification key for the table entities.
- *id*: The foreign key relating to the *sites* table.
- *texture*: The macroscopic spatial relationships between the mineralisation constituents.

orientation: Records the spatial attitude information of the mineralised body using standard geological conventions.

- *orid*: The primary identification key for the table entities.
- *id*: The foreign key relating to the *sites* table.
- *strike*: The longitudinal direction of a planar body, at a right angle to the dip direction (0-360°).
- *dip*: The direction towards which the planar body dips (0-360°).
- *plunge*: The inclination of a linear body (0-90°).

genesis: Infers the genetic process and its age.

- *gid*: The primary identification key for the table entities.
- *id*: The foreign key relating to the *sites* table.
- *process*: The main genetic process (e.g., hydrothermal, skarn, sedimentary)
- *age*: the process age, generally expressed as the Period (e.g., Carboniferous, Ordovician)

host: Documents the lithology (e.g., limestone, dolomite, sandstone, shale, mafic dikes) and geological age of the immediate host rock.

- *lid*: The primary identification key for the table entities.
- *id*: The foreign key relating to the *sites* table.
- lithology: The host rock lithology (e.g., limestone, shale)
- *age*: the geochronological age, generally expressed as the Period (e.g., Carboniferous, Ordovician)

4.1.1. Controlled Vocabularies

The database employs controlled vocabularies to standardise terminology across key descriptive domains, ensuring data consistency and facilitating interoperability with international geological databases.

All terms have been standardised to English (lowercase) following international scientific conventions.

Uncertain classifications are marked with a question mark '(?)' suffix.

They are listed in APPENDIX B.

4.1.2. Data Quality and Integrity

To guarantee that the information is accurate, consistent, and the most reliable possible for spatial analysis and decision-making, a multi-layered strategy was implemented, combining database-level integrity checks on Postgres (through the PgAdmin interface) with application-level validation on QGIS.

Spatial Validation

All entities are represented by point vectors located using:

- satellite and aerial photos (from the 1950s) to check the presence of exploration or mining-related activities such as road construction, excavations, and waste depositions.
- topographic maps to match the toponyms and eventual recorded excavations. The national 1:10000 scale CTR and 1:25000 scale GMT were used.

- geological maps from the official 1:50000 official cartography for choosing the best representative location to frame the mineralisation in its geological context.

The locally projected layers are used as a reference to locate the mineralised sites brought to adopt the 3003: Monte Mario / Italy Zone 1 coordinate system.

Attribute Accuracy

Attribute accuracy is ensured through a combination of controlled vocabularies and relational integrity. As detailed in Appendix B (Controlled Vocabularies), key descriptive fields like lithology, commodities, and genetic process are populated with discrete terms listed in dedicated lookup tables. This approach prevents inconsistencies such as having "pegmatite" in one record and "pegmatites" in another, ensuring that data is not only stored but is also semantically consistent and ready for reliable analysis. Moreover, the vocabularies can be implemented with new terminology to add detail or to correct imprecise records.

4.2. Database symbology for cartographic representation

The cartographic symbology for the new Metallogenic Map of Sardinia is developed for its digital use and scalability. It was designed within the GIS environment to highlight Critical and Strategic Raw Materials (C-SRMs), their geological context, and economic relevance.

- Colour and Shape: Different colours identify the most common raw material associations, following the 2008 Metallogenic Map. In this version, each association is also assigned a unique geometric shape and size to visualise overlapping associations and to emphasise S-CRMs.
- Status Indicator: A circle around the symbol indicates the site's status: a solid black line for a deposit/mine, and a dashed line for mineral occurrences.
- Type: the most indicative 5 types, including hydrothermal veins, greisen, skarn, MVT and SEDEX are shown by symbols positioned on the top of the commodities and status indicators. For the types that tend to have a preferential elongation (veins and skarns), the symbol rotate clockwise from the north around the other site symbols, according to the strike direction of the mineralised body.
- Labels: Each symbol is accompanied by the “*id*” of the site.

This simple, structured and versatile design ensures the database scalability and representativeness.

Below, a brief description of the symbols.

Commodities

Aluminum/Bauxite: large orange circle	Vanadium - (Uranium - Thorium): small pink star in the bottom left of the site centre
Antimony – Arsenic: small mamgenta circle	(Gold - Tellurium): small yellow star in the top right corner of the symbol of the site centre
Cobalt - Nickel – Bismuth: small yellow circle	(Coal): small black dot
Copper: large green circle	(Talc): small white square
Fluorite – Barite: blue trapezoid	(Quartz): small with four-pointed star
Germanium: large light blue circle	(Perlite): small white dot
Rare Earth Elements (Light): Large yellow circle with dashed line	(Mica): small light grey parallelogram
Manganese – Iron: Small red pentagon	(Kaolinite): small white pentagon
Niobium – Tantalium: small brown circle	(Ceramic clay): orange rectangle
(Lead - Zinc - Silver - Pyrite): large transparent pentagon	(Bentonite): light grey rectangle
Tungsten - (Molybdenum - Tin): small grey circle	Feldspar: large pink square

Status

Ore deposit: large transparent, black contoured circle	Mineral occurrence/hint: large transparent, black dashed circle

Type

Greisen: green triangle on the top of the other site symbols	SEDEX: green horizontal rectangle on the top of the other site symbols
Hydrothermal vein: black vertical rectangle positioned of the strike direction of the mineralised body, counting clockwise for the north	Skarn: black dot positioned of the strike direction of the mineralised body, counting clockwise for the north
MVT: light blue horizontal rectangle on the top of the other site symbols	

4.3. The challenge of syntheses and ore modelling on a regional scale

The synthesis, schematisation and rationalisation of data to describe complex mineral systems is a difficult but essential task. Building a database to serve this purpose, however, requires navigating a fundamental tension between its ideal aims and the reality of available data. The architecture and vocabulary of a database must be defined by its intended use, and in the context of this PhD, the database must serve a broad purpose, balancing scientific, technical, and economic considerations to allow for some level of evaluation and prediction.

This wide-ranging objective is immediately constrained by the data that can realistically be accessed within the time and resources of a doctoral project. Much of the economic, technical, and detailed geological data is either confidential due to its commercial nature or remains locked in paper archives that are difficult and time-consuming to access. These practical limitations forced us to focus on a more accessible primary source: the reports of the Ente Minerario Sardo (EMSA).

The decision to use EMSA reports came with an inherent cost: data quality. These regional prospection campaigns were conducted in a short period during the 1980s with limited personnel. The descriptions of mineralisations are often concise, relying on abbreviated terms to avoid verbosity. This creates a significant interpretive challenge, as some terms had "local" meanings at the time that differ from modern use (e.g., "schist" was used for most types of siltstones and argillites). Furthermore, crucial details regarding textures, morphology, and structural indicators are frequently omitted, and the quality and style of information vary from one prospector team to another.

Given these constraints, acquiring new, high-resolution geological and compositional data is logistically impossible for more than a few select occurrences within the PhD timeline. Our response to this has been:

- Targeted prospection: We chose a restricted number of mineralisations and areas for new investigation, strategically leveraging other ongoing studies in those locations to reduce the investment of time and resources.
- Comparative Modelling: To address the broader gaps in the dataset, we used well-constrained data from a type locality to infer the characteristics of lesser-known, but analogous, occurrences. This generalisation is a physiological and necessary step at this preliminary stage of the database development and regional synthesis.

This iterative approach of choosing attributes based on our aims and available data, populating the database, and then using it to test and refine our models has not only built a working dataset but has also highlighted criticalities and guided our subsequent investigations. The following case study demonstrates this process.

4.4. Statistical analyses and quantification – extrapolating the intrinsic schematisation of ore deposits and mineral occurrences

During the database population and vocabulary definition phases, we schematized and synthesised a large volume of data, which naturally revealed recurring patterns in the descriptive words and characteristics associated with groups of ore deposits and mineral occurrences. These patterns inherently represent the mineralisation models, while the groups of ore deposit themselves correspond to the mineralisation types.

The database describes 622 sites and a wide variety of associations of cell values. Some sites exhibit more than one type and commodity, along with diverse morphological and textural features, resulting in varying mineral concentrations and distributions. Certain sites were exploited in the past, while others are merely hints of mineralisation that were never properly explored due to their limited economic interest.

The rationalisation of these schemes is made possible by querying the Metallogenic Database using SQL to extrapolate, visualise and cross-reference information.

4.4.1. Operating periods and activities

The database contains chronological data for just over 200 mining sites. The earliest recorded start of activity dates to 1851, while the most recent began in 2021 (Figure 4.2). Although 19 sites hold technically valid concessions, only 6 permits have been released since 2000.

It is estimated that for the period from 1851 to 2003, considering the combined duration of exploration permits, concessions, and mining permits, an average of 42 simultaneous activities is estimated. Mining-related activity increased gradually and steadily until 1927, when 56 sites were active. The commodity spectrum is already well-defined (Figure 4.3), with lead and zinc as the dominant metals, accompanied by silver, barite, fluorite and minor copper. MVT (Mississippi Valley-Type) deposits are the most numerous, along with hydrothermal veins, reflecting the exploitation of the classic Cambrian carbonate-hosted deposits of the Iglesiente district, the Pb-Zn polymetallic vein system of Montevecchio district, the barite-fluorite veins and the karstic barite of the Sulcis-Iglesiente area.

A first surge followed, reaching 85 sites by 1949, where lead remains the undisputed primary commodity, closely followed by zinc, with barite and silver co-products. During this period hydrothermal veins remain the most common type, but karst-related mineralisation got consistently present, and skarn deposits got increasingly more important.

A second rise culminated in the 1960s with a peak of 105 sites operating concurrently.

From the 1970s the activity declined sharply, stabilising in the 1990s at around 20 sites, mostly involved in maintenance or held under perpetual concessions. During this period, lead and zinc remain the most frequent commodities, but their counts decrease proportionally. Barite and fluorite also show declining numbers. Hydrothermal veins continue to be the most common deposit type, but with decreasing counts, while karst and MVT deposits also diminish.

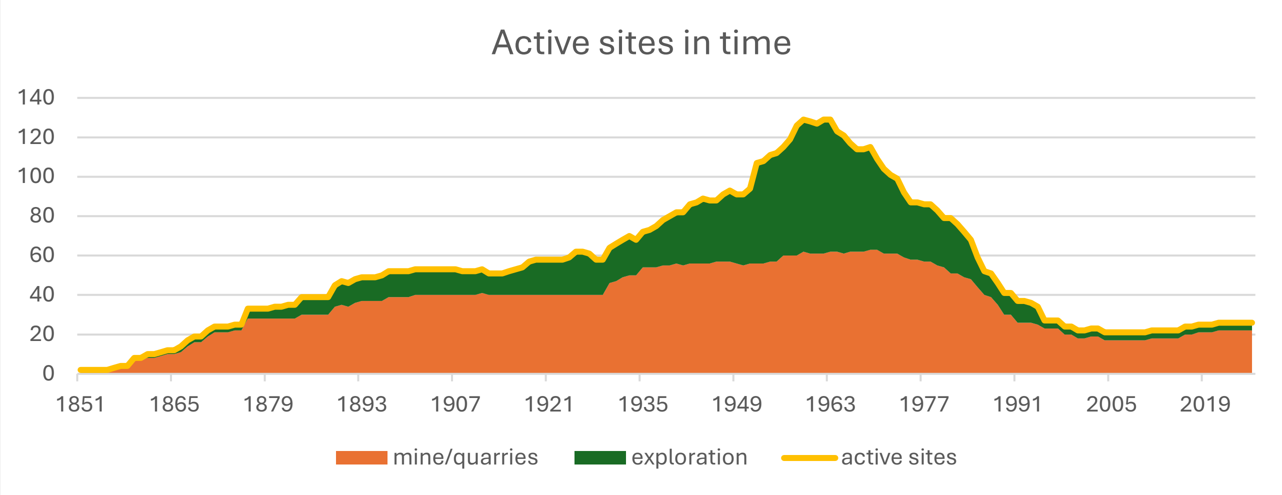

Figure 4.2: Number of estimated active sites per year (active and inactive mines and quarries + exploration) based on the operating_start and operating_end values of the sites table.

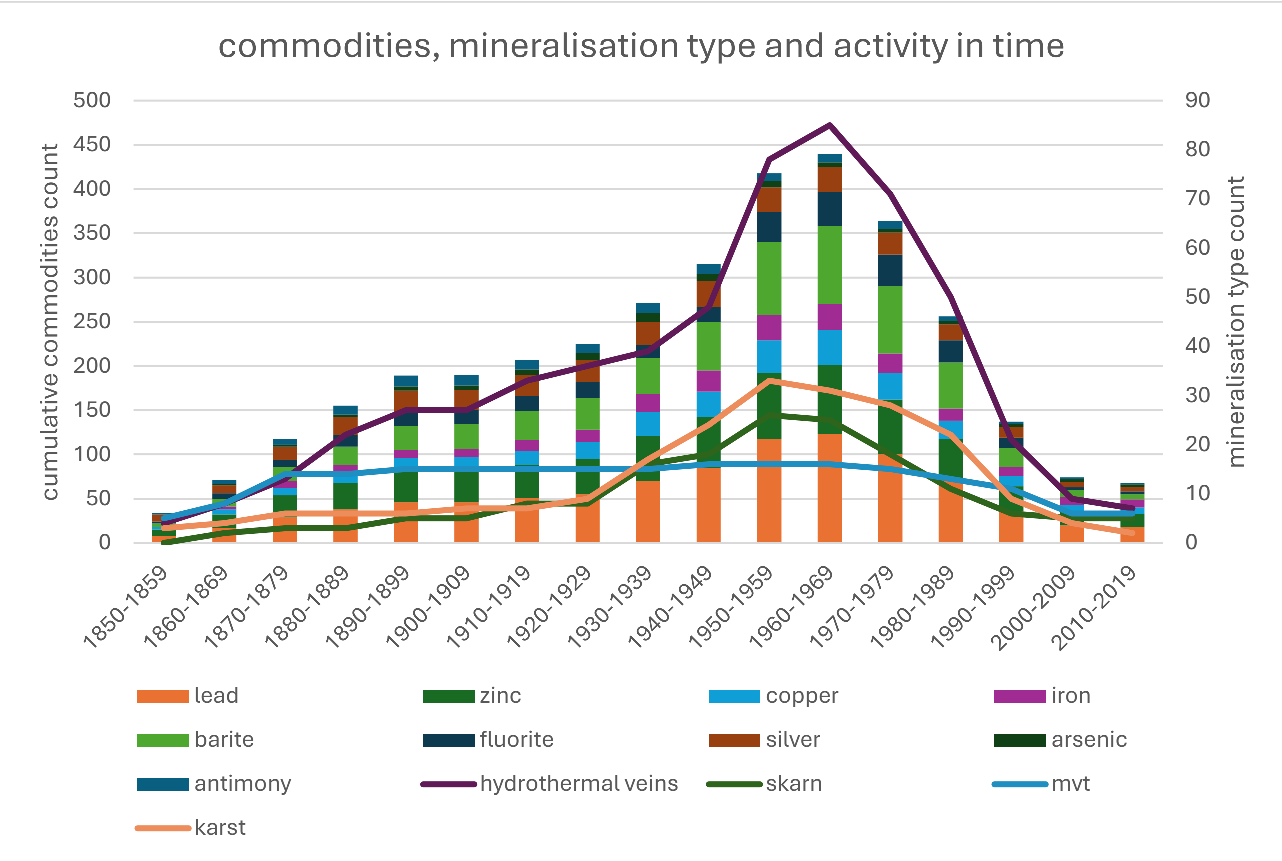

Figure 4.3: Commodities per type of mineralisation that were involved in exploration or mining activities.

As shown in Table 4.2a, the classified activities consist of:

- exploration activities - carried out in a total of 312 sites, 283 of which never resulted in mining.
- exploitation activities - involving 180 currently inactive, 16 currently active mines, 1 inactive quarry, and 2 active quarries.

Furthermore, 96 sites have relevant waste deposits, associated with mining (74 sites – currently inactive) and with exploration (17 sites) (Table 4.2b - Figure 4.4). The large amount of waste deposits associated with old mining and exploration activities brought many researchers to start working on the Sardinian mining waste deposits, both for their economic potential as a secondary mineral resources (Sedda et al., 2025) and for the environmental risk they represent.

On the other hand, at least 2 sites are former mines environmentally restored and 6 sites, whose activity nature is not specified, but are currently anthropised.

Work type	***exploration***	***inactive mine***	***waste***	***active mine***	***anthropised***	***active quarry***	***restored***	***inactive quarry***
count of sites	312	180	96	16	6	2	2	1

Work type associations	***N. of sites***	***percentage***
exploration	283	56.83
inactive mine	91	18.27
inactive mine + waste	74	14.86
exploration + waste	17	3.41
active mine	14	2.81
exploration + inactive mine	8	1.61
exploration + inactive mine + waste	4	0.8
active quarry	2	0.4
inactive mine + restored	2	0.4
active mine + inactive mine	1	0.2
active mine + waste	1	0.2
inactive quarry	1	0.2

Table 4.2: a) work type and count per site; b) work type associations and count per site.

The status of the works is recorded (Table 4.3 - Figure 4.4), counted by site, as 471 mineral occurrences (hint), 258 ore deposits and 2 access-restricted zones. However, 108 sites have overlapping occurrences and ore deposits, while the 2 access-restricted zones are also occurrence one, and ore deposit the other. The overlap of mineral occurrences and ore deposit is due to the addition of numerous commodities that were overlooked during mining and/or exploration activities. They include most CRMs and other economically valuable minerals that were recently discovered with modern analytical instruments (e.g., Ni-Co-Bi minerals at the Silius mine).

Status	Mineral occurrence (hint)	ore deposit	access restricted zone
count of sites	471	258	2

Table 4.3: Status of the sites.

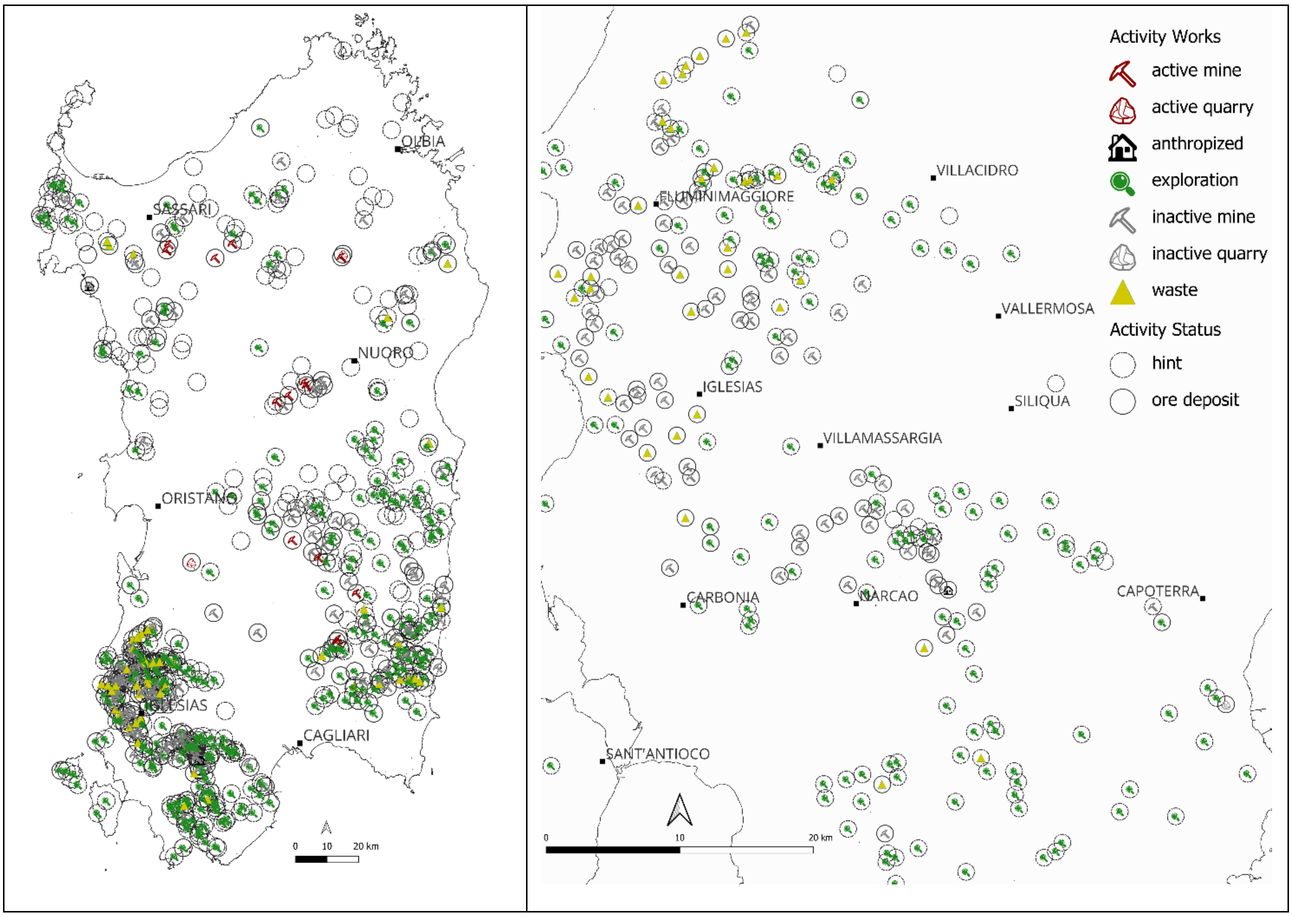

Figure 4.4: Activity work and status spread in Sardinia, with a focus on the Sulcis-Iglesiente-Arburese area.

4.4.2. Commodities and Critical Raw Materials

Considering 621 sites recording commodities, 502 also record critical raw materials occurring within the ore minerals.

The commodities frequency distribution (Figure 4.5) reveals a strong dominance of base metals, with lead (Pb) occurring in 373 distinct sites, zinc (Zn) in 266 sites, and copper (Cu) in 221 sites. These are followed by minerals such as barite (213 sites) and fluorite (115 sites), and by precious and associated metals including silver (Ag) (73 sites), gold (Au) (53 sites), and arsenic (As) (88 sites).

At the opposite end of the spectrum, several rare commodities appear in fewer than five sites, including lithium, niobium, tantalum, vanadium, perlite, mercury, and phosphorus, indicating either their geological scarcity or a historical lack of targeted exploration.

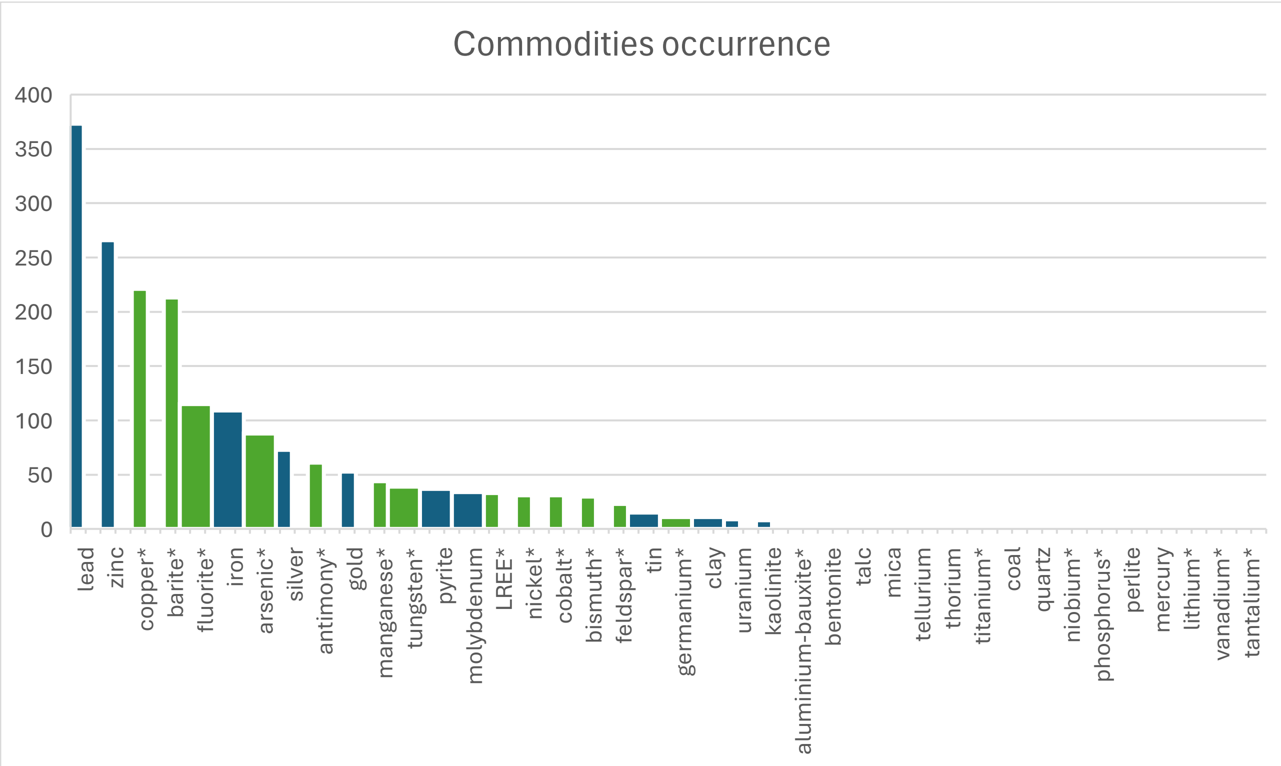

Figure 4.5: Count of commodities occurrences. In green are the Critical and Strategic Raw Materials, in blue the economic but not critical ones.

Critical and Strategic Raw Materials

The dataset has been cross-referenced with the 2023 European Union list of Critical Raw Materials (CRMs) to assess the strategic importance of Sardinian mineral occurrences. The following CRMs are present (Figure 4.6): copper, barite, fluorite, arsenic, antimony, manganese, tungsten, LREE, cobalt, nickel, bismuth, feldspar, germanium, aluminium-bauxite, titanium, phosphorus, niobium, tantalum, lithium, vanadium.

Copper, barite, and fluorite are the most abundant CRMs, reflecting their role as either primary commodities or widespread gangue minerals in the region's base metal deposits. Their high frequency (over 100 sites each) indicates a strong regional endowment.

Arsenic and antimony (88 and 61 sites respectively) are frequently associated with gold and silver mineralization, typically in hydrothermal systems.

Tungsten (W), present in 39 sites, is frequently associated with copper, molybdenum, and bismuth, generally associated to skarn and greisen.

Rare Earth Elements (LREE) are documented in 33 sites, notably in combination with barite, fluorite, and lead in hydrothermal veins, as well as in more exotic associations with thorium, uranium, and molybdenum when involved in intrusion-related mineralisation.

Bismuth (Bi), cobalt (Co), and nickel (Ni) each appear in around 30 sites. These elements frequently co-occur in polymetallic assemblages with arsenic and silver, pointing to complex hydrothermal or remobilised mineral systems.

Germanium (Ge) in 11 sites, though modest, is a high-value CRM typically found as a trace element in sphalerite.

At the lower end of the frequency spectrum, elements such as niobium, tantalum, lithium, and vanadium (1-2 sites each) represent targets for further investigation. Their rarity in the database reflects genuine geological scarcity (lithium) and very low concentrations (niobium, vanadium), but also a historical lack of targeted exploration. Even single occurrences of these metals are significant given the EU's strategic autonomy goals.

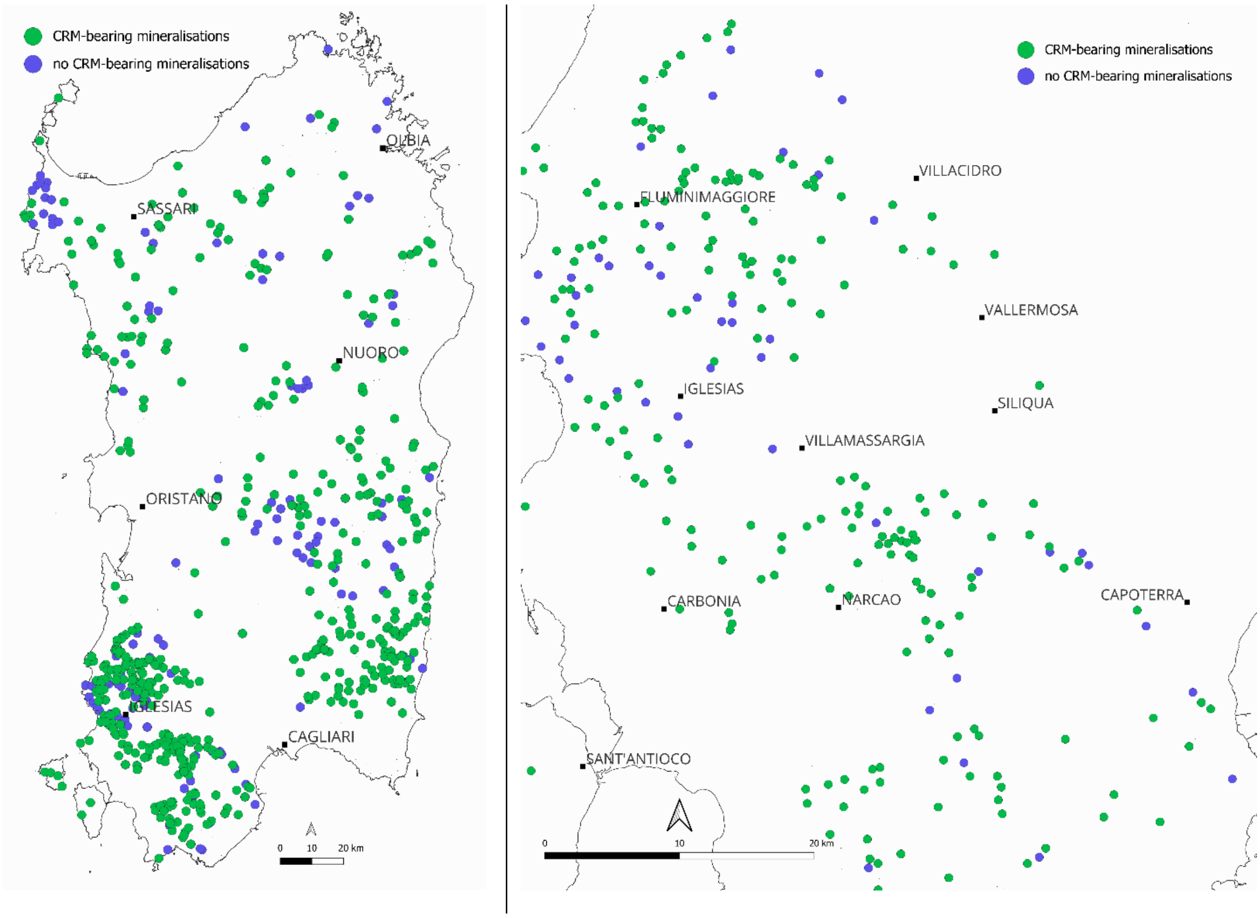

Figure 4.6: Critical and Strategic Raw Materials and not spread in Sardinia, with a focus on the Sulcis-Iglesiente-Arburese area.

Commodity associations

Commodity analysis reveals highly complex ore mineral associations (Figure 4.7) yet highlights several recurrent and geologically meaningful parageneses.

The most frequent association is the lead-zinc-copper triad, present in 175 sites, among which the ore classes are hydrothermal veins (81), skarn (62), porphyry (10), and greisen and MVT, representing a wide range of physical-chemical formation conditions. The typical primary mineral assemblage includes galena, sphalerite, and chalcopyrite, along with their secondary phases related to supergene alteration (e.g., cerussite, hemimorphite, covellite), often accompanied by iron sulfides (pyrite, marcasite, pyrrhotite), as seen in the copper-iron-lead-zinc association (32 sites, mostly skarn).

A distinct and economically important group is the barite-fluorite-galena association found in 73 hydrothermal veins, 2 MVT and in greisen and skarn, representing low- to medium- temperature systems. These types of mineralisation are widespread across Sardinia, with strong clustering in the southern part of the region.

Another family comprises antimony-arsenic, appearing in 35 hydrothermal veins and 3 skarns. They can be associated with a variety of economic materials such as gold, silver, copper, tungsten, nickel, cobalt and LREE. Gold is characteristic of the Sarrabus – Gerrei districts in southeastern Sardinia (e.g., Baccu Locci, Brecca). Their mineralogy consists of a more or less complex assemblage of sulfosalts and native elements and highly diagnostic of mesothermal systems, featuring arsenopyrite, stibnite, tetrahedrite, bournonite, and electrum or native gold. The latest variants of these systems are occasionally enriched by tungsten, manganese, or tellurium, as seen in the presence of scheelite, pyrolusite, and tellurides in some assemblages.

Feldspar is commonly associated with micas in 3 pegmatitic facies or LREE (REE-bearing phosphates) in 5 granitoid intrusions. LREE are also present in 3 bauxite deposits.

Finally, a set of rare and complex assemblages (e.g., containing Bi, Co, Ni, Ge, LREE, Mo, Sn, W, U, Th) occurs in a limited number of sites, often combining up to ten different elements.

The consistent presence of Ni-Co-Bi arsenides and sulfoarsenides (e.g., ullmannite, cobaltite, bismuthinite) alongside cassiterite, scheelite, wolframite, molybdenite, and REE-bearing minerals (monazite, bastnaesite, synchysite) points to a high-temperature, intrusion-related origin, likely in a skarn or greisen environment.

These represent potentially high-value targets for critical raw materials, as their historical production or exploration was focused on base metals.

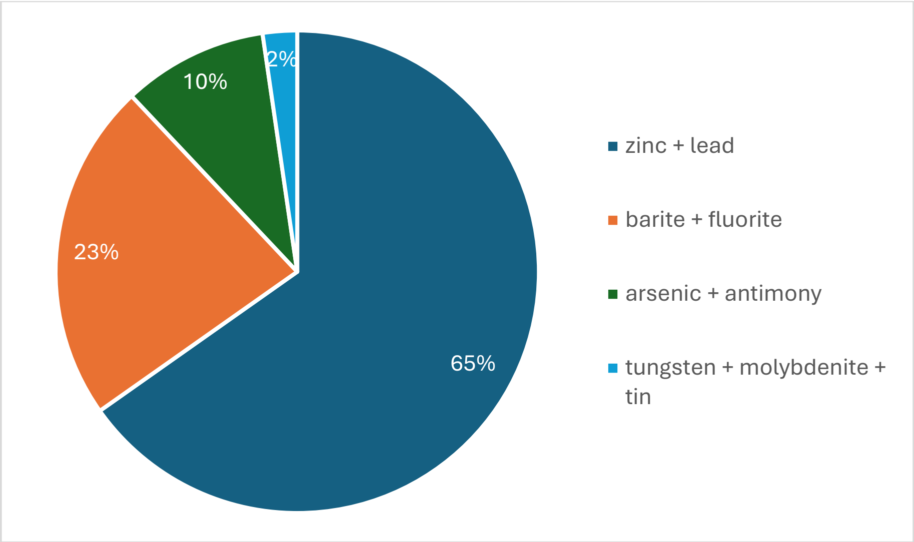

Figure 4.7: The distribution of the most common commodities associations per site.

4.4.3. Analysis of mineralisation types

Each type of mineralisation summarises the typical features described by database parameters such as the genetic process, composition, morphology, texture and structural features. Different types often share the same geodynamic context or remobilise previous ores. The database records 647 occurrences of mineralisation types across 622 sites (Table 4.4), with 45 sites missing this attribute due to lack of descriptive data.

Type	***Count***	***Fraction***
hydrothermal veins	308	47.5
skarn	95	14.7
karst	51	7.9
sedimentary manganese deposit	36	5.5
MVT	30	4.6
greisen	27	4.2
clay deposit	22	3.4
pegmatite	16	2.5
porphyry	14	2.2
oolitic ironestone	11	1.7
sedimentary	9	1.5
sedex	7	1.1
metamorphic	6	0.9
bauxite	5	0.8
low sulphidation epithermal deposit	2	0.3
paleoplacer	2	0.3
placer	2	0.3
aplite	1	0.1
high sulphidation epithermal deposit	1	0.1
magmatic intrusion	1	0.1
volcanic deposit	1	0.1

Types association	***Count***
hydrothermal veins, karst	23
hydrothermal veins, skarn	13
karst, MVT	10
greisen, porphyry	5
hydrothermal veins, MVT	5
greisen, hydrothermal veins	2
greisen, skarn	2
MVT, skarn	2
greisen, pegmatite	1
clay deposit, pegmatite	1

Table 4.4: Count of mineralisation types and association of types per site.

The database records reveal a strong predominance of hydrothermal vein systems (47.5%) and skarn deposits (14.7%), alongside a significant diversity of stratabound, sedimentary, and intrusion-related deposit styles. The mineralisation types are described by summarising the peculiar features of the sites hosting them (Table 4.9).

The integration of genesis age data with deposit types and genetic processes provides a robust temporal framework for understanding the metallogenetic evolution of the island, while structural orientation data (dip, plunge, and strike), morphological characteristics, and textural features offer insights into the tectonic controls, geometry, and physical conditions of mineralisation.

Hydrothermal Veins

General characteristics: Hydrothermal veins represent the most abundant category, accounting for 308 sites (47.5%). The hydrothermal process is correlated to metasomatic (13 sites - skarn), and karstic process (23 sites). They are widely distributed across the island, with a major concentration in southwestern Sardinia and significant occurrences in the Sarrabus-Gerrei district.

Age: The age spectrum of hydrothermal veins is broad, reflecting multiple mineralising events whose endings remains nebulous. The dominant age is post-Variscan, recorded at 194 sites, but the lack of time-constraint structural features and in-situ dating for the closing age of the mineralising events made impossible an accurate dating.

A significant inferred Permian event is documented at 52 sites, for the mineralisations strictly correlated with the Permian intrusion phase. Followed by Carboniferous (43 sites), the highest peak of the Variscan metallogenesis. Minor ages include, Miocene (6 sites), Post-Eocene, Oligocene and a general Tertiary (6 sites) for the hydrothermal fluids correlated with the Oligo-Miocenic volcanism.

Commodities: The most frequent commodity association is barite + fluorite + lead (33 sites), a classic low-temperature vein assemblage, exclusively linked to this deposit type (Figure 4.8). Similar common associations include barite + lead (30 sites, also found in karst and sedimentary settings) and barite + fluorite (12 sites). The different mineral assemblages for hydrothermal barite-fluorite deposits may reflect different structural levels of the same ore deposit model, entirely known at the Silius deposit (southern Sardinia – Chapter 5.3).

The polymetallic copper + lead + zinc association (31 sites). Its structural association with MVT and skarn deposits indicate a remobilisation of Cambrian to Permian mineralisations during the collapse of the Variscan chain.

More complex associations, including as antimony + arsenic + bismuth + cobalt + nickel + copper, are exclusively hydrothermal and point to focused mineralizing systems strictly associated with characteristic intrusions.

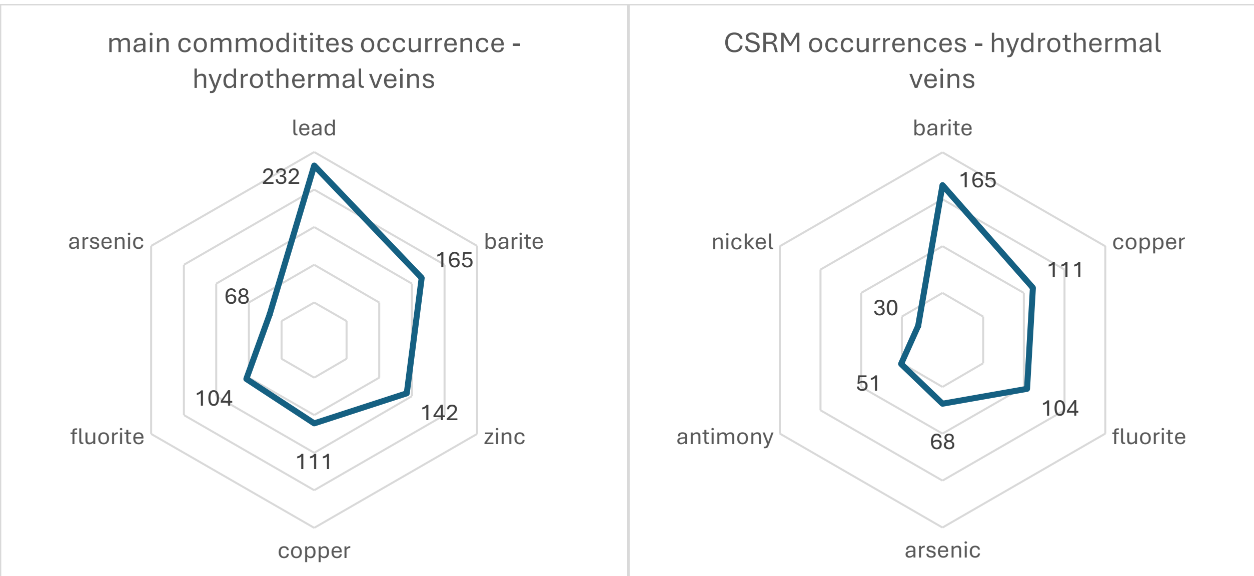

Figure 4.8: Hydrothermal veins main commodities highlighting the Critical and Strategic Raw Materials.

Morphology and texture: Morphologically, hydrothermal veins are dominated by tabular forms (286 sites), reflecting their nature as planar fracture-fillings.

Texturally, hydrothermal veins display a diverse range of fabrics. Brecciated (116 sites) and banded (67 sites) textures are common, indicating multiple episodes of fracturing and mineral precipitation. Disseminated (111 sites), massive (92 sites) and stockwork (54 sites) textures are significant indicating pervasive and spread mineralisations.

Host rocks: The rheological properties of the host rock fundamentally control fracture propagation. Host lithologies include schist (122 sites), limestone (71), sandstone (55), granite (32), and porphyry (31), indicating a prevalence of highly cohesive lithologies.

Structural data: 91 sites (Table 4.5) reveal an average dip direction of 198.5°, with a large standard deviation of 101°. Half of the ore bodies vary greatly with dip directions between 112.5° and 292.5° (southern quadrants), but the rest is bimodal, clustering respectively on the ENE (20% of the values ranging 45°-55°) and NNW (20% of the values ranging 292.5°-350°) quadrants. Strike has a smaller standard deviation (55.3°), with a perfect E-W median while ranging 20°-180°. Half of the veins strike between 45° and 147.5°, slightly shifted towards the lower value, covering a wide fan between NE-SW and WNW-ESE. The ore bodies show a steep inclination averaging 66.9°, and 75% of them plunging over 60°, with rare (>5%) sub horizontal bodies (Figure 4.9).

The NE-SW and WNW-ESE strikes and the high inclination are coherent with the regional post-Variscan extensive tectonic, while the main directions of strikes and dips suggest at least two main striking directions of fracture systems plus their conjugated fractures.

Hydrothermal veins	***measures***	***min***	***p05***	***p10***	***p25***	***p50***	***p75***	***p90***	***p95***	***max***	***avg***	***st.dev.***
dip dir	91	5	45	55	112.5	180	292.5	315	350	360	198.5	101
plunge	91	10	45	50	60	70	75	80	85	85	66.9	13.6
strike	91	20	22.5	25	45	90	147.5	180	180	180	99.4	55.3

Table 4.5: Orientation data of the hydrothermal veins with percentiles.

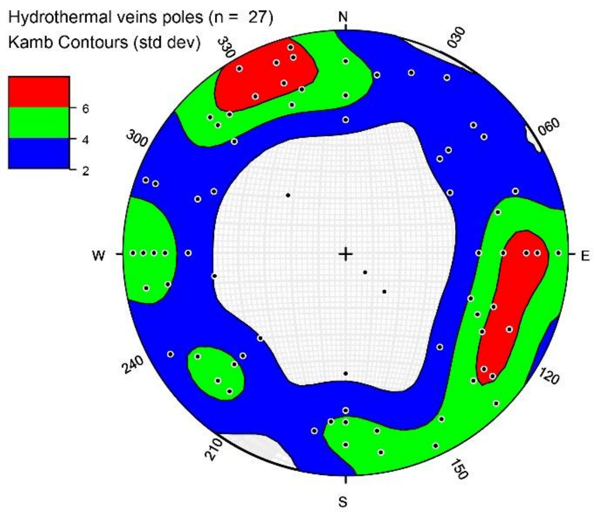

Figure 4.9: Poles distribution of the hydrothermal veins' planar orientation with Kamb Contours (software from www.rickallmendinger.net/).

Skarn Deposits

General characteristics: Skarn deposits are the second most frequent type, with 95 sites (14.7%). They are concentrated in areas of intrusive-carbonate contact, particularly in central and southern Sardinia.15 sites with skarn occurrences have hydrothermal veins cutting across them, reflecting the common paragenetic sequence where skarn formation is followed by hydrothermal veining in the same intrusive centers.

Age: The age distribution is strictly connected to the two main late-variscan intrusive phases: the Permian event (over 100 sites), and a Carboniferous event (36 sites).

Commodities: The characteristic commodity assemblage (Figure 4.10) is copper + lead + zinc (31 sites), often expanded with iron (16 sites), reflecting the presence of magnetite and hematite. In some cases, tungsten (13 sites), tin (7 sites), molybdenum (4 sites) and fluorite (8 sites) are associated with skarn deposits when coupled with greisen, proximal to granitic intrusions.

It's not rare to find arsenic (13 sites) mineralisations, generally crystallised as arsenopyrite in skarn ore deposits, even thou a later hydrothermal impulse is generally the main genetic process (e.g., Medau Ganoppi – Fluminese, Mitza Sermentus – SW Sardinia).

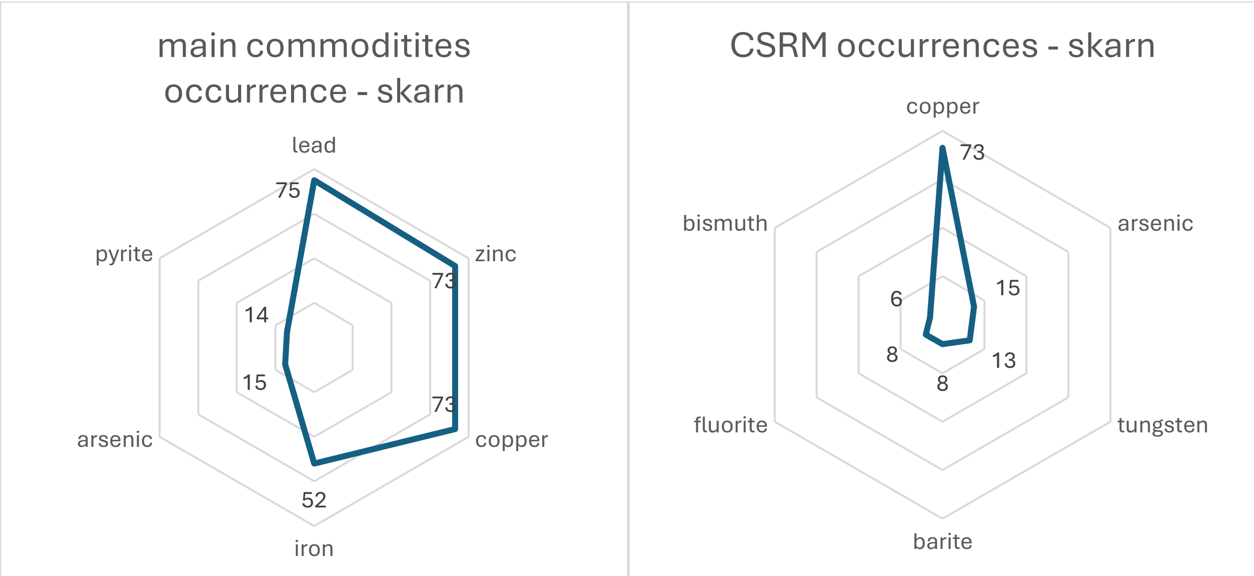

Figure 4.10: Skarn main commodities highlighting the Critical and Strategic Raw Materials.

Morphology and texture: Morphologically, skarn deposits are predominantly lentiform (86 sites), reflecting their replacement origin and the tectonically guided geometry of the carbonate protoliths.

The predominant textures are disseminated (66 sites) and massive (52 sites) indicating both the occurrences of sparce and clustered ore minerals. Banded texture (7 sites) is rarer, but genetically significant, displaying the gradual metasomatic replacement.

Structural data: Structural measurements from 27 sites (Table 4.6) indicate a mean dip direction of 154.6° and a wide standard deviation (106.1°). Two main orientations are recognised, 20% of the bodies dip towards NNE (33°-47.5°), while 20% dip towards WSW (227.5°-315°). Strikes complaint to the orientations, with 50% of values laying in the SE quadrant (130°-180°). Inclinations have a low standard deviation averaging 50° and the same median showing a low plunge angle (Figure 4.11).

The moderate dipping with a NW-SE striking, and the lens-shaped ore bodies indicate the prevailing Variscan structural control correlated with the thrust-and-fold architecture of the Nappe Zone, which emplaced tectonic slices of the Cambrian-to-Devonian carbonate formations.

Skarn	*measures*	*min*	*p05*	*p10*	*p25*	*p50*	*p75*	*p90*	*p95*	*max*	*avg*	*st.dev.*
dip dir	27	10	33	40	47.5	165	227.5	306	315	350	154.6	106.1
plunge	27	30	30	30	40	50	60	70	73.5	85	50.4	14.4
strike	27	30	45	45	80	130	137.5	158	177	180	110.2	44.8

Table 4.6: Orientation data of the skarn bodies with percentiles.

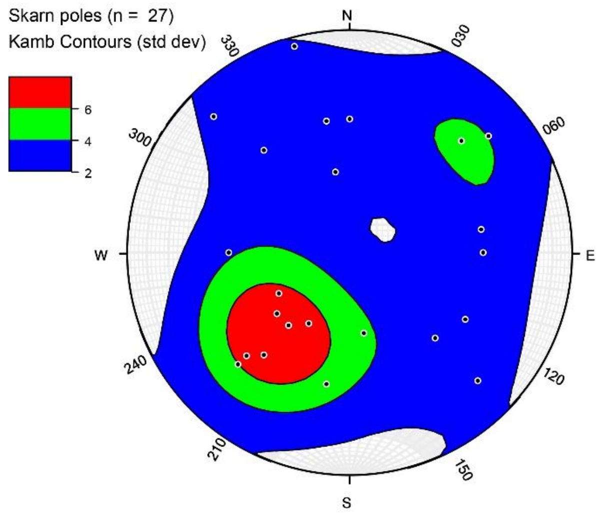

Figure 4.11: Poles distribution of the skarn bodies planar orientation with Kamb Contours (software from www.rickallmendinger.net/)

Mississippi Valley-Type (MVT) Deposits

General characteristics: MVT deposits account for 30 sites (4.6%), forming a classic association with the Cambrian carbonate sequences of southwestern Sardinia. These are linked to hydrothermal processes during the Cambrian period and consistent with their origin from basinal brines, later reworked during supergene alteration (30 sites) and in karstic systems (11 sites).

Commodities: Lead + zinc association is always present (Figure 4.12), often with barite (14 sites), copper (7 sites) and rarely fluorite, pyrite, antimony. Galena commonly bears silver (16 sites).

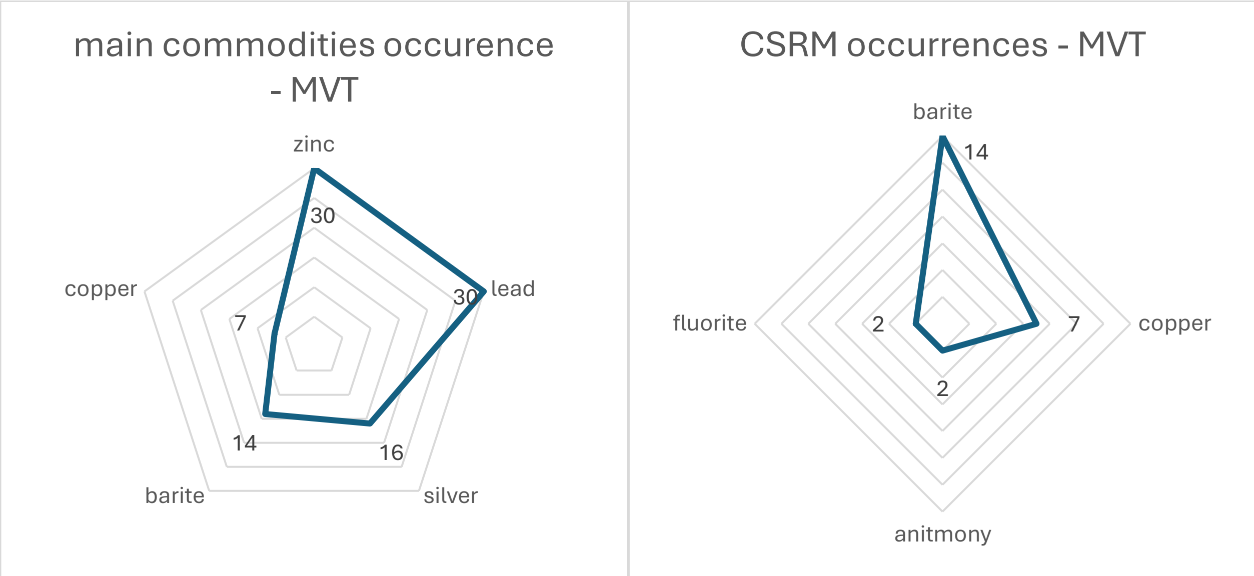

Figure 4.12: MVT main commodities highlighting the Critical and Strategic Raw Materials.

Morphology and texture: Morphologically, MVT deposits are dominated by clustered and stratabound (23 sites each) forms, reflecting their stratigraphic control. Tabular morphologies are also significant (12 sites) reflecting the sub-vertical manifestation in fractures.

Texturally, MVT deposits show a predominance of massive (21 sites) and disseminated (20 sites) fabrics. Brecciated (8 sites) and stockwork (6 sites) textures are also present, coherently with the hydraulic fracturing during diagenesis.

Structural data: Orientations measured at 12 sites (Table 4.7) show a mean dip direction of 150° (ranging from 50° to 360°) with a standard deviation of 113°. Two classes are clearly distinct: 45% of the measures dip toward ENE, ranging 61° to 90°, 25% of the measures vary from WSW to WNW, raging 241° to 335°.

The mean plunge is 62° (ranging from 45° to 80°), indicating moderate to steep dips coherent with the typical MVT general morphology: over 25% of the measures can be correlated to the sub-vertical stratabound filled fractures, while the rest are slightly inclined manifestations coherent with the Cambrian stratigraphy of the area.

The average strike is N138°, with a large standard deviation of 56°. 50% of the orebodies trends NNW-SSE (160°-180°), 10% being NE-SE and the rest ESE-WSW. The large variability of the strike is coherent with the intersection of different hydraulic-induced fractures.

MVT	***measures***	***min***	***p05***	***p10***	***p25***	***p50***	***p75***	***p90***	***p95***	***max***	***avg***	***st.dev.***
dip dir	12	50	61	70	70	90	241	312	335	360	150	113
plunge	12	45	48	50	50	62	70	70	74	80	62	11
strike	12	20	34	49	124	160	180	180	180	180	138	56

Table 4.7: Orientation data of the MTV mineralisations with percentiles.

Karst Mineralisation

General characteristics: Karst-related mineralization is recorded at 51 sites (7.9%), primarily in the Iglesiente district (sheets 546, 555, 556). These are often altered in the supergene environment (14 sites) and associated with hydrothermal veins (24 sites). They are also common in MVT deposits (11 sites). *Age:* The age of the karst process il generally inferred to be post-Variscan for the assumption of the structural uplift, during the orogenesis, of the Cambrian formations represented by large volumes of carbonates. They are in fact hosted by limestones (48 sites) and dolostones (13 sites).

Commodities: The ore minerals typically consist of mainly barite and subordinate galena, often associated with hydrothermal veins bearing sphalerite (25 sites), and occasionally copper minerals (7 sites).

Morphology and texture: The morphology is tendentially clustered for the natural shape of karst cavities but can occur as tabular (19 sites) and columnar (7 sites) when associated with other fractures systems that enhanced the water flow.

The deposits are often stratified (36 sites), mostly near the bottom the cavities and in close spaces, disseminated (25 sites) is mostly specific to the galena occurrences along the barite, massive (25 sites) specifically when barite crystallize on the walls of the cavities, and brecciated (12 sites) occurs when the barite cement breccias in karstified fractures.

Structural data: Structural data from 10 sites (Table 4.8) shows a clear guide of high angle faults on the elongated karst bodies, with 50% of them having inclination above 65°. The prevalent trend is NNW-SSE, with 50% of the measures over N135°.

Karst	*measures*	*min*	*p05*	*p10*	*p25*	*p50*	*p75*	*p90*	*p95*	*max*	*avg*	*st.dev.*
dip dir	10	45	45	45	53.8	120	216.3	315	315	315	150	107.8
plunge	10	10	23.5	37	51.3	65	77.5	80.5	82.8	85	60	22.7
strike	10	45	45	45	85	135	135	170	170	170	115	45.8

Table 4.8: Orientation data of the karst mineralisations with percentiles.

Greisen Deposits

General characteristics: Greisen deposits (27 sites, 4.2%) are dominantly associated with hydrothermal (22 sites) and intrusive igneous (11 sites) processes, reflecting their high-temperature, magmatic-hydrothermal origin, with a minor metasomatic component (3 sites) when reactive lithologies are present.

Age: The age distribution is strictly linked to the two main late-Variscan intrusive suites, showing a Permian peak (15 sites), followed by Carboniferous (10 sites). In fact, they are generally associated with other intrusion-related mineral deposits such as porphyry (5 sites), skarn (3 types), and pegmatite (1 sites), and are mainly hosted by granitic lithologies (19 sites), and secondly by schists (6 sites).

Commodities: The usual commodity present in greisen environment (Figure 4.13) is molybdenite (25 sites), followed by copper (14 sites), tungsten (11 sites), lead and zinc (9 – 8 sites).

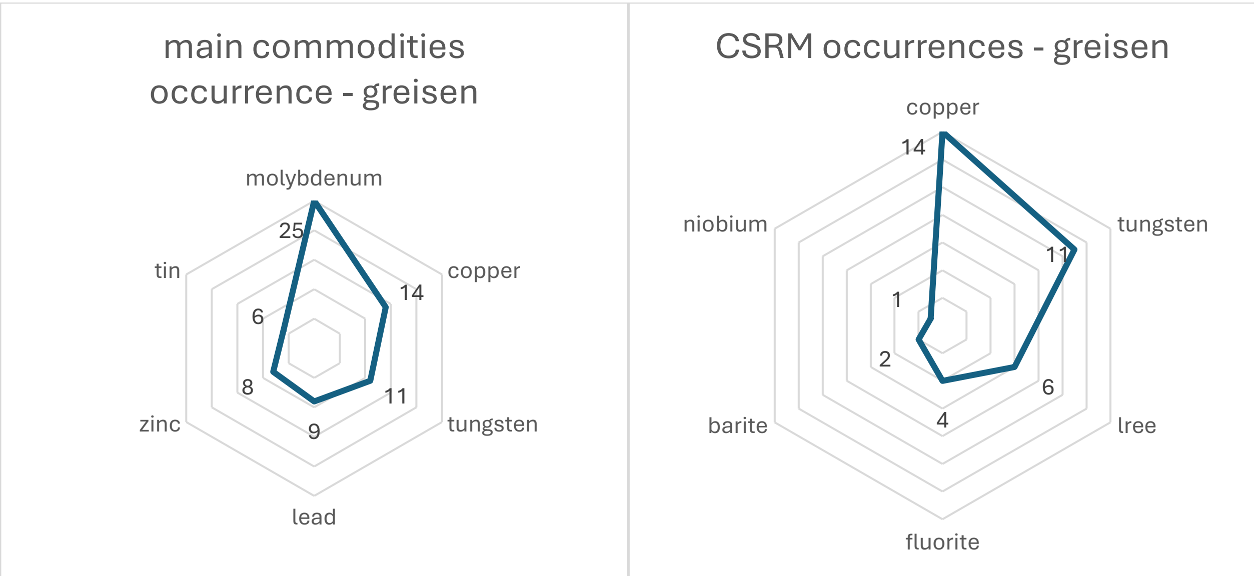

Figure 4.13: Greisen main commodities highlighting the Critical and Strategic Raw Materials.

Morphology and texture: The morphology of greisen deposits is mainly influenced by the intrusive contacts but often occur as vein-like tabular bodies (15 sites), sometimes clustering (13 sites) in stubby shapes.

The ore minerals are usually disseminated (24 sites) in the rock, sometimes aggregating in massive assemblages (4 sites). Molybdenite also occurs as the characteristic “dry” veinlets (6 sites).

Structural data: Only 5 structural datasets are recorded for the lack of preferential orientation of the greisen bodies. Coherently, the measures do not follow specific trends but are aligned with the local intrusive contact and/or radial with it.

Porphyry Systems

General characteristics: Porphyry systems (14 sites, 2.2%) are equally associated with hydrothermal (14 sites) and intrusive igneous (13 sites) processes, as expected for this deposit type.

Age: The age is associated with both the Variscan and post-Variscan magmatism and hydrothermal events: Carboniferous (6 sites), Miocene (4 sites), and Oligocene (4 sites). In fact, these are hosted by carboniferous granites and porphyries, Oligocene andesites and dacites, and Miocene andesites.

Commodities: Associations (Figure 4.14) involve copper (13 sites), lead and zinc (10 sites), molybdenum (9 sites), gold (8 sites) and manganese (6 sites). Their association with greisen deposits in 5 sites highlight the molybdenum occurrence. Gold and manganese are only found in the Miocene and Oligocene deposits, along with 2 occurrences of arsenic and 1 of barite.

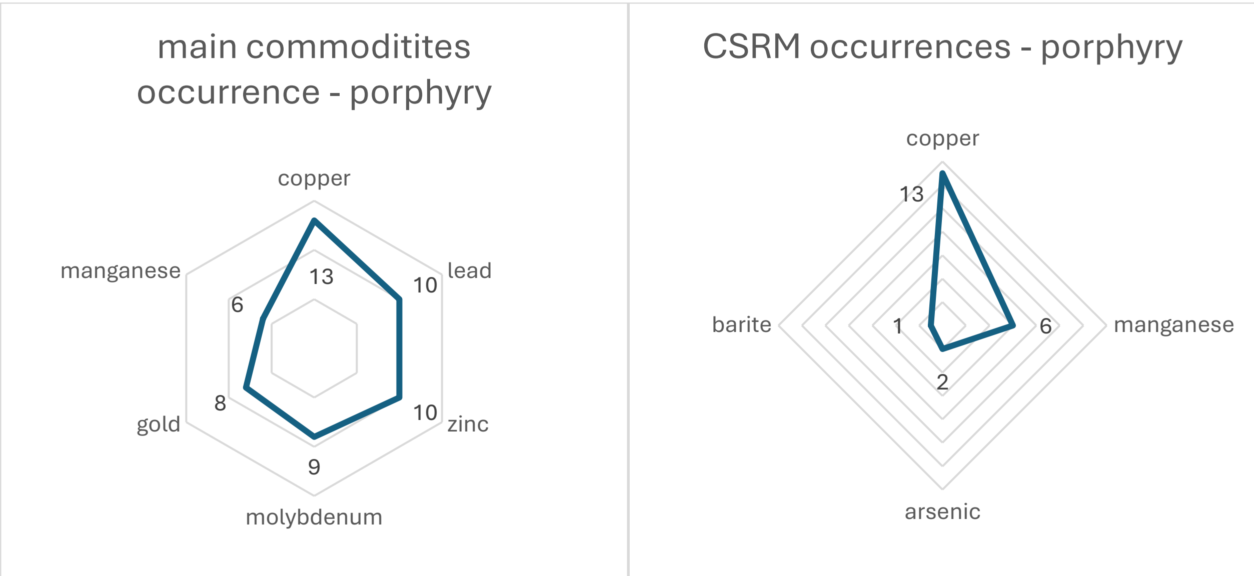

Figure 4.14: Porphyry main commodities highlighting the Critical and Strategic Raw Materials.

Morphology and texture: These are mostly clustered (10 sites) and tabular bodies (6 sites), with the ore minerals being generally disseminated (14 sites), or as stockworks (3 sites) in the host-rock.

Structural data: Structural measurements from 4 sites yield a quite consistent trend with a mean strike of N112.5° (ranging from N90° to N135°) and always plunging with a high angle, over 75°. These data are indicative of a sub-vertical intrusion-related fracture system in very shallow crustal levels.

Pegmatite Deposits

General characteristics: Pegmatite deposits (16 sites, 2.5%) are late-staged intrusion-related as well, being associated with the generic genetic term intrusive igneous (10 sites) and genetically linked with hydrothermal processes (11 sites). They are mainly associated with Carboniferous (13 sites) and secondly Permian (2 sites) granitoid suites. In fact, they are hosted by both intrusive lithologies such as granite (5 sites), granodiorites (4 sites), tonalites (3 sites), and metamorphic lithologies such as gneiss (2 sites), schist (2 sites).

Commodities: Sardinian pegmatites bear CRM such as feldspar (15 sites), LREE (5 sites) mainly in disseminated aggregates of phosphates, and 1 recorded site with occurring lithium-bearing, niobium and tantalum-bearing minerals. Also 2 sites with mica exploitation are evidenced (Figure 4.15).

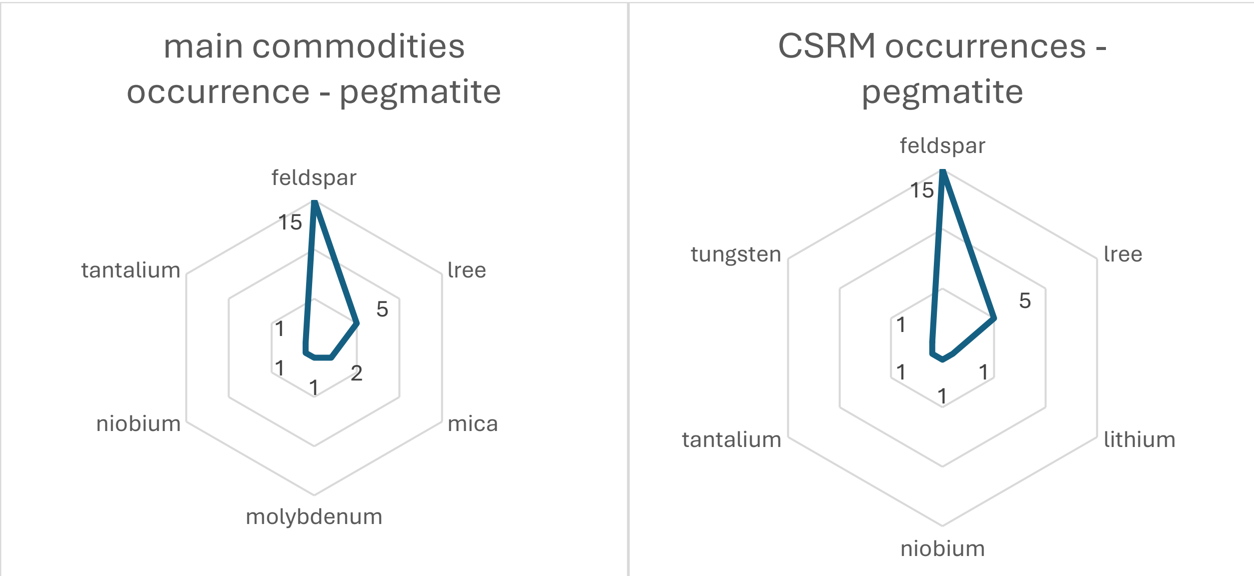

Figure 4.15: Pegmatite main commodities highlighting the Critical and Strategic Raw Materials.

Morphology and texture: These typically occur as lentiform or tabular bodies (10 sites), sometimes clustered (5 sites) at the peripheries of the intrusions, along with greisen. The commodity-bearing minerals are both massive (feldspars) and disseminated (LREE-bearing minerals).

Sedimentary Manganese Deposits

General characteristics: Sedimentary manganese deposits (36 sites, 5.5%) are almost exclusively linked to hydrothermal processes being formed in seafloor environments from volcanic-related exhalative fluids. These deposits are all related to the Oligo-Miocene volcanism, specifically associated with sub-horizontal lying pyroclastic rocks. They also show supergene alteration (2 sites).

Morphology and texture: Typically occurring as stratiform (32 sites), lentiform (8 sites) and tabular (4 sites) shapes, the manganese minerals can be massive (20 sites), disseminated (14 sites) and sometimes gathered in stockworks of veinlets (6 sites). They are rarely commuted with iron oxides (4 sites).

Clay Deposits

General characteristics: Clay deposits (22 sites, 3.4%) show a mixed genetic signature, with sedimentary accumulation (12 sites) and hydrothermal alteration (10 sites) processes taking place mostly during the Jurassic (11 sites) and Miocene (9 sites).

Morphology and texture: The morphologies for the two genetic classes are naturally guided by the shape of sedimentary basins and hydrothermal conduits, being stratiform (17 sites), lentiform (5 sites), cluster and tabular (4 sites), while the textures are generally stratified (15 sites) and massive (6 sites).

Commodities: The commodities include ceramic clays (11 sites), bentonite (6 sites) and kaolinite (6 sites).

They are hosted by conglomerate (11 sites), limestone (11 sites) and pyroclastic rocks (9 sites), linked to the diverse mechanism of physical and chemical concentration of the clays.

Oolitic Ironstones

General characteristics: Oolitic ironstones (11 sites, 1.7%) are exclusively sedimentary (11 sites) and dated to the Upper Ordovician (11 sites), representing a distinct Paleozoic metallogenetic event.

Commodities: The ore minerals are represented by oolites made from siderite (8 sites), limonite (5 sites), magnetite (4 sites), hematite (3 sites).

Morphology and texture: They are stratified in sub-horizontal oolitic beds with stratiform (11 sites), lentiform and stratabound (10 sites) geometries hosted in Palaeozoic phyllites (8 sites), quartzite (1 sites), schist (1 site) and limestone (1 site).

Bauxite Deposits

Bauxite (5 sites, 0.8%) deposits are linked to residual processes dated to the Cretaceous, representing a significant Mesozoic weathering event. They are characterized by massive and stratified aluminium-bearing bauxite strata associated with clay levels hosting LREE-minerals (bastnaesite, cerianite). These are hosted by limestones lithologies.

SEDEX Deposits

General characteristics: SEDEX deposits (7 sites, 1.1%) are linked to a composite process made from hydrothermal, sedimentary and supergene alteration.

Age: The age is predominantly Cambrian (6 sites), with minor post-Variscan (2 sites) overprints. These are hosted by dolomite (5 sites), sandstones (5 sites) and limestones (2 sites).

Commodities: The ore minerals are Pb-Zn sulfide associated to pyrite, barite and iron-oxides.

Morphology and texture: Morphologically, these deposits are dominated by stratiform (5 sites), lentiform and tabular geometries, reflecting their syn-sedimentary exhalative origin.

Texturally, SEDEX deposits are characterized by massive (6 sites) and stratified (1 site) fabrics, reflecting both massive sulfide accumulation and primary sedimentary layering.

Sedimentary Deposits

General characteristics: Sedimentary deposits (9 sites, 1.5%) are linked to sedimentary (5 sites) and residual (6 sites) processes, with ages ranging from Permian (4 sites) to Miocene (5 sites).

Morphology and texture: Naturally, their morphologies stratiform (5 sites) and lentiform (4 sites). Texturally, they are dominated by stratified (9 sites) fabrics, with minor massive (3 sites) occurrences.

Commodities: The commodities typically include heavy minerals such as iron-oxides (4 sites), feldspar (2 sites) and quartz (2 sites), along with kaolinite (2 sites), hosted in limestone (6 sites), schist (4 sites) and sandstones (3 sites).

Metamorphic Deposits

General characteristics: Metamorphic deposits (6 sites, 0.9%) are genetically correlated to metamorphic and hydrothermal fluids interacting with the host rocks to produce talc (5 sites) and pyrite (1 site) deposits. The host lithologies include granodiorite (5 sites), marble (5 sites), schist (5 sites).

Age: The age of the deposits is mainly Carboniferous (6 sites) with one occurrence inferring a Silurian reworking.

Morphology and texture: They are lentiform and clustered, generally massive textured.

Low and high sulfidation epithermal deposits

General characteristics: Epithermal deposits (3 sites) are linked to epithermal and hydrothermal processes, occurred during the Oligo-Miocene volcanism.

Morphology and texture: Morphologically, they show lentiform (1 site), stratiform (1 site), and tabular (1 site) forms. Texturally, they display disseminated (1 site) and stratified (1 site) fabrics.

Commodities: Their economic potential is linked to high valuable commodities such as gold (3 sites), silver (2 site) found as electrum and native gold. The LS deposits have arsenic and antimony-bearing minerals like stibnite and tetrahedrite, while the HS have tellurides and copper minerals such as enargite and chalcopyrite.

Paleoplacers and placers

General characteristics: Paleoplacer (2 sites) and placer (2 sites) deposits are both stratiform sedimentary deposits specifically formed by mechanical accumulation on heavy minerals.

The paleoplacers are lithified and dated to the Upper Ordovician (2 sites), displaying stratified texture (2 sites), concentrating monazite (LREE), and titanium oxides (rutile and anatase).

The placers are Quaternary (1 site) and have disseminated (1 site) cassiterite and uranium oxides.

The Table 4.9 summarises the most common characteristics of each ore deposit types.

Type	Count	Tipical age	Tipical commodities	Morphology	Texture	Host rock lithology
hydrothermal veins	308	permian(?), post-variscan(?)	barite, lead, zinc	lentiform, tabular	brecciated, disseminated	limestone, schist
skarn	95	carboniferous, permian	copper, lead, zinc	lentiform, tabular	disseminated, massive	limestone, schist
karst	51	cambrian, post-variscan(?)	barite, lead, zinc	cluster, tabular	disseminated, stratified	dolomite, limestone
sedimentary manganese deposit	36	miocene, permian	iron, manganese, tungsten	lentiform, stratiform	disseminated, massive	pyroclastic rock, rhyolite
MVT	30	cambrian, post-variscan(?)	lead, silver, zinc	cluster, stratabound	disseminated, massive	dolomite, limestone
greisen	27	carboniferous, permian	copper, molybdenum, tungsten	cluster, tabular	disseminated, stockwork	granite, schist
clay deposit	22	jurassic, miocene	bentonite, clay, kaolinite	lentiform, stratiform	massive, stratified	conglomerate, limestone
pegmatite	16	carboniferous, carboniferous(?)	feldspar, LREE, mica	lentiform, tabular	disseminated, massive	granite, tonalite
porphyry	14	carboniferous, oligocene	copper, lead, zinc	cluster, tabular	disseminated, stockwork	andesite, granite
oolitic ironstone	11	upper ordovician	aluminium-bauxite, iron, zinc	lentiform, stratiform	-, stratified	phyllite, schist
sedimentary	9	miocene, permian	copper, iron, kaolinite	lentiform, stratiform	massive, stratified	limestone, schist
sedex	7	cambrian, post-variscan(?)	lead, pyrite, zinc	cluster, stratiform	massive, stratified	dolomite, sandstone
metamorphic	6	carboniferous, silurian	pyrite, talc	cluster, lentiform	disseminated, massive	marble, schist
bauxite	5	cretaceous	aluminium-bauxite, LREE, zinc	stratiform	massive, stratified	limestone
paleoplacer	2	upper ordovician	LREE, phosphorus, thorium	stratiform	stratified	sandstone
low sulphidation epithermal deposit	2	miocene, tertiary	antimony, gold, mercury	lentiform, tabular	disseminated, stratified	pyroclastic rock, volcanic rock
placer	2	-, quaternary	tin, uranium	stratiform	disseminated	clastic sediment
volcanic deposit	1	pliocene	perlite	cluster	massive	rhyolite
magmatic intrusion	1	pliocene	feldspar, LREE	cluster	disseminated	phonolite
aplite	1	permian	feldspar	tabular	massive	granite
high sulphidation epithermal deposit	1	miocene	arsenic, gold, silver	cluster	brecciated, disseminated	andesite, pyroclastic rock

Table 4.9: Summary of the most common features of every mineralisation type.

5. Case Studies for implementing the database

One of the core ideas of the metallogenic database of Sardinia is stated to be a continuous data implementation for both new records and updated data for the known ones. The progressive advancement in Sardinian mineralisation knowledge during the process of building the database, over a temporal arc of three years, allowed us to contemporaneously add data, and helped us in the architecture framing, data selection and hierarchisation, and the metallogenic representation.

The core of historical data is represented by the Sardinian Mining Agency (EMSA) archive, comprising over 4400 reports drafted in the 1980s to investigate known occurrences and mining data. They were often drafted rapidly and with limited resources during extensive prospecting campaigns and can be fragmented and lack completeness. The critical integration and interpretation of modern information and knowledge gave us a powerful basis for localisation and classification of the ore deposits and mineral occurrences. A limit of this work is the unreliable economic quantification of the ore deposits due to the lack of precise information on tonnage and grades: in the common case of deposits exploited in the past, we gathered partial information on the production of some mines, but we don't have reliable information on the remaining reserves. Consequently, while our models effectively identify where and why mineralisation occurs and is exploited, quantifying the economic potential of remaining resources is difficult due to this data gap.

Comparative modelling is the approach we chose to synthesise ore deposit types by interpreting historical data. It is the process of comparing geological features, processes, or systems to understand their similarities, differences, and potential relationships to draw inferences about the unknown based on the known. The key aspects of this approach are:

- Definition of analogues based on the target
- Data comparison from both the analogue and target systems
- Creating a model to represent the target system based on the insights gained from the analogue
- Using the model to make predictions and test these predictions through focused data collection or analysis

We elected areas as main representatives for several ore deposits:

- the Rosas-Orbai area for Cu-Pb-Zn skarn, Ba-Pb-Zn karst and barite-fluorite hydrothermal veins.
- Su Laccheddu-Giacone (northern Sardinia) greisen and hydrothermal system for intrusion-related Sn-Mo-(W)-F-REE deposits.
- Silius (central-south Sardinia) for fluorite-barite veins.
- The Fluminese district (SW Sardinia) for F-Ba hydrothermal veins, polymetallic (Co-Ni-Bi-As) veins and Cu-Pb-Zn, Fe skarn.
- The Brecca (SE Sardinia) mineralisation for the Sb-As veins system and fluorite veins as well.

While implementing the database records (targets), we compared the given data with our models, then we filled the gaps with the modelled data, and eventually updated the data based on new studies.

The filling data generally consisted of:

- minerals and especially CRMs.
- genetic process of mineralisation and classification.

- host-rock tectonic unit.
- structural features and eventual current interpretation in the geodynamic context, resulting in age constraining and eventually a genetic model.

5.1. The structural and metallogenic map of the Rosas-Orbai District (SW Sardinia): database development and structural control on ore deposits

The Sulcis-Iglesiente region in southwestern Sardinia was the most economically relevant area of the island, hosting some of its largest ore deposits, including Mississippi Valley-Type (MVT) Pb-Zn sulfide deposits, Pb-Zn-Cu-Fe skarn, barite-Pb karst, and barite-fluorite veins. Despite varying ore types and grades, all these mines had a common feature: high concentrations of economic materials at shallow depth. This permitted their long history of exploitation since the 19th century, but the scarce interest in economic investments for exploration also led to a lack of knowledge regarding the deeper mineralised systems, ultimately stalling advanced exploration in modern times.

The Rosas – Orbai district exhibits a variety of ore deposit types within a relatively small area, supported by a solid structural interpretation. Previous geological studies, conducted at scales of 1:2500 to 1:10000, were primarily aimed at synthesising regional 1:50,000 scale mapping (Funedda, 2009). In these works, ore deposits were often treated as simple lithological units without a detailed metallogenic context. More localised investigations have since been carried out on skarn deposits and the structures controlling their features (Attardi et al. 2020, Cocco et al. 2022). We have selected this area as a model for skarn ore deposits and as a laboratory for implementing both the structure of our database and the dataset itself.

5.1.1. Geological Framework of the Rosas-Orbai District

The Rosas-Orbai area provides a well-exposed transect through the Variscan foreland of the Sulcis-Iglesiente region, whose stratigraphy (Figure 5.1, Figure 5.2) was profoundly influenced by the emplacement of the Arburese Thrust and the associated development of the Rosas Shear Zone (RSZ).

Stratigraphy

The geological framework is dominated by a Lower Cambrian to Upper Ordovician sequence, intruded by gabbroic dikes.

The basal, Lower Cambrian Nebida Formation (Pillola et al., 1995) includes biogenic limestones with archaeocyath reefs (Matoppa Member) (Debrenne et al., 1993) and siliciclastics, sandstones, shales, and dolomitic algal mats (Punta Manna Member) (Debrenne et al., 1988). These are overlain by the carbonate succession of the Gonnesa Formation (Pillola et al., 2002), which comprises, from base to top: the well-stratified dolostone ("Dolomia rigata"), and the massive grey limestone ("Calcare ceroide") at the top.

This is overlain by the Middle Cambrian Campo Pisano Formation, comprising approximately 50 metres of marly and nodular limestone (Pillola et al., 1995), and the Cabitza Formation, a 400 m thick siliciclastic succession.

The succession is truncated by the Sardic Unconformity (von Raumer et al., 2015; Cocco and Funedda, 2019; Oriolo et al., 2022; Loi et al., 2023), above which lie the Upper Ordovician siliciclastic deposits of the Monte Argentu Formation (heterometric conglomerates, megabreccias, phyllites) and the fossil-rich Monte Orri, Portixeddu, Domusnovas, and Rio San Marco formations.

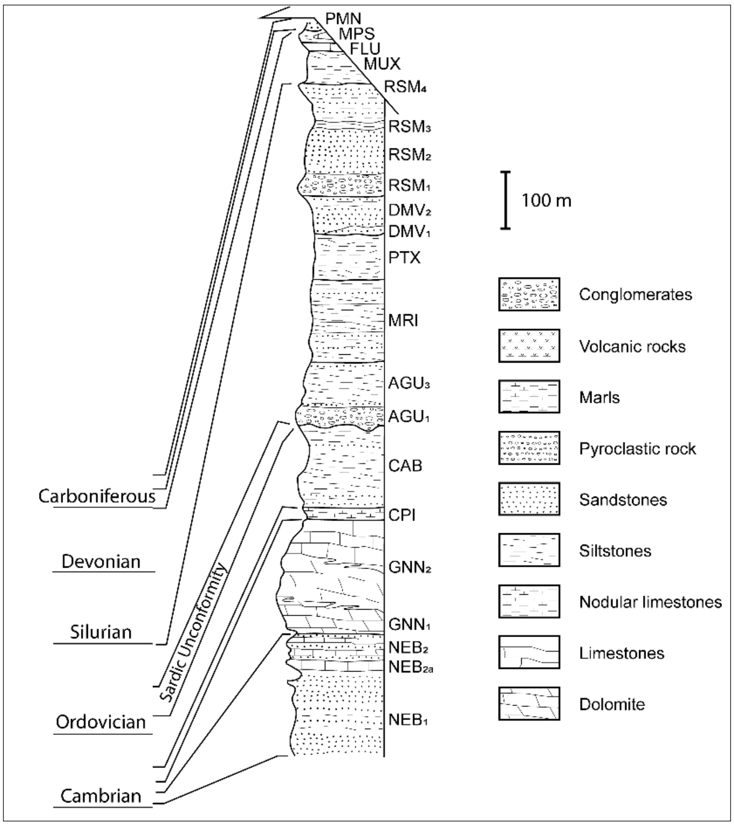

Figure 5.1: Lithostratigraphic log of the Sulcis – Iglesiente region.

Structural Geology

The district is dominated by the Arburese Thrust (AT) and the Rosas Shear Zone (RSZ) developed in its footwall (Conti et al., 2001; Conti and Patta, 1998; Funedda, 2009). The Variscan Nappe Zone (Arburese Unit, Conti and Patta, 1998) is represented by the "Arenarie di San Vito" formation, consisting of metasandstones and metasiltstones (Barca et al., 1981). The high strain associated with thrusting caused the slicing of competent Cambrian limestones and created a pervasive structural fabric that controlled later fluid flow (Cocco et al., 2022a; Funedda, 2009).

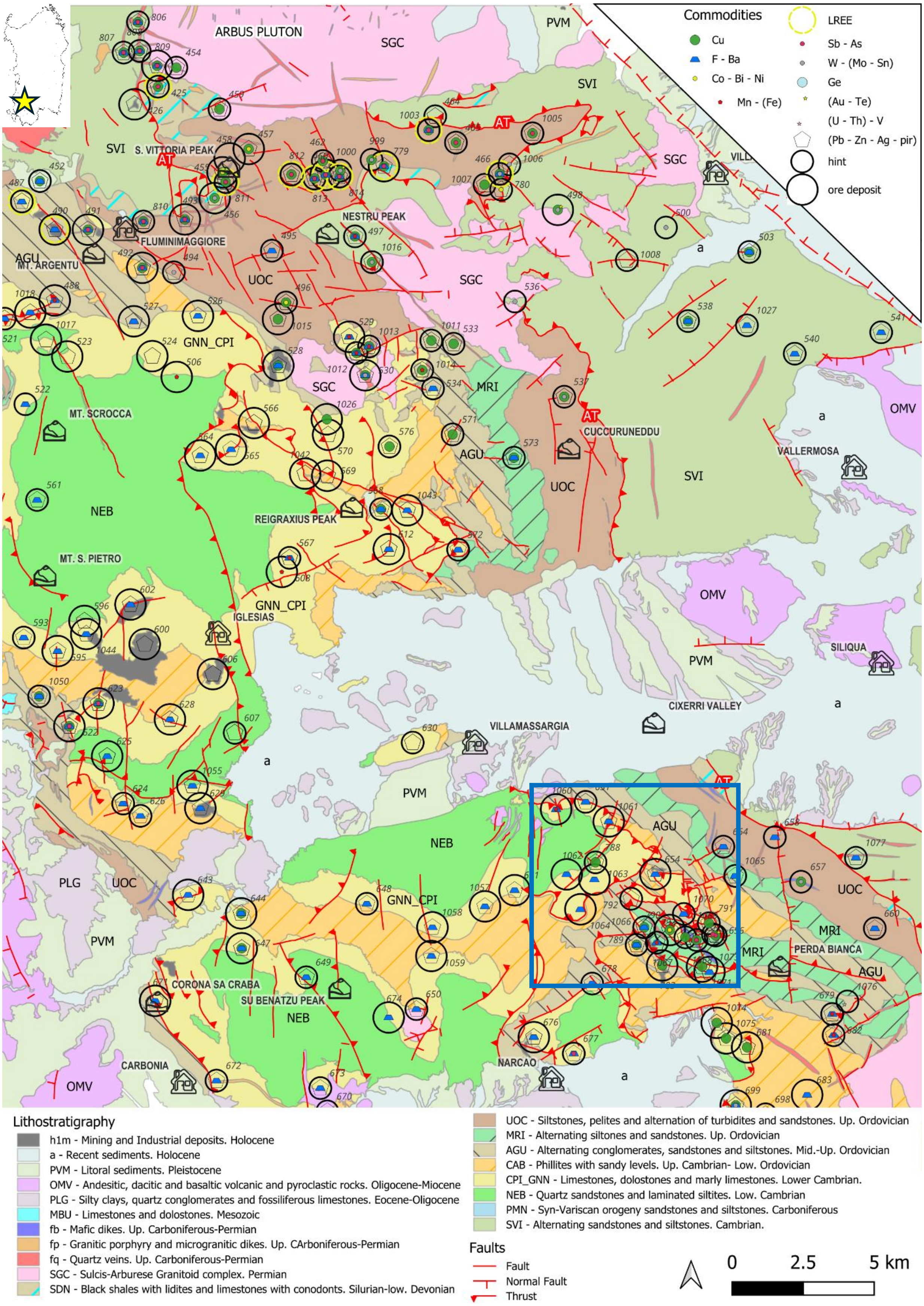

Figure 5.2: Metallogenic sketch Map of the Sulcis-Iglesiente District AT = Arburese Thust. Re blue square indicate the Rosas – Orbai district.

5.1.2. Ore deposits of the Rosas-Orbai district

The Rosas–Orbai area exhibits a variety of ore deposit types within a relatively small area. The primary identified ore genetic types are:

Skarns (9 occurrences)

They are mostly hosted within tectonic slices of the Cambrian Gonnesa Formation limestone (Figure 5.3a,b), but metasomatisation of a mafic dike protolith is documented (Mitza Sermentus, Attardi et al., 2020), primarily within the Rosas Shear Zone (e.g., Barisonis, Punta Atzori, Mitza Sermentus), where large-scale thrusting and fracturing enhanced fluid circulation (Cocco et al., 2022a). Some skarn bodies also exhibit late-stage veining. They are polymetallic deposits (Figure 5.3b,c) characterised by sphalerite, chalcopyrite, magnetite, tetrahedrite, alongside traces of precious metals such as Ag and Au. Gangue minerals include diopside, andradite-grossularite, wollastonite, tremolite-actinolite, chlorite, quartz, and calcite.

Hydrothermal Veins (24 occurrences)

Predominantly composed of barite, occasionally associated with galena, chalcopyrite, sphalerite, and pyrite. They are controlled by NE-SW to ENE-WSW trending normal fault systems related to post-orogenic extension (Padalino et al., 1972). Quartz veins and stockworks, generally N-S oriented, crosscut the mineralised veins (e.g. Punta Filippeddu). A single occurrence of NNW-SSE arsenopyrite veins swarm was found at Mitza Sermentus (Figure 5.3d), clearly cutting across the ENE-WSW trending skarn orebodies (Attardi et al., 2020).

Karst-hosted Deposits (11 occurrences)

Dominated by barite with minor galena, sphalerite, and secondary oxides (limonite, cerussite). The distinctive textural features (crustiform banding, stratified levels and brecciation) help to distinguish karst-barite from veins-barite. These are controlled by karstic cavities within carbonate sequences, often elongated along vertical fault-breccias and sub-horizontal backthrusts, suggesting karstification was enhanced by faulting (Figure 5.3e,f). Several deposits exhibit mixed vein and karst characteristics.

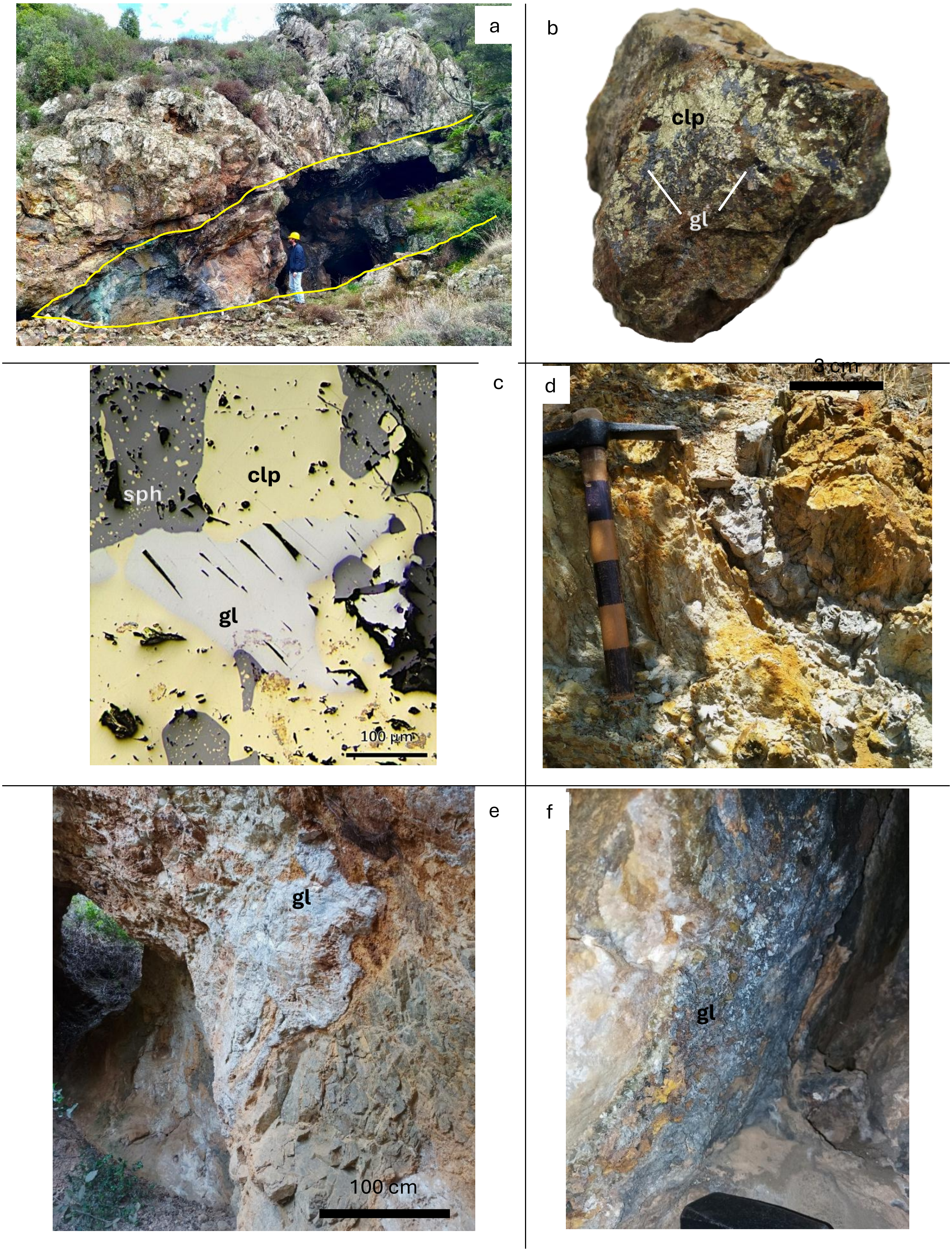

Figure 5.3: a) Barison skarn slice (outlined in yellow) embedded between a mafic dike (below) and Ordovician siliciclastic rocks; b) sample of the Barisonis skarn bearing chalcopyrite (clp - golden yellow) and galena (gl - metallic, dark grey); c) Reflected light microscopy picture of Mitza Sermentus skarn displaying the chalcopyrite, galena and sphalerite (sph) assemblage; d) Arsenopyrite vein at Mitza Sermentus site; e) Remnant of a N-S barite vein (milky white) at Punta Filipeddu site; f) barite tabular crystals (milky and dark grey) covering a karst cavity wall at Punta Filipeddu.

Table 5.1 summarises the most significant past exploration permits and/or mining concessions.

Mining License	*Key Localities*	*Primary Commodities*	*Historical Notes & Production Highlights*
Punta Filippeddu	Monte Modditzi, Punta Filippeddu	Barite (Karst & Veins)	20,000 tonnes crude ore @ 90% $BaSO_4$ (1971). Mining via open-pit benching.
Orbai	Orbai Vein	Barite, Fluorite, Ag-rich Galena, Chalcopyrite (Veins)	High-grade Pb-Ag production: 138,373 tonnes galena (1943-1957).
Sedda Antiogu Sabiu	Sedda Antiogu Sabiu, Punta Perd'e Fogu	Barite (Veins & Karst)	Large-scale barite potential; estimated reserves >650,000 tonnes.
Truba Niedda	Truba Niedda	Barite, Galena, Sphalerite, (Skarn)	Polymetallic vein system and skarn. Production: 10,200 tonnes crude ore.
Rosas	Rosas Mine	Sphalerite, Galena (Skarn)	The district's most prominent mine. Evolving resource estimates (10k - 64k tonnes).
Mitza Sermentus	Mitza Sermentus	Galena, Sphalerite (Skarn), Arsenopyrite (Veins)	Small-scale production; skarn lenses in cataclasite; arsenopyrite veins a Au target.
Punta Is Ollastus	Serra Martis, Conca de Quaddu	Barite (Karst)	Karst mineralisation controlled by NE-SE normal faults.
Punta Spinarba / S. Pietro	Eastern part of the map	Barite, Fluorite, Galena (Veins)	Surface prospecting only; no recorded production.
Monte Ettoi	Truba Niedda, others	Barite, Fluorite, Galena (Veins)	Mostly research permits overlapping with known concessions.

Table 5.1: Main exploration permits and mining concessions in the Rosas – Orbai area.

Genetic and Exploration Model

Our data support a genetic model comprising four distinct but genetically linked stages, reflecting a transition from deep-seated magmatic-hydrothermal systems to near-surface meteoric fluid regimes.

Pre-Concentration

The Cambrian sedimentary sequences provided both a proto-ore concentration (Aponte et al., 1988, Boni et al., 1996; Santoro et al., 2023), a chemical trap reactive to mineralising fluids (Cambrian limestones) and, after cataclasis and karstification, the structural fabric for later fluid flow.

Skarn Formation (Syn- to Post-Collisional Magmatism)

High-temperature, magmatic-hydrothermal fluids associated with Permian intrusions metasomatized the carbonate lithologies along thrust-related structures to form the skarn rocks. Retrograde alteration involved mixing with meteoric waters (Boni et al., 1990) and the precipitation of the Zn-Pb-Cu-bearing ore minerals.

Hydrothermal Vein Formation (Post-Orogenic Extension)

Lower-temperature fluids deposited barite-dominant veins, with variable Pb-Zn-Ag content, in normal fault systems during and/or after orogenic collapse, plausibly enhancing the mixing of residual magmatic or metamorphic fluids with meteoric or basinal waters; a common feature in post-orogenic hydrothermal systems (Boni et al., 2003; Simmons et al., 2005).

Karst-fill Mineralisation (Supergene Processes)

Near-surface, low-temperature deposition of barite within karst cavities by meteoric water, during regional uplift and exposure, potentially remobilising barium from earlier stages (Sass-Gustkiewicz et al., 1982).

This model leads to a coherent exploration strategy which can be applied on a regional scale:

- Skarn potential is highest in the footwall of the main Variscan thrusts, proximal to granitoid intrusions.
- Vein-style mineralisation is best targeted along high-angle, late/post-Variscan normal faults.
- Karst-hosted deposits are usually small and localised, but their spatial association to hydrothermal veins can be a guide for exploration within the weathered upper sections of the Cambrian carbonate sequence.

This model not only clarifies the metallogenic evolution of the Rosas-Orbai district but also provides a scalable methodology for re-evaluating mineral prospectivity in similar mature terrains, highlighting significant residual potential in Sardinia.

This genetic and exploration model meet the historical mining data from the Sardinian Mining Agency (EMSA) archive. The review of past concessions reveals a clear economic distinction: high-grade, fault-controlled vein systems (e.g., the Orbai deposit, rich in Ag-Pb) and skarn bodies (e.g., Rosas, Truba Niedda) were the primary targets for base metal mining. In contrast, extensive karst-hosted and vein-style barite mineralisation (e.g., Punta Filippeddu, Sedda Antiogu Sabiu) represented a major, bulk-tonnage resource. Critically, the spatial distribution of these historical mines and prospects aligns perfectly with the proposed structural controls, with production consistently localised along the specific thrust and fault trends that define our model.

5.2. Petrological, and geochronological constraints of the Su Laccheddu W-Mo-LREE greisen and fluorite-hydrothermal ore deposits

The Gallura region in northern Sardinia is vastly occupied by granites intruding the Variscan High-Grade Metamorphic Complex of Sardinia. The metallogeny of the area includes granite-related ore occurrences, mostly W-Sn-Mo-Bi and fluorite-LREE (Figure 5.4). Due to their known small volumes and difficult logistics, they were never actually exploited; a small amount of data covers the area.

Due to the interest in Critical and Strategic Raw Materials, the region may now be considered an interesting prospect.

5.2.1. Geological and metallogenic features

Mineralised greisen, pegmatites and hydrothermal veins are hosted at the intrusive contacts between the late-Variscan granites and their Variscan high-grade metamorphic host rocks (Figure 5.4). These contacts are often reactivated as normal and transpressive faults (Cossu et al., 2023) presumably during the collapse of the Variscan chain.

We studied the Giacone - Su Laccheddu mineral system (Figure 5.5), a three-kilometers fluorine-rich, open hydrothermal system developed at the periphery of late-Variscan granites, forming Mo-W-F-LREE greisen and fluorite veins at the intrusive contacts with high-grade Variscan metamorphic rocks (Cossu et al., 2024).

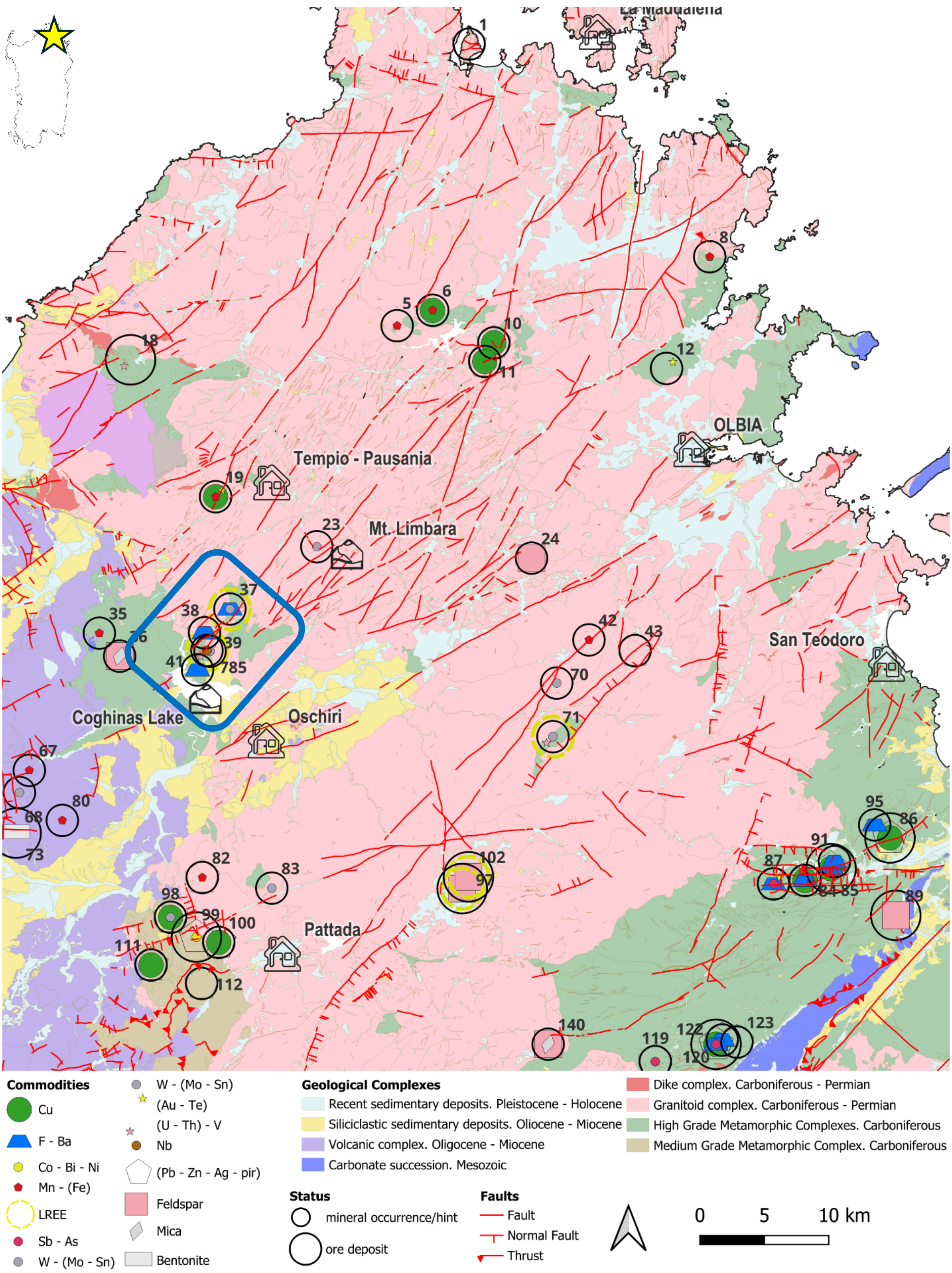

Figure 5.4: Metallogenic sketch map of north-eastern Sardinia. The blue square indicates the Su Laccheddu – Giacone mineral system (Figure 5.5).

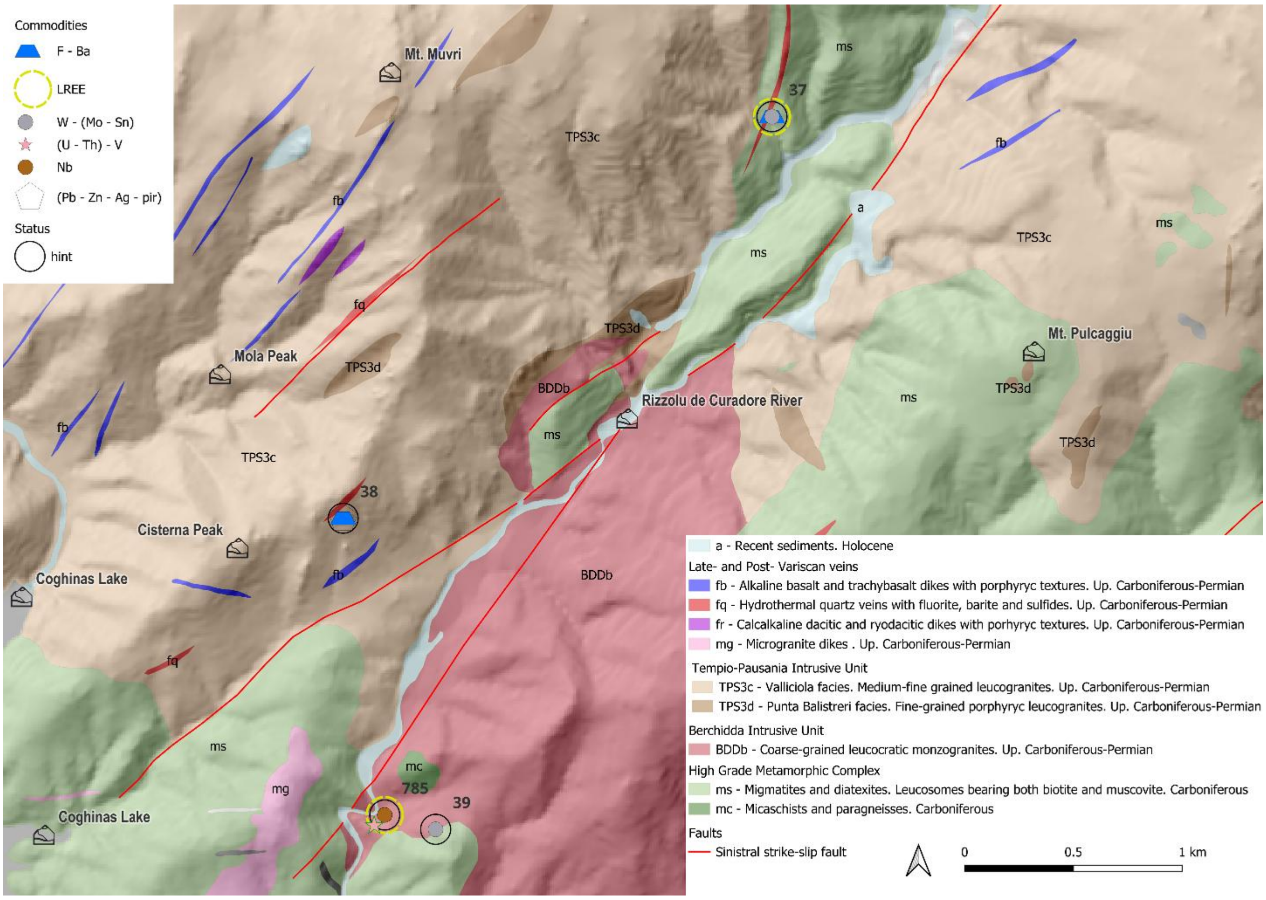

Figure 5.5: Metallogenic Map of the Su Laccheddu (id: 785) - Giacone (id: 37) mineral system. id: 38 is the fluorite veins system of Punta Lanzinosa and id: 39 the Monte Mannu Mo-W greisen.

The Giacone mineralisation (Figure 5.5, id: 37) is composed of two systems of high-angle hydrothermal veins strike NE-SW dipping in opposite directions, and are composed of fluorite, quartz, and rare barite, galena and apatite. They range in thickness from a few centimeters to several decimeters, with brecciated and layered structures, respectively. The banded ones permeate the granites as stockworks of fluorite and quartz veinlets departing from thicker veins (Figure 5.6a). A vertical fault breccia made of metamorphic rocks and greisen clasts (Figure 5.6b) crosscut the banded system and is cemented by fluorite and subordinate quartz and molybdenite. At the footwall of the brecciated fault system, fault mirrors on quartz display sub-vertical slicklines and argillic alteration. It hosts fluorite veins, molybdenite spreading, and greisen breccia blocks.

The greisen facies of Giacone is analogous to the Su Laccheddu (Figure 5.5, id: 785) one. The rock is massive and mainly composed of white mica and quartz (Figure 5.6c,d), with disseminations of molybdenite veinlets (Figure 5.6e,f - “dry veins”). Scheelite is common, but at the outcrop scale it is difficult to distinguish from quartz.

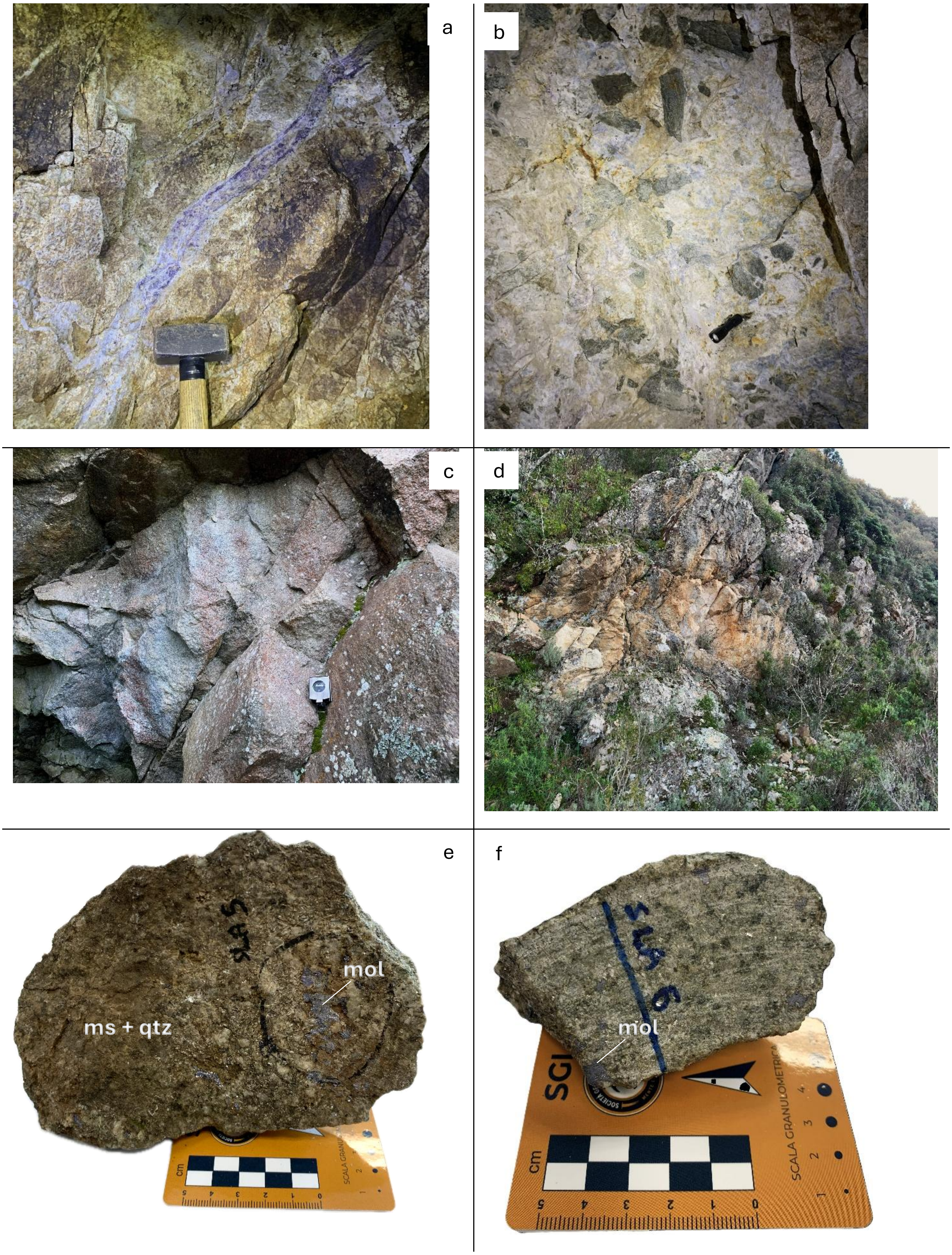

Figure 5.6: a) Banded quartz, purple and white fluorite vein inside a Giacone gallery; b) breccia cemented by fluorite and quartz inside a Giacone gallery; c) Su Laccheddu greisen outcrop, cut by a d) N30° trending trench; e,f) Su Laccheddu greisen with molybdenite (mol - metallic grey) and scheelite (light grey/milky white, easily confusable with quartz).

At Punta Lanzinosa (Figure 5.5, id: 38), the fluorite vein system reaches its maximum development, forming a NE-SW trending vein swarm with single veins exceeding 1 m in thickness, consisting of quartz, purple fluorite, and blue fluorite (Figure 5.7).

Figure 5.7: Punta Lanzinosa vein with purple and blue fluorite vein.

5.2.2. The mineralogy of Su Laccheddu Greisen

The greisen comprises of magmatic relics including K-feldspar, plagioclase, zircon, monazite and biotite (Figure 5.8a,bFigure 5.8: SEM-EDS images of the ore minerals from Su Laccheddu – Giacone greisen. a) k-feldspar crystal (kfs – light grey) fractured and altered with growth of secondary phyllosilicates in a quartz matrix, from the TUC1 sample; b) monazite (mnz - white) and zircon (zrn – light grey) relics at the border of a phyllosilicate (phs) in the sample SLA5; c,d,e) white micas with evident zonation bordered by molybdenite (mol), secondary phyllosilicates/sericite (ser) and quartz from Su Laccheddu greisen (respectively samples SLA1, SLA1, SLA5 and SLA6).) while the greisen-phase assemblage is predominantly composed of zoned white mica (Figure 5.8c,d,e,f), quartz and sericite along with the ore minerals (Figure 5.9a,b,c,d,e,f):

- scheelite [$CaWO_4$] with wolframite [$(Fe,Mn)WO_4$] and columbite-tantalite [$(Fe,Mn)(Nb,Ta)_2O_6$] inclusions (Figure 5.9a).
- fluorocarbonates-(Ce) [Synchysite-(Ce): $CaCe(CO_3)_2F$, Parisite-(Ce): $CaCe_2(CO_3)_3F_2$] (Figure 5.9b) associated with zircons and monazites [$(Ce,La,Nd,Th)PO_4$], and rare thorite/uraninite [$ThSiO_4$ and UO_2].
- Molybdenite [MoS_2] dry-veins with interstitial Bi-Te phases (Figure 5.9c).
- rare hematite, titanite [$CaTiSiO_5$], Ti-oxides [TiO_2], pyrite and columbite-tantalite.
- Banded and massive fluorite [CaF_2] (at Giacone and Punta Lanzinosa - Figure 5.9d).
- disseminated apatite [$Ca_5(PO_4)_3(F,Cl,OH)$] (at Giacone - Figure 5.9e,f).

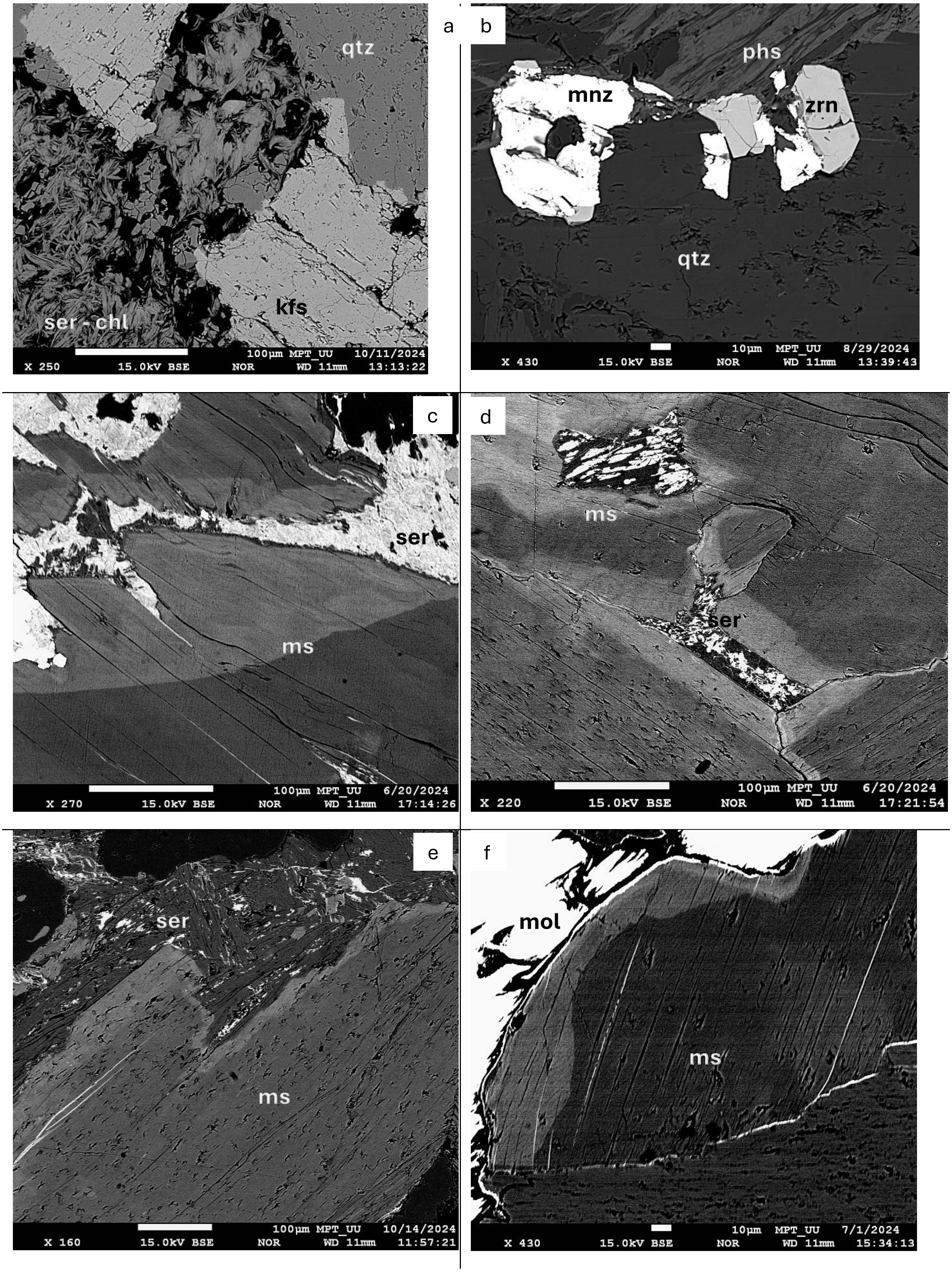
a
qtz
ser - chl
kfs
X 250 15.0kV BSE 100µm MPT_UU NOR WD 11mm 10/11/2024 13:13:22
b
phs
mnz
zrn
qtz
X 430 15.0kV BSE 10µm MPT_UU NOR WD 11mm 8/29/2024 13:39:43
c
ser
ms
X 270 15.0kV BSE 100µm MPT_UU NOR WD 11mm 6/20/2024 17:14:26
d
ms
ser
X 220 15.0kV BSE 100µm MPT_UU NOR WD 11mm 6/20/2024 17:21:54
e
ser
ms
X 160 15.0kV BSE 100µm MPT_UU NOR WD 11mm 10/14/2024 11:57:21
f
mol
ms
X 430 15.0kV BSE 10µm MPT_UU NOR WD 11mm 7/1/2024 15:34:13

Figure 5.8: SEM-EDS images of the ore minerals from Su Laccheddu – Giacone greisen. a) k-feldspar crystal (kfs – light grey) fractured and altered with growth of secondary phyllosilicates in a quartz matrix, from the TUC1 sample; b) monazite (mnz - white) and zircon (zrn – light grey) relics at the border of a phyllosilicate (phs) in the sample SLA5; c,d,e) white micas with evident zonation bordered by molybdenite (mol), secondary phyllosilicates/sericite (ser) and quartz from Su Laccheddu greisen (respectively samples SLA1, SLA1, SLA5 and SLA6).

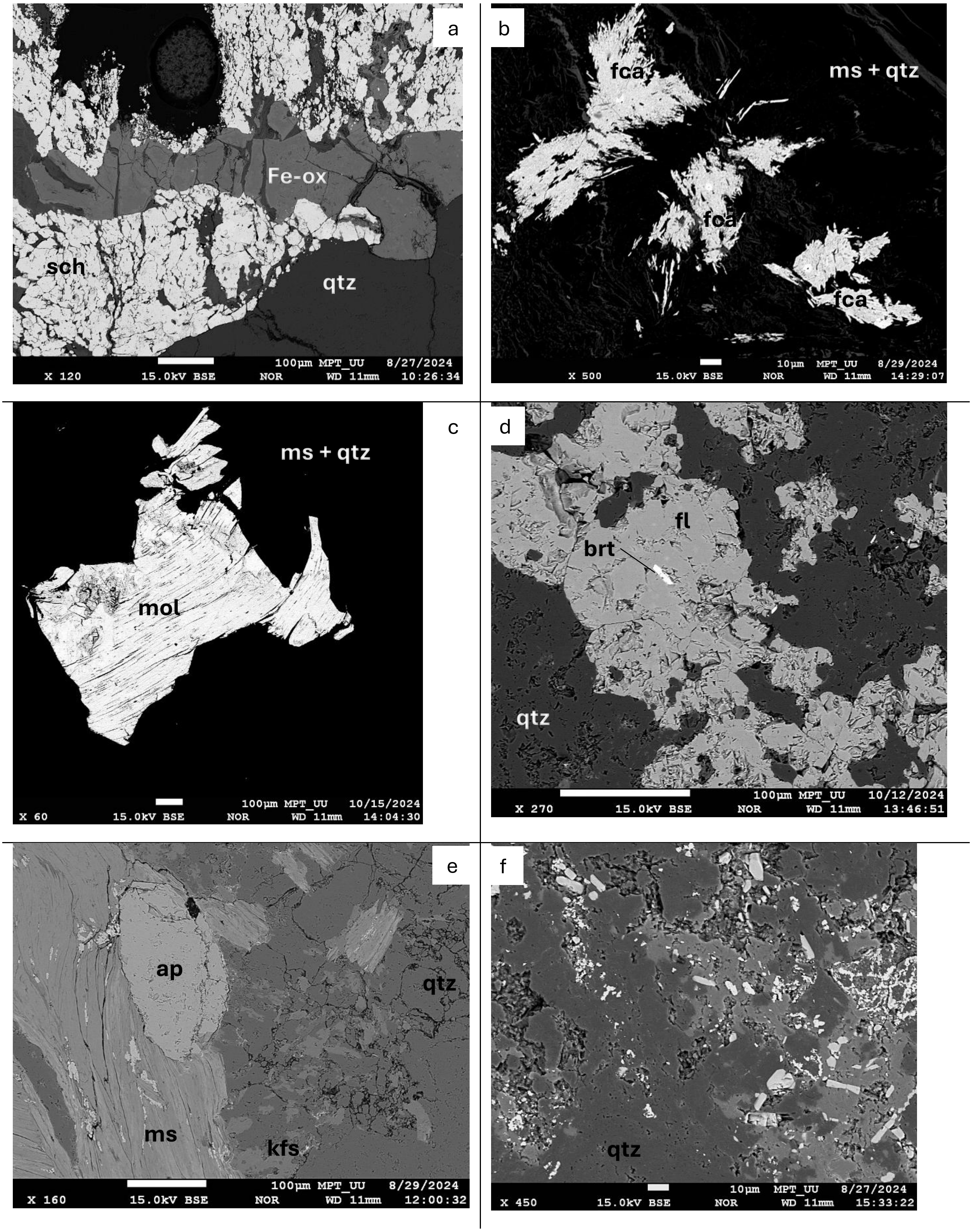

Figure 5.9: SEM-EDS images of the ore minerals from Su Laccheddu – Giacone greisen. a) Fractured and altered scheelite (sch - white) with iron oxide (dark grey) from the sample SLA3a; b) REE-bearing fluorocarbonate crystals (fca -

grey) from the sample SLA6. They are extremely delicate, as shown by the white dots left by the instrument's beam, and difficult to analyse; c) molybdenite crystal in a matrix composed of white mica and quartz from the sample SLA6; d) fluorite crystals aggregate(fl – light grey) including a barite crystal (brt – white) immersed in a quartz matrix (qtz) from a Giacone hydrothermal vein; e-f) Apatites (ap - white and lighter grey) crystals disseminated in the quartz, sericite and mica matrix in the Giacone greisen.

Evolution of the Su Laccheddu Greisen System

The geochemical and geochronological data provide a multi-proxy record of the magmatic-hydrothermal evolution of the Su Laccheddu greisen system. Integration of mineral chemistry, REE geochemistry, and in situ Rb–Sr geochronology allows reconstruction of a protracted history of fluid circulation and ore deposition spanning the late Carboniferous to early Permian (ca. 293–270 Ma).

Electron microprobe analyses were performed on key minerals to investigate the evolution of the greisenization process and the connected redistribution of the Critical Raw Materials. Rare Earth Elements (REE) are the more evidently redistributed in association with the variation of F budget which later developed the fluorite mineralisation during hydrothermal process. The chosen minerals are:

- Feldspars, which greisenization alter into phyllosilicates (e.g., white mica).
- White micas, which grow during the greisenization.
- Monazite, which bear the most significant REE budget from the intrusive stage to the greisen system.
- Apatite and REE-carbonates (e.g., synchysite), bearing REE and F they play an important role into understanding the distribution of these elements during the intrusive-greisenization-hydrothermal transition.

The greisenization recorded: feldspars and white micas

Feldspars

Relict feldspars preserved in the greisen record the early magmatic stage of the system. The feldspar crystals refer to two populations (Table 5.2: Feldspar EMP analyses results in apfu from the Su Laccheddu (SLA) and Giacone (ITU) greisens.Table 5.2): albite (Na-feldspar) from sample SLA1 and K-feldspar from ITU7a.

Albite (Ab93–Ab98) and K-feldspar (Or96–Or99) from samples SLA1 and ITU7a retain compositions consistent with crystallization from a fractionated granitic melt.

The presence of minor F (0.05–0.09 apfu in albite; 0.03–0.16 apfu in K-feldspar) indicates that the magmatic system was already enriched in volatiles, a prerequisite for subsequent greisenization (Pirajno, 2009) and it's coherent with the YMP granits from southern Sardinia (Conte et al., 2017).

Feldspar ranges | apfu normalised to 8 O						
	SLA1			***ITU7a***		
Ion	Na-feldspar			k-feldspar		
Si	2.978	-	3.014	2.991	-	3.245
Al	0.992	-	1.031	0.753	-	1.016
K	0.005	-	0.021	0.725	-	0.985
Na	0.902	-	0.972	0.007	-	0.018
Ca	0.008	-	0.034	0.001	-	0.003
Ba	0.001	-	0.001	0.001	-	0.004
Fe	0.0004	-	0.004	0.001	-	0.003
Mn	0.001	-	0.002	0.001	-	0.002
Mg	0	-	0	0.001	-	0.003
F	0.052	-	0.09	0.032	-	0.157
Cl	0.001	-	0.001	0.001	-	0.002
Σ wt%	95.58	-	99.74	97.57	-	101.17
Or	0.5	-	2.3	97.7	-	99.2
Ab	94.6	-	98.2	0.7	-	1.9
An	1.2	-	3.1	0	-	0.4

Table 5.2: Feldspar EMP analyses results in apfu from the Su Laccheddu (SLA) and Giacone (ITU) greisens.

White micas

White micas from the Su Laccheddu greisen display systematic chemical zonation from core to rim (Table 5.3), recording the progressive evolution of the hydrothermal fluids. Core domains (n=96) are characterized by muscovitic compositions (Si ≈ 3.13 apfu, Al^{VI} ≈ 1.90 apfu, F ≈ 0.19 apfu), while rims (n=107) show a shift toward phengitic compositions (Si ≈ 3.19 apfu, Al^{VI} ≈ 1.75 apfu, Fe ≈ 0.33 apfu) coupled with decreasing F (≈ 0.14 apfu) (Figure 5.10a). This trend is consistent with the Tschermak substitution (Velde, 1965) where $Al^{IV} + Al^{VI} \leftrightarrow Si + Fe,Mg$ (Figure 5.10b), which is typical of progressive fluid–rock interaction during greisenization (Monier and Robert, 1986). This substitution is quantified using the Phengite Index = (Si – 3) / 0.5 (Massonne and Schreyer, 1987), which increases from core (0.26) to rim (0.38), confirming progressive phengitization (Figure 5.10a). Although phengite is classically considered an indicator of high-pressure metamorphic conditions, its occurrence in the SLA greisen system reflects is coherent with the evolution of fluid composition. The increasing negative Tschermak Balance values toward the rim (from -0.054 to -0.122) indicate that the substitution $Al^{IV} + Al^{VI} \leftrightarrow Si + (Fe,Mg)$ is not perfectly balanced, suggesting additional substitutions (e.g., involving vacancies or Ti) or slight analytical uncertainties. The decrease in F from core to rim suggests that early fluids were richer in volatiles, whereas later fluids became progressively more hydrous and enriched in Fe, likely derived from the breakdown of ferromagnesian phases in the host rocks (e.g. biotite) (Cathelineau, 1988).

Intermediate compositions (n=21) display transitional chemistry between core and rim, recording progressive chemical evolution during crystal growth.

	CORE (n=96)			MID (n=21)			RIM (n=107)		
Parameter	**Mean ± SD**	**Min**	**Max**	**Mean ± SD**	**Min**	**Max**	**Mean ± SD**	**Min**	**Max**
Si	3.13 ± 0.03	3.07	3.19	3.17 ± 0.06	3.06	3.25	3.19 ± 0.09	3.07	3.34
Al^{IV}	0.87 ± 0.03	0.81	0.93	0.83 ± 0.06	0.75	0.94	0.81 ± 0.09	0.66	0.93
Al^{VI}	1.90 ± 0.04	1.82	1.97	1.84 ± 0.08	1.71	1.96	1.75 ± 0.16	1.52	1.95
Fe	0.16 ± 0.03	0.12	0.22	0.29 ± 0.06	0.18	0.41	0.33 ± 0.25	0.11	1.26
Mg	0.01 ± 0.01	0	0.02	0.02 ± 0.02	0	0.08	0.03 ± 0.05	0	0.23
K	0.89 ± 0.03	0.84	0.94	0.92 ± 0.04	0.85	0.99	0.92 ± 0.05	0.83	0.99
Na	0.08 ± 0.02	0.06	0.12	0.04 ± 0.02	0.01	0.09	0.03 ± 0.02	0	0.07
F	0.19 ± 0.05	0.1	0.29	0.17 ± 0.07	0.07	0.29	0.14 ± 0.07	0.03	0.29
OH	1.81 ± 0.05	1.71	1.9	1.83 ± 0.07	1.72	1.94	1.85 ± 0.07	1.7	1.98
Phengite Index	0.26 ± 0.06	0.15	0.38	0.33 ± 0.11	0.12	0.5	0.38 ± 0.18	0.14	0.68
Tschermak Index	0.75 ± 0.12	0.55	1	0.65 ± 0.12	0.46	0.88	0.62 ± 0.15	0.33	0.93
Tschermak Balance	-0.054 ± 0.022	-0.087	-0.008	-0.099 ± 0.031	-0.166	-0.059	-0.122 ± 0.043	-0.238	-0.042
Corrected Total (%)	96.8 ± 1.2	94.2	98.9	96.6 ± 1.2	94.2	98.5	97.1 ± 1.1	94.4	99.6

Table 5.3: Average chemical composition (apfu - EMPA) of micas cores and rims.

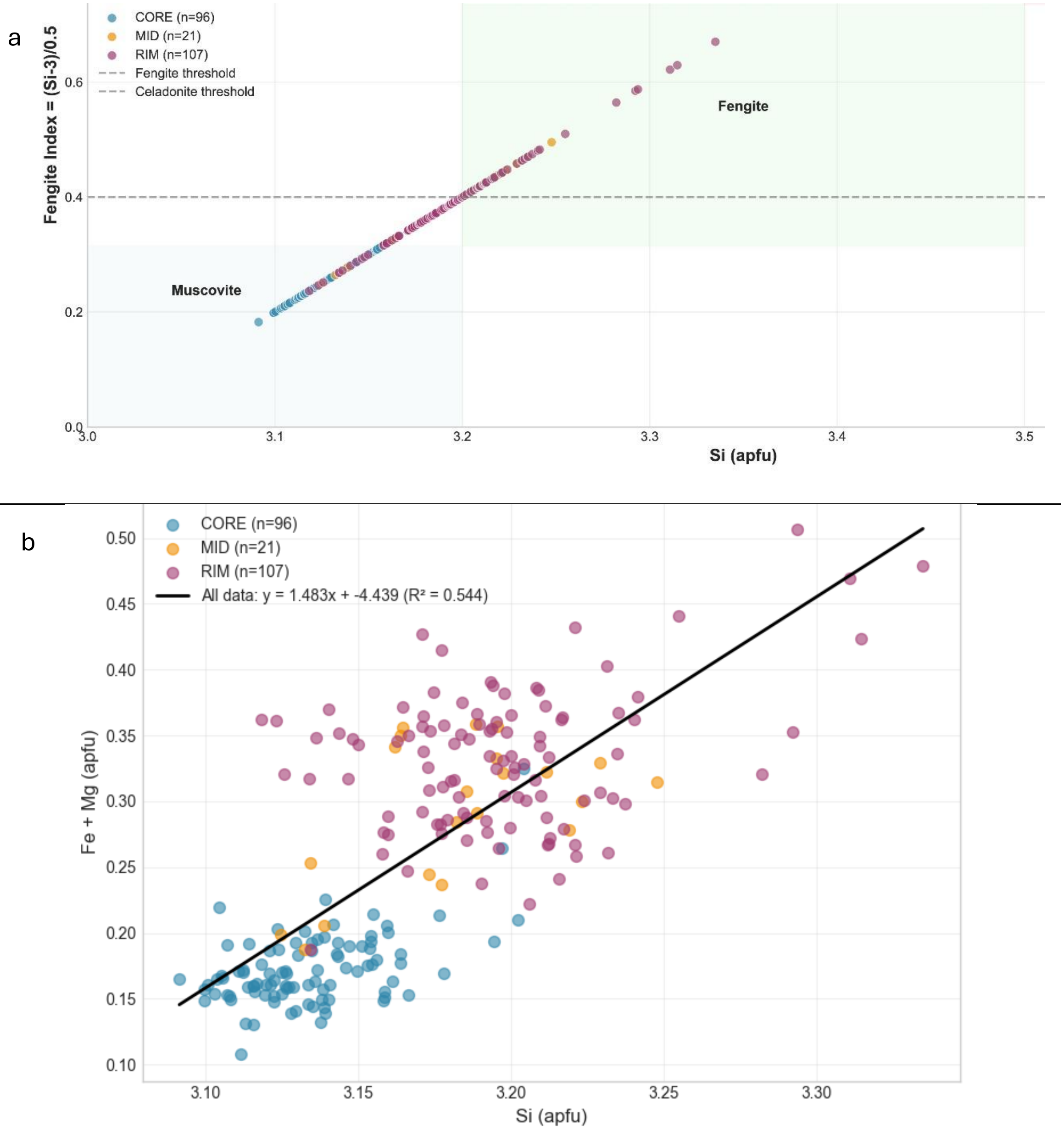

Figure 5.10: Chemical composition and classification of Su Laccheddu greisen white micas. a) Distribution of the compositions for micas rims and cores in a Phengite Index vs Si diagram (celadonite – phengite-muscovite); b) Tschermak substitution distribution and linear regression function.

REE Redistribution and fluorocarbonate formation

Monazite

The analyses on 7 monazite corroded crystals from the Su Laccheddu greisen (Table 5.4) show a homogeneous composition with Ce as the dominant REE (0.390–0.434 apfu). The lanthanide budget is controlled by the light rare-earth elements (LREE), whose sum (La + Ce + Pr + Nd + Sm) ranges from 0.802 to 0.878 apfu (mean 0.846 apfu). Within the LREE, the abundance sequence La > Nd > Pr > Sm is maintained in all analyses, consistent with a typical igneous monazite (Förster, 1998). Heavy rare-earth elements (HREE) are present only in minor amounts: Gd ranges from 0.011 to 0.018 apfu, while Tb, Er, Tm, Yb, Lu, and Ho are all below 0.003 apfu. Eu and Dy were systematically below the detection limit. Yttrium contributes between 0.016 and 0.031 apfu.

The positive covariation between Th and Si (0.030–0.055 apfu) is consistent with the huttonite substitution ($Th^{4+} + Si^{4+} \leftrightarrow REE^{3+} + P^{5+}$), indicating that these monazites crystallized from a magmatic fluid (Förster, 1998; Montel et al., 2002). They are inferred to be the primary REE sources in the system.

Monazite | apfu normalised to 4 O

	SLA2a-a1	SLA2a-a1	SLA2a-a5	SLA2a-a5	SLA2a-a5	SLA2a-a4	SLA6-a1
Ion	Mnz1	Mnz2	Mnz1	Mnz2	Mnz3	Rerun	Mnz
P	0.9669	0.9841	0.9645	0.993	0.9784	0.9845	0.9605
Si	0.05	0.0328	0.0518	0.0302	0.0382	0.0471	0.0548
La	0.2037	0.216	0.2045	0.2139	0.2185	0.181	0.1835
Ce	0.4024	0.4279	0.4063	0.4337	0.4303	0.3902	0.398
Pr	0.0453	0.0474	0.0454	0.0434	0.0471	0.0461	0.0476
Nd	0.1543	0.158	0.1543	0.1557	0.1554	0.1534	0.1588
Sm	0.0264	0.0266	0.0267	0.0275	0.0263	0.0309	0.0333
Gd	0.0113	0.0115	0.0116	0.0124	0.0106	0.0168	0.0179
Tb	0.0015	0.0014	0.0014	0.0014	0.0016	0.0018	0.0018
Ho	0.0003	0.0004	0.001	-	0.0002	-	-
Er	0.0005	0.001	0.0001	0.0003	0.0007	0.0009	0.0005
Tm	0.0025	0.0021	0.0029	0.0027	0.0024	0.0029	0.0027
Yb	0.0007	0.0002	0.0002	0.0004	-	0.0001	0.0004
Lu	0.0005	-	-	0.0003	0.0009	0.0001	-
Y	0.0198	0.0175	0.0193	0.0159	0.016	0.0258	0.0311
Th	0.0765	0.0458	0.0726	0.0397	0.0488	0.0714	0.0753
U	0.002	0.0011	0.0022	0.0021	0.0012	0.0022	0.0026
Ca	0.02	0.0142	0.0196	0.0103	0.0125	0.0192	0.02
Pb	0.0022	0.0014	0.0017	-	-	0.0015	-
Fe	-	-	0.0026	0.0021	-	0.0014	-

Table 5.4: Monazite EMP analyses results in apfu from the Su Laccheddu greisen.

REE carbonates

REE-fluorocarbonate minerals were identified in samples SLA6 and SLA1 (Table 5.5), postdating monazite and recording the late-stage redistribution of REE. Structural formulae were not calculated for REE-fluorocarbonates because carbon was measured as total C, not as CO_3; this approach cannot distinguish between C in the carbonate group, possible surface contamination, or amorphous carbon, thus precluding a reliable charge balance and site occupancy. However, based on the Ca/(Ca+ΣREE) weight ratio, most analyses are consistent with synchysite-(Ce) ($CaCe(CO_3)_2F$; Ca/(Ca+REE) ≈ 0.35–0.37), while analyses from SLA6_8 show intermediate compositions towards parisite-(Ce) ($CaCe_2(CO_3)_3F_2$; Ca/(Ca+REE) ≈ 0.27–0.32). The transition from synchysite to parisite suggests a progressive evolution of the fluid composition during REE-fluorocarbonate precipitation, with changes in Ca and REE activity (Smith et al., 2000).

The consistently high F content (4.45–8.16 wt%) in these phases confirms that REE transport and deposition were mediated by F-rich fluids (Williams-Jones et al., 2012).

REE-fluorocarbonates | EMP data (wt%)

Sample	SLA6_4 c1	SLA6-4 c2	SLA6-4 c3	SLA6-4 c4	SLA6_4 c5	SLA6_8 c6	SLA6_8 c7	SLA1_1 c8	SLA1_2 c9	SLA1_2 c10
Phase	Syn-(Ce)	Syn-(Ce)	Syn-(Ce)	Syn-(Ce)	Syn-(Ce)	Par-(Ce)?	Par/Syn	Par/Syn	Syn-(Ce)	Syn-(Ce)
CaO	19.38	18.37	19.35	18.94	19.67	15.29	18.91	18.94	18.59	19.07
Ce2O3	13.26	12.34	12.78	13.46	14.14	19.19	16.56	16.6	16.55	14.54
Nd2O3	8.03	7.79	7.22	7.49	8.2	9.29	8.53	9.59	6.45	8.27
La2O3	4.69	3.99	4.81	4.66	4.82	4.34	6.03	5.37	8.05	5.62
Sm2O3	2.71	2.36	1.98	2.16	2.5	2.77	2.49	2.52	1.37	2.68
ΣREE (wt%)	35.22	33.05	33.33	34.25	36.76	41.93	40.71	41.00	37.02	38.23
F	7.68	7.31	8.16	7.84	5.50	6.20	5.52	5.20	7.31	4.45
C	29.48	27.61	28.40	28.43	30.16	29.15	31.22	31.20	29.39	30.19
FeO	0.50	0.14	0.09	0.05	0.31	0.72	0.45	0.15	0.00	0.17
MgO	0.00	0.00	0.00	0.00	0.00	0.07	0.00	0.00	0.00	0.00
Σ wt%	92.36	86.57	89.32	89.54	92.42	93.42	96.81	96.52	92.42	92.11
$\frac{Ca}{Ca+REE}$	0.355	0.357	0.367	0.356	0.349	0.267	0.317	0.316	0.334	0.333

Table 5.5: REE-fluorocarbonates EMP analyses results in wt% from the Su Laccheddu greisen. C is reported as total carbon measured by EMPA; values are systematically high due to analytical constraints (see text for details).

Apatites

Six fluoroapatite analyses from sample ITU7L-a5 further documents the F- and REE-enriched character of the hydrothermal system (Table 5.6). The Ca site ranges from 4.885 to 5.001 apfu (mean 4.932 apfu), approaching the ideal occupancy of 5.000 apfu, with minor substitution by Na (0.011–0.024 apfu), Mn (0.031–0.036 apfu), Fe (0.016–0.028 apfu), and Y + LREE (< 0.015 apfu combined). The P site is stoichiometrically filled (P = 3.000 apfu by normalisation), with negligible Si substitution (≤ 0.006 apfu). The X site is dominated by F (1.086–1.260 apfu), with minor Cl (0.007–0.011 apfu), classifying all analyses as fluorapatite. Fluorapatite compositions (F = 1.09–1.26 apfu) with minor LREE incorporation (Ce + La + Nd ≤ 0.012 apfu) indicate that apatite acted as an additional sink for both F and REE during greisenization.

Apatite | apfu normalised to P = 3

Sample	***ITU7L-5 4***	***ITU7L-5 5***	***ITU7L-5 6***	***ITU7L-5 7***	***ITU7L-5 9***	***ITU7L-5 10***
Ca	4.9045	4.7967	4.8403	4.8177	4.8305	4.8362
Na	0.0135	0.0106	0.0223	0.0204	0.0241	0.0155
Sr	-	-	-	0.0010	-	0.0020
Fe	0.0246	0.0283	0.0169	0.0164	0.0272	0.0245
Mn	0.0360	0.0365	0.0365	0.0315	0.0348	0.0324
Y	0.0085	0.0092	0.0079	0.0089	0.0099	0.0059
P	3.0000	3.0000	3.0000	3.0000	3.0000	3.0000
Si	0.0023	0.0027	0.0058	-	0.0040	0.0032
F	1.2596	1.0856	1.1411	1.1039	1.1353	1.1295
Cl	0.0078	0.0078	0.0106	0.0073	0.0083	0.0080
Ce	0.0050	0.0014	0.0025	0.0035	0.0033	0.0026
La	0.0035	-	-	0.0014	-	-
Nd	0.0033	0.0012	0.0016	0.0017	0.0042	0.0031
Σ wt%	102.83	102.11	102.45	102.99	103.12	103.03
Sm+Eu+Pr	0.0019	0.0014	0.0006	0.0006	0.0015	0.0013

Table 5.6: Apatite EMP analyses results in apfu from the Giacone greisen.

Timing and duration of greisenization

Five samples were selected for in situ Rb/Sr white mica geochronology using laser ablation–inductively coupled plasma mass spectrometry (LA-ICP-MS) and age calculation using IsoplotR (Vermeesch, 2018) following the Rb/Sr dating method of (Rösel and Zack, 2022) over a total of 541 Point Analyses (Table 5.7, Table 5.8).

Sample	***P.A. Core***	***P.A. Rim***	***Total P.A.***
SLA1	36	72	108
SLA2a	55	49	104
SLA3a	35	77	112
SLA5	39	78	117
SLA6	40	60	100

Table 5.7: Number of LA-ICP-MS point analyses and their distribution on white micas from Su Laccheddu greisen.

		Rb87/Sr86	**err[Rb87/Sr86] (±2SE)**	**Sr87/Sr86**	**err[Sr87/Sr86] (±2SE)**
SLA1	Range	2.7 – 1995.1	0.4 – 77.2	0.77 – 8.44	0.01 – 0.34
	Avg ± σ	595 ± 335	22 ± 15	3.08 ± 1.30	0.10 ± 0.06
SLA2a	Range	31.2 – 1930.0	0.9 – 106.8	0.88 – 8.69	0.01 – 0.46
	Avg ± σ	288 ± 239	10 ± 14	1.84 ± 0.96	0.05 ± 0.06
SLA3a	Range	264.6 – 2552.6	6.0 – 123.9	1.76 – 10.78	0.04 – 0.56
	Avg ± σ	782 ± 430	29 ± 22	3.79 ± 1.68	0.13 ± 0.09
SLA5	Range	168.4 – 4844.6	7.8 – 276.3	1.21 – 19.37	0.03 – 1.09
	Avg ± σ	824 ± 609	31 ± 32	3.97 ± 2.38	0.14 ± 0.13
SLA6	Range	189.5 – 1232.2	6.2 – 75.0	1.42 – 5.13	0.04 – 0.27
	Avg ± σ	553 ± 157	21 ± 11	2.81 ± 0.59	0.11 ± 0.04

Table 5.8: Summary of Rb-Sr isotopic data for white mica from the Giacone - Su Laccheddu greisen system. For each sample, the range and average values (±1σ standard deviation) of $^{87}Rb/^{86}Sr$ and $^{87}Sr/^{86}Sr$ ratios are reported. Errors on individual spot analyses are expressed as ±2SE.

The analyses reveal a protracted history of hydrothermal activity between ca. 293 and 270 Ma (Table 5.9, Figure 5.11). Sample SLA1 preserves resolvable age zoning (Figure 5.12a,b), with an older core age (292.6 ± 5.8 Ma) and a younger rim age (277.3 ± 2.9 Ma). This two-stage record is interpreted as the transition from incipient greisenization mica to later hydrothermal overgrowths associated with greisenization, ending with the depletion of F and the fluorite vein system development. In contrast, samples SLA2a, SLA3a, SLA5, and SLA6 yield core and rim ages that overlap within uncertainty (Figure 5.12c,d,e,f), with total ages ranging from 269 ± 3.9 Ma (SLA2a) to 285.6 ± 4 Ma (SLA5). The absence of resolvable age zoning in these samples may reflect:

- Complete recrystallization during the hydrothermal stage.
- Homogenized isotopic system.

The overall age range (293 - 270 Ma) spans approximately 23 million years, indicating that the Su Laccheddu system developed over a protracted intrusion-related mineralising event spacing from greisen to hydrothermal consistent with the evolution of post-collisional magmatic systems in the Variscan belt, where repeated pulses of fluid release from crystallizing granite plutons can sustain hydrothermal activity over millions of years (Cerny and Ercit, 2005).

Sample	***Core age***	***Rim age***	***Total age***
SLA1	292.6 ± 5.8	277.3 ± 2.9	
SLA2a	273.6 ± 4.9	266 ± 5.5	269.8 ± 3.9
SLA3a	279.2 ± 5.6	279.2 ± 4.0	278.6 ± 3.3
SLA5	282.9 ± 4.6	285.8 ± 5.1	285.6 ± 4
SLA6	272 ± 11	275.1 ± 7.3	275 ± 6

Table 5.9: White micas rim and core dates calculated from the isochrones in Figure 5.12 using IsoplotR Figure 5.12: Isochrones from LA-ICP analyses on cores and rims of Su Laccheddu white micas greisen. Created using IsoplotR (Vermeesch, 2018).

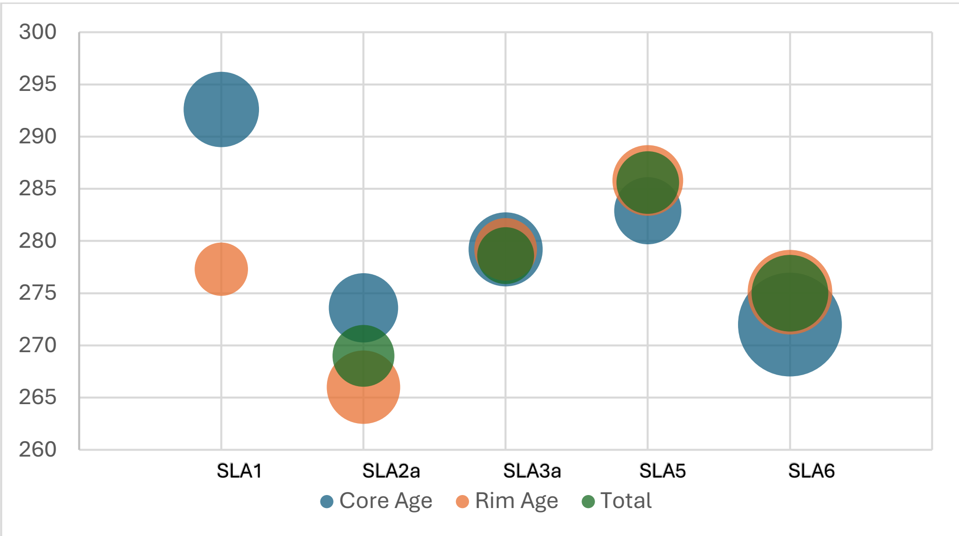

Figure 5.11: Distribution of micas' rims and cores ages (Ma) of Su Laccheddu greisen. The radius of the bubbles is equal to the estimated error.

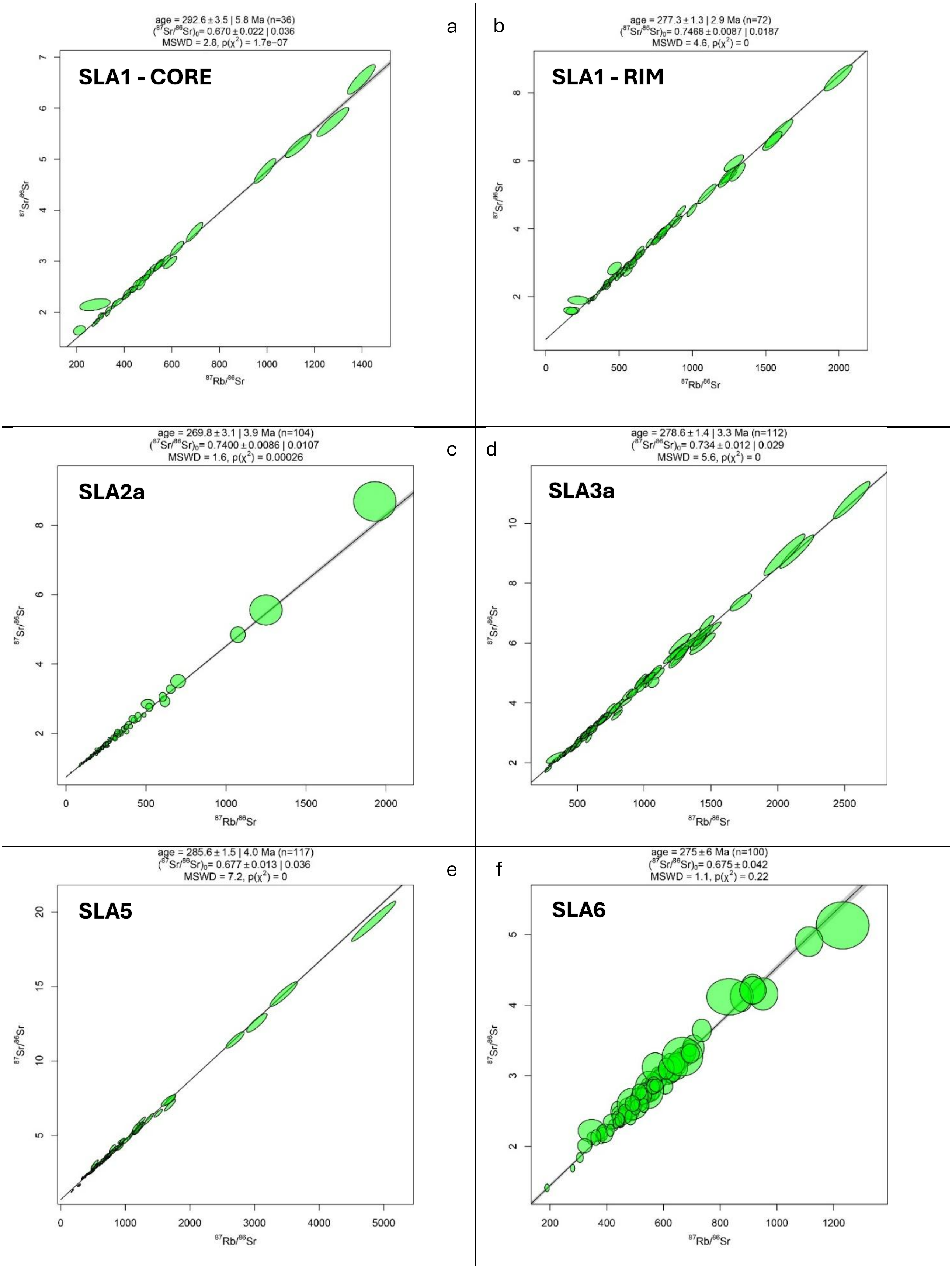

Figure 5.12: Isochrones from LA-ICP analyses on cores and rims of Su Laccheddu white micas greisen. Created using IsoplotR (Vermeesch, 2018).

The Su Laccheddu greisen system model

Integration of mineral chemical and geochronological data supports a three-stage model for the evolution of the Su Laccheddu greisen system:

Stage 1: Magmatic Crystallization (ca. 293–285 Ma)

Emplacement of the late-Variscan granite and crystallization of primary phases: K-feldspar, albite, biotite, monazite, and zircon. The magmatic system was enriched in F, LREE and Th as recorded by the composition of monazite relicts.

Stage 2: Greisenization and early Hydrothermal ore deposition (ca. 285–277 Ma).

Circulation of F-rich, magmatically derived fluids induced pervasive alteration of feldspars and biotite to white mica. This stage is recorded by:

- Core-to-rim chemical zoning in white mica (muscovite → phengite)
- Precipitation of scheelite, molybdenite, and early REE-fluorocarbonates (synchysite)
- Huttonite substitution in monazite, reflecting Th and Si mobility

Stage 3: Late hydrothermal activity and fluorite vein formation (ca. 277–270 Ma)

Circulation of more hydrous, Fe-enriched fluids led to:

- Formation of hydrothermal breccias cemented by fluorite and quartz
- Development and infilling of fluorite veins (Punta Lanzinosa, Giacone)
- Crystallisation of late-stage REE-fluorocarbonates with compositions approaching parisite
- Partial resetting or recrystallization of white mica, recorded by the homogeneous ages in most samples

Implications for Exploration

The results of this study have direct implications for exploration targeting in granite-related mineral systems:

1. The dating results are coherent with the fertility of the Sardinian granitoid units associated with the YMP (Naitza et al., 2024).
2. The hydrothermal fluid flow is not homogeneous, but white mica compositional zonation may represent a useful tool for targeting domains of efficient fluid focusing and higher-grade mineralization.
3. The identification of synchysite-(Ce) and parisite-(Ce) in the Su Laccheddu system demonstrates that REE can be concentrated in fluorocarbonate minerals during greisenization. Fluorite-rich zones (e.g., Punta Lanzinosa) may host significant REE resources, particularly where associated with apatite and monazite relicts.
4. The prolonged hydrothermal activity (ca. 23 Myr) recorded at Su Laccheddu suggests that late-Variscan granites in Sardinia can sustain long-lived hydrothermal systems, increasing the potential for the development of economically significant CRM deposits.

5.3. The Fluminese district: a case for comparative modelling

5.3.1. Geological framework

The Fluminese district in southwestern Sardinia is set within the footwall of the Arburese Thrust, the major Variscan structure marking the contact between the Nappe Zone and the External Zone. The External Zone hosts numerous mineralised deposits of different classes, formed during distinct metallogenic phases and controlled by the complex structural setting of the Variscan orogeny, within very low-grade metamorphic successions (Figure 5.14). Post-Variscan tectonics is characterized by high-angle normal faults trending NW-SE, NE-SW, and N-S with strike-slip, dextral kinematics (Mulas et al., 2025). These faults represent the primary structural control for later vein development and mineralisation.

5.3.2. Mineralisation types

Based on recent work by Moroni et al. (2019), Scano (2023), and Mulas et al. (2025) and integrated field observations, the Fluminese district hosts at least three distinct metallogenic events, distinguished by their dominant structural control, mineral assemblages, and textures:

1. Stratabound (Mississippi Valley Type) sulfide ores

Hosted in the early Cambrian carbonate succession, Zn-Pb stratiform to stratabound sulfide ores form large deposits exploited for centuries. The deposits consist of clusters of sub-vertical sulfide bodies forming large columns extending for hundreds of meters at depth. According to Boni et al. (1996) these deposits testify a large-scale metallogenic event encompassing stratiform SEDEX-type and stratabound MVT deposits; Santoro et al. (2023) proposed an attribution of stratabound ores to Irish-type MVT sub-class. These deposits are present in the southern part of the Fluminese district, the most important area being that north of Buggerru.

2. Granite-related deposits

Skarn mineralization occurs in two distinct sectors, indicating the presence of a buried granite intrusion:

- North-eastern sector (Perda s'Oliu/Medau Ganoppi areas): mixed sulfide base metal (Zn-Pb-Cu) skarn deposits within metasomatised Silurian-Devonian limestone protolith, also cut by later As-Sn hydrothermal veins (Figure 5.13a,b). In Figure 5.14: Perda s'Oliu – *id*:493, Medau Ganoppi – *id*:456.
- Southern sector (Su Zurfuru mine, in Figure 5.14 - *id*:492): a mixed sulfide base metal (Zn-Pb-Cu) and fluorite skarn body within an early Cambrian limestone/dolostone protolith. According to Aponte et al. (1988) Variscan remobilization of Cambrian Zn-Pb sulfides played the role of metal sources in the mineralisation of base metal skarn deposits like Su Zurfuru. Naitza et al. (2017) framed the deposit into the metallogeny of the Monte Linas late Variscan granite suite.

3. Low-Temperature hydrothermal veins

This is the most widespread type in Fluminese, forming veins along the high-angle fault systems that cut all previous structures. Three vein systems are recognised: NW-SE, NE-SW, and N-S, with the NW-SE system being by far the most extensive, particularly exploited in the Santa Lucia-Sa Mena de S'Oreri (Figure 5.13c,d - Figure 5.14 *id*:487) and Filone Palazzo (Figure 5.14 *id*:490) old mining areas, where Ba-F-Pb polymetallic quartz-carbonate veins occur. Primary host rock of the mineralised veins is a tectonic slice of Cambrian limestone (Gonnesa Formation), locally metamorphosed to marble and calc-schist. This carbonate slice is tectonically emplaced within the siliciclastic Ordovician succession (Cabitza, Monte Argentu, Monte Orri, and Portixeddu formations). The Gonnesa marble slice is bounded by E-verging backthrusts (low-angle shear zones) related to the second Variscan phase, associated with cataclasites. The paragenesis includes barite, fluorite, and galena with quartz gangue. Textures are typically banded and brecciated, indicating multiple fluid pulses along the faults. Fluid inclusion studies on fluorite from the S'Oreri mine (Valera, 1974) determined a homogenization temperature of 80°C, classifying this as a low-temperature hydrothermal system referred by (Boni et al., 1992)) to post-Variscan metallogenic stages.

4. Karst deposits

Paleo-karst cavities within the Gonnesa Formation limestones formed during emersion phases (likely post-Sardic or post-Variscan). They show a primary filling consisting of red clays, iron oxides/hydroxides, and barite (Padalino et al., 1972), later reworked by hydrothermal events depositing colourless fluorite and microcrystalline quartz.

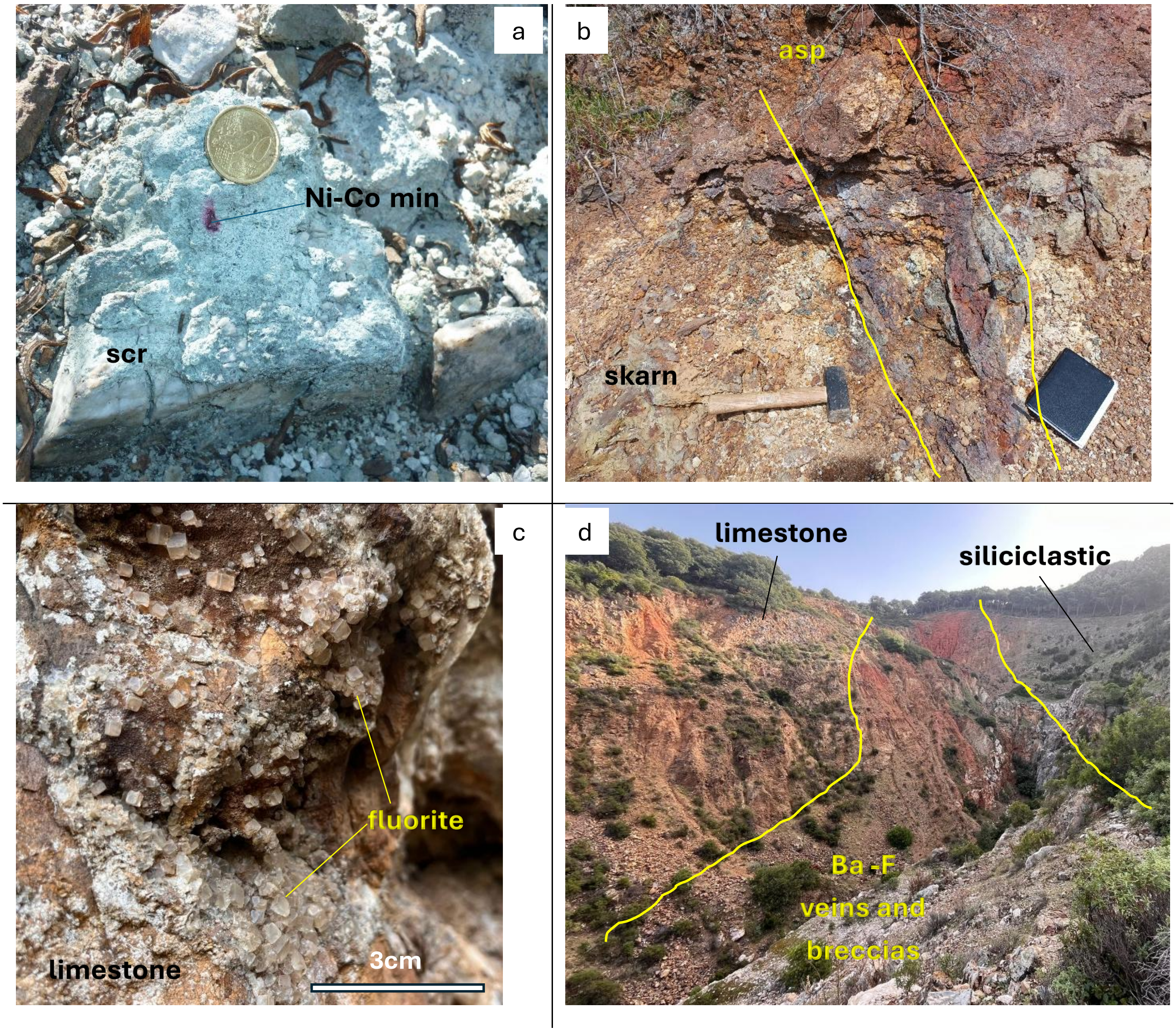

Figure 5.13: a) Arsenopyrite/scorodite (scr - grey) vein hosting Ni-Co assemblages (Ni-Co min - dark red dot) in the Medau Ganoppi area; b) Arsenopyrite veins (highlighted in yello) cutting across a mixed-sulfides skarn at Sa Menga, a few hundred meters N from Medau Ganoppi; c) fluorite crystal in the s'Oreri breccia pictured in d).

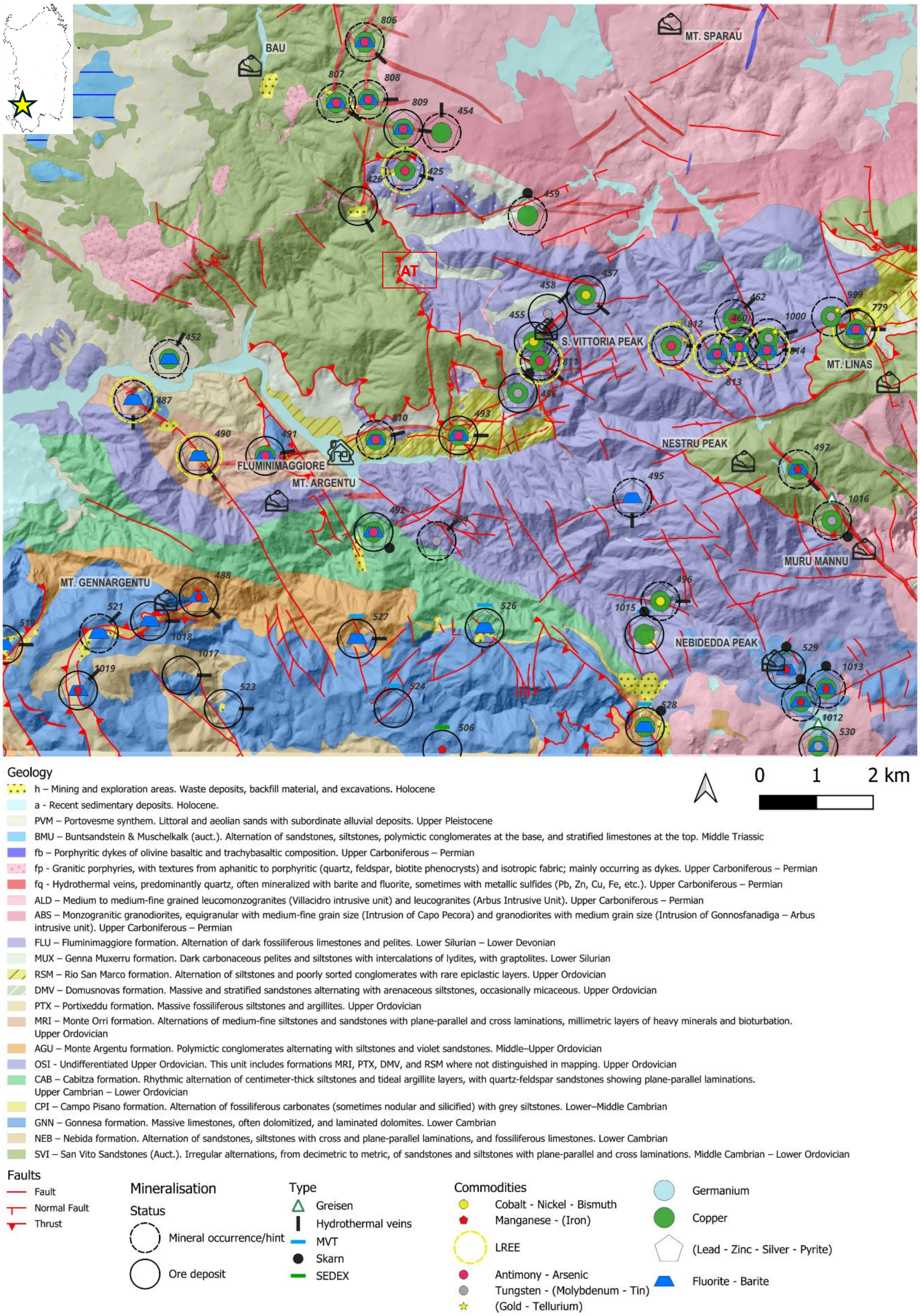

Figure 5.14: Metallogenic map of the Fluminese district. AT indicates the Arburese Thrust, the northern intrusion (pink) is the Arbus pluton and on the east it's the Mt. Linas Pluton.

5.3.1. Comparative Analysis: Applying the Rosas-Orbai Model

The application of the structural and metallogenic model developed for the Rosas-Orbai district to the Fluminese district serves as a powerful test of our comparative methodology (Table 5.10). This exercise not only helps to justify the presence and features of Cambrian limestones embedded within previously undefined Ordovician formations but also aids in reconstructing the Ordovician lithostratigraphic sequence in the Fluminese. The ore deposit features of the two areas show striking analogous patterns, strengthening the case for a common, unified genetic model.

Feature	Rosas-Orbai District	Fluminese District
Skarns	Mixed sulfide skarns (Zn-Pb-Cu-Fe) at peripheries of Cambrian limestone bodies, clustering north of Rosas (Barisonis, Mitza Sermentus)	Skarns in NE sector with Silurian-Devonian protolith (Medau Ganoppi); buried skarn with Cambrian protolith in S sector (Su Zurfuru)
Polymetallic Veins	NW-SE arsenopyrite veins hosted in cataclasites at Mitza Sermentus	As-Sn veins in NE sector, near Arburese Thrust contact (Medau Ganoppi)
Barite-Fluorite Veins	Abundant NE-SW barite-rich veins in NW (Nuraghe Meloni) and in S sector hosted by limestone slices and Ordovician siliciclastics (Truba Niedda)	Abundant N-S and NW-SE sub-vertical veins in Santa Lucia sector, hosted by Cambrian limestone slices at contact with siliciclastics (s'Oreri, Filone Palazzo)
Barren Structures	Non-mineralized N-S quartz veins and normal faults cutting the Rosas Shear Zone	Swarms of E-W and NW-SE non-mineralized quartz veins and faults in S sector
Karst Deposits	Karstic barite deposits at contact of regional backthrusts, where Cambrian limestones overthrust Ordovician siliciclastics	Karst cavities in Gonnesa limestones with barite, clays, and later hydrothermal fluorite

Table 5.10: Comparison of the ore deposits in the Rosas-Orbain and Fluminese districts.

5.3.2. The Comparative Metallogenic Model

The similarities between the two districts support a shared genetic model linked to the Variscan tectonics. The regional structural architecture, particularly the Arburese Thrust and associated thrusting and shearing, emplaced reactive lithological bodies (Cambrian carbonates) within fluid-conductive structural positions. However, the resulting fluid-rock interaction was not uniform across the two districts.

This variability is likely due to:

- **Differences in lithological reactivity** (Cambrian vs. Silurian-Devonian carbonates)
- **Distinct mineralisation events** overprinting one another
- **Variable contributions from magmatic and meteoric fluids**, with a mixed-source model already established for the Rosas Shear Zone skarn genesis (Boni et al., 1990; Cocco et al., 2022a).

The comparison between the two districts reveals similarities in their structural architecture, despite some differences in their spatial relationship with the main Variscan thrust.

Distance from causative intrusions

The two districts occupy similar positions relative to exposed intrusive bodies. The Rosas-Orbai deposits are situated 8-9 km from the outcropping Villacidro Intrusive Unit, while the Santa Lucia area is located approximately 10 km from the Monte Linas pluton outcrops. This comparable distal position suggests that the mineralising systems operated at similar scales and thermal gradients. The presence of a large, only partially outcropping skarn at Su Zurfuru, in the southern sector of the Fluminese district, hints at the possible existence of concealed intrusions at shallow depth beneath both areas.

Structural Architecture: Secondary Thrusts and Shear Zones

Both districts are characterized by a system of secondary thrusts and shear zones associated with the Arburese Unit emplacement. In the Rosas-Orbai district (4-6km from the AT), the Rosas Shear Zone (RSZ) enhance fluid flow into the reactive Cambrian carbonate slices. In the Fluminese district (0.5km from the AT), the s'Oreri carbonate slices are bounded by secondary thrusts that served an analogous fluid-conduit function.

Despite these similarities, the two districts differ in their proximity to the main Variscan structure. The Rosas-Orbai deposits lie 4-6 km from the Arburese Thrust, whereas the Fluminese mineralisations are located much closer, from to 2km for Su Zurfuru, to 0.5km for s'Oreri and directly within its footwall (e.g., Medau Ganoppi). This suggests that proximity to the main thrust is not a necessary condition for skarn development, as the Rosas deposits demonstrate. Rather, what matters is the presence of a well-developed secondary structural network capable of channelling fluids, regardless of distance from the primary thrust.

The Medau Ganoppi Skarn: A Distinct Case

The Medau Ganoppi skarn, located in the north-eastern sector of the Fluminese district near the Arburese Thrust contact, represents a distinct case. Here, the protolith consists of Silurian-Devonian limestones rather than the Cambrian carbonates that host the other skarns. While shearing and thrusting may not have played an active role in the *emplacement* of this reactive lithology, the structural network most probably maintained its function in creating the conduits for mineralizing fluid circulation, as evidenced by the later As-Sn vein systems that cut across the skarn, indicating multiple hydrothermal pulses exploiting the same structural pathways. This overprinting relationship with younger polymetallic veins crosscutting older skarn bodies mirrors the pattern observed at Mitza Sermentus in the Rosas-Orbai district, where arsenopyrite veins cut the skarn, suggesting a common sequence of hydrothermal events across the region.

Barite-Fluorite Veins: Lithological and Structural Controls

The distribution of post-orogenic barite-fluorite veins in the two districts reveals important lithological and structural controls. In the Rosas-Orbai district, abundant NE-SW trending barite-rich veins are hosted in two contrasting settings: in the northwest, they cut the Cambrian siliciclastic sediments of the Nebida Formation (e.g., Sedda Antiogu Sabiu), while in the southern sector they cut across limestone slices and Ordovician siliciclastics (Truba Niedda). This duality suggests that the Nebida Formation sandstones provided competent, fracture-prone lithologies capable of hosting extensive vein systems even in the absence of carbonate reactivity. At the same time, the small barren veins and more extended faults in the RSZ demonstrate the rheological mineralisation’s need for competent rocks.

In the Fluminese district, the barite-fluorite veins exhibit N-S and NW-SE orientations and are concentrated in three structural positions: i) within the Cambrian limestone slices at s'Oreri, where the carbonate competence favoured brittle fracture, ii) within siliciclastic rocks (Filone Palazzo).

The prevalence of barite-fluorite veins in the northwestern sector of Rosas-Orbai (Nebida Formation) versus their concentration in carbonate and siliciclastic rocks in Fluminese may reflect different structural levels exposed. According to the Silius model (Chapter 5.4), the higher content in fluorite and enrichment in galena in the Santa Lucia veins suggest a deeper structural level than the Rosas-Orbai veins, where barite is by far the main ore mineral. Moreover, the different vein trends (NW-SE, N-S, NE-SW) may represent conjugate fracture or plausibly the reactivation of older fault systems associated with the local rotation of the stress field near the Arburese Thrust. In both districts, the most productive veins occur where fracture-prone lithologies (competent sandstones, carbonates, or their contacts) intersect the regional fault systems, indicating that rheological contrast and not just bulk permeability is a key control on vein localisation.

The shared metallogenic model

All the mineralization styles fit a simplified, evolving model:

Stage 1: Late Variscan Skarn Formation

High-temperature, intrusion-related metasomatism forming the skarn bodies during a prograde stage. This stage is more strictly linked to magmatic heat, with metasomatism focused on carbonate contacts. A following retrograde hydrothermal phase with increased meteoric fluid contribution overprinted the skarns, producing mixed sulfide and fluorite mineralisation. Simultaneously, high-angle As-Sn veins (still with a significant magmatic fluid input) were opened along extensional faults, particularly near major thrust contacts.

Stage 2: Post-Variscan Reactivation

This final, and probably repeatedly reactivated, stage is marked by a late (Permian?, Triassic?) and widespread circulation of low-temperature hydrothermal fluids in the basement, with formation of barite-fluorite polymetallic veins along high-angle fault systems. Remobilization of previous ores, including early Cambrian Pb-Zn and granite-related fluorite, is highly probable.

5.4. The Silius Vein System: A Case Study from the Gerrei District

The Gerrei district in southeastern Sardinia is a notable mining area hosting several large mineralised systems (Figure 5.15). These include the silver-rich hydrothermal system known as the "Filone Argentifero," which strikes E-W in the southern portion of the district, the Baccu Locci veins to the north, and regionally extensive N-S striking Ba-F hydrothermal veins that cut across the area for kilometres (e.g., Bruncu Molentinu). The most significant deposit, however, is the Silius fluorite hydrothermal vein system, which we investigated.

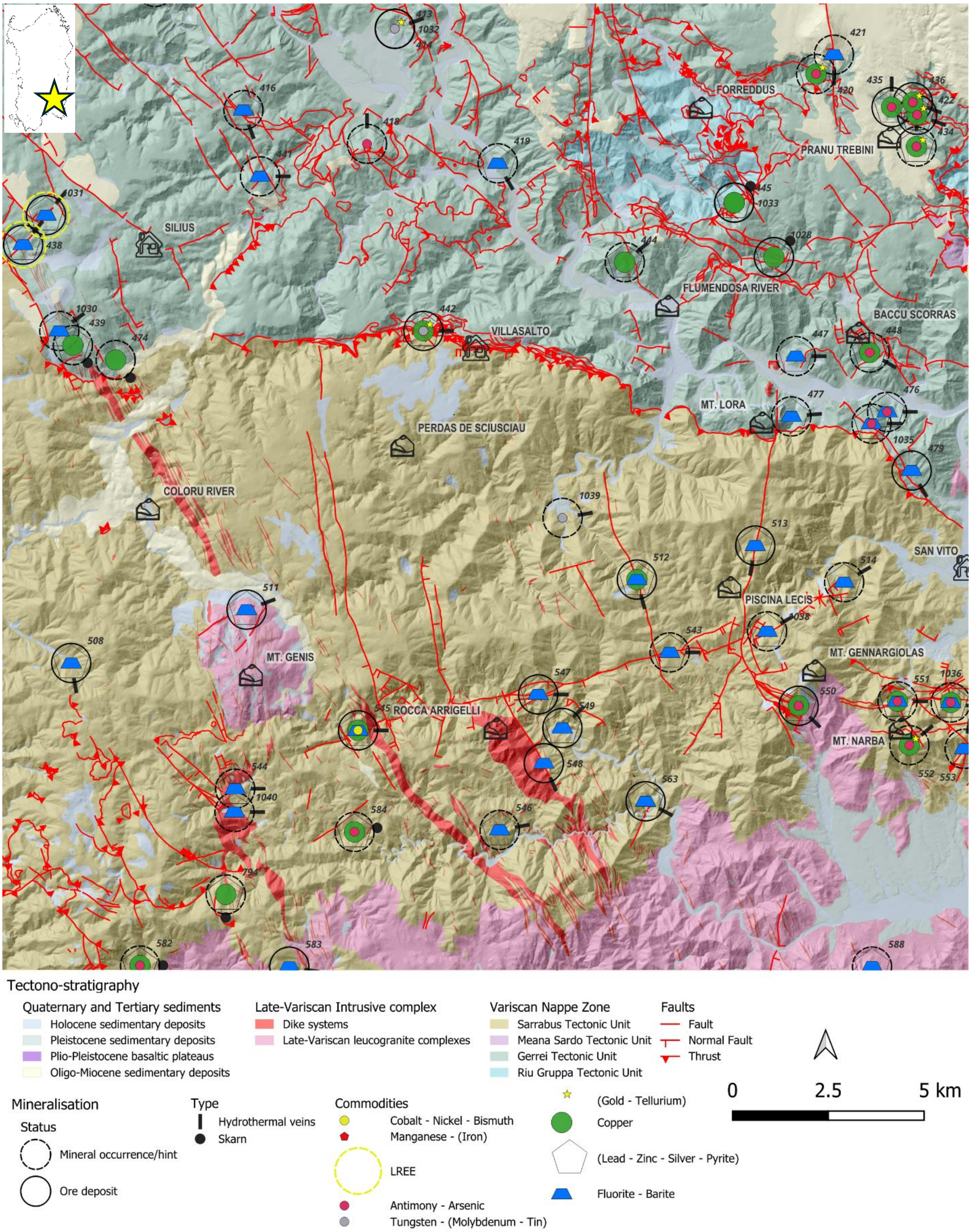

Figure 5.15: Metallogenic Map of the Gerrei district. The Rocca Arrigelli - Piscina Lecis – Mt. Narba alinement in the south sign part of the "Filone Argentifero"; id:438 and id:1031 on the northwest indicate the Silius vein; in the northwest id:422, id: 434, id:435, id:436 are relative to the Baccu Locci mining area.

The Silius mine was exploited for fluorite, galena, and barite for over 50 years. Following a standby period of about 20 years, it is currently the only active underground mine in the region. Certified reserves amount to over 2.1 Mt at 32% CaF_2 and 3% Pb (Benz et al., 2001). Furthermore, LREE in the carbonate gangue (Mondillo et al., 2016; Balassone et al., 2021) may be a prospect for the future and for analogous deposits.

The mineralisation exhibits a general vertical zonation: it was predominantly barite-rich at the shallower, now-exhausted levels, transitioning to fluorite-dominated veins at depth. With increasing depth, galena, accompanied by accessory Zn-Cu sulphides, becomes increasingly abundant.

Lithostratigraphy

The host rocks comprise a strongly folded low-grade metamorphic pre-Variscan succession that includes (Figure 5.16):

- Middle Ordovician calc-alkaline felsic metavolcanics ("Porfiroidi Auct." Formation), essentially metarhyolites and metarhyodacites related to arc magmatism.
- Upper Ordovician metasandstones and siliciclastics.
- Silurian to Devonian black shales and meta-limestones.

Late Variscan granitoids are poorly exposed in the immediate area and are essentially represented by a large NW-SE swarm of Early Permian felsic dikes. These dikes are spatially connected to the Sàrrabus pluton of Monte Genis, which crops out approximately 15 km to the southeast.

Tectonic framework

The Silius mine is located within the External Nappe Zone of the Variscan basement in southeastern Sardinia. The host rocks belong to the Gerrei and Sàrrabus tectonic subunits (Forci et al., 2012). The Variscan succession of the Gerrei Unit is situated in the hanging wall of the regional Villasalto Thrust and is characterised by kilometre-scale recumbent folds verging towards the SW, with parasitic folds occurring at all scales. This folding produced an apparent thickening of the involved formations and their repetition at depth.

Subsequent Variscan post-collisional extension (late Carboniferous–Early Permian) led to widespread reactivation of thrust structures, with the progressive development of low-angle to high-angle faults. A further reactivation of Palaeozoic structures is documented by NW-SE, N-S, and E-W trending faults, associated with the rotation of the Sardinian block during the Oligo-Miocene. These late-stage structures determined the block-faulting of both the basement and the Eocene covers, which currently define the morphology of the area.

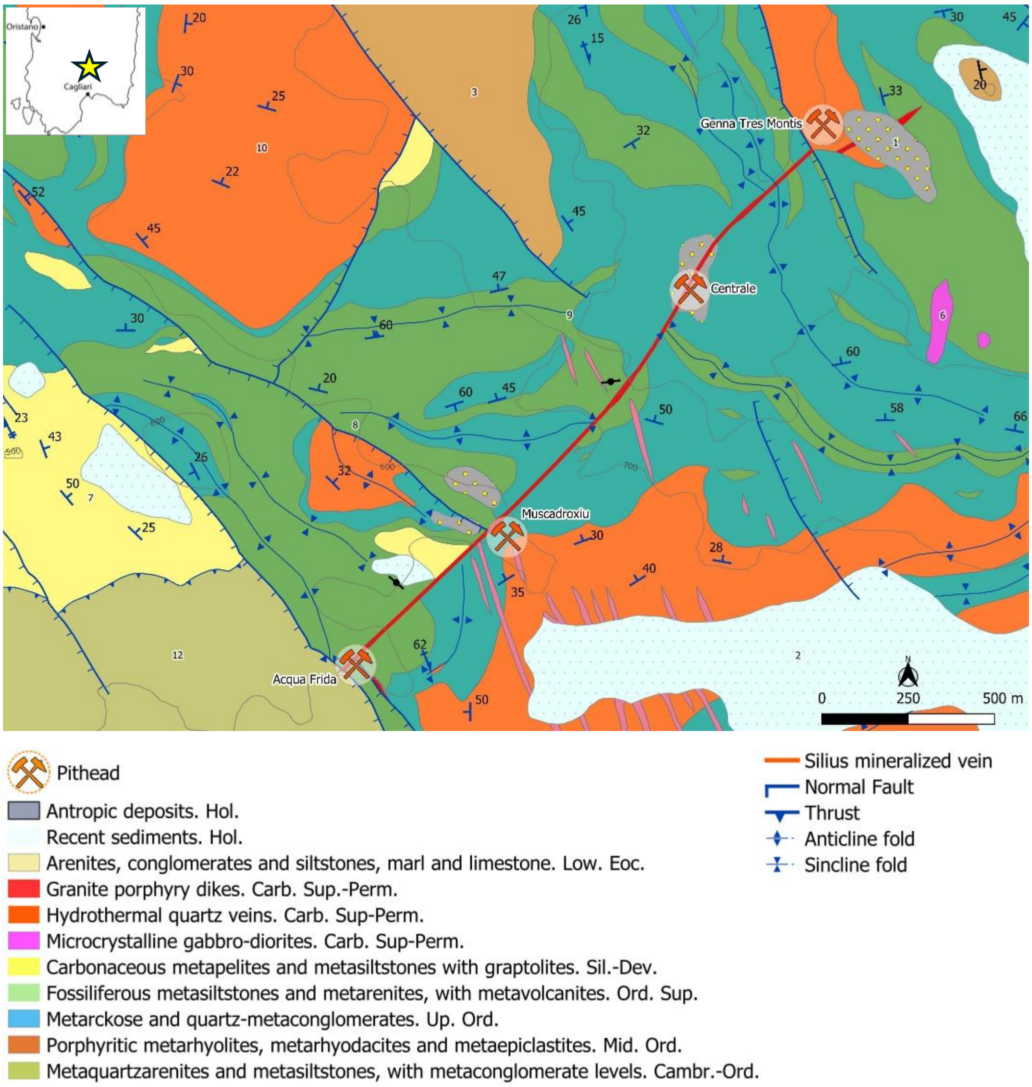

Figure 5.16: Geological sketch map of the Silius area. From (Scano et al., 2023)

Structural architecture of the vein system

The ore deposit is a pinch-and-swell vein system extending for 2–4 km along a NE-SW trend and is currently known to depths of up to 500 metres (Marino et al., 1997). It is hosted primarily in the metavolcanics of the "Porfiroidi Auct." Formation and in the sandstones of the “Metarcose di Genna Mesa” Formation. These highly competent lithologies allowed the large extension and the long-life of the hydrothermal system thanks to their structural stability even after fracturation. The veins distinctly crosscut all Variscan structures, including the Early Permian felsic dikes, establishing a relative minimum age for the mineralising event(s) (Natale, 1969).

The mineralised system consists of two principal parallel veins at shallow levels: the San Giorgio and San Giuseppe veins. They strike NE-SW to ENE-WSW and dip steeply towards the NW, coalescing at a depth of approximately 350 m above sea level. At their point of coalescence, they reach a combined thickness of up to 16 m, compared to the typical 1 to 3.5 m thickness of a single vein. The overall geometry, structural context, and kinematic features indicate a dextral sense of shear, which appears to prevail over the vertical component. The vertical kinematics remain unclear but likely reflect later reactivation as a high-angle normal fault.

The continuity of the vein system is interrupted to the NE and SW by two major NW-SE trending normal faults, giving the deposit a trapezoidal shape that extends for about 2 km at the surface and nearly 4 km at the deepest exploited level (level 100, named for its elevation above sea level). The NW-SE Muscadroxiu fault displaces the western sector of the vein of about 100m towards S-SE. Several minor normal faults with a strike-slip component crosscut the deposit at various angles, producing displacements ranging from negligible to about 2 metres.

Vein textures and paragenesis

The San Giorgio vein formed first, cutting across and within the San Giuseppe vein, and is characterised by alternating bands of chalcedony, fluorite, barite, and calcite. The San Giuseppe vein is generally banded (Figure 5.17a,b), but locally brecciated by the San Giorgio vein. It exhibits a more complex mineralogy with predominant fluorite, with quartz and calcite as gangue; galena appears as aggregates and bands (Figure 5.17a); minor sphalerite (Figure 5.17c), chalcopyrite, and pyrite/marcasite are disseminated. Various Ni-Co-Fe-As-S phases (nickeline, rammelsbergite, gersdorffite, cobaltite, arsenopyrite, bismuthinite) are found as less than 1mm aggregates disseminated in the fluorite and quartz of the deepest levels of the mine, about 400–500 metres below the surface (Zara et al., 2022; Scano et al., 2023).

At the deposit scale, the mineralisation shows a clear vertical compositional evolution:

- **Shallow levels:** Ore consists predominantly of barite, associated with fluorite, quartz, and minor calcite.
- **Intermediate levels:** Fluorite content strongly increases (up to 25% or more), accompanied by quartz, calcite and sulphides, while barite almost entirely disappears.
- **Deep levels:** Calcite is often dolomitised, fluorite consistently exceeds 30%, and sulphide content, mainly galena, secondly sphalerite, increases markedly (Marino, 1997). Ni-Co-Fe arsenide and sulfarsenide minerals appear.

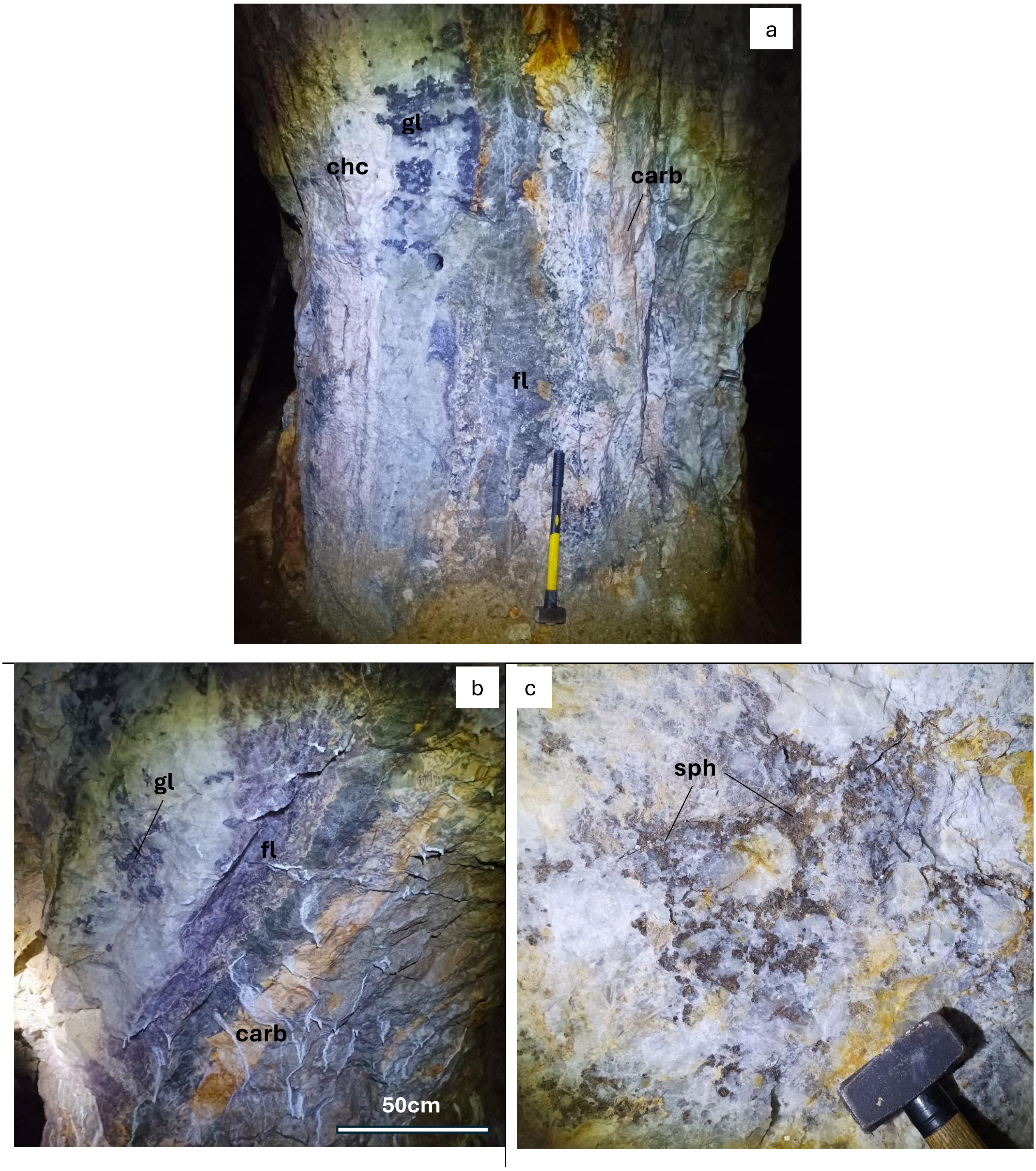

Figure 5.17: Silius vein at level 200 (~200m a.s.l.) and related sublevels. Here, the sulfides content increase, and the Ni-Co mineral phases appear. a) Gallery's pillar made of green and blue fluorite (fl) hosting large aggregates of galena (gl - dark grey), chalcedony (chc - white) and carbonates (carb - yellowish); b) blue and green fluorite (fl) vein on the gallery's roof with a carbonate (carb - ankerite/dolomite/calcite) band; c) sphalerite-rich zone (sph, golden brown).

Fluid chemistry, age, and ore genesis

Fluid inclusion studies on fluorite and calcite indicate ore formation at temperatures between 120 and 180 °C, from fluids with salinities reaching up to ~18 wt.% NaCl eq. (Boni et al., 2009). Strontium and neodymium isotopic ratios, together with REE+Y contents in fluorite, suggest a crustal origin for the mineralising fluids, likely resulting from mixing, in varying proportions, of evaporated seawater brines with fluids derived from the Palaeozoic basement and Late Variscan magmatic rocks (Castorina et al., 2020).

Sm-Nd dating of carbonate gangue from the San Giuseppe vein yielded an age of 294 ± 40 Ma (Castorina et al., 2020). Given that the vein clearly cuts Permian porphyry dikes, the younger portion of this age range is geologically most plausible, constraining the mineralisation to the middle–late Permian.

Metallogenic database implementation and guidelines for exploration

The Silius ore deposit stands as a perfect example of how advancing in comprehensive research on CRM-bearing ore deposits can generate concrete data for updating the Metallogenic Database of Sardinia. The database was substantially enriched by the direct implementation of newly documented critical raw materials, including LREE, Ni, Co, Bi, Sb, and As, which were previously overlooked during decades of fluorite-barite exploitation.

The Silius model yields three fundamental exploration guidelines applicable to fluorite-barite vein systems across Sardinia:

- Vertical zonation as a depth predictor: The documented progression from barite-dominated to fluorite-rich to Ni-Co-As-Bi-bearing assemblages with depth suggests that the mineralisation level exposed at surface indicates the potential at depth. Therefore:
    - Barite-dominated veins (e.g., Rosas-Orbai, Bruncu Molentinu, Su Zurfuru) may represent the shallow, eroded levels of systems that could transition to fluorite-rich mineralization at depth.
    - Fluorite veins with base metal enrichment (e.g., Santa Lucia, Monte Genis, Asuni-Castel Medusa) are prime targets for exploring the deepest, Ni-Co-As-Bi-bearing levels, and the carbonate gangue LREE contents, as documented at Silius.
- Structural control: Mineralisation is consistently associated with NE-SW trending, steeply dipping fault systems developed during post-Variscan extension. Exploration should focus on these structural trends, particularly where they intersect favourable lithologies.
- Host rock rheology as a critical constraint: The Silius vein system maintains its thickness and continuity only where hosted by competent lithologies (metavolcanics, metasandstones, felsic dikes), thinning or disappearing where it enters less competent units (phyllites, schists). Therefore, exploration should prioritize areas where fault systems intersect competent lithologies, while areas dominated by incompetent units can be considered lower priority even if faulted.

Overall, the Silius model provides a useful interpretative tool for re-examining the extensive EMSA archives on fluorite-barite veins across Sardinia, transforming a descriptive catalogue into a predictive exploration framework capable of guiding future discoveries of CRM-bearing mineralization.

6. Application of the database in Mineral Prospectivity modelling for Skarn Deposits

This chapter outlines the design and application of a simplified mineral prospectivity modelling (MPM) workflow to demonstrate how the Metallogenic Database serves as the foundational engine for predictive modelling, serving for:

- Modelling and schematising the ore deposit type.
- Indirect data-source for geological features by geospatial analyses, coupling it with structural and geological feature maps.
- Validating the final MPM by statistical analyses.

A simplified 2-dimensional MPM for skarn deposit in Sardinia is proposed as a methodological study of the Metallogenic Database application. We applied a fuzzy logic (0 – 1 continue scoring) to capture uncertainty and the gradational nature of geological controls. The base scoring and the weight of the parameters relies on knowledge-based and expert-defined criteria and the results serve as a descriptive and targeting tool. Both scores and weights can be adjusted to test alternative conceptual models or to suit different prospection or exploration priorities.

Sardinia hosts several CRM-bearing skarn deposits, including numerous examples as Rosas, Perda Niedda, San Leone, Su Zurfuru, Sa Marchesa, Monte Tamara Monte Lapanu mines in SW Sardinia, and Funtana Raminosa, Giaccurru, Talentinu, Sa Lilla, Monte Nieddu and Correboi in central Sardinia. Hence, we considered the central and southern parts of the island.

We chose three parameters that represent the main structural and geological controls on a skarn deposit, namely:

- Intrusion proximity: metasomatisation needs a heat and fluid input from magmatic intrusions.
- Lithology: they need a reactive lithology as a protolith.
- Fault proximity: in Sardinia, faults control the localisation of the reactive lithologies and the main fluid paths circulating on regional scale.

The general study grid

We created a study grid comprising central and southern Sardinia to quantify and model these three parameters and calculate a predictive fuzzy score. The grid cells are 13754, 1000x1000m squares, considered adequate for both regional and district-scale studies, and for time-convenience. In fact, 77 skarn occurrences lie in one cell each; ten of them are paired in a cell for every couple, and just one cell hosts up to three skarns.

Each cell has a fuzzy score, calculated based on each component peculiar to the cell:

- f_intrusion: the fuzzy component describing the influence of intrusions on the cell.
- f_lithology: the fuzzy component assigned to the lithological feature of the cell.
- f_faults: the fuzzy component quantifying the proximity of faults to a cell.
- f_score (fuzzy score): f(f_intrusion * f_lithology * f_fault)

The greatest volume of pre-Variscan carbonates is represented by the Cambrian-Ordovician carbonates of the Gonnesa and Campo Pisano Formation, and by the Silurian-Devonian sequences of the Genna

Muxerru and Fluminimaggiore Formations in SW Sardinia. Smaller volumes are embedded in the Silurian Black Shales, the San Vito Formation and others in the Nappe Zone of Central and SE Sardinia.

We used the official geological data from the geoportalesardegna.

6.1. Intrusion component evaluation

Data preparation and filtering

The Variscan granitoids are the main heat and fluid source for their genesis (Naitza et al., 2017). We isolated the intrusions based on descriptive keywords such as %granit%, %intrus%, and %pluton%. This filter allows us to include microgranite and granitic dikes and sills, which could indicate the proximity to a buried, reactive intrusive body.

Since focusing on central and southern Sardinia, the northern Sardinia intrusions were cut off.

To avoid the risk of digitalisation problems such as overlapping and to maintain data integrity, our other simplification is limited to a joining process between polygons smaller than 0.1 km^2, in a radius of 300m.

We end up with 1229 entities over a surface of 2322.30 km^2 with areas varying greatly from about 10000 m^2 to about 140 km^2.

We then classified the intrusions based on their surface (Table 6.1), keeping in mind that: a) the larger intrusions are mostly composite, and/or subunits of even larger intrusions, b) smaller intrusions, veins and dikes are the ones that are most often isolated. For these reasons, the chosen ranges scale diminishes from the larger intrusions to the smaller and most localised ones:

- Larger intrusions ≥ 1km^2
- Smaller intrusions ≥ 0.1 km^2
- Localised veins/dikes < 0.1 km^2

Intrusive Class	*Area (km^2)*	*Number*	*Number (%)*	*Avg. (km^2)*	*Total area (km2)*	*Area (%)*	*St. dev. (km^2)*
Larger	≥ 1	149	12.12	14.8	2205.63	94.98	26.05
Smaller	≥ 0.1	276	22.46	0.33	90.14	3.88	0.23
Localised	< 0.1	804	65.42	0.03	26.53	1.14	0.02

Table 6.1: Area-based intrusive classes statistics.

The chosen approach to assign the intrusion proximity values can be schematised in two points and different features:

- A direct component is given by the intersection on an intrusion with a cell.
- A buffer component is given to all the cells into a radius assigned to every intrusion area class.
- The highest score was assigned to each cell.

Intersection Component

The dimension of intrusions is generally related to their thermal budget (Jaeger, 1964), and we represent that using their area. Hence, the intersection component in a grid cell practically means its intersection with an intrusion.

As previously stated, most of the intrusions in Sardinia are aggregated and close to each other, but the isolated, generally smaller ones are potentially linked to ore-forming processes for two reasons: a) their own limited thermal budget, but in many cases for b) representing apical part of larger bodies, their presence inferring the proximity of a buried intrusion.

For the intersection component, we assumed the factors *a* and *b* and assigned different weights for each intrusion area class (Table 6.2). We chose to exclude all the cells that are completely covered by an intrusion since a) the probability of skarn genesis is basically 0 since no other lithology crops out, and b) statistics would be heavily affected by the huge number of high values.

Intrusion Class	***Area (km^2)***	***Weight***
Larger intrusions	≥ 1	1.0
Medium intrusions	≥ 0.1	0.9
Localised veins/dikes	< 0.1	0.8

Table 6.2: Area-based intrusive classes weights.

The SQL query for the intersection weighting is based on a coalesce case when the conditions of area are true:

```
sql
COALESCE(MAX(
    CASE
      WHEN ST_Intersects(smr.geom, i.geom) THEN
        CASE
          WHEN i.area_m2 >= 1000000 THEN 1.0
          WHEN i.area_m2 >= 100000 THEN 0.9
          WHEN i.area_m2 < 100000 THEN 0.8
        END
      ELSE 0
    END
  ), 0) as direct_component,
```

Buffer component with segmented linear decay

The buffer component employs a linear distance-decay function to model the diminishing thermal/metasomatic influence with increasing distance from intrusive contacts.

The known skarn occurs at an average distance of 1.57 km from the intrusion outcrops, varying from almost 0 to 8.21 km and has a standard deviation of 2.33 km.

The segmented linear decay function was selected over exponential and logarithmic alternatives to best fit the skarn occurrence's location. The segmentation is used to mimic the eventual presence of a buried intrusion in the immediate surroundings of the outcrops: it drops by just 10% in the first kilometre (one cell) and continues dropping down to a value of 0.1 at the buffer peripheries. Furthermore, we classified intrusive bodies into four hierarchical categories based on surface area (Table 6.3), reflecting their relative capacity to sustain different thermal budgets and more extensive fluid circulation systems, as determined by their surface or volume (Jaeger, 1964). We assigned to each intrusive class a buffer range (Table 6.3, range of effect) based again on the skarn occurrences.

Intrusion Class	***Area (km²)***	***Buffer range (km)***
Larger intrusions	≥ 1	8
Smaller intrusions	≥ 0.1	6
Localised veins/dikes	< 0.1	4

Table 6.3: Area-based intrusive classes buffer range.

A significant consideration is the influence on structures as heat-fluid conduits. For instance, the delicate fitting of the Rosas skarns into the buffer was particularly relevant in choosing the buffer values.

The area has a relevant concentration of skarn occurrences as evidenced in detail by recent studies (Cocco et al., 2022a); it lies at about 8km NW from a larger intrusion (Monte Lattias, Monte Arcosu) and about 9km NE from a smaller one (Monte s'Orcu). On one hand, the presence of a buried intrusion (Cocco et al., 2022b), on the other hand, the Rosas Shear Zone associated with the regional Arburese Thrust and striking NW-SE, probably contributed to the propagation of heat and fluids from the SW intrusion. We calibrated the buffers to reach that area to mimic the structural influence and the interaction between different intrusion fluids.

The SQL query is based on an arrayed case verifying the area class of the intrusions, applying the respective buffer and then giving a value corresponding to 10% of the direct component at the first kilometre, and then applying the formula:

Buffer score = (10% direct component - 0.1) x (distance cell from intrusion – 1000) / (buffer range – 1000)

A cell will probably be affected multiple times by buffers of the same and different intrusions, but it will take the highest value to avoid excessive cumulative effects, using the GREATEST function.

```
sql
ARRAY_AGG(
    CASE
      -- CLASSE 1: ≥ 1km²
      WHEN i.area_m2 >= 1000000 AND ST_DWithin(smr.geom, i.geom, 8000) THEN
        CASE
          WHEN ST_Distance(smr.geom, i.geom) <= 1000 THEN 0.9
          ELSE
            GREATEST(0.1, 0.9 - (0.9 - 0.1) * (ST_Distance(smr.geom, i.geom) - 1000) / (8000 - 1000))
        END
```

The results

A total of 9703 cells have a f_intrusion score > 0 with an average score of 0.59 and a standard deviation of 0.30 (Table 6.4 - Figure 6.1).

N. of cells > 0	Avg. f_intrusion	St. dev.	min	max	p25	p50	p75
9703	0.59	0.30	0.1	1.0	0.35	0.47	1

Table 6.4: f_intrusion statistics of the cells scoring above 0.

All 90 skarn fell into the intrusion area of influence with scores ranging from 0.14 at the peripheries to 1.0 closer to the buffer limits (Table 6.5 - Figure 6.1).

N. of skarns	Avg. f_intrusion	St. dev.	min	max	p25	p50	p75
90	0.68	0.30	0.14	1.0	0.42	0.8	1.0

Table 6.5: f_intrusion statistics for cells hosting a skarn.

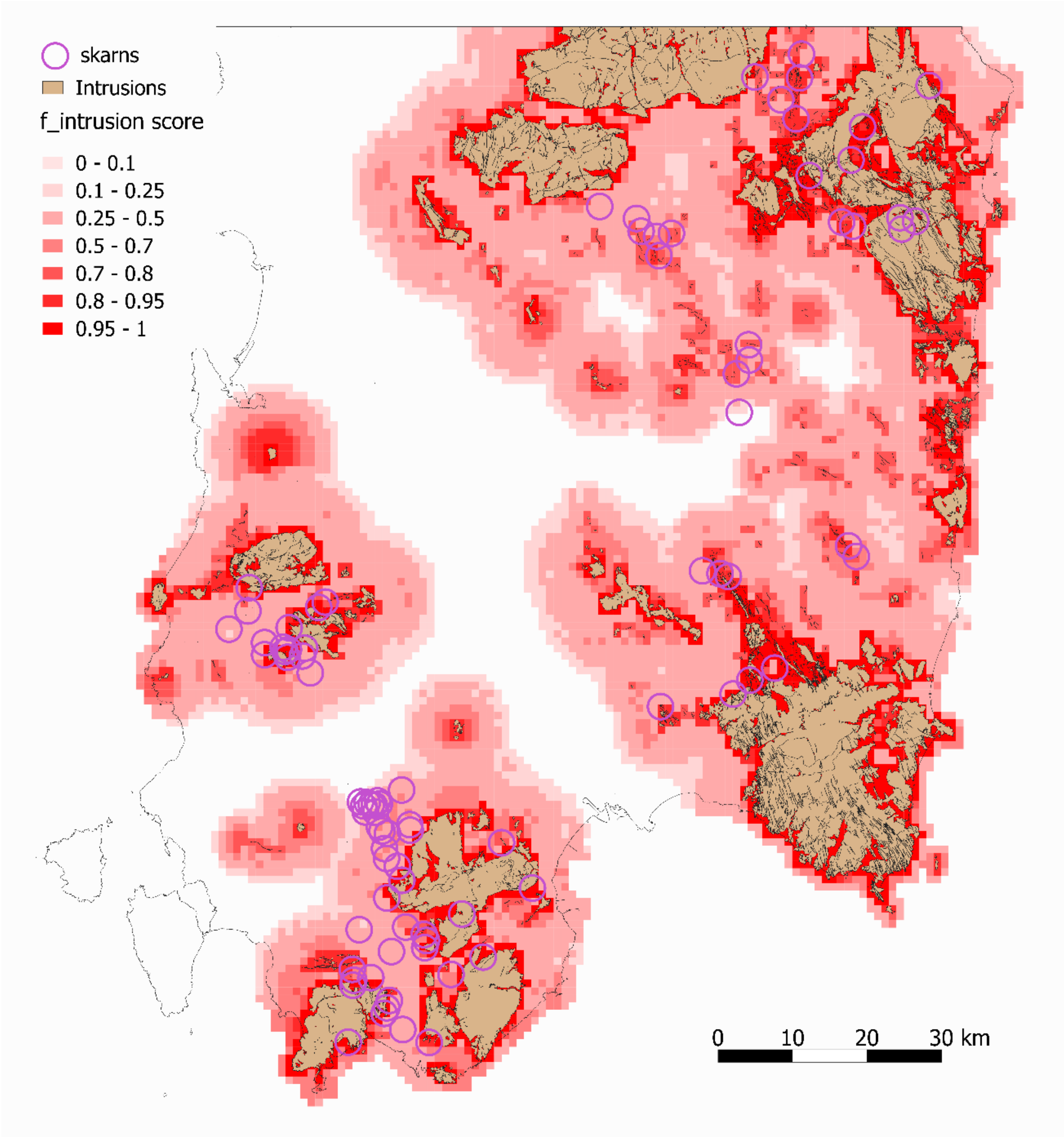

Figure 6.1: Intrusion fuzzy score values (f_intrusion) and skarn occurrences map.

6.2. Lithological favourability

Data preparation and filtering

We filtered all the geological data for the area of study, considering only the lithologies that have at least some potential for metasomatisation and skarn genesis.

Skarns in Sardinia often occur as localised alteration of carbonate units or, rarely, as alteration of mafic veins (Cocco et al., 2022b). We selected entities whose description contains keywords referring to skarn, limestone, marble, dolomite, carbonate, carbonaceous sediments, marl, mafic, gabbro, basalt, and basic (Table 6.6). We end up with 5177 polygons covering a total area of 638.604 km^2, with an average of 0.123 km^2, ranging from 3.6×10^{-5} km^2 to over 37.488 km^2. Assuming that carbonate rocks are optimal for skarn formation, marl rocks have moderate potential, and mafic rocks have limited but non-zero potential, we assigned a score to each one.

Lithology keyword	*Total area (km2)*	*N. entities*	*Lithology Weight*
Limestones	234.116	1382	1.0
Dolomite	281.285	1237	1.0
Carbonate	86.887	303	1.0
Marble	142.157	2282	1.0
Carbonaceous	141.040	529	0.7
Marl	8.271	350	0.7
Gabbro	2.776	263	0.5
Basalt	5.178	864	0.5
Basic	174.250	907	0.5

Table 6.6: Features of the reactive lithological categories associable with skarn.

Over a total of 5672 entities, 2713 have more than one lithology keywords (up to three) in their description. While the different associated keywords usually have the same weight (e.g., dolomitic limestone), sometimes they have different weights (e.g., calcareous marl and marly limestone).

To represent latent potential and geological knowledge uncertainty, we assigned a default baseline of 0.1 for the unfiltered lithologies.

Weighted keywords and hierarchy

During the score attribution, we considered a weighted average between the different values of the lithological keywords, considering the most notable one in each polygon description and assigning it a 1.5× weight factor, while other terms get 1.0×.

The used formula is:

polygon_score = Σ(LW x WF) / Σ(WF)

Where:

- LW is the Lithology Weight.
- WF is the Weight Factor, equal to 1.5 for the first keyword and 1.0 for the others.

Which translates in SQL language to:

```sql
SUM(LW * WF) / NULLIF(SUM(WF), 0) as polygon_score
```

Weighted score based on area

Furthermore, since we will calculate the f_lithology score on 1km^2 grid cells, we will weigh the polygon_score in proportion to the intersected area for each cell, while considering the empty cell portion with a given baseline value of 0.1. The relationship incorporates a non-linear amplification factor to give more weight to partial presences of reactive lithologies.

f_lithology = (Σ(polygon_score × intersected_area) / Σ(intersected_area)) × (Σintersected_area)^exp + BL × (1 – Σintersected_area)^exp

where:

- polygon_score = Σ(LW x WF) / Σ(WF) is the contribution of each polygon inside the grid cell.
- Σ(polygon_score × intersected_area) / Σ(intersected_area) represents the average reactive lithology score within occupied areas (weighted by intersected area).
- Σintersected_area is the total area of the grid cell occupied by reactive polygons (normalized to a 0-1 proportion).
- BL is the baseline with a default score of 0.1.
- (1 – Σintersected_area) is the area proportion that is not occupied by reactive polygons.
- exp is the amplification exponent (set to 0.5), which gives greater influence to partial occupancies.

The final score calculation follows three scenarios:

1. No reactive lithologies (Σintersected_area = 0): f_lithology = 0.1 (baseline)
2. Partial occupancy (0 < Σintersected_area < 1): Weighted combination of reactive score and baseline with non-linear area influence
3. Full occupancy (Σintersected_area ≥ 1): f_lithology = average reactive lithology score (capped at 1.0)

The results

Table 6.7 and Figure 6.2 illustrate the results. Over the 13754 cells of the grid, 2878 have values over the baseline 0.1 and up to 1.0. Counting the cells scoring over 0.1, the average f_lithology is 0.42, with a standard deviation of 0.27. Quartiles have values of q10 = 0.13, q25 = 0.17, q50= 0.36, q75 = 0.61 and q90 = 0.88, showing a shifting towards lower scores explained by the frequency of less reactive lithologies such as basic dikes that occupy small areas, making more impactful the contribution from the baseline in the same cells where they crop out. 18 cells have a value of 1.0, completely covered by a high-reactivity class.

Cells > 0.1	*Avg. f_lithology*	*St. dev.*	*min*	*max*	*p10*	*p25*	*p50*	*p75*	*p90*
2878	0.42	0.27	0.1	1.0	0.13	0.17	0.36	0.61	0.88

Table 6.7: f_lithology statistics of the cells scoring < 0.1.

Moreover, except for 17 skarn that fall into cells with the baseline value 0.1, the skarn occurs as in Table 6.8:

f_lithology range	*N. of skarn*	*Percentage*	*Avg. f_lithology*
0.1 – 0.1	17	18.89	0.1
0.11 - 0.20	8	8.89	0.16
0.21 - 0.40	18	20.00	0.29
0.41 - 0.6	24	26.67	0.50
0.61 - 0.80	16	17.78	0.68
0.81 - 1.0	7	7.78	0.87

Table 6.8: f_lithology values distribution.

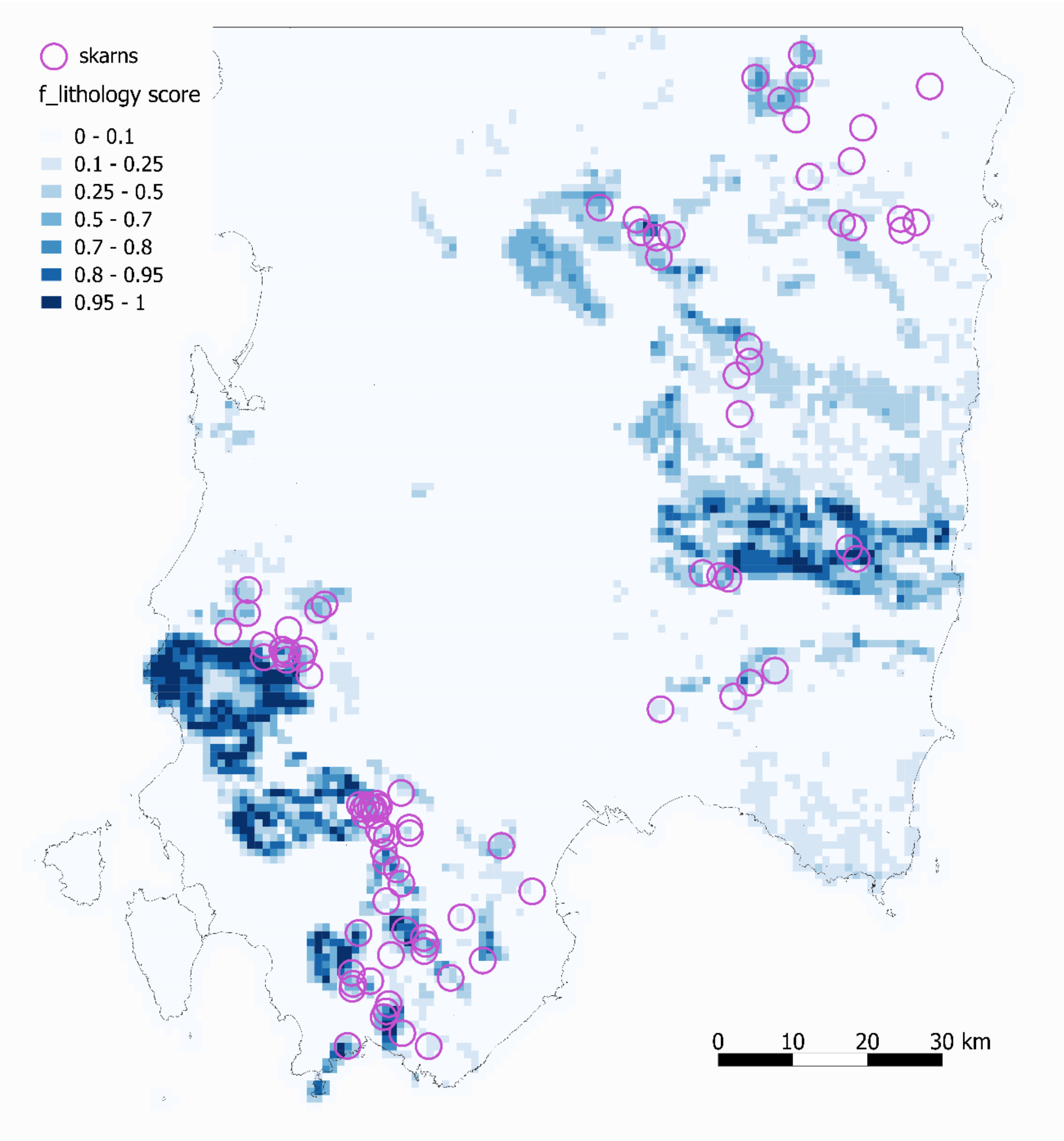

Figure 6.2: Lithology fuzzy score values (f_lithology) and skarn occurrences map.

6.3. Proximity to faults

Skarn in Sardinia are often spatially and genetically linked to Variscan thrusts and inverse faults, which allowed the more reactive rocks, the pre-Variscan carbonate lithologies, to be emplaced within fluid-conductive systems concurrently formed as shear and cataclastic zones (Cocco et al., 2018; Funedda et al., 2018; Cocco et al., 2022b; Naitza et al., 2024).

Data preparation and filtering

To analyse the spatial distribution of skarn in relation to fault types, we considered the two categories correlated to the Variscan orogeny: thrusts and reverse faults (Table 6.9).

Type	*Count*	*Total length (km)*	*Avg. length (km)*	*Min (km)*	*Max (km)*
Thrust	1557	1109.64	0.713	0.015	8.823
Reverse	419	197.15	0.470	0.013	4.236

Table 6.9: Types of faults associated with skarn genesis, their count, and length.

The approach is like the one we used for f_intrusion calculation, applying a score on the intersecting cell and a buffer from the faults, applying different ranges and weight to the two fault categories.

Direct fault influence (Interacting faults)

We calculated the total length of thrust and reverse faults intersecting each cell and applied a normalized scoring system with square root transformation to elevate lower values.

Direct Fault Score = √(Intersecting Length / Reference Length)

Where:

- Thrust: Reference Length = 1.0 km
- Reverse: Reference Length = 1.1 km

For cells intersected by multiple faults, we take the maximum score among all intersecting faults. Major intersecting faults dominate the scoring.

Surrounding faults influence (buffer zone)

We considered faults within a certain radius of each cell (without intersecting it). The radius varies with fault type, reflecting their relative geological importance:

- Thrust: 3.5 km buffer radius
- Reverse: 2.5 km buffer radius

The buffer score starts from 0.95 (5% reduction from maximum) at cell boundary and decays linearly to 0 at the maximum radius. We applied a square root transformation to elevate lower values while keeping high values near 1.0; to better represents the non-linear relationship between fault length and skarn-forming potential:

Buffer Score = √[(Fault Length / Reference Length) × (0.95 - (Distance / Buffer Radius))]

Where Reference Lengths are:

- Thrust: 0.8 km
- Reverse: 1.0 km

For cells in the buffer zone of multiple faults, we calculate the average score of all influencing faults. Multiple nearby faults contribute proportionally to buffer zones.

f_fault calculation

We implemented a priority-based approach for final score calculation:

1. Cells intersected by faults → Take maximum direct fault score
2. Cells in buffer zone only (not intersected) → Take average buffer score
3. Cells with no fault influence → Score = 0

The results

Table 6.10 and Figure 6.3 summarise the results. We obtained 5544 cells scoring f_faults > 0 and ranging from minimal (0.001) to maximum (1.000) fault impact. The median score of 0.45 indicates that half of the influenced cells exhibit moderate fault control, while the lower quartile (p25 = 0.31) and upper quartile (p75 = 0.624) demonstrate a good spreading of values. The distribution is slightly right skewed, with the average of 0.487 exceeding the median, associated to the effect of the buffer zone over most cells, while the intersecting cells receives exceptionally strong fault control. The 90th percentile at 0.867 reveals that the top 10% of influenced cells approach maximum fault impact, while the bottom 10% (below p10 = 0.205) experience relatively weak fault relationships. The standard deviation of 0.24 confirms moderate variability around the mean, with fault influence scores distributed across the full spectrum from negligible to dominant control.

Positive cells	***Avg***	***Std_dev***	***min***	***Max***	***p10***	***p25***	***p50***	***p75***	***p90***
5544	0.49	0.24	0.01	1.0	0.21	0.31	0.45	0.62	0.87

Table 6.10: f_faults statistics for cells scoring > 0.

Over the 90 skarn occurrences, 17 have f_fault = 0, showing no evidence of direct tectonic control.

The remaining ones have the values shown in Table 6.11. The skarn occurrences show how moderate f_fault ranges (0.2-0.6) are in this case relevant hosting about 42% of the occurrences, but the most impactful are surely the scores from 0.6 up.

f_fault range	***n. skarn***	***percentage***	***avg f_fault***	***min f_fault***	***max f_fault***
0.01-0.20	4	5.48	0.258	0.236	0.270
0.21-0.40	17	23.29	0.327	0.244	0.397
0.41-0.60	14	19.18	0.508	0.413	0.599
0.61-0.80	20	27.40	0.696	0.610	0.776
0.81-1.00	18	24.66	0.917	0.825	1.000

Table 6.11: Distribution of f_fault scores.

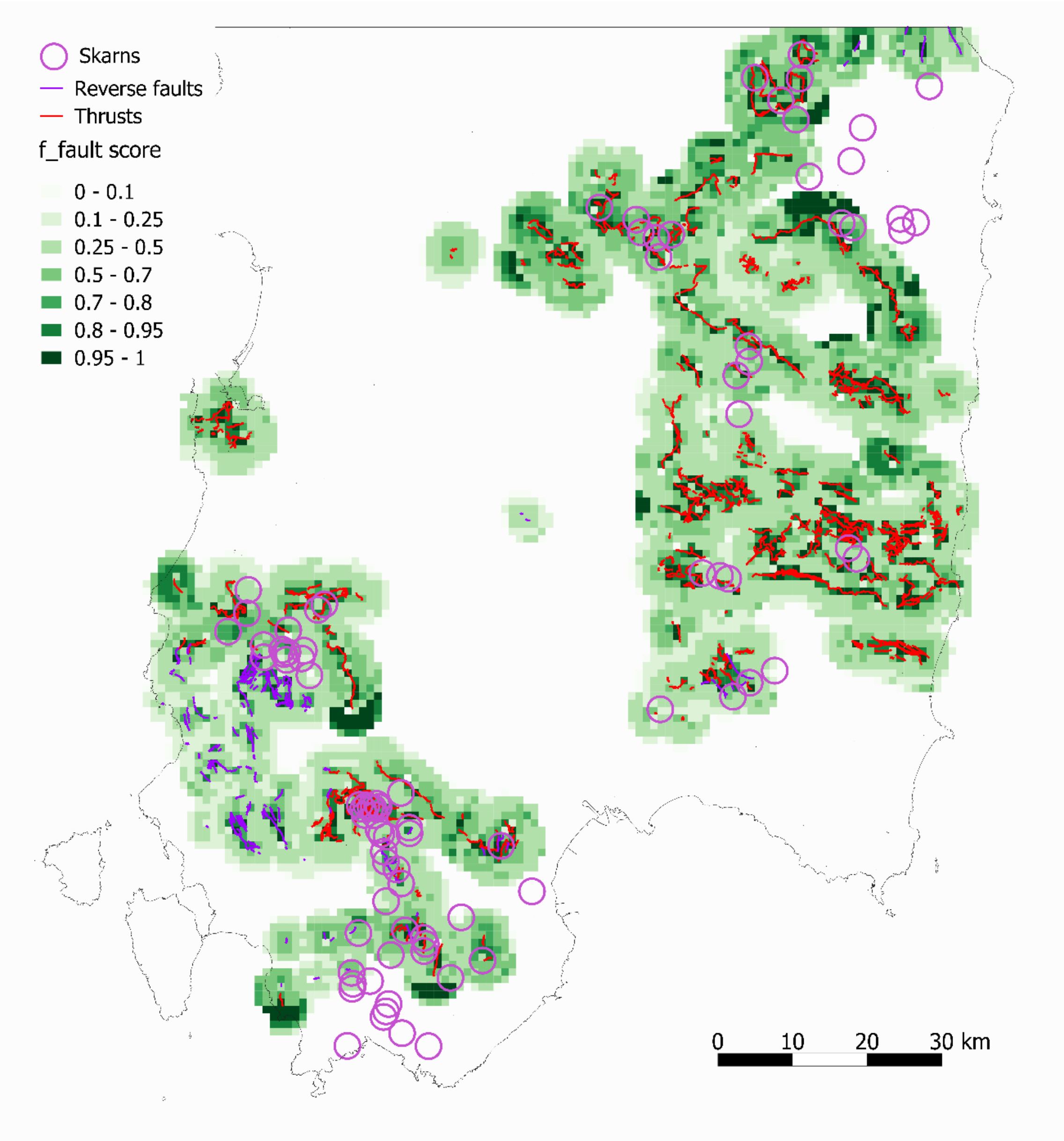

Figure 6.3: Fault fuzzy score values (f_fault) map with faults and skarn occurrences.

6.4. Final Prospectivity Map

To determine an integrated prospectivity value, we combined the three evidence scores f_intrusion, f_lithology, and f_faults by applying the Fuzzy Gamma Operator (Zimmermann & Zysno, 1980; Bonham-Carter, 1994), widely used in mineral prospectivity mapping (An et al., 1991; Carranza & Hale, 2001; Nykänen et al., 2008). It allows to continuously balance the fuzzy AND (intersection) and the fuzzy OR (union) operators given a series of fuzzy scores (with values 0 to 1).

The gamma operator (μ_γ) is defined as:

$$\mu_\gamma = [\mu_{AND}]^{(1-\gamma)} \times [\mu_{OR}]^{\gamma}$$

Where:

$\mu_{AND} = \mu_1 \times \mu_2 \times \mu_3$ is the fuzzy product (intersection, they all need to have a positive value to give a result over 0)

$\mu_{OR} = 1 - [(1-\mu_1) \times (1-\mu_2) \times (1-\mu_3)]$ is the fuzzy algebraic sum (union, the result is 0 only if all the values are 0)

$\gamma \in [0,1]$ is the calibration parameter balancing between AND and OR operators

In our implementation, the formula is:

final_score = [(f_intrusio × f_litholog × f_faults)]^(1 - γ) × [1 - ((1 - f_intrusio) × (1 - f_litholog) × (1 - f_faults))]^γ

Which translates to SQL as:

```sql
final_score = POWER((f_intrusio * f_litholog * f_faults), (1.0 - γ))
            * POWER((1.0 - ((1.0 - f_intrusio) * (1.0 - f_litholog) * (1.0 - f_faults))), γ)
```

Calibration of the γ Parameter

The Gamma operator indicates the permissiveness of the formula: higher gamma is more permissive, and one positive factor is enough to give a positive score; lower gamma is less permissive, and more factors or all of them are necessary to give a positive score (Table 6.12).

γ = 0	μ_γ = μ_AND (product)	All the factors must be over 0
γ = 0.5	μ_γ = μ_AND = μ_OR	Perfect balance between AND and OR
γ = 0.9	μ_γ very close to μ_OR (sum)	At least one the factors over 0 is enough for a good score
γ = 1.0	Complete μ_γ = μ_OR	Factors can have any value

Table 6.12: Examples of gamma operators meaning.

The result prediction based on our data (Table 6.13), given 13754 cells, shows the drastic increase in the average final score with the increasing of the gamma factor, and the increase of the cells with a good score (< 0.7). As previously stated, this is normal and it reflects the increase in the number of cells with factors good enough to contribute to the score.

gamma	*Avg. score*	*Std. Dev.*	*Cells w. score > 0.5*	*Cells w. score > 0.7*
0.5	0.08	0.13	294	32
0.6	0.11	0.16	515	71
0.7	0.15	0.19	953	176
0.8	0.21	0.22	2140	509
0.9	0.33	0.27	3604	1940
1.0	0.58	0.35	7898	6035

Table 6.13: Average prospectivity final_scores applying different gamma operators.

We selected $\gamma = 0.9$ based on statistical analysis of our data since it is appropriate for skarn deposits. With $\gamma = 0.9$, the operator behaves predominantly as a fuzzy OR, reflecting the fact that in our case two out of three conditions are mandatory, and one may be a very important factor, but not necessarily (Carranza, 2008; Porwal & Carranza, 2015):

- Intrusion is essential but not sufficient alone.
- Reactive lithology is fundamental but requires heat and fluids from an intrusion.
- Faults create a favourable environment for fluid circulation but are not essential.

Moreover, some of our occurrences happens to be in formations where the reactive lithology is just a level, or not predominant, hence scoring low, but under the right effect of the other factors, can become a prospect and deserve higher values.

The result

Table 6.14 and Figure 6.4 summarise the resulting prospectivity score. This dataset describes the distribution of fuzzy gamma prospectivity scores across all 13754 cells in the study area, with a mean score of 0.33, indicating moderate to low prospectivity for the average cell, but with a quite wide dispersion (Std. Dev. = 0.27), reflecting strong heterogeneity in geological favourability. The statistics also show that 25% of cells have near-zero prospectivity (25th percentile = 0.05, and that just the 10^{th} percent are highly prospective (90th percentile = 0.74). With a median = 0.33, nearly identical to the mean, the distribution is symmetrical in the central range but stretched at the upper tail (90p). The maximum = 0.98 achieved in some cells confirms the model's capacity to generate high-contrast targets from a large, low-scoring background. The top 10% of cells (>0.74) represent high-priority exploration targets, while the bottom 25% (<0.05) are clearly non-prospective.

Cells n.	*Min*	*Max*	*Mean*	*Std. Dev.*	*10p*	*25p*	*Median*	*75p*	*90p*
13754	0.03	0.98	0.33	0.27	0.03	0.05	0.33	0.52	0.74

Table 6.14: Distribution of the final prospectivity scores.

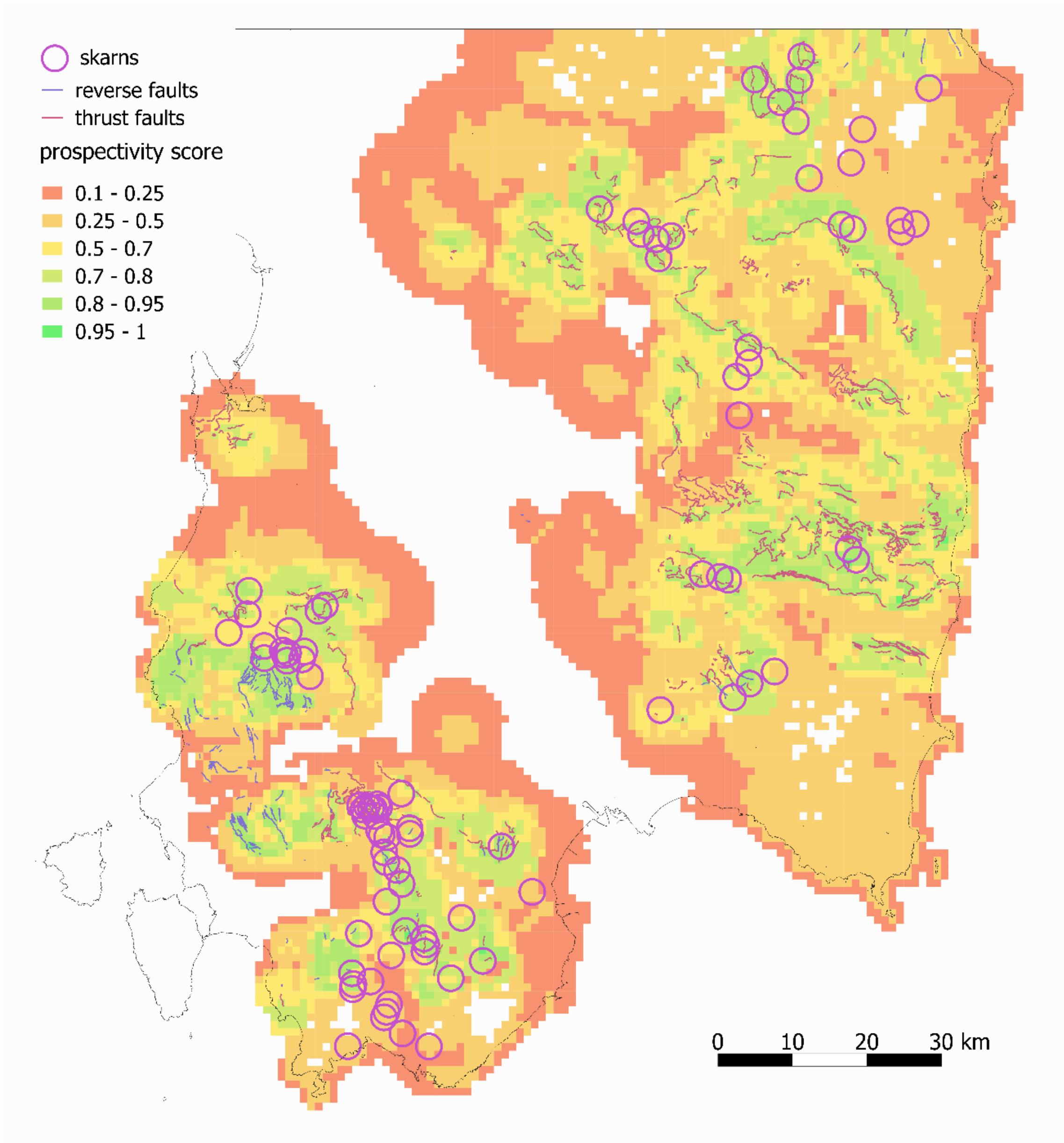

Figure 6.4: Final fuzzy score map for prospectiviness values for skarn deposits.

6.5. Validation with Known Deposits

The analysis of 83 skarn occurrences lying in cells with positive prospective values, reveals a bimodal distribution with two main concentration peaks (Table 6.15). Most skarns (55.4%) occur in high-prospectivity areas (score ≥0.7), with a remarkable concentration in the 0.8-0.9 range (32 deposits, 38.6% of total). This indicates that the prospectivity model effectively identifies favourable zones for skarn mineralization.

A secondary peak occurs in the low-prospectivity range (0.3-0.5), hosting 18 skarns (21.7%), suggesting either:

- The presence of skarn types with different genetic characteristics
- Potential model limitations in capturing all skarn-forming environments

Medium-prospectivity areas (0.5-0.7) contain 17 skarns (20.4%), while the highest scores (0.9-1.0) include only 5 deposits (6.0%), representing the most promising targets with exceptional geological favourability.

Score range	*Skarn count*	*Distribution %*	*Min score*	*Max score*	*Avg score*
0.0-0.3	2	2.4	0.23	0.28	0.25
0.3-0.5	18	21.7	0.33	0.49	0.41
0.5-0.6	7	8.4	0.51	0.59	0.57
0.6-0.7	10	12.0	0.60	0.69	0.65
0.7-0.8	9	10.8	0.71	0.79	0.74
0.8-0.9	32	38.6	0.80	0.89	0.85
0.9-1.0	5	6.0	0.90	0.94	0.92

Table 6.15: Distribution of final score for the cells containing skarn occurrences.

.

Average scores distinct by prospective classes

The analysis of the three fuzzy factors reveals their relative wights to the prospective score determination (Table 6.16, Figure 6.5). High prospectivity class (> 0.7) average at 0.83 of prospectiveness with dominant controls of f-intrusion (0.71) and f-faults (0.66), while f-lithology (0.53) provides moderate support, indicating that the best skarn occurrences require the simultaneous presence of favourable intrusions and structural settings. In the moderate class 0.5-0.7 the average prospectiveness is 0.62, and all factors decrease significantly, with f-intrusion (0.50) and f-faults (0.47) dropping by approximately 30%, and f-lithology (0.25) showing the most dramatic reduction, suggesting that lithological suitability becomes a limiting factor.

Interestingly, in the low prospectivity class (<0.5) with an average prospective score of 0.40, f-intrusion remains surprisingly high (0.74), even higher than in the high class, while f-lithology (0.25) and especially f-faults (0.08) are very low.

prospectivity	*count*	*avg. Prospectivity*	*avg. f-intrusion*	*avg. f_lithology*	*avg. f_faults*
High (>0.7)	53	0.83	0.71	0.53	0.66
Moderate (0.5-0.7)	17	0.62	0.50	0.25	0.47
Low (<0.5)	20	0.40	0.74	0.25	0.08

Table 6.16: Average components for the final prospectivity score classes.

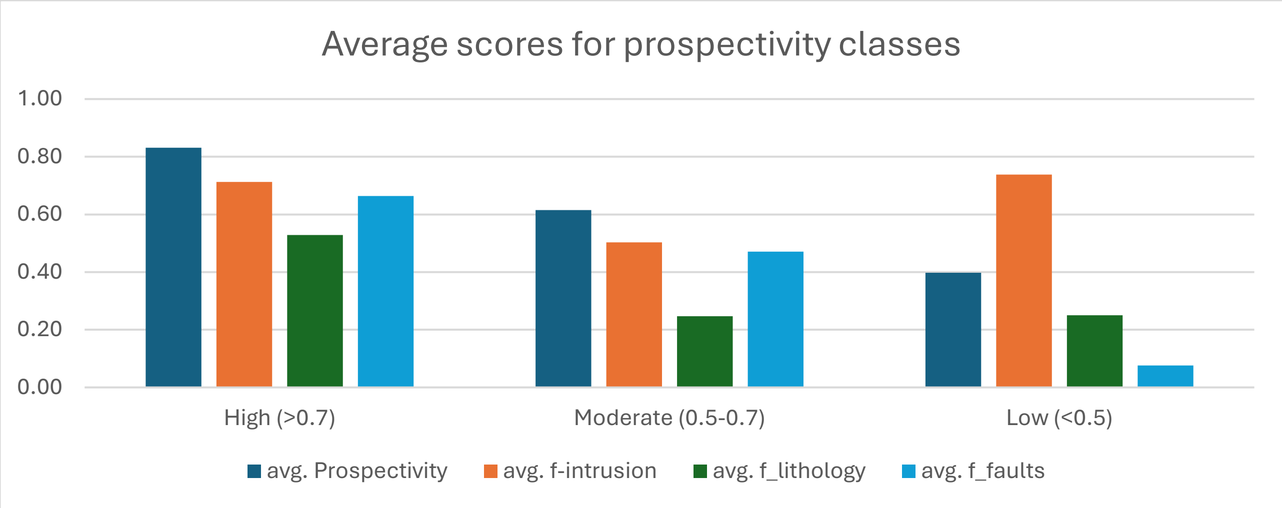

Figure 6.5: Average components for the final prospectivity score classes.

This demonstrates the crucial non-linear aspect of the interaction between fuzzy factors: one high intrusion value alone is insufficient to generate high prospectivity scores when structural control (f-faults) is absent and lithological conditions are unfavourable. Nonetheless, skarn still occurs where the resulting prospectivity is low, indicating the need for ulterior refining of the model.

These limitations are due to both unconsidered reactive lithologies (for instance, we did not consider thin layers of carbonate rocks in greater units), and the unprecise geological data we adopted (mainly for scaling reasons, since we are working on a regional scale).

Cells with skarn and cells without skarn

The applied fuzzy gamma model demonstrates a distinct discriminatory power, with cells containing known skarn occurrences exhibiting a mean prospectivity score of 0.69, while cells without skarn show a considerably lower mean score of 0.33. This separation, though less pronounced than in previous iterations, confirms the model's capacity to distinguish skarn-positive from skarn-negative cells, with skarn-positive cells scoring on average twice as high as their skarn-negative counterparts (Table 6.17).

Skarn-positive cells display moderate uncertainty (standard deviation = 0.19), with scores reasonably clustered around medium-to-high values. The 25th quartile of skarn cells scores 0.54, indicating that even the lower-performing skarn occurrences maintain moderate prospectivity, while the median score of 0.75 confirms that half of all skarn-positive cells exceed the high-prospectivity threshold. Notably, the 90th percentile reaches 0.89, and the maximum score attains 0.94, demonstrating that the best-skarn cells achieve excellent prospectivity scores.

In contrast, skarn-negative cells exhibit higher variability (standard deviation = 0.26), spanning from extremely low scores (10th percentile = 0.03, minimum = 0.03) to values that rival skarn-bearing cells (75th percentile = 0.51, 90th percentile = 0.73, maximum = 0.98). This extraordinary range, from nearly zero to near-perfect, indicates substantial overlap between the two distributions and highlights the presence of extensive areas with high prospectivity but no recorded skarn mineralization. These high-scoring, skarn-negative cells represent high-priority exploration targets for undiscovered deposits.

Skarn	***Cells count***	***avg***	***std. dev.***	***min***	***max***	***p10***	***p25***	***P50***	***p75***	***p90***
Occurs	83	0.69	0.19	0.23	0.94	0.40	0.54	0.75	0.84	0.89
Do not occurs	13671	0.33	0.26	0.03	0.98	0.03	0.03	0.33	0.51	0.73

Table 6.17: Prospectivity score statistics comparison between skarn-positive and non-skarn-positive cells.

Geologically, the clustering of skarn cells at medium-to-high scores confirms that the model captures the favourable conjunction of intrusions, reactive lithologies, and structural elements. The inclusion of both extremely low and exceptionally high scores within skarn-negative cells demonstrates the model's ability to identify both low-probability background areas and potential skarn occurrences in underexplored terrain.

The partial statistical overlap between the two distributions indicates that the fuzzy gamma operator with $\gamma = 0.9$, while appropriately balancing multiple favourable factors, may benefit from further calibration or the incorporation of additional evidence layers to enhance separation. Nonetheless, the model successfully generates meaningful prospectivity contrasts and delineates viable exploration targets within the study area.

Mineralogy-based skarn deposits discrimination

While 64 skarn occurrences are composed of the sphalerite, galena, magnetite/hematite assemblage, 26 skarns occurring in central and eastern Sardinia also bear heavy, “granophile” elements such as W, Sn, As and Sb, sometimes including silver and gold minerals. These elements are generally associated to intrusion-related deposits, and a major high temperature magmatic input is inferred, while the others vert towards lower temperatures and more hydrothermal systems mixing with meteoric waters. The comparation of the two types reveals significant differences in their prospectivity score distributions and the behaviour of the three fuzzy factors.

The two groups exhibit fundamentally different Prospectivity Score distribution. Skarn without “granophile” metals display a spreader distribution, with a dispersed population around 0.4 and a dense cluster above 0.8. This is reflected in a wide interquartile range (IQR: 0.57–0.86) and a high median (0.78) that sits near the top of the lower quartile. In contrast, skarn with “granophile” metals show a unimodal, right-skewed distribution with a slightly narrower IQR (0.59–0.82) and a median (0.737) centrally located within its quartiles. This indicates that heavy metal-bearing skarns are consistently confined to moderate-to-high prospectivity areas (mean 0.689), while “common” skarns can form in both very poor (min 0.228) and excellent (max 0.944) environments.

The magmatic control represented by f_intrusion indicate that both groups show generally high median intrusion values (0.80 without vs 0.67 with), but their distribution patterns differ markedly. The granophile-metals-devoid group displays a continuous distribution skewed toward high values, with a gradual spread from low (0.14) to high (1.00) and a well-represented mid-range. The skarn-positive group, however, exhibits a polarised distribution, with a cluster of very low values (<0.4) and a dominant cluster of very high values (>0.8). This suggests that "granophile" metal skarns form under extreme intrusion conditions, either highly favourable or strongly compensated by other factors.

Lithology reveals the most striking behavioural difference. The granophile-metals-devoid group has a much wider spread (range 0.10–0.89, IQR: 0.22–0.60), with a long tail of high values strongly associated with the high-mode prospectivity cluster. The skarn-positive group shows a much tighter and consistently low pattern (range 0.10–1.00, but IQR: 0.11–0.60, median 0.35), with most deposits concentrated at low values. This indicates that exceptionally favourable host rocks are not a primary driver for heavy metal enrichment.

Structural control emerges as the most discriminating factor. The granophile-metals-devoid group displays a highly skewed distribution (median 0.47), where deposits with no structural control (min 0.00) form the low-mode cluster, while those with very high fault values (Q3: 0.72, max 1.00) constitute the high-mode cluster. The skarn-positive group has a higher median (0.64 vs 0.47) and a greater proportion of deposits with excellent structural fluid-pathways. Critically, it's very highest prospectivity scores (>0.85) are almost invariably associated with f_faults values near 1.00, demonstrating that excellent structural permeability is the key ingredient for upgrading a skarn to a high-value heavy metal deposit.

Minimum Threshold

The skarn-positive group has a substantially higher minimum prospectivity score (0.362 vs 0.228), suggesting a natural cutoff: below approximately 0.36, geological conditions are simply too unfavourable to generate skarns capable of hosting W-Sn-As-Sb mineralization, regardless of other factors (Figure 6.6, Table 6.18). This reinforces that "granophile" metal skarns represent a more specialised metallogenic feature requiring consistently favourable conditions across multiple factors.

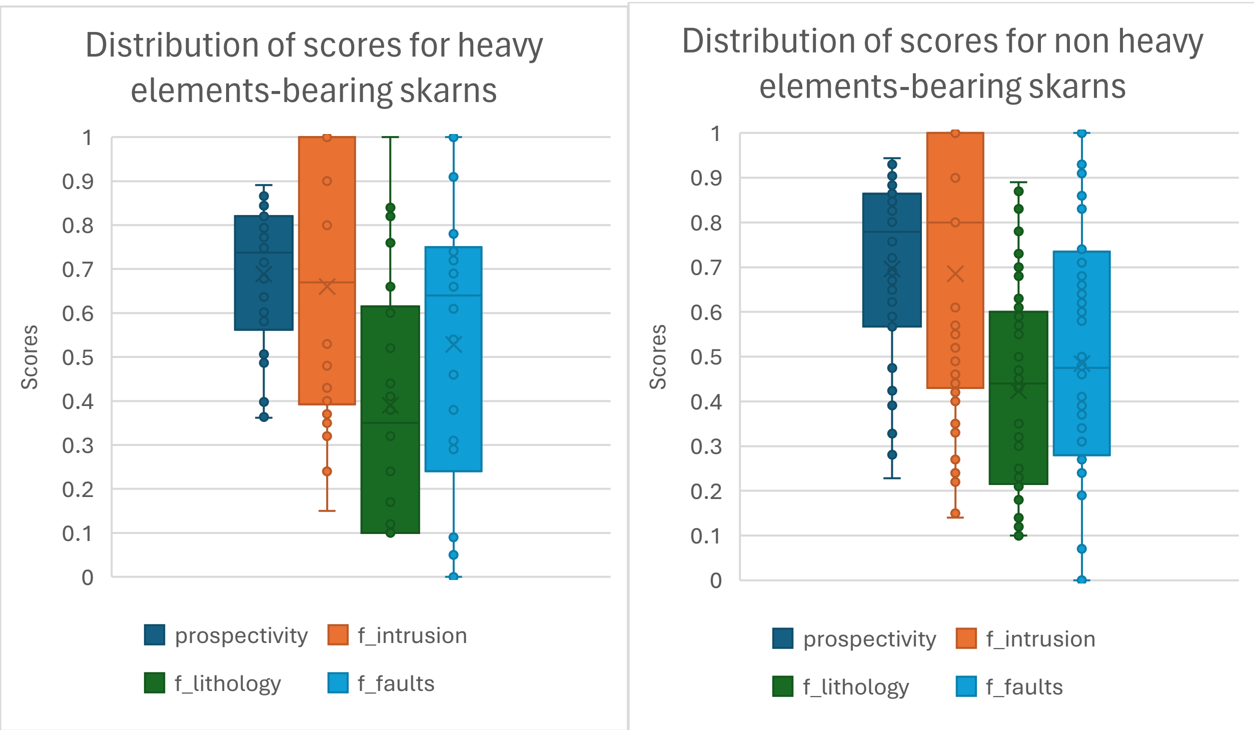

Figure 6.6: Distribution of prospecitivy components for skarn bering heavy elements and for skarn do not bearing them.

		with W-Sn-As-Sb	*without W-Sn-As-Sb*
	count	***26***	***64***
prospectivity	min	0.362	0.228
	max	0.891	0.944
	avg	0.689	0.696
	25p	0.587	0.567
	median	0.737	0.779
	75p	0.817	0.862
f_intrusion	min	0.15	0.14
	max	1	1
	avg	0.66	0.69
	25p	0.4	0.43
	median	0.67	0.8
	75p	1	1
f_lithology	min	0.1	0.1
	max	1	0.89
	avg	0.39	0.42
	25p	0.11	0.22
	median	0.35	0.44
	75p	0.6	0.6
f_faults	min	0	0
	max	1	1
	avg	0.53	0.48
	25p	0.3	0.28
	median	0.64	0.47
	75p	0.75	0.72

Table 6.18: Distribution of prospectivy components for skarn bearing heavy elements and for skarn do not bearing them.

6.5.1. ROC curve

The Receiver Operating Characteristic (ROC) validation process evaluates how well a predictive model distinguishes between mineralised and non-mineralised cells. For every possible prospectivity score, it calculates the True Positive Rate (sensitivity, the proportion of actual mineralised cells correctly identified) and the False Positive Rate (1 – specificity, the proportion of non-mineralised cells incorrectly classified as prospective). These values are plotted to generate the ROC curve, and the Area Under the Curve (AUC) provides a global measure of model performance, with values closer to 1 indicating better predictive ability (Fawcett, 2006; Nykänen et al., 2015).

Data preparation

The validation dataset was extracted directly from the database using a Python script connected to PostgreSQL. The query retrieved all 13754 grid cells comprising the study area, including:

- 83 skarn-positive cells (all known skarn occurrences, with some cells containing multiple deposits).
- 13671 skarn-negative cells.

For each cell, the query returned the fuzzy prospectivity score (ranging from 0 to 1) and a binary label (1 for skarn-positive, 0 for skarn-negative).

ROC Curve Analysis

We used a Python script with the scikit-learn library (Pedregosa et al., 2011), to perform Receiver Operating Characteristic (ROC) curve analysis. This method evaluates the model's discriminatory power across all possible decision thresholds:

- For every potential prospectivity score, the script calculates:
  - True Positive Rate (TPR) or Sensitivity: The proportion of skarn-positive cells correctly identified by the model.
  - False Positive Rate (FPR) or 1 - Specificity: The proportion of skarn-negative cells with higher prospectivity score.

The ROC curve is generated by plotting TPR against FPR for all thresholds, and the Area Under the Curve (AUC) provides a global measure of model performance, representing the probability that the model will rank a randomly chosen skarn-positive cell higher than a skarn-negative one (Figure 6.7).

The optimal decision threshold maximizes the balance between sensitivity and specificity and was determined using the Youden Index (J = TPR + Specificity - 1) for every prospectivy score (Youden, 1950).

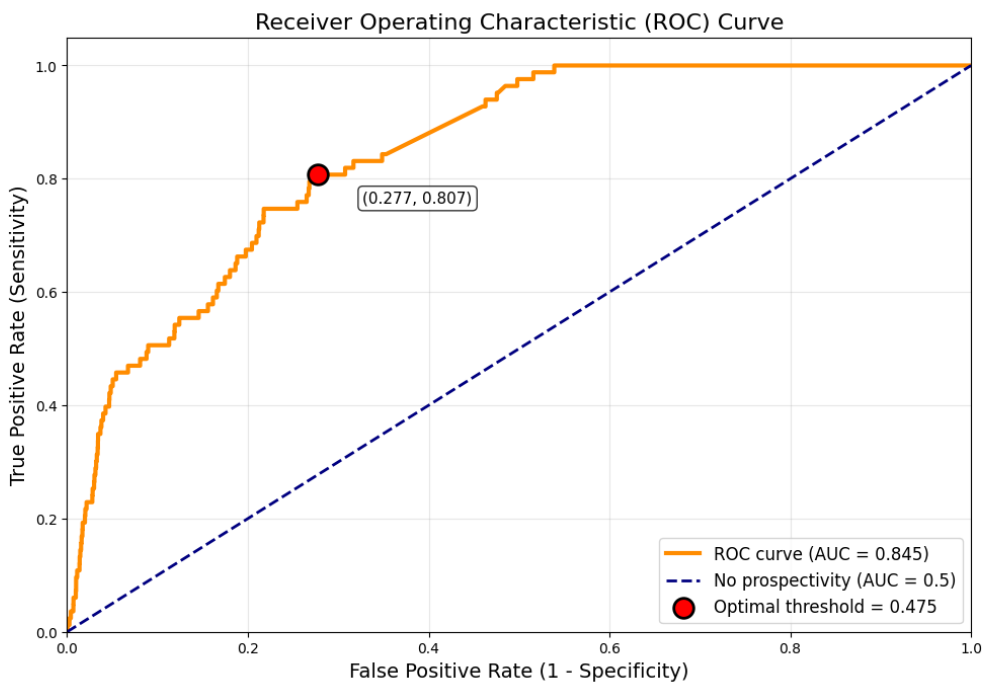

Figure 6.7: ROC curve (orange) of the skarn prospectivity model in Sardinia, with the optimal prospectivity score threshold (red dot) for good predictive performance according to the Youden Index. The blue dashed line is the non-predictive model threshold (TPR = FPR).

Summary and Validation of the Fuzzy Prospectivity Model

The mineral prospectivity model for skarn-type deposits in Sardinia was developed by integrating three critical geological criteria through a Fuzzy Gamma operator ($\gamma = 0.9$). Each criterion was calibrated using geologically meaningful rules:

Intrusion proximity (f_intrusion) was calculated considering both direct intersection and buffer effects, with buffer distances scaled by intrusion size: 8 km for large intrusions (≥1 km^2), 6 km for medium intrusions (100000–1000000 m^2), and 4 km for small intrusions (<100000 m^2). Values decay linearly from 0.9 at 1 km distance to 0.1 at the maximum buffer limit.

Lithological favourability (f_lithology) was derived from a weighted analysis of lithological terms, assigning scores based on rock type (1.0 for carbonates, 0.7 for marls, 0.5 for mafic rocks) and incorporating the proportional area of fertile lithologies within each grid cell, with a base value of 0.1 for non-fertile areas.

Structural control (f_faults) distinguished between thrust and reverse faults, applying different buffer distances (3.5 km for thrusts, 2.5 km for reverses) and using square-root scaling to moderate the influence of fault length and proximity. Cells intersecting faults received priority scores based on the length of intersection.

The model was validated using **Receiver Operating Characteristic (ROC)** curve analysis on the complete dataset of 13,754 grid cells, comprising 83 skarn-positive cells (all known skarn occurrences) and 13,671 skarn-negative cells.

The validation demonstrates strong predictive capability with an Area Under the Curve (AUC) of 0.845, indicating an 84.5% probability that the model correctly ranks a random skarn-positive cell higher than a skarn-negative one.

The optimal decision threshold of 0.475 is determined by the Youden Index (Youden, 1950), and the relative confusion matrix shows:

	Predicted Positive ***Prospectivity ≥ 0.475***	***Predicted Negative*** ***Prospectivity < 0.475***
Actual Positive	67 (True Positives)	16 (False Negatives)
Actual Negative	3788 (False Positives)	9883 (True Negatives)

It correctly identifies 67 out of 83 known skarn occurrences (True Positive Rate -sensitivity of 80.7%), while maintaining a False Positive Rate of 27.7% (3788 false positives out of 13671 skarn-negative cells).

True Positive Rate (Sensitivity) = True Positives / (True Positives + False Negatives) = 0.807

False Positive Rate = False Positives / (False Positives + True Negatives) = 0.277

At this threshold, the model achieves an overall accuracy of 72.3 % (correct classification in 9950 out of 13754 cells) and a

Accuracy = True Positives + True Negatives) / Total cells = 0.723

The statistical distribution of prospectivity scores confirms good discrimination between the two classes: skarn-positive cells exhibit a mean prospectivy score of 0.686 (±0.194), while skarn-negative cells average 0.331 (±0.265), yielding a clear mean difference of 0.355.

The 16 missed skarns have prospectivity scores ranging from 0.228 to 0.434, with a mean of 0.375, significantly below the optimal threshold. These represent either a lack of precision in data input for the predictive model, or areas where the model underestimate the geological potential.

The low precision (1.74%) despite good AUC (84%) reflects the rarity of skarn occurrences, with just 83 out of 13,754 cells (0.6%) containing mineralisation, and the model slightly conservative approach, prioritising the identification of potential targets (only 16 missed) at the cost of flagging more false positives (3788).

Precision = True Positives / True Positives + False Positives = 0.0174

The distribution of prospectivity scores for skarn-positive and skarn-negative cells intersect at a prospectivity score of 0.492, which represents the theoretical equilibrium point where the probability density of misclassifying a skarn-positive cell as negative equals that of misclassifying a skarn-negative cell as positive (Figure 6.8). The optimal threshold of 0.475 determined by the Youden Index is very close to this intersection (difference of 0.017), confirming that the selected threshold effectively approximates the statistically optimal decision boundary.

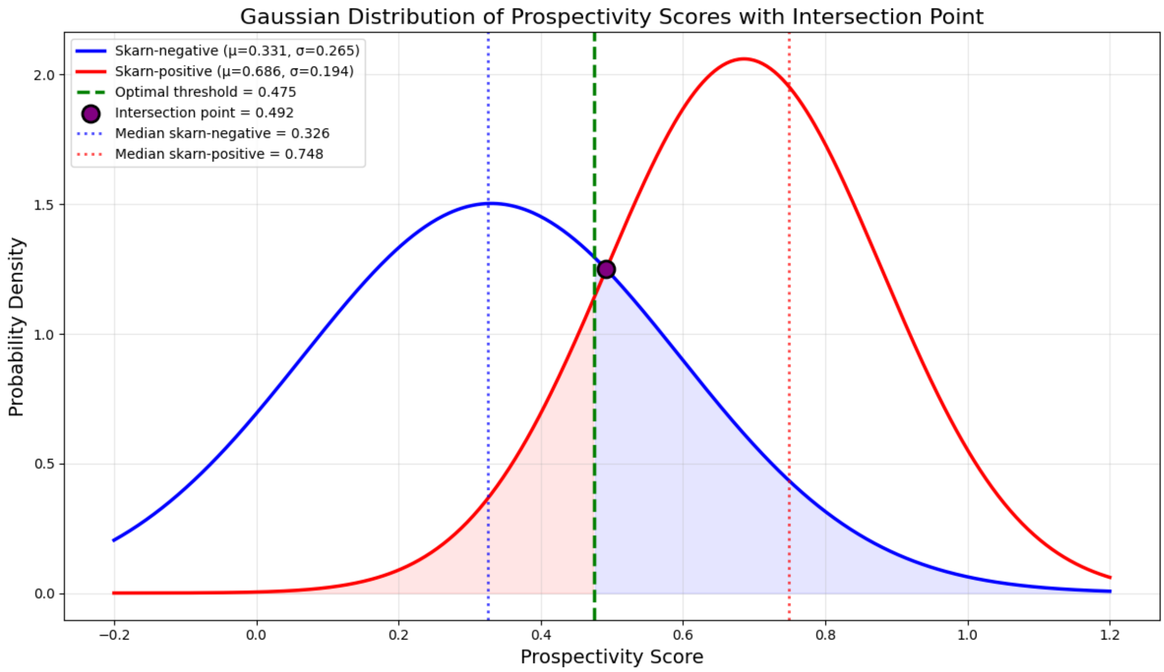

Figure 6.8: Gaussian distributions of Prospectivity scores for skarn-positive and skarn-negative cells, with their intersections similar to the optimal threshold determined by the validation model.

6.5.2. The other mineralisation types in the prospective areas

It's interesting to note that area with a good prospectivity value >0.7 contains a total of 120 hydrothermal veins, 25 karst, 19 MVT, 10 greisen, 4 SEDEX, 2 clay deposits and 1 pegmatite (Table 6.19).

All of them have a mean score over 0.8 and the distinct f_intrusion, f_lithology and f_faults varying with type.

Karst, MVT and SEDEX share the lithological potential for the carbonates. In fact, these have mean f_lithology values consistently over 0.87, while f_intrusion and f_faults are low, averaging between 0.39 and 0.58.

On the other hand, hydrothermal veins, greisen, pegmatites and clay deposits share the thermal and fluids contribution from the magmatic intrusions. Hydrothermal veins and clay deposits have both f_intrusion and f_faults scoring over 0.6; greisen average at 0.89 for the intrusion proximity and also have a good 0.67 f_fault average, but the lithology is naturally very low; the pegmatite happens to have a perfect intrusion and faults score.

prospectivity	type	count	avg. Prospectivity	avg. f-intrusion	avg. f_lithology	avg. f_faults
High (>0.7)	hydrothermal veins	120	0.81	0.60	0.54	0.68
	skarn	53	0.83	0.71	0.53	0.66
	karst	25	0.84	0.52	0.87	0.58
	MVT	19	0.82	0.48	0.88	0.51
	greisen	10	0.83	0.89	0.38	0.67
	SEDEX	4	0.80	0.49	0.89	0.39
	clay deposit	2	0.80	0.76	0.43	0.61
	pegmatite	1	0.93	1.00	0.49	1.0

Table 6.19: Breakdown of prospectivy score components for various types of mineralisation occuring in high prospectivity cells for skarn.

6.6. Other parameters

The chosen parameters can be significantly refined to reduce model uncertainty, better constrain target rankings, and increase the probability of discovering buried skarn mineralization.

- Distance from intrusions could be refined by distinguishing intrusion composition (e.g., oxidized vs. reduced (Meinert et al., 2005) and calculating weighted distance functions based on intrusion age and fertility.
- Structural complexity indices, such as fault density, intersection density, or proximity to fault intersections, would better capture the role of permeability and fluid focusing than simple distance-to-fault alone.
- Stratigraphic and lithological descriptors could be enhanced by incorporating host-rock reactivity rankings, permeability estimates, and the presence of carbonate units of appropriate composition and thickness.

Moreover, additional parameters could significantly improve the predictive capacity of the skarn prospectivity model.

- Geophysical datasets represent one of the most powerful tools for exploring buried skarn systems, as they extend prospectivity analysis into the third dimension, overcoming the limitations imposed by cover and erosion. Their integration within a predictive model allows reconstruction of intrusive geometry, mapping of permeable structures, and identification of altered carbonate contact zones that do not crop out at surface. The main methods are:
    - Magnetics: Detects magnetite, hematite, and pyrrhotite in skarn systems. Positive elliptical anomalies can indicate buried intrusions or magnetite-rich skarns (Fan et al., 2025).
    - Gravity: Massive sulfides and magnetite-rich horizons can produce detectable high-amplitude anomalies. Bouguer anomaly and residual gravity analysis delineates lateral extent and depth of buried intrusive complexes, which are key controls on skarn localisation, especially when coupled with magnetic methods (Clark, 2014).
    - Seismic Reflection: Provides high-resolution imaging of strong impendence lithological contacts and structures at depth that are demonstrated effective in crystalline terrains (Malehmir et al., 2011, 2012, 2014; Wu et al., 2014).
    - Integration and 3D Modeling. Joint interpretation of magnetic, gravity, IP, and seismic data within a unified 3D model allows each method to compensate for the limitations of others. This multi-physics approach is essential for targeting buried skarns where surface geological indicators are absent (Lara et al., 2017; Malehmir et al., 2006; Roy and Clowes, 2000).
-
- Geochemical data considering the distribution of Cu, Mo, Zn, Pb, Au, and Ag would provide direct evidence of hydrothermal alteration and mineralizing processes, serving as proximal indicators of skarn systems.
- Alteration mineral maps derived from multispectral satellite imagery (ASTER, Sentinel-2) or hyperspectral surveys allow direct detection of diagnostic mineral assemblages such as garnet, pyroxene, epidote, and wollastonite.
  Geomorphology parameters (elevation, slope, aspect, curvature) may indirectly reflect differential erosion levels and expose deeper, potentially mineralized zones.

7. Conclusions

This PhD research delivers a comprehensive review of the metallogenic knowledge of Sardinia, transforming legacy data and new investigations into a dynamic, queryable, and predictive digital framework. The work directly addresses the European Union's call for a secure and sustainable supply of Critical and Strategic Raw Materials (CRMs and SRMs) by providing a foundational tool for the re-evaluation of Sardinia's mineral potential, a historically significant mining region.

7.1. Summary of the key findings and scientific contributions

7.1.1. The New Metallogenic Database of Sardinia

The primary outcome of this thesis is the creation of the most up-to-date metallogenic database of Sardinia. Moving beyond static maps, this relational geodatabase, built on a PostgreSQL/PostGIS architecture, now catalogues over 630 mineral occurrences, deposits, and active mines. Its core innovations include:

- **Synthesised Knowledge:** It integrates and rationalizes data from the historical archives of the *Ente Minerario Sardo* (EMSA), the previous metallogenic maps (1978, 2008), and modern scientific literature.
- **CRM-Focused Table:** The database highlights Critical and Strategic Raw Materials. The detailed analysis of commodities (Chapter 4.4.2) revealing Sardinia's significant endowment in CRMs such as fluorite, barite, copper, arsenic, antimony, tungsten, and REEs, alongside a suite of rare and complex polymetallic assemblages (Bi, Co, Ni, Ge) that were historically overlooked.
- **Quantified Metallogenic Patterns:** Statistical queries on the database have, for the first time, quantitatively characterized the island's mineral systems. This includes defining the typical features (commodity associations, morphology, texture, structural orientation) of its main deposit types, from the dominant hydrothermal veins and skarns to MVT, karst, and greisen deposits (Chapter 4.4.3). This schematization provides the fundamental frame needed for predictive modelling.

7.1.2. Refined Genetic Models through Integrated Case Studies

The detailed investigation of key districts served as fuel for the database's iterative improvement and provided robust genetic models applicable at a regional scale.

The Rosas-Orbai and Fluminese Districts (southwestern Sardinia): Detailed structural and metallogenic mapping in the Rosas-Orbai district confirmed a polyphase genetic model, with mineralization evolving from high-temperature, Permian-age skarns (e.g., Rosas, Mitza Sermentus) structurally controlled by the Rosas Shear Zone, to post-orogenic, low-temperature hydrothermal barite-fluorite-galena veins emplaced along high-angle normal faults, and finally to supergene karst-hosted barite deposits. This model finds a strong analogue in the Fluminese district, where the same three-stage evolution is recorded: skarn bodies with both Cambrian (Su Zurfuru, buried) and Silurian-Devonian (Medau Ganoppi) protoliths; high-angle Ni-Co-As polymetallic veins cutting the skarns; and extensive low-temperature barite-fluorite veins (s'Oreri, Filone Palazzo, Su Zurfuru) emplaced along N-S and NW-SE fault systems. The comparative analysis validates the regional applicability of the model and demonstrates that skarn potential is highest in the footwall of major Variscan thrusts, particularly where secondary shear zones enhance permeability, while post-orogenic vein targets are consistently associated with late-Variscan normal fault systems intersecting competent lithologies.

The Silius Vein System (southeastern Sardinia): The Silius deposit provides the exemplificative type for understanding the vertical zonation and regional exploration potential of fluorite-barite hydrothermal vein systems. The mine exhibits a clear vertical evolution from shallow, barite-dominated levels to fluorite-rich zones at depth, with increasing base metal (galena) and, in the deepest exploited levels, the appearance of complex Ni-Co-As-Bi assemblages. This zonation, combined with structural control by NE-SW trending, steeply dipping faults hosted in competent metavolcanic and metasandstone lithologies, establishes a predictive model applicable across Sardinia. According to this model, shallow barite veins (e.g., Rosas-Orbai, Bruncu Molentinu) may represent the upper levels of deeper, potentially fluorite-rich systems, while fluorite veins with base metal enrichment (e.g., Santa Lucia, Monte Genis, Asuni) could host Ni-Co-As-Bi mineralization at the deepest levels, as documented at Silius. The model also highlights the critical role of host rock competence as a key constraint for exploration targeting: the Silius vein system maintains its thickness and continuity only where hosted by competent lithologies (porphyries, sandstones), thinning or disappearing where it enters less competent phyllite.

The Su Laccheddu Greisen System (northern Sardinia): This study showcased a geochemical and geochronological approach. Novel *in-situ* Rb/Sr dating of white mica from the greisen yielded ages ranging from 293 to 270 Ma, revealing a prolonged (~23 Myr) fluid circulation clustered in two different events of fluid circulation and mineralisation associated with the later stages of the Variscan orogeny. This finding, coupled with detailed EMPA analysis on white micas and ore minerals, describe the entire evolution from a high-temperature, F-rich magmatic-hydrothermal system (W-Mo-LREE) to a later, lower-temperature, more hydrous stage (fluorite veins), refining the genetic model for granite-related deposits in the Sardinian Batholith.

7.1.3. A Data-Driven Mineral Prospectivity Model for Skarn Deposits

The ultimate test of the database's utility was its application in predictive modelling. A fuzzy logic-based Mineral Prospectivity Model (MPM) was developed for skarn deposits in central and southern Sardinia, integrating three critical criteria derived from the genetic model:

- Fuzzy membership maps were created for proximity to intrusions (scaled by intrusion size), lithological favourability (potentially reactive protoliths), and proximity to Variscan thrusts and reverse faults.
- The integration of the fuzzy memberships using a Fuzzy Gamma operator ($\gamma = 0.9$) produced a regional prospectivity map.

Validation of the model using Receiver Operating Characteristic (ROC) curve analysis on 83 known skarn occurrences yielded an Area Under the Curve (AUC) of 0.845, indicating excellent predictive performance (84.5% probability of correctly ranking a skarn-positive cell higher than a skarn-negative one). The Youden Index established an optimal prospectivity threshold of 0.475, which could be raised by further refinements of the predictive model.

Beyond simple prediction, the model provided deeper geological insights:

- It highlighted the non-linear interaction of controlling factors: intrusion proximity alone is insufficient without a reactive lithology, and a favourable structural setting is crucial for skarn metallogenesis in distal intrusion environments.
- It highlighted the non-linear nature of the fuzzy membership calculation, demonstrating that the volume of intrusions, fault extent, and volume of favourable lithologies are critical parameters. Notably, even without direct geophysical data, the model's calculus can implicitly account for the potential influence of buried intrusions and fault extensions.
- Critically, the analysis of skarns bearing heavy, “granophiles” metals (W, Sn, As, Sb) revealed a distinct signature: they are strongly associated with the highest structural control scores (f-

faults near 1.0), suggesting that exceptional structural permeability is the key ingredient for upgrading a skarn to a high-value, polymetallic deposit.

7.2. Implications for research, exploration and policy

The thesis systematically documents and quantifies Sardinia's endowment of Critical and Strategic Raw Materials, directly supporting the objectives of the EU Critical Raw Materials Act (CRMA). It provides the scientific basis and methodology for assessing regional potential, guiding future planning in domestic exploration. By identifying not only where but also *why* and *how* these resources occur, this work moves beyond simple resource auditing to provide the genetic understanding necessary for intelligent, targeted exploration strategies.

The database synthesises the metallogenic history of Sardinia, providing a powerful, dynamic platform for generating and testing new hypotheses about the metallogenic evolution of the island and the broader Southern Variscan realm. The methodology, combining rigorous data architecture with detailed case studies and predictive modelling, offers a transferable template for modernising mineral resource assessments in other geologically complex regions.

Mineral Exploration: A New Set of Guidelines

The metallogenic models derived from the database and case studies, offers critical guidelines for several deposit types:

Mixed sulfides skarn (Cu-Pb-Zn-Fe)

Target the footwall of major Variscan thrusts (e.g., Arburese Thrust) where tectonic slices of Cambrian-Ordovician carbonates are emplaced within fluid-conductive shear zones. High prospectivity requires the confluence of: i) proximity to late-Variscan intrusions (especially the ilmenite-series granites of the YMP), ii) presence of reactive carbonate lithologies, and iii) structural permeability (fault/fracture density). For polymetallic skarns enriched in W-Sn-As-Sb, prioritize areas highly influenced by thrusts as exceptional permeability is the key upgrading factor. Key examples of this type are Rosas, Perda Niedda, San Leone, Funtana Raminosa and Correboi (Figure 7.1).

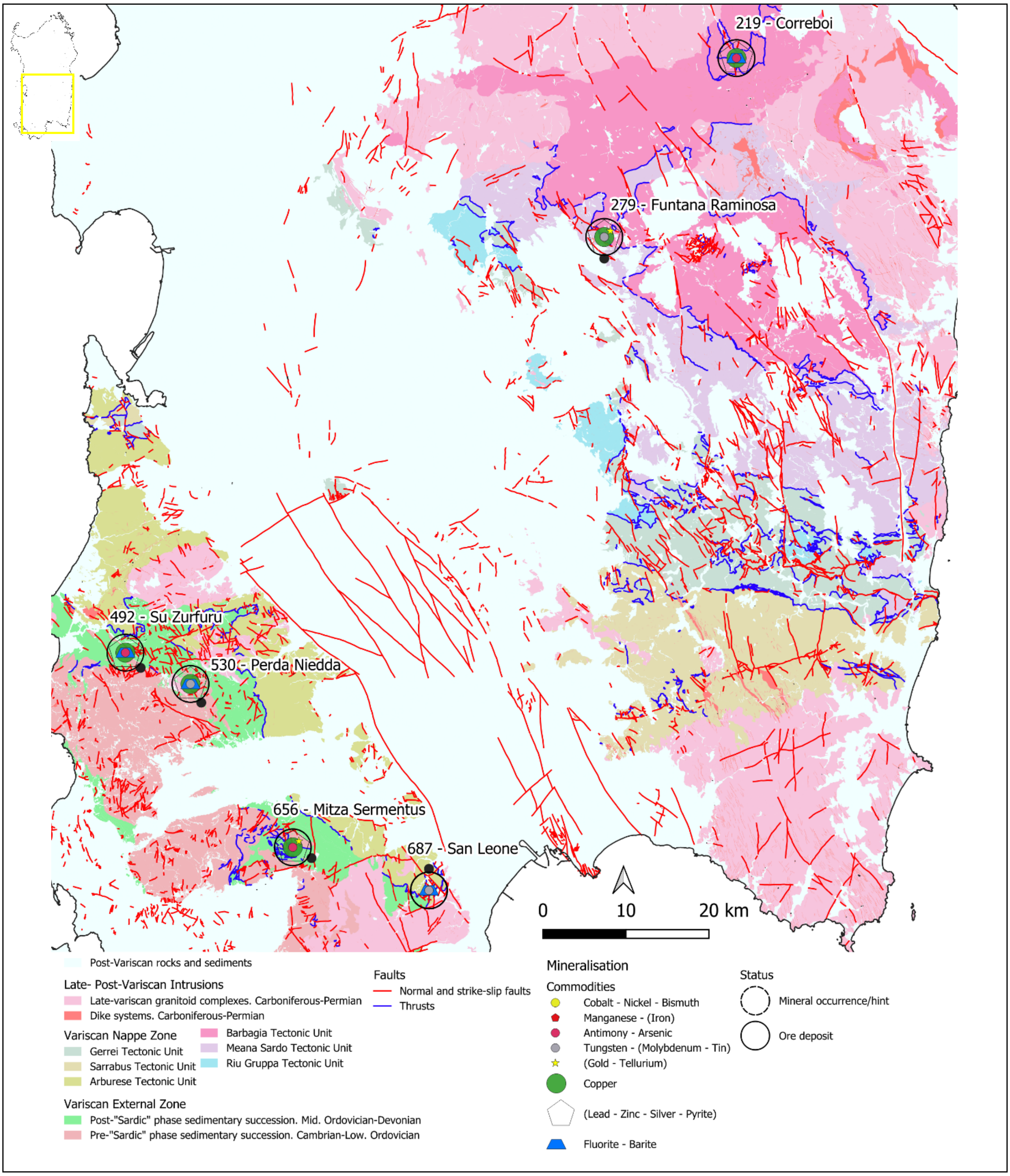

Figure 7.1: Metallogenic Map for some of the key skarn ore deposits in Sardinia.

Hydrothermal Veins (F-Ba-Pb-Zn-Ag)

Explore along high-angle, post-Variscan normal fault systems (NE-SW, NW-SE, N-S) that cut competent lithologies (e.g., volcanics, sandstones, granites). The Silius deposit provides a critical vertical zoning model: shallow, barite-dominant veins may transition at depth to fluorite-rich zones with increasing base metals (Pb, Zn) and, in the deepest levels, may host Ni-Co-As-Bi assemblages. This zonation is recorded in other analogous such as the s'Oreri mine (Santa Lucia, Fluminimaggiore), where fluorspar and sulphides increasing proportionally with depth relative to barite (Bakos et al., 1972b). Therefore, barite veins should be re-evaluated as potential indicators of deeper, more valuable mineralization. Key examples: Silius, Santa Lucia-s'Oreri, Orbai, Bruncu Molentinu veins (Chapters 5.15.35.4).

Sb-As-Au Orogenic Veins

Target second-order structures (e.g., shear zones, fold hinges, fault splays) within and adjacent to regional-scale, crustal-scale shear zones (e.g., the Baccu Locci Shear Zone in the Gerrei district). Mineralization is hosted in low-grade metasedimentary rocks (phyllites, schists) and is characterized by complex sulfosalt assemblages (arsenopyrite, stibnite, tetrahedrite) with native gold/electrum. Key sites are Baccu Locci and Brecca (Chapter 5.4).

Greisens and Pegmatites (Sn-W-Mo-LREE)

Focus on the apical zones and peripheral contacts of the highly evolved, F-bearing, ilmenite-series leucogranites of the Young Magmatic Peak (ca. 290-280 Ma). Mineralisation is geochemically controlled by autometamorphism and late-stage fluid circulation along the related fractures. The Su Laccheddu model demonstrates that greisenization and associated ore deposition are not single events but prolonged, episodic processes (spanning >20 Ma); thus, areas showing evidence of multiple hydrothermal pulses (e.g., brecciation, stockworks, multiple vein generations) are particularly prospective. Key examples are Su Laccheddu, Perda Lada, Su Seinargiu.

MVT & Karst (Pb-Zn-Ag, Barite)

The Cambrian carbonates where post-Variscan tectonics and deep fluid circulation have remobilized and upgraded primary mineralisation. Karst-hosted barite deposits are often spatially associated with hydrothermal veins along reactivated faults; therefore, karst development along fault zones (fault-controlled karst) represents a high-priority target for both barite and residual sulfide concentrations. Key districts are Iglesiente and Sulcis.

Sedimentary Manganese

Explore within the Oligo-Miocene volcanic sequences of western Sardinia, particularly in sub-horizontal pyroclastic horizons where exhalative hydrothermal systems operated in shallow marine or lacustrine basins. Stratiform geometry and association with volcaniclastic rocks are key recognition criteria. Key areas are Northern Sulcis, Logudoro.

Appendix A: The EU Regulatory Framework for Critical and Strategic Raw Materials

This appendix outlines the European Union's policy framework for Critical and Strategic Raw Materials (CRMs and SRMs), which serves as the primary input for this thesis project. The definitions, lists, and legislative benchmarks referenced are based on Regulation (EU) 2024/1252 – the Critical Raw Materials Act (CRMA), which entered into force in May 2024, and the preceding Green Deal Industrial Plan.

Policy Context

The European Green Deal aimed to make the EU climate-neutral by 2050. This transition is materially intensive, requiring a secure and sustainable supply of raw materials essential for key technologies such as renewable energy systems, electric vehicles, digital infrastructure, and defence applications. To mitigate the risks associated with concentrated global supply chains and geopolitical dependencies, the European Commission enacted the Critical Raw Materials Act (CRMA).

The Critical Raw Materials Act (CRMA) – Core Objectives

The CRMA's core objectives is to strengthen the EU's supply security for critical raw materials by diversifying the imports of strategic raw materials and improving the EU's capacity for monitoring, extraction, processing, and recycling of these materials, while ensuring a high level of environmental protection, circularity, and social sustainability throughout the value chain.

Classification System: Critical vs. Strategic Raw Materials

The CRMA establishes a two-tier classification system for raw materials of concern.

Critical Raw Material (CRM): A raw material which is of high strategic importance for the European economy and whose supply is associated with a high risk of disruption. The assessment considers both the material's economic importance and its supply risk, based on factors such as concentration of global production, governance in producing countries, and substitutability.

Strategic Raw Material (SRM): A subset of Critical Raw Materials. A material is designated as strategic if it is both critical and vital for specific strategic technologies pivotal to the ecological and digital transitions, and for which projected future EU demand is expected to grow significantly more rapidly than supply, creating a potential strategic bottleneck.

In essence, all Strategic Raw Materials are Critical, but not all Critical Raw Materials are deemed Strategic. The SRM list triggers more stringent regulatory actions and binding benchmarks.

Official Lists of Critical and Strategic Raw Materials

The official C-SRMs list comprise the materials presented in Table A.0.1.

Antimony (Sb)	Feldspar	Niobium (Nb)
Arsenic (As)	Hafnium (Hf)	Phosphorus (P) / Phosphate Rock
Baryte ($BaSO_4$)	Helium (He)	Platinum Group Metals (PGMs)*
Bauxite (Al-source)	Light Rare Earth Elements (LREEs)*	Scandium (Sc)
Beryllium (Be)	Heavy Rare Earth Elements (HREEs)*	Silicon Metal (Si)

Bismuth (Bi)	Lithium (Li)*	Strontium (Sr)
Boron (B) / Borate	Magnesium (Mg)	Tantalum (Ta)
Cobalt (Co)*	Manganese (Mn)	Titanium Metal (Ti)
Coking Coal	Natural Graphite*	Tungsten (W)*
Copper (Cu)*	Nickel (Ni)*	Vanadium (V)

Table A.0.1: Critical Raw Materials (CRMs) as defined by Regulation (EU) 2024/1252. Materials marked with an asterisk (*) are also classified as Strategic Raw Materials (SRMs).

Notes:

Platinum Group Metals (PGMs) include platinum (Pt), palladium (Pd), rhodium (Rh), iridium (Ir), osmium (Os), and ruthenium (Ru)

Light Rare Earth Elements (LREEs) include lanthanum (La), cerium (Ce), praseodymium (Pr), neodymium (Nd), promethium (Pm), and samarium (Sm)

Heavy Rare Earth Elements (HREEs) include europium (Eu), gadolinium (Gd), terbium (Tb), dysprosium (Dy), holmium (Ho), erbium (Er), thulium (Tm), ytterbium (Yb), lutetium (Lu), and yttrium (Y)

Binding Benchmarks for Strategic Raw Materials (2030 Targets)

For the subset of Strategic Raw Materials, the CRMA establishes the following binding capacity benchmarks to be achieved within the EU by 2030:

Benchmark	Target	Description
Extraction	≥ 10%	At least 10% of the EU's annual consumption
Processing	≥ 40%	At least 40% of the EU's annual consumption
Recycling	≥ 25%	At least 25% of the EU's annual consumption, using waste originating in the EU
External Diversification	≤ 65%	Not more than 65% of the EU's annual consumption of any strategic raw material at any relevant stage of processing should come from a single third country

Appendix B: Database Dictionaries

activity

WORK	DESCRIPTION		STATUS	DESCRIPTION
active mine	A mine that is currently operating.		access restricted zone	Areas where site access is legally or physically restricted (e.g., military zones, protected areas).
active quarry	An active surface operation extracting industrial minerals and construction materials.		hint	Mineral occurrence with unknown economic potential, but considered significant for prospection and exploration targeting.
anthropized	Areas where mineralisation is partially or completely inaccessible due to anthropogenic surface modifications (e.g., urban areas, infrastructure).		ore deposit	A mineralised body that has been economically evaluated and may have been exploited, regardless of current production status.
exploration	Sites where prospection or exploration activities (trenches, boreholes, galleries) have been conducted.			
inactive mine	Former mining operations that are currently not in production but may or may not be maintained.			
inactive quarry	Former quarries that are currently not in production, with or without maintenance or rehabilitation.			
restored	Former mining or quarrying areas that have been naturally or artificially requalified and reintegrated into the landscape.			
waste	Deposits of mining-related waste materials (tailings, slag heaps, waste rock) from past or present operations.			

type

TYPE	DESCRIPTION
aplite	A fine-grained, leucocratic igneous rock of granitic composition, composed primarily of quartz, K-feldspar, and plagioclase. Aplites typically occur as shallow-level dikes and veins, often representing the last phase of magmatic crystallisation.
bauxite	A residual sedimentary rock, the primary ore of aluminium, formed by intense chemical weathering (lateritization) of aluminosilicate rocks under tropical to subtropical conditions. It is characterised by a dominance of aluminium hydroxide minerals.

clay deposit	A sedimentary accumulation composed primarily of clay minerals (e.g., kaolinite, illite, smectite). Deposits form through residual weathering of parent rock, sedimentary transport and settling in basins, or hydrothermal alteration of volcanic or other aluminosilicate materials.
greisen	An auto-metasomatic altered granitic rock, composed mainly of quartz and muscovite, with variable amounts of fluorite and tourmaline. Formed by the interaction of granite with high-temperature, fluorine-rich fluids, greisen is commonly associated with the introduction of tin, tungsten, molybdenum, bismuth, and REE (e.g., Ce, Y).
high sulphidation epithermal deposit	A hydrothermal deposit formed from acidic, oxidising, magmatic fluids at shallow crustal levels. Characterised by advanced argillaceous alteration (alunite, pyrophyllite). Gold, copper, and silver are the primary economic metals.
hydrothermal veins	Tabular or sheet-like mineral bodies filling fractures in rocks, precipitated from circulating high-temperature, water-rich fluids (hydrothermal solutions). Their composition is highly variable, reflecting the fluid's chemistry and temperature, and can include economic concentrations of fluorite, barite, base metals, arsenic, nickel and cobalt, etc.
karst	A type of mineral deposit formed within dissolution cavities and conduits in soluble rocks, primarily carbonates (limestone, dolomite) and evaporites (gypsum). Ore minerals (typically barite and ± galena) and associated sediments fill these openings, and their geometry is controlled by the three-dimensional array of the pre-existing karst system.
low-sulphidation epithermal deposit	A hydrothermal deposit formed from near-neutral pH, reduced, meteoric-dominant fluids at shallow depths (<1 km). Mineralisation is often vein-hosted, with banded quartz, calcite, and adularia. Gold and silver are usually the ore minerals.
magmatic intrusion	A mineral deposit formed directly by the crystallisation and accumulation of oxide or sulfide minerals from a cooling magma within an intrusive igneous body. Classic examples include stratiform chromitite layers in mafic-ultramafic intrusions and feldspar deposits.
metamorphic	A mineral deposit formed or modified by the processes of metamorphism. This includes deposits created by metamorphic fluids (e.g., some gold deposits), deposits formed by recrystallisation and upgrading of pre-existing mineral concentrations (e.g., marble from limestone), and metamorphosed deposits where original ores are deformed and recrystallised.
MVT	(Mississippi Valley-Type - An epigenetic, stratabound lead-zinc deposit hosted in carbonate rocks (limestone, dolomite), typically on the margins of sedimentary basins. They are formed by the large-scale movement of basinal brines, are not associated with igneous activity, and have a simple sulfide mineralogy (sphalerite, galena, pyrite)
oolitic ironstone	A sedimentary iron deposit composed of small, spherical to sub-spherical concretions (ooids) of iron-rich minerals, typically hematite, chamosite, or siderite. They form in shallow marine environments under specific geochemical conditions and can constitute an important iron ore resource.
paleoplacer	A fossil (ancient) placer deposit, formed by the concentration of heavy, resistant minerals by flowing water or wind in a past geological environment and subsequently buried and lithified.
pegmatite	An exceptionally coarse-grained igneous rock, typically of granitic composition, formed from volatile-rich, highly fractionated melts in the final stages of magma crystallisation. They can host economic concentrations of rare elements, including lithium, caesium, beryllium, tantalum, niobium, tin, and industrial minerals such as feldspar and mica.
placer	A surficial mineral deposit formed by the mechanical concentration of heavy, durable minerals (e.g., gold, cassiterite, rutile, hematite) from weathered source rocks by the action of flowing water (alluvial) or waves (beach).
porphyry	A large-tonnage, low-grade deposit associated with porphyritic intrusions in magmatic arcs. Mineralisation occurs as disseminated sulfides and in stockwork veinlets within and around the intrusion, typically containing copper, molybdenum, and gold as primary commodities.

sedex	Sedimentary Exhalative - A stratiform lead-zinc deposit formed on the seafloor by the venting of metal-rich hydrothermal fluids into marine basins, contemporaneous with sedimentation. Ores occur as laminated sulfides interbedded with sedimentary rocks like chert, shale, or carbonate.
sedimentary	A general term for mineral deposits formed by sedimentary processes, including chemical precipitation (e.g., evaporites, iron formations), mechanical accumulation (e.g., placers, oolitic ironstones), and biogenic accumulation (e.g., diatomite, phosphate deposits).
sedimentary manganese deposit	A manganese deposit formed in marine or lacustrine sedimentary environments. Manganese oxides or carbonates accumulate through direct precipitation from seawater, diagenetic remobilisation, or hydrothermal exhalative activity, often forming stratiform or stratabound bodies within clastic or chemical sedimentary sequences.
skarn	A deposit formed by the metasomatisation of reactive rocks (limestone, dolomite) by hydrothermal fluids associated with a nearby igneous intrusion. Characterised by a calc-silicate gangue mineralogy (e.g., garnet, pyroxene, epidote) and can contain economic concentrations of copper, iron, zinc, lead.
volcanic deposit	A general term for mineral deposits directly related to volcanic processes. This includes epithermal deposits in volcanic host rocks, massive sulfide deposits formed on the seafloor associated with submarine volcanism (VMS), and deposits within volcaniclastic sequences.

commodities and csrm

COMMODITIES		
Commodity	Geological occurrence	Primary uses
C-SRM		
aluminium-bauxite	Forms from intense tropical weathering of aluminosilicate rocks (lateritization). Bauxite is a residual deposit composed of gibbsite, boehmite, and diaspore	Primary ore for aluminum metal production (used in transport, packaging, construction). Also used in abrasives and refractories.
antimony	The principal ore mineral is stibnite, found in hydrothermal quartz veins and replacement deposits. Often associated with arsenic, gold, and mercury.	Primarily used as a flame retardant synergist in plastics, textiles, and electronics. Also used in lead-acid batteries, alloys, and as a hardener for ammunition.
arsenic	Primary arsenic minerals (arsenopyrite, realgar, orpiment) occur in hydrothermal vein and replacement deposits	Primarily used in electronics (gallium-arsenide semiconductors) and as an alloying agent
barite	Forms in a range of settings, including sedimentary beds, hydrothermal veins, and as a gangue mineral in many ore deposits. Often associated with base metals and fluorite.	Used primarily as a weighting agent in drilling fluids for oil and gas exploration. Also used in medical applications, paint, and plastics
bismuth	Bismuth minerals (native bismuth, bismuthinite) occur in hydrothermal vein and skarn deposits.	Used in pharmaceuticals, low-melting-point alloys (fire detection/suppression).

cobalt	Primarily a byproduct of copper and nickel mining. Found in sediment-hosted copper deposits (DRC), magmatic nickel-copper sulfides, and lateritic nickel deposits.	Critical for rechargeable batteries (Li-ion cathodes), superalloys (jet engines), catalysts, and magnetic recording media.
copper	Occurs in porphyry deposits (low-grade, disseminated), sediment-hosted stratiform deposits, volcanogenic massive sulfides (VMS), and hydrothermal veins. Primary ore minerals include chalcopyrite, bornite, and chalcocite.	Essential for electrical wiring, electronics, plumbing, and construction. Used extensively in renewable energy systems (EVs, wind turbines) and industrial machinery.
feldspar	Mined from granitic pegmatites, albitites, and weathered feldspar-rich sands and rocks	Used extensively in glassmaking (as a flux and alumina source) and in ceramics (porcelain, pottery, tile). Also used in paints, plastics, and rubber
fluorite	Occurs as hydrothermal veins, as a gangue mineral in many ore deposits, and in sedimentary rocks as bedded replacements. Often associated with barite, galena, and sphalerite.	Used as a flux in steelmaking, in aluminium production, and to manufacture hydrofluoric acid (for refrigerants and Teflon). Also used in optics and as a gemstone.
germanium	A trace element recovered as a byproduct of zinc smelting (from sphalerite) and from coal fly ash. Also occurs in some silver and copper deposits.	Used in fibre optics, infrared optics (night vision), solar cells, and as a semiconductor in electronics. Vital for high-efficiency multi-junction solar panels
lithium	Occurs in three main deposit types: 1) Lithium-rich brines in salt flats (salars), 2) pegmatites (like the only occurrence in Sardinia), and 3) Lithium-bearing clays.	Required for rechargeable batteries (EVs, electronics), ceramics, glass, and lubricants
LREE	Primarily mined from carbonatites and alkaline igneous rocks (bastnäsite, monazite).	Light Rare Earth Elements (La, Ce, Pr, Nd) are used in catalysts, permanent magnets (NdFeB), glass polishing, and battery alloys. Critical for EV motors and wind turbines.
manganese	Found in sedimentary deposits (often as marine nodules or crusts), residual accumulations from weathering, and metamorphosed manganese formations. Key ore minerals include pyrolusite, psilomelane, and rhodochrosite.	Critical for steel production (removes impurities and adds hardness). Also used in dry-cell batteries, aluminium alloys, and as a pigment.

nickel	Mined from two main deposit types: 1) Magmatic sulfide deposits (pentlandite, pyrrhotite) associated with mafic-ultramafic intrusions, and 2) Lateritic deposits formed by weathering of ultramafic rocks	Essential for stainless steel production, superalloys, and rechargeable batteries (Ni-Cd). Also used in coinage and plating
niobium	Primarily found in granite-related mineralisations, often associated with pyrochlore.	Used as an alloying agent to strengthen steel for pipelines, jet engines, and aerospace components.
titanium	Mined from anorthosite/gabbro deposits (ilmenite, rutile) and heavy-mineral sand placers (ilmenite, rutile, leucoxene)	Two main uses: 1) Titanium dioxide pigment (paints, paper, plastics). 2) Lightweight, strong metal alloys for aerospace, medical implants, and sporting goods
tungsten	Primarily sourced from intrusion-related deposits, forming wolframite and scheelite. Skarn deposits are also significant.	Used in cemented carbides (wear-resistant tools), light bulb filaments, and high-temperature alloys due to its extremely high melting point
vanadium	Mined as a byproduct from magnetite ores in layered mafic-ultramafic intrusions, from vanadium-bearing clays, and from uranium-vanadium deposits in sandstones.	Used as a steel alloying agent (high-strength low-alloy steel) and in titanium alloys for aerospace. Vanadium redox batteries are emerging for grid-scale energy storage.
ORE MINERALS		
gold	Occurs in hydrothermal veins deposited by ascending solutions, as disseminated particles in some sulfide deposits, and in placer deposits as native metal.	Used in jewellery, coinage, and as a financial store. Essential in electronics (circuit boards, connectors), medical devices, and aerospace due to its conductivity and corrosion resistance
iron	Found in a variety of rock types, with enrichment in ultramafic and mafic igneous rocks (IOCG) and banded iron formations (BIF). Secondary Fe oxides (hematite, goethite) form through weathering.	The primary raw material for steel manufacturing is used in construction, transportation, machinery, and tools.
lead	The most important ore mineral is galena, followed by anglesite and cerussite. Lead and zinc minerals often occur together in MVT, SEDEX, hydrothermal veins, skarn, etc.	Over 80% is used in lead-acid batteries (automotive, industrial). Also used in radiation shielding and alloys
mercury	The principal ore mineral is cinnabar (HgS), deposited by hydrothermal solutions in fractured rocks. Often found in areas of recent volcanic activity and hot springs	Has important uses in the chemical and electrical industries, and in dental applications, though its use has declined due to toxicity

molybdenum	Ore deposits are typically related to felsic intrusions (granitic rocks). Molybdenum occurs mainly as molybdenite (MoS_2) in sulfide deposits, often associated with copper, tungsten and tin	Primarily used in steel alloys to increase strength, hardness, and corrosion resistance (used in engines, drills, saw blades).
phosphorus	Sedimentary phosphorite deposits account for ~75% of resources, formed from phosphorus-rich seawater, upwellings, and biological remains. Also occurs in igneous (apatite) and residual deposits.	Critical for fertilisers and pesticides in agriculture. Emerging uses include new energy batteries and the electronic information industry (lithium iron phosphate batteries)
silver	Occurs as a native element, in silver minerals (acanthite, proustite) in hydrothermal deposits. Most production today is a byproduct of copper, lead, and zinc mining.	Used in electronics (highest electrical conductivity), jewellery, tableware, coins, and photographic films. Also essential in solar panels, batteries, and brazing alloys
talc	Forms by hydrothermal alteration (steatitization) of ultramafic igneous rocks (serpentinites, peridotites) and magnesium-rich carbonates. Often associated with serpentine.	Used in ceramics (electrical insulators), paint, paper, plastics, rubber, and cosmetics. Massive talc (steatite) is used for specialised industrial and electrical applications.
tantalium	Found in pegmatites and carbonatites, often with niobium in similar geologic environments.	Essential for tantalum capacitors in electronics (computers, communications, aerospace systems). Used in superalloys for jet engines and in metal-cutting tools as tantalum carbide
tellurium	Mostly recovered as a byproduct from copper and gold ores (especially from porphyry copper deposits).	Used in metallurgy (steel and copper alloys to improve machinability), as a catalyst in petroleum refining, in glass colouring, and in thermoelectric materials (bismuth telluride) for cooling devices
thorium	Occurs primarily in monazite (a rare-earth phosphate) in placer deposits and carbonatites. Also found in thorite and thorianite in pegmatites and vein deposits.	Used in gas mantles for portable lighting, in high-quality optics, and as a potential nuclear fuel in molten-salt reactors. Also used in tungsten alloys for welding electrodes.
tin	Principal ore is cassiterite (SnO_2), found in hydrothermal veins, greisens, and skarns associated with granitic intrusions.	Used as a corrosion-resistant coating for steel (tinplate), in solders for electronics, in alloys (bronze, pewter), and in chemical compounds (flame retardants, PVC stabilisers).

uranium	Occurs in a variety of deposit types: unconformity-related, sandstone-hosted (roll-front), quartz-pebble conglomerates, and vein-type deposits. Principal ores include uraninite and pitchblende.	Primary use is as fuel for nuclear power generation. Also used in medical isotopes, military applications, and as ballast in aerospace and marine applications.
zinc	Principal ore is sphalerite (ZnS), typically found in sedimentary-exhalative (SEDEX), Mississippi Valley-Type (MVT), and volcanogenic massive sulfide (VMS) deposits, often associated with lead.	Used primarily for galvanising steel to prevent corrosion. Also in die-casting alloys, brass production, and as zinc oxide in rubber, paints, and pharmaceuticals.
INDUSTRIAL MINERALS		
bentonite	Formed by alteration of volcanic ash (glass) in situ. Composed mainly of smectite-group clay minerals (montmorillonite). Occurs in beds of altered pyroclastic material.	Used in drilling fluids (oil and gas wells), as a binding agent in foundry sands and pelletizing iron ore, and as an absorbent in cat litter, cosmetics, and pharmaceuticals.
clay	Formed by weathering and hydrothermal alteration of aluminosilicate minerals. Occurs as sedimentary deposits, residual weathering profiles, and hydrothermal alteration zones.	Used in ceramics (bricks, tiles, pottery), paper coating and filling, refractories, cement manufacturing, and as a geotechnical barrier in landfills.
coal	Occurs as sedimentary beds (seams) in coal-bearing basins.	Primary fuel for electricity generation. Also used in steel production (coke), cement manufacturing, and as a source of industrial heat. Coal byproducts are used in chemicals and activated carbon.
kaolinite	Formed by hydrothermal alteration or intense tropical weathering (kaolinization) of feldspar-rich rocks (granites, pegmatites).	Used in paper coating, ceramics (porcelain), paint, rubber, plastics, and as a filler in various products. Cosmetic and pharmaceutical applications.
mica	Occurs in pegmatites, granites, and metamorphic rocks (schists, gneisses). Muscovite and phlogopite are the economically important varieties.	Used as an electrical insulator in electronics, as a filler and extender in paints and plastics, in drywall joint compound, and as a decorative pigment in cosmetics and automotive paints.
perlite	A volcanic glass (rhyolitic composition) that expands (pops) when heated rapidly. Occurs in lava flows and domes of felsic volcanic rocks.	Used in construction (lightweight concrete, plaster, insulation), horticulture (soil amendment for aeration), and as a filter aid in food and pharmaceutical industries.

pyrite	Occurring in virtually all geological environments: igneous, sedimentary, and metamorphic rocks. Forms in hydrothermal veins, as disseminations, and in sedimentary pyrite beds.	mainly used as a source of sulfur in the chemical industry, and sometimes as a byproduct for gold recovery (as gold is often associated with pyrite). Also used in jewelry (marcasite).
quartz	High-purity deposits occur in pegmatites, hydrothermal veins, and as siliceous sedimentary rocks (quartzite, sandstone).	Used in electronics (oscillators, frequency controls), optics (lenses, prisms), glassmaking, abrasives, and as a flux in metallurgy. High-purity quartz is critical for semiconductor and solar industries.

minerals

PRIMARY MINERALS			
Mineral	**Formula**	**Class**	**Category**
bastnaesite	$(Ce,La)CO_3F$	carbonate	P
ree carbonates	$(REE)CO_3$	carbonate	p
synchysite	$Ca(REE)(CO_3)_2F$	carbonate	p
witherite	$BaCO_3$	carbonate	P
bismuth	Bi	native element	P
gold	Au	native element	p
silver	Ag	native element	p
electrum	(Au,Ag)	native element (alloy)	P
cassiterite	SnO_2	oxide	P
cerianite	$(Ce,Th)O_2$	oxide	p
columbite-tantalite	$(Fe,Mn)(Nb,Ta)_2O_6$	oxide	p

PRIMARY/SECONDARY MINERALS			
Mineral	**Formula**	**Class**	**Category**
siderite	$FeCO_3$	carbonate	P/S
fluorite	CaF_2	halide	P/S
hematite	Fe_2O_3	oxide	P/S
iron oxides	Fe_2O_3, Fe_3O_4, etc.	oxide	P/S
rutile	TiO_2	oxide	P/S
epidote	$Ca_2(Al,Fe)_3(SiO_4)_3(OH)$	silicate (epidote)	P/S
quartz	SiO_2	silicate (tecto)	P/S
barite	$BaSO_4$	sulfate	P/S
pyrite	FeS_2	sulfide	P/S
agardite-(ce)	$(Ce,Ca)Cu_6(AsO_4)_3(OH)_6 \cdot 3H_2O$	arsenate	S
mimetite	$Pb_5(AsO_4)_3Cl$	arsenate	S

magnetite	Fe_3O_4	oxide	P
pitchblende	UO_2 (with U_3O_8)	oxide	P
uraninite	UO_2	oxide	p
uranium oxides	UO_2, U_3O_8, etc.	oxide	p
apatite	$Ca_5(PO_4)_3(F,Cl,OH)$	phosphate	P
monazite	$(Ce,La,Nd,Th)PO_4$	phosphate	P
xenotime	YPO_4	phosphate	p
allanite	$(Ce,Ca,Y)_2(Al,Fe^{3+})_3(SiO_4)_3(OH)$	silicate (epidote)	p
albite	$NaAlSi_3O_8$	silicate (feldspar)	P
feldspar	$(K,Na,Ca)AlSi_3O_8$	silicate (feldspar)	P
microcline	$KAlSi_3O_8$	silicate (feldspar)	p
mica	$KAl_2(AlSi_3O_{10})(OH)_2$	silicate (mica)	p
elbaite	$Na(Li,Al)_3Al_6(BO_3)_3Si_6O_{18}(OH)_4$	silicate (tourmaline)	P
perlite	volcanic glass	silicate (volcanic)	P
argentite	Ag_2S	sulfide	p
bismuthinite	Bi_2S_3	sulfide	p
bornite	Cu_5FeS_4	sulfide	P
chalcopyrite	$CuFeS_2$	sulfide	P
galena	PbS	sulfide	p

azurite	$Cu_3(CO_3)_2(OH)_2$	carbonate	S
cerussite	$PbCO_3$	carbonate	S
copper carbonates	-	carbonate	S
malachite	$Cu_2CO_3(OH)_2$	carbonate	S
smithsonite	$ZnCO_3$	carbonate	S
illite	$(K,H_3O)(Al,Mg,Fe)_2(Si,Al)_4O_{10}[(OH)_2,(H_2O)]$	clay	S
kaolinite	$Al_2Si_2O_5(OH)_4$	clay	S
bentonite	$Al_2O_3\cdot 4SiO_2\cdot H_2O$	clay (altered volcanic)	S
anatase	TiO_2	oxide	S
copper oxides	-	oxide	S
psilomelane	$(Ba,H_2O)_2Mn_5O_{10}$	oxide	S
pyrolusite	MnO_2	oxide	S
senarmontite	Sb_2O_3	oxide	S
valentinite	Sb_2O_3	oxide	S
gummite	$UO_3\cdot nH_2O$	oxide (uranium)	S
limonite	$FeO(OH)\cdot nH_2O$	oxide/hydroxide	S
autunite	$Ca(UO_2)_2(PO_4)_2\cdot 10\text{-}12H_2O$	phosphate	S
metatorbernite	$Cu(UO_2)_2(PO_4)_2\cdot 8H_2O$	phosphate	S
torbernite	$Cu(UO_2)_2(PO_4)_2\cdot 12H_2O$	phosphate	S

molybdenite	MoS_2	sulfide	p
pyrrhotite	$Fe_{1-x}S$	sulfide	P
sphalerite	ZnS	sulfide	P
stannite	Cu_2FeSnS_4	sulfide	p
stibnite	Sb_2S_3	sulfide	p
arsenopyrite	FeAsS	sulfosalt	P
bournonite	$PbCuSbS_3$	sulfosalt	P
cobaltite	CoAsS	sulfosalt	p
enargite	Cu_3AsS_4	sulfosalt	p
fahlore	$(Cu,Ag)_{10}(Fe,Zn)_2(As,Sb)_4S_{13}$	sulfosalt	P
proustite	Ag_3AsS_3	sulfosalt	P
stephanite	Ag_5SbS_4	sulfosalt	p
tetrahedrite	$(Cu,Fe)_{12}Sb_4S_{13}$	sulfosalt	p
ullmannite	NiSbS	sulfosalt	P
ni-co-bi arsenides and sulfoarsenides	(Ni,Co,Fe)AsS	sulfosalt/arsenide	P
tellurides	$(Au,Ag)Te_2$	telluride	p
scheelite	$CaWO_4$	tungstate	p
wolframite	$(Fe,Mn)WO_4$	tungstate	P

uranophane	$Ca(UO_2)_2(SiO_3OH)_2 \cdot 5H_2O$	silicate	S
chamosite	$(Fe,Mg)_5Al(AlSi_3O_{10})(OH)_8$	silicate (chlorite)	S
talc	$Mg_3Si_4O_{10}(OH)_2$	silicate (phyilo)	S
chrysocolla	$Cu_2H_2Si_2O_5(OH)_4$	silicate (phylo)	S
hemimorphite	$Zn_4Si_2O_7(OH)_2 \cdot H_2O$	silicate (sorosilicate)	S
chalcocite	Cu_2S	sulfide	S
covellite	CuS	sulfide	S
stolzite	$PbWO_4$	tungstate	S

morphology

MORPHOLOGY	***DESCRIPTION***
cluster	a group of closely spaced individual features (e.,g., crystals, aggregates.
columnar	a ore-rock or mineral aggregate that is elongated in one direction, like a pillar.
disseminated	individual crystals or grains of a mineral (such as a sulfide ore) are scattered sparsely throughout the mass of a host rock.

lentiform	a body of rock or mineral that is thick in the middle and thins out towards the edges, resembling a convex lens in cross-section.
stratabound	a mineral deposit that is confined to a specific single unit or layer of rock (a stratum). The ore body may not necessarily be perfectly parallel to the bedding; it can be irregular or even cut across the layering, but it is still restricted to that particular stratigraphic unit, which give the morphological feature to the mineralised body.
stratiform	a type of "stratabound" where the mineralisation is exactly parallel to the bedding planes of the host rock, forming a layer that is concordant with the surrounding strata.
tabular	a mineralisation that is flat and table-shaped, with a broad, plate-like form.

texture

TEXTURE	***DESCRIPTION***
banded	a rock consisting of alternating, thin layers (typically 1 mm to multiple cm) of more than one mineral differing in compositions and/or generations.
brecciated	a rock composed of angular fragments (clasts) cemented together in a finer-grained matrix. Breccias form through brittle deformation, typically in fault zones. The clasts are generally angular to subrounded (chemical corrosion), variable in grain size, and derived from the local bedrock and/ore previous mineralisation.
disseminated	a texture where individual crystals or ore assemblages are scattered sparsely throughout the mass of a host rock.
massive	unlayered deposits consisting of material that appears homogeneous in texture. Massive texture lacks internal structure or preferred mineral orientation.
nodular	rounded aggregates (nodules) set in a contrasting matrix. Nodules typically occur as spherical to ovoidal aggregates ranging from less than 1 cm to several dm in diameter. Larger nodules may form through physical agglomeration of smaller nodules. This texture typically develops through disequilibrium crystallization processes, often in response to elevated degrees of undercooling.
stockwork	a network of veinlets that intersect in all directions. The mineral cementing the veinlets is also commonly disseminated in the host rock surrounding the stockwork. At the deposit scale, stockworks can involve millions of tons of rock. Fragments within stockwork breccias may be cemented by quartz or calcite, but fluorite as well. This texture is diagnostic of feeder zones in many hydrothermal ore systems.
stratified	the arrangement of layers in a sequence, describing the vertical and lateral stacking patterns of beds.

genesis

PROCESS	**DESCRIPTION**
INTRUSION RELATED	
intrusive igneous	Mineralisation related to subsurface magma crystallization, including cumulate deposits, pegmatites, and intrusion-related hydrothermal systems.
effusive igneous	Mineralisation associated with erupted volcanic rocks, including lava-hosted deposits and exhalative systems.
volcanoclastic	MineraliSation within fragmented volcanic materials deposited by pyroclastic or epiclastic processes.

HYDROTHERMAL PROCESSES	
hydrothermal	Mineral precipitation from circulating hot aqueous fluids in fractures and pore spaces.
epithermal	Shallow, low-temperature hydrothermal mineralization typically in volcanic settings.
metasomatic and hydrothermal	Hydrothermal alteration involving chemical replacement of original minerals.
SURFACE-RELATED PROCESSES	
sedimentary	Mineral formation through surface depositional mechanisms.
residual	In-place accumulation of insoluble minerals by chemical weathering.
supergene alteration	Secondary enrichment of deposits by near-surface weathering.
karstic	Mineral accumulation in dissolution cavities of soluble rocks.
METAMORPHIC PROCESSES	
metamorphic	Deposit formation or modification by recrystallization and fluid flow under metamorphic conditions.

host

LITHOLOGY	
IGNEOUS ROCKS - INTRUSIVE (PLUTONIC)	
aplite	Fine-grained granitic intrusive, quartz and K-feldspar
diorite	Intermediate intrusive, plagioclase and hornblende dominant
dolerite	Medium-grained mafic intrusive, shallow-level
gabbro	Mafic intrusive, Ca-plagioclase and pyroxene
granite	Coarse-grained, felsic intrusive rock with quartz, K-feldspar, plagioclase
granodiorite	Intermediate intrusive, plagioclase > K-feldspar, quartz-bearing
pegmatite	Exceptionally coarse-grained, volatile-rich igneous rock
tonalite	Quartz-plagioclase intrusive with minimal K-feldspar
IGNEOUS ROCKS - EXTRUSIVE (VOLCANIC)	
andesite	Intermediate volcanic, plagioclase and hornblende/biotite/pyroxene
dacite	Intermediate-felsic volcanic, plagioclase and quartz
phonolite	Silica-undersaturated volcanic with feldspathoids
porphyry	Texture with phenocrysts in finer matrix; also deposit type
rhyolite	Felsic volcanic, quartz and K-feldspar, fine-grained
trachyte	Alkaline volcanic, K-feldspar dominant
volcanic rock	Generic effusive rock
METAMORPHIC ROCKS	
gneiss	High-grade, compositional banding
greisen	Altered granite mainly made of quartz and muscovite
marble	Metamorphosed carbonate rock
metamorphic rock	Generic methamorphosed rock
migmatite	High-grade, mixed metamorphic and melt components
mylonite	Ductile shear zone rock, grain size reduction
phyllite	Low- to medium-grade, silky sheen on foliation
quartzite	Metamorphosed quartz-rich sandstone
schist	Medium- to high-grade, visible platy minerals, well-foliated

SEDIMENTARY ROCKS - CLASTIC	
argillite	Slightly metamorphosed mudstone/shale
breccia	Consolidated angular fragments >2 mm
clastic sediment	Unconsolidated fragmental material
conglomerate	Consolidated rounded fragments >2 mm
organic argillite	Mudstone/shale rich in carbonaceous material
sandstone	Consolidated sand-sized grains
siltstone	Consolidated silt-sized grains
SEDIMENTARY ROCKS - CHEMICAL/BIOCHEMICAL	
limestone	Carbonate rock, calcite dominant
marl	Calcareous mudstone, clay and carbonate
dolomite	Carbonate rock, dolomite dominant
VOLCANICLASTIC ROCKS	
pyroclastic rock	Consolidated volcanic ejecta
tuffite	Mixed pyroclastic and sedimentary material

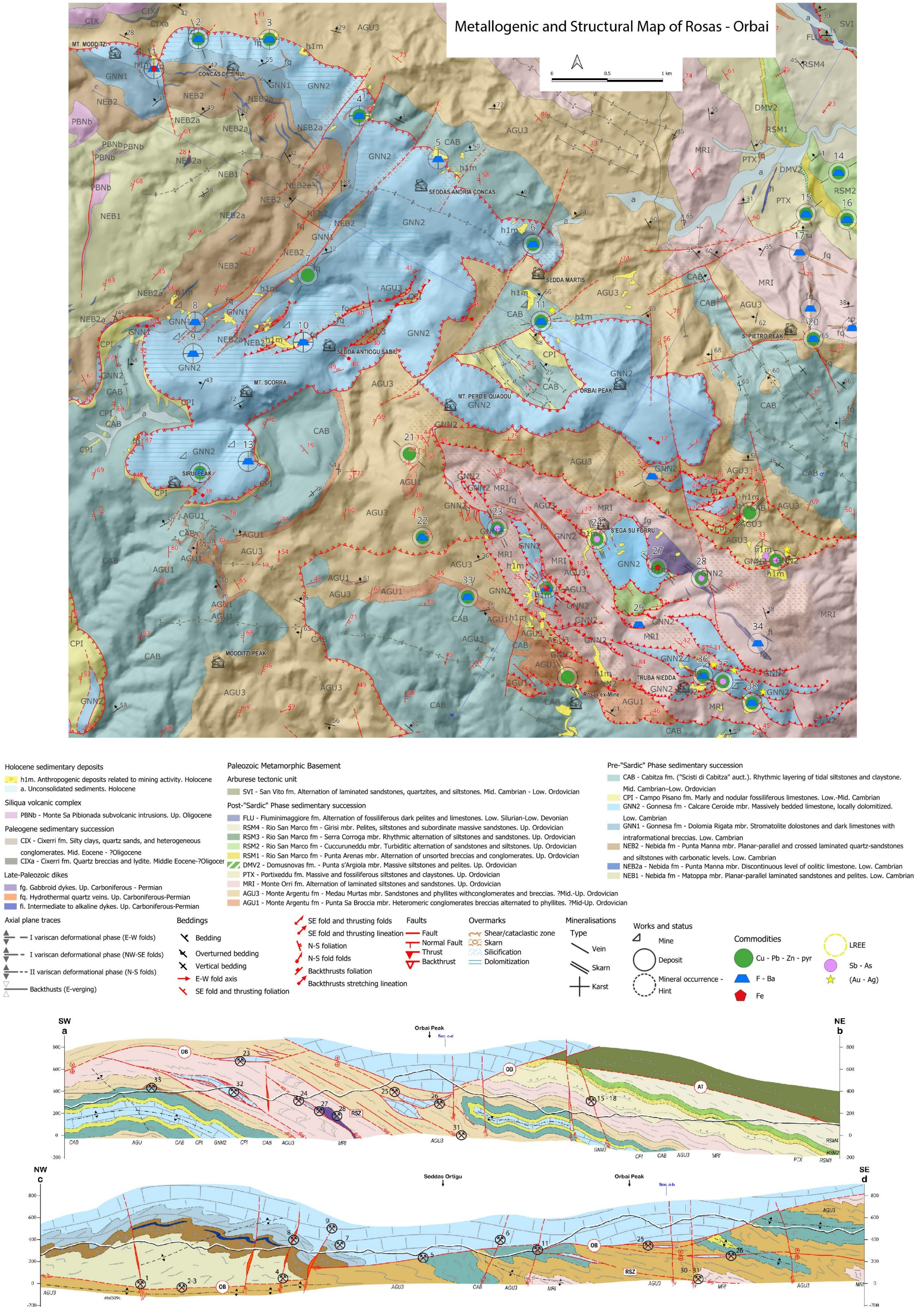
Metallogenic and Structural Map of Rosas - Orbai
Holocene sedimentary deposits
h1m. Anthropogenic deposits related to mining activity. Holocene
a. Unconsolidated sediments. Holocene
Siliqua volcanic complex
PBNb - Monte Sa Pibionada subvolcanic intrusions. Up. Oligocene
Paleogene sedimentary succession
CIX - Cixerri fm. Silty clays, quartz sands, and heterogeneous conglomerates. Mid. Eocene - ?Oligocene
CIXa - Cixerri fm. Quartz breccias and lydite. Middle Eocene-?Oligocene
Late-Paleozoic dikes
fg. Gabbroid dykes. Up. Carboniferous - Permian
fq. Hydrothermal quartz veins. Up. Carboniferous-Permian
fi. Intermediate to alkaline dykes. Up. Carboniferous-Permian
Paleozoic Metamorphic Basement
Arburese tectonic unit
SVI - San Vito fm. Alternation of laminated sandstones, quartzites, and siltstones. Mid. Cambrian - Low. Ordovician
Post-"Sardic" Phase sedimentary succession
FLU - Fluminimaggiore fm. Alternation of fossiliferous dark pelites and limestones. Low. Silurian-Low. Devonian
RSM4 - Rio San Marco fm - Girisi mbr. Pelites, siltstones and subordinate massive sandstones. Up. Ordovician
RSM3 - Rio San Marco fm - Serra Corroga mbr. Rhythmic alternation of siltstones and sandstones. Up. Ordovician
RSM2 - Rio San Marco fm - Cuccuruneddu mbr. Turbiditic alternation of sandstones and siltstones. Up. Ordovician
RSM1 - Rio San Marco fm - Punta Arenas mbr. Alternation of unsorted breccias and conglomerates. Up. Ordovician
DMV2 - Domusnovas fm. - Punta s'Argiola mbr. Massive siltstones and pelites. Up. Ordovician
PTX - Portixeddu fm. Massive and fossiliferous siltstones and claystones. Up. Ordovician
MRI - Monte Orri fm. Alternation of laminated siltstones and sandstones. Up. Ordovician
AGU3 - Monte Argentu fm - Medau Murtas mbr. Sandstones and phyllites withconglomerates and breccias. ?Mid.-Up. Ordovician
AGU1 - Monte Argentu fm - Punta Sa Broccia mbr. Heteromeric conglomerates breccias alternated to phyllites. ?Mid-Up. Ordovician
Pre-"Sardic" Phase sedimentary succession
CAB - Cabitza fm. ("Scisti di Cabitza" auct.). Rhythmic layering of tidal siltstones and claystone. Mid. Cambrian–Low. Ordovician
CPI - Campo Pisano fm. Marly and nodular fossiliferous limestones. Low.-Mid. Cambrian
GNN2 - Gonnesa fm - Calcare Ceroide mbr. Massively bedded limestone, locally dolomitized. Low. Cambrian
GNN1 - Gonnesa fm - Dolomia Rigata mbr. Stromatolite dolostones and dark limestones with intraformational breccias. Low. Cambrian
NEB2 - Nebida fm - Punta Manna mbr. Planar-parallel and crossed laminated quartz-sandstones and siltstones with carbonatic levels. Low. Cambrian
NEB2a - Nebida fm - Punta Manna mbr. Discontinuous level of oolitic limestone. Low. Cambrian
NEB1 - Nebida fm - Matoppa mbr. Planar-parallel laminated sandstones and pelites. Low. Cambrian
Axial plane traces
I variscan deformational phase (E-W folds)
I variscan deformational phase (NW-SE folds)
II variscan deformational phase (N-S folds)
Backthusts (E-verging)
Beddings
Bedding
Overturned bedding
Vertical bedding
E-W fold axis
SE fold and thrusting foliation
SE fold and thrusting folds
SE fold and thrusting lineation
N-S foliation
N-S fold folds
Backthrusts foliation
Backthrusts stretching lineation
Faults
Fault
Normal Fault
Thrust
Backthrust
Overmarks
Shear/cataclastic zone
Skarn
Silicification
Dolomitization
Mineralisations
Type
Vein
Skarn
Karst
Works and status
Mine
Deposit
Mineral occurrence - Hint
Commodities
Cu - Pb - Zn - pyr
F - Ba
Fe
LREE
Sb - As
(Au - Ag)
SW a
Orbai Peak
NE b
NW c
Seddas Ortigu
Orbai Peak
SE d

The Metallogenic Map of Sardinia

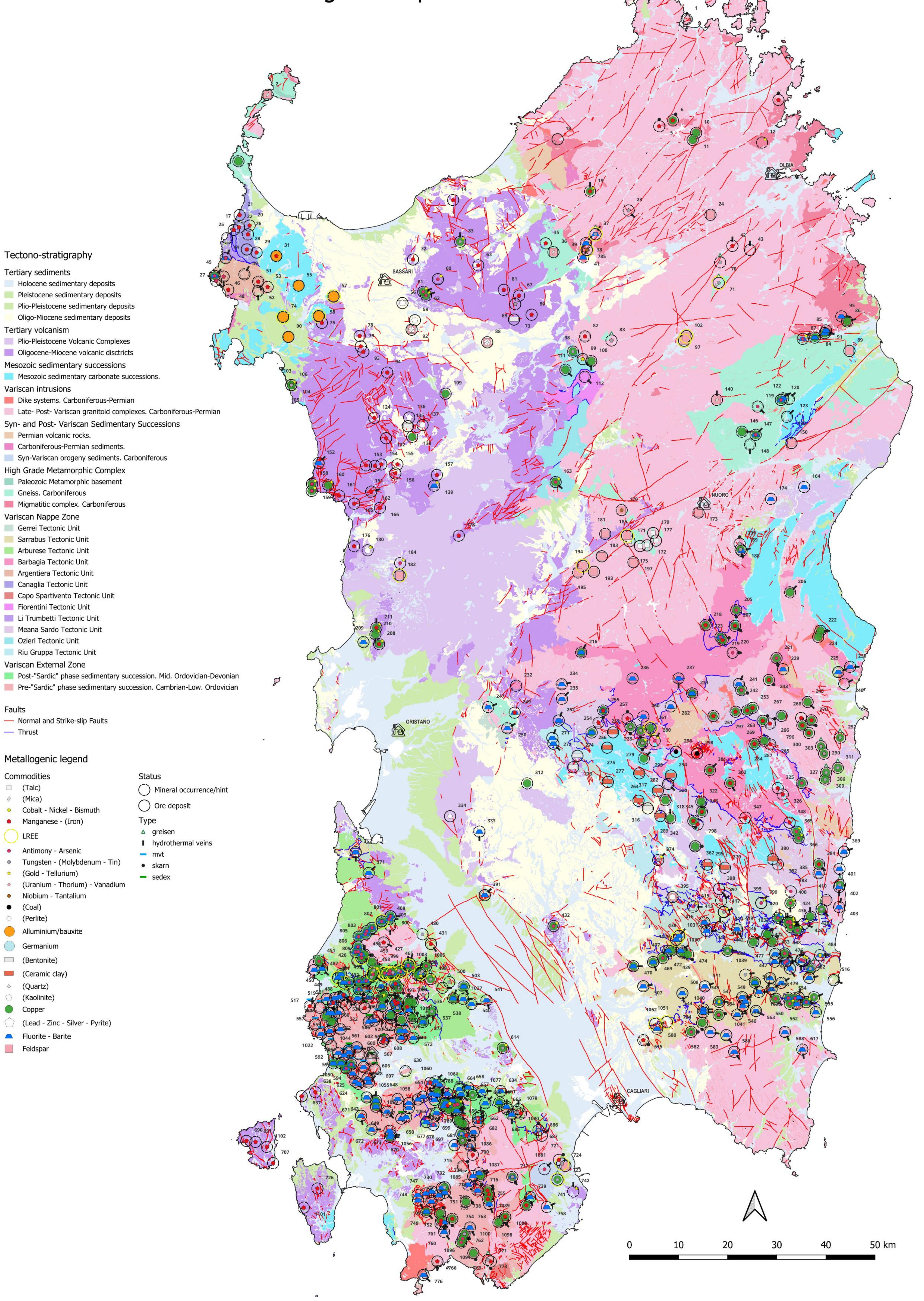

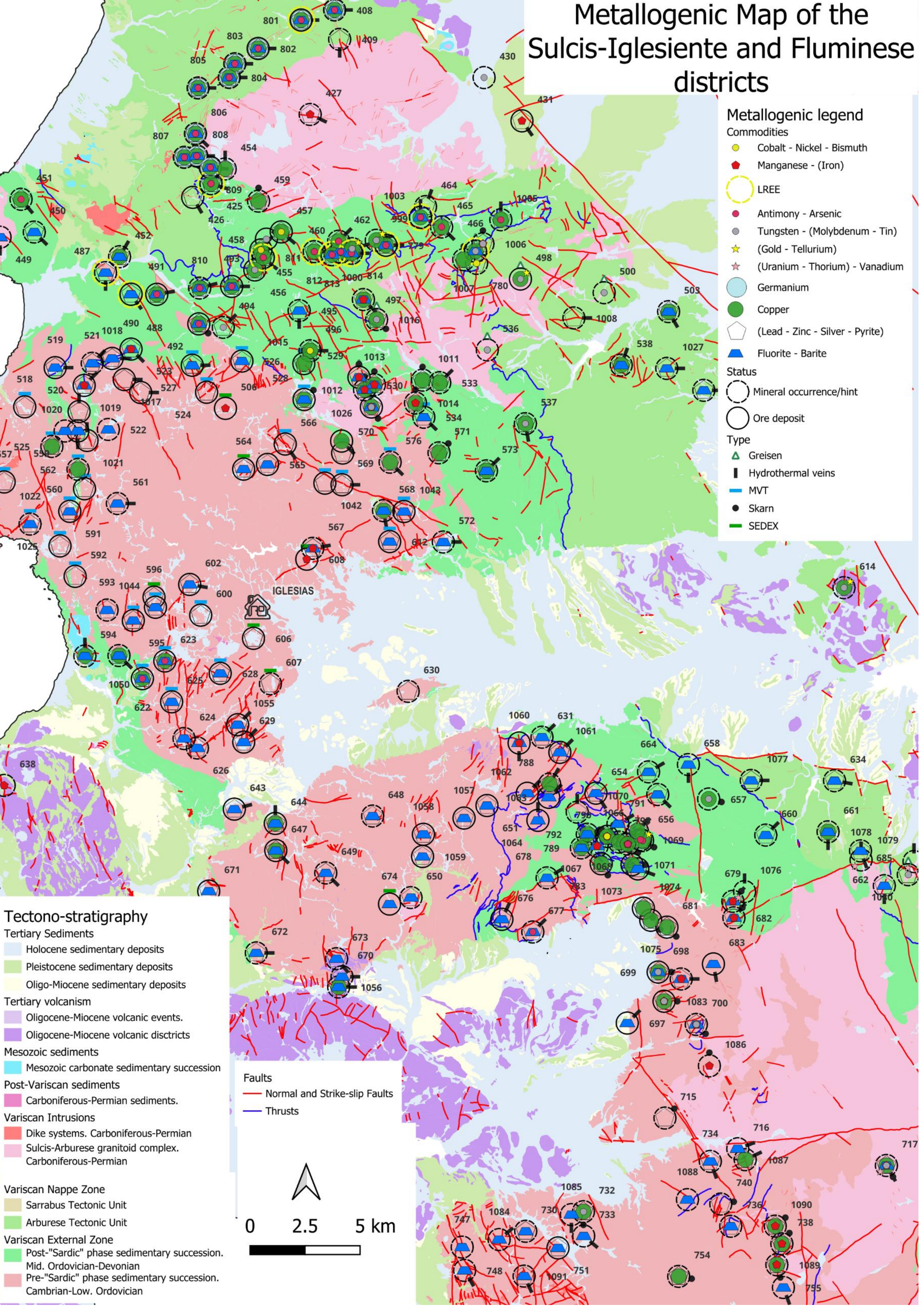
Metallogenic Map of the Sulcis-Iglesiente and Fluminese districts
Metallogenic legend
Commodities
Cobalt - Nickel - Bismuth
Manganese - (Iron)
LREE
Antimony - Arsenic
Tungsten - (Molybdenum - Tin)
(Gold - Tellurium)
(Uranium - Thorium) - Vanadium
Germanium
Copper
(Lead - Zinc - Silver - Pyrite)
Fluorite - Barite
Status
Mineral occurrence/hint
Ore deposit
Type
Greisen
Hydrothermal veins
MVT
Skarn
SEDEX
IGLESIAS
Tectono-stratigraphy
Tertiary Sediments
Holocene sedimentary deposits
Pleistocene sedimentary deposits
Oligo-Miocene sedimentary deposits
Tertiary volcanism
Oligocene-Miocene volcanic events.
Oligocene-Miocene volcanic disctricts
Mesozoic sediments
Mesozoic carbonate sedimentary succession
Post-Variscan sediments
Carboniferous-Permian sediments.
Variscan Intrusions
Dike systems. Carboniferous-Permian
Sulcis-Arburese granitoid complex. Carboniferous-Permian
Variscan Nappe Zone
Sarrabus Tectonic Unit
Arburese Tectonic Unit
Variscan External Zone
Post-"Sardic" phase sedimentary succession. Mid. Ordovician-Devonian
Pre-"Sardic" phase sedimentary succession. Cambrian-Low. Ordovician
Faults
Normal and Strike-slip Faults
Thrusts
0 2.5 5 km

Bibliography

Aponte F., Balassone G., Boni M., Costamagna L., Di Maio G., 1988. Variscan Skarn Ores in South·West Sardinia: their relationships with Cambro·Ordovician stratabound deposits. Rendiconti della società italiana di mineralogia e petrologia, 43-2, 445-462.

Attardi A., Cocco F., Deidda M., Funedda A., Naitza S., 2020. Caratterizzazione giacimentologica e geologico-strutturale del settore nord dell'area mineraria di Rosas (Narcao, Sardegna SW). [Master's Thesis] University of Cagliari, Cagliari.

Bakos F. & Valera R., 1972a. Il campo filoniano di Castel Medusa (Asuni - Sardegna Centrale). Associazione Mineraria Subalpina, Atti della giornata di studio sulle fluoriti italiane, 2, 283-298.

Bakos F. & Valera R., 1972b. Le mineralizzazioni fluoritiche di Santa Lucia (Sardegna Sud - Occidentale). Associazione Mineraria Subalpina, Atti della giornata di studio sulle fluoriti italiane, 2, 299-324.

Balassone, G., Manfredi, C., Vasca, E., Bianco, M., Boni, M., Di Nunzio, A., Lombardo, F., Mozzillo, R., Marino, A., Mormone, A., Mura, G., Trifuoggi, M., Mondillo, N., 2021. Recycling REEs from the Waste Products of Silius Mine (SE Sardinia, Italy): A Preliminary Study. Sustainability 13, 14000. https://doi.org/10.3390/su132414000

Barca S., Forci A., Funedda A., 2003. Nuovi dati stratigrafico-strutturali sul flysch ercinico dell'Unità del Gerrei (Sardegna SE). In: V. Pascucci (Ed.): Geo. Sed. 2003, 291-298, Alghero

Barca, S., Cocozza, T., Del Rio, M., Demelia, P.P., 1981. Discovery of Lower Ordovician acritarchs in the "Postgotlandiano" sequence of southwestern Sardinia (Italy); age and tectonic implications. Ital. J. Geosci. 100, 377–392.

Bechstädt, T.H., Boni, M., 1994. Sedimentological, stratigraphical and ore deposits field guide of the autochthonous Cambro - Ordovician of Southwestern Sardinia. ITA.

Benz J.P., Féraud J., Save M., Tréhin J.L., 2001. Expertise technico-économique de la mine de fluorine de Silius (Sardaigne) Rapport final: évaluation des réserves au 27.6.2001 et études de rentabilité. Rapport BRGM/RC- 51042-FR

Billa, M., Cassard, D., Lips, A.L.W., Bouchot, V., Tourlière, B., Stein, G., Guillou-Frottier, L., 2004. Predicting gold-rich epithermal and porphyry systems in the central Andes with a continental-scale metallogenic GIS. Ore Geol. Rev. 25, 39–67. https://doi.org/10.1016/j.oregeorev.2004.01.002

Bonham-Carter G., 1995. Geographic information systems for geoscientists: modelling with GIS. No. 13 in computer methods in the geosciences. Pergamon Press, Elsevier, Kidlington, Oxford, UK

Boni, M., Mondillo, N., Santoro, L., Balassone, G., 2025. Vanadium and other critical elements in North Gondwana Silurian black shales: The SE Sardinia (Italy) case. J. Geochem. Explor. 275, 107760. https://doi.org/10.1016/j.gexplo.2025.107760

Boni, M., Gilg, H.A., Aversa, G., Balassone, G., 2003. The "Calamine" of Southwest Sardinia: Geology, Mineralogy, and Stable Isotope Geochemistry of Supergene Zn Mineralization. Econ. Geol. 98, 731–748. https://doi.org/10.2113/gsecongeo.98.4.731

Boni, M., Balassone, G., Fedele, L., Mondillo, N., 2009. Post-Variscan hydrothermal activity and ore deposits in southern Sardinia (Italy): selected examples from the Iglesiente district and from Gerrei (Silius vein system). https://doi.org/10.2451/2009PM0010

Boni, M., Balassone, G., Iannace, A., 1996. Base Metal Ores in the Lower Paleozoic of Southwestern Sardinia, in: Sangster, D.F., Anderson, G.M., Garven, G., Hagni, R.D., Shelton, K.L., Coveney, R.M., Jr., Gregg, J.M., Kesler, S.E. (Eds.), Carbonate-Hosted Lead-Zinc Deposits: 75th Anniversary Volume. Society of Economic Geologists, p. 0. https://doi.org/10.5382/SP.04.03

Boni, M., Iannace, A., Koeppel, V., Frueh-Green, G.L., Hansmann, W., 1992. Late to post-Hercynian hydrothermal activity and mineralization in Southwest Sardinia (Italy). Econ. Geol. 87, 2113–2137. https://doi.org/10.2113/gsecongeo.87.8.2113

Boni, M., Rankin, A.H., Salvadori, M., 1990. Fluid inclusion evidence for the development of Zn–Pb–Cu–F skarn mineralization in SW Sardinia, Italy. Mineral. Mag. 54, 279–287. https://doi.org/10.1180/minmag.1990.054.375.13

Buske, S., Bellefleur, G., and Malehmir, A., 2015, Seismic methods for deep mineral exploration: Mature technologies adapted to new targets: *Geophysical Prospecting*, v. 63, p. 457–461. https://doi.org/10.1190/1.1587683

Calvino F., 1967. Note illustrative della Carta Geologica d'Italia. F°227 "Muravera": Boll. Serv. Geol. d'It., 60 pp.

Calvino F., 1963. Carta Geologica d'Italia, Foglio 227 – Muravera. Servizio Geologico d'Italia, Roma.

Calvino F., 1959. Lineamenti strutturali del Sarrabus-Gerrei (Sardegna sud-orientale). Bollettino del Servizio Geologico d'Italia, 81, 489–556.

Carmignani, L., Carosi, R., Di Pisa, A., Gattiglio, M., Musumeci, G., Oggiano, G., Carlo Pertusati, P., 1994. The hercynian chain in Sardinia (Italy). Geodin. Acta 7, 31–47. https://doi.org/10.1080/09853111.1994.11105257

Carmignani, L., Cocozza, T., Ghezzo, C., Pertusati, P., Ricci, C.A., 1982. Guida alla geologia del Paleozoico sardo.

Carmignani, L., Conti, P., Pertusati, P., Barca, S., Cerbai, N., Eltrudis, A., Funedda, A., Oggiano, G., Patta, E.D., 2001. Note illustrative della Carta Geologica d'Italia alla scala 1:50.000 -Foglio 549 Muravera.

Carranza, 2012. Geochemical Anomaly and Mineral Prospectivity Mapping in GIS.

Carranza, E.J.M., Hale, M., 2001. Geologically Constrained Fuzzy Mapping of Gold Mineralization Potential, Baguio District, Philippines. Nat. Resour. Res. 10, 125–136. https://doi.org/10.1023/A:1011500826411

Casini, L., Cuccuru, S., Maino, M., Oggiano, G., Tiepolo, M., 2012. Emplacement of the Arzachena Pluton (Corsica–Sardinia Batholith) and the geodynamics of incoming Pangaea. Tectonophysics 544–545, 31–49. https://doi.org/10.1016/j.tecto.2012.03.028

Castorina, F., Masi, U., Gorello, I., 2020. Rare earth element and Sr-Nd isotopic evidence for the origin of fluorite from the Silius vein deposit (southeastern Sardinia, Italy). J. Geochem. Explor. 215, 106535. https://doi.org/10.1016/j.gexplo.2020.106535

Cathelineau, M., 1988. Cation site occupancy in chlorites and illites as a function of temperature. Clay Miner. 23, 471–485. https://doi.org/10.1180/claymin.1988.023.4.13

Cerny, P., Ercit, T.S., 2005. THE CLASSIFICATION OF GRANITIC PEGMATITES REVISITED. Can. Mineral. 43, 2005–2026. https://doi.org/10.2113/gscanmin.43.6.2005

Chaudhry, N., Yousaf, M.M., 2019. Spatial querying of mineral resources using PostGIS, in: 2019 2nd International Conference on Advancements in Computational Sciences (ICACS). Presented at the 2019 2nd International Conference on Advancements in Computational Sciences (ICACS), pp. 1–6. https://doi.org/10.23919/ICACS.2019.8688999

Clark, D. A., 2014. Methods for determining remanent and total magnetisations of magnetic sources – a review. *Exploration Geophysics*, *45*(4), 271–304. https://doi.org/10.1071/EG14013

Cocco, F., Attardi, A., Deidda, M.L., Fancello, D., Funedda, A., Naitza, S., 2022. Passive Structural Control on Skarn Mineralization Localization: A Case Study from the Variscan Rosas Shear Zone (SW Sardinia, Italy). Minerals 12, 272. https://doi.org/10.3390/min12020272

Cocco, F., Funedda, A., 2019. The Sardic Phase: field evidence of Ordovician tectonics in SE Sardinia, Italy. Geol. Mag. 156, 25–38. https://doi.org/10.1017/S0016756817000723

Cocco, F., Oggiano, G., Funedda, A., Loi, A., Casini, L., 2018. Stratigraphic, magmatic and structural features of Ordovician tectonics in Sardinia (Italy): a review. J. Iber. Geol. 44, 619–639. https://doi.org/10.1007/s41513-018-0075-1

Conte, A.M., Cuccuru, S., D'Antonio, M., Naitza, S., Oggiano, G., Secchi, F., Casini, L., Cifelli, F., 2017. The post-collisional late Variscan ferroan granites of southern Sardinia (Italy): Inferences for inhomogeneity of lower crust. Lithos 294, 263–282.

Conti, P., Carmignani, L., Funedda, A., 2001. Change of nappe transport direction during the Variscan collisional evolution of central-southern Sardinia (Italy). Tectonophysics 332, 255–273. https://doi.org/10.1016/S0040-1951(00)00260-2

Conti, P., Patta, E.D., 1998. Large-scale Hercynian West-directed tectonics in southeastern Sardinia (Italy). Geodin. Acta 11, 217–231. https://doi.org/10.1080/09853111.1998.11105321

Corradini C., Leone F., Loi A. & Serpagli E., 2001. Conodont stratigraphy of a highly tectonised Silurian-Devonian section in the San Basilio area (SE Sardinia, Italy). Boll. Soc. Paleont. It.: 40 (3): 315-323, Milano.

Cuccuru, S., Naitza, S., Secchi, F., Puccini, A., Casini, L., Pavanetto, P., Linnemann, U., Hofmann, M., Oggiano, G., 2016. Structural and metallogenic map of late Variscan Arbus Pluton (SW Sardinia, Italy). J. Maps 12, 860–865. https://doi.org/10.1080/17445647.2015.1091750

Debrenne, F., Gandin, A., Debrenne, M., 1993. Archaeocyath limestones from the Lower Cambrian, Matoppa member (Nebida formation) south-west Sardinia. Ann. Paleontol. 79, 77–118.

Debrenne, F., Gandin, A., Pillola, G.L., 1988. BIOSTRATIGRAPHY AND DEPOSITIONAL SETTING OF PUNTA MANNA MEMBER TYPE-SECTION (NEBIDA FORMATION, LOWER CAMBRIAN, SW SARDINA, ITALY). Riv. Ital. Paleontol. E Stratigr. 94. https://doi.org/10.54103/2039-4942/13142

Edel, J.-B., Casini, L., Oggiano, G., Rossi, P., Schulmann, K., 2014. Early Permian 90° clockwise rotation of the Maures–Estérel–Corsica–Sardinia block confirmed by new palaeomagnetic data and followed by a Triassic 60° clockwise rotation.

Fadda, S., Fiori, M., Pretti, S., Valera, P., 2017. VOLCANIC – SEDIMENTARY METAL DEPOSITION IN PALEOMARGIN ENVIRONMENT: A " PROTORE " OCCURRENCE IN CENTRAL SARDINIA (ITALY). Bull. Geol. Soc. Greece 43, 2446. https://doi.org/10.12681/bgsg.11646

Fan, Z., Xiong, S., Ge, T., He, J., Yang, X., Liu, Y., & Luo, J., 2025. Mineral prospectivity prediction from airborne magnetic data based on the RPCA-ResNet hybrid learning framework. *Journal of Asian Earth Sciences*, 292. https://doi.org/10.1016/j.jseaes.2025.106718

Fawcett, T., 2006. An introduction to ROC analysis. Pattern Recognit. Lett., ROC Analysis in Pattern Recognition 27, 861–874. https://doi.org/10.1016/j.patrec.2005.10.010

Fiori, M., Grillo, S.M., 2001. The Furtei high sulphidation epithermal gold deposit (Sardinia, Italy): mineral assemblage and its evolution, in: Mineral Deposits at the Beginning of the 21st Century. CRC Press.

Forci A., Carmignani, L., Funedda, A., Pisanu, G., Pertusati, P., Marongiu, F., Calzia, P., & Serra, M., 2012. Note Illustrative della Carta geologica d'Italia alla scala 1:50.000, F. 548 Senorbì, Servizio Geologico d'Italia - ISPRA. oar. https://doi.org/10.15161/oar.it/143449

Ford, A., Blenkinsop, T.G., 2008. Combining fractal analysis of mineral deposit clustering with weights of evidence to evaluate patterns of mineralization: Application to copper deposits of the Mount Isa Inlier, NW Queensland, Australia. Ore Geol. Rev. 33, 435–450. https://doi.org/10.1016/j.oregeorev.2007.01.004

Förster, H.-J., 1998. The chemical composition of REE-Y-Th-U-rich accessory minerals in peraluminous granites of the Erzgebirge-Fichtelgebirge region, Germany, Part I: The monazite-(Ce)-brabantite solid solution series. Am. Mineral. 83, 259–272. https://doi.org/10.2138/am-1998-3-409

Franceschelli, M., Puxeddu, M., Cruciani, G., 2005. Variscan metamorphism in Sardinia, Italy: review and discussion. J. Virtual Explor. 19. https://doi.org/10.3809/jvirtex.2005.00121

Funedda, A., 2009. Foreland- and hinterland-verging structures in fold-and-thrust belt: an example from the Variscan foreland of Sardinia. Int. J. Earth Sci. 98, 1625–1642. https://doi.org/10.1007/s00531-008-0327-y

Funedda, A., Naitza, S., Buttau, C., Cocco, F., Dini, A., 2018. Structural Controls of Ore Mineralization in a Polydeformed Basement: Field Examples from the Variscan Baccu Locci Shear Zone (SE Sardinia, Italy). Minerals 8, 456. https://doi.org/10.3390/min8100456

Funedda, A., Naitza, S., Conti, P., Dini, A., Buttau, C., Tocco, S., Carmignani, L., 2011. The geological and metallogenic map of the Baccu Locci mine area (Sardinia, Italy). J. Maps 7, 103–114. https://doi.org/10.4113/jom.2011.1134

Garbarino, C., Naitza, S., Tocco, S., Farci, A., Rayner, J., 2003. Orogenic gold in the Paleozoic basement of SE Sardinia (Italy).

Garbarino, G., Grillo, S.M., Padalino, G., Tocco, S., Violo, M., 1989. Lithospheric evolution and metallogenesis : The Pb-Zn-Ffe-Ba mineralization of the Cambrian carbonatic platform, the sulphides of the Ordovician-Silurian volcanism and Hercynian magmatism of Sardinia 427–443.

Gattacceca, J., Deino, A., Rizzo, R., Jones, D.S., Henry, B., Beaudoin, B., Vadeboin, F., 2007. Miocene rotation of Sardinia: New paleomagnetic and geochronological constraints and geodynamic implications. Earth Planet. Sci. Lett. 258, 359–377. https://doi.org/10.1016/j.epsl.2007.02.003

Gattacceca, J., Orsini, J.-B., Bellot, J.-P., Henry, B., Rochette, P., Rossi, P., Cherchi, G., 2004. Magnetic fabric of granitoids from Southern Corsica and Northern Sardinia and implications for Late Hercynian tectonic setting. J. Geol. Soc. 161, 277–289. https://doi.org/10.1144/0016-764903-115

Grohol, Grohol, M., Veeh, C., 2023. Study on the critical raw materials for the EU 2023: final report. Publications Office of the European Union.

Hronsky, J.M.A., Kreuzer, O.P., 2019. Applying spatial prospectivity mapping to exploration targeting: Fundamental practical issues and suggested solutions for the future. Ore Geol. Rev. 107, 647–653. https://doi.org/10.1016/j.oregeorev.2019.03.016

Jaeger, J.C., 1964. Thermal effects of intrusions. Rev. Geophys. 2, 443–466. https://doi.org/10.1029/RG002i003p00443

Knox-Robinson, C.M., Wyborn, L.A.I., 1997. Towards a holistic exploration strategy: Using Geographic Information Systems as a tool to enhance exploration. Aust. J. Earth Sci. 44, 453–463. https://doi.org/10.1080/08120099708728326Lang, A.H., 1961. Metallogenic maps. Econ. Geol. 56, 1123–1132. https://doi.org/10.2113/gsecongeo.56.6.1123

Lara, G., Klinger, F.L., Perucca, L., Rojo, G., Vargas, N., Leiva, F., 2017. Multiple geophysical methods examining neotectonic blind structures in the Maradona valley, Central Precordillera (Argentina). Tectonophysics. https://doi.org/10.1016/j.tecto. 2017.06.021.

Larson, K.P., Button, M., Shrestha, S., and Camacho, A., 2023, A comparison of 87Rb/87Sr and 40Ar/39Ar dates: Evaluating the problem of excess 40Ar in Himalayan mica: Earth and Planetary Science Letters, v. 609, p. 118058, doi:10.1016/j.epsl.2023.118058.

Larson, K.P., Dyck, B., Shrestha, S., Button, M., and Najman, Y., 2024, On the viability of detrital biotite Rb–Sr geochronology: Geochronology, v. 6, p. 303–312, doi:10.5194/gchron-6-303-2024.

Lattanzi, P., 1999. Epithermal precious metal deposits of Italy–an overview. Miner. Deposita 34, 630–638. https://doi.org/10.1007/s001260050224

Loi, A., Cocco, F., Oggiano, G., Funedda, A., Vidal, M., Ferretti, A., Leone, F., Barca, S., Naitza, S., Ghienne, J.-F., Pillola, G.L., 2023. The Ordovician of Sardinia (Italy): from the 'Sardic Phase' to the end-Ordovician glaciation, palaeogeography and geodynamic context, in: Harper, D.A.T., Lefebvre, B., Percival, I.G., Servais, T. (Eds.), A Global Synthesis of the Ordovician System: Part 1. Geological Society of London, p. 0. https://doi.org/10.1144/SP532-2022-121

Luo, X., Dimitrakopoulos, R., 2003. Data-driven fuzzy analysis in quantitative mineral resource assessment. Comput. Geosci. 29, 3–13. https://doi.org/10.1016/S0098-3004(02)00078-X

Lustrino, M., Morra, V., Fedele, L., Serracino, M., 2007. The transition between orogenic and anorogenic magmatism in the western Mediterranean area: the Middle Miocene volcanic rocks of Isola del Toro (SW Sardinia, Italy).

Malehmir, A., Koivisto, E., Manzi, M., Cheraghi, S., Durrheim, R.J., Bellefleur, G., Wijns, C., Hein, K.A.A., King, N., 2014. A review of reflection seismic investigations in three major metallogenic regions: The Kevitsa Ni–Cu–PGE district (Finland), Witwatersrand goldfields (South Africa), and the Bathurst Mining Camp (Canada). Ore Geol. Rev. 56, 423–441. https://doi.org/10.1016/j.oregeorev.2013.01.003.

Malehmir, A., Durrheim, R., Bellefleur, G., Urosevic, M., Juhlin, C., White, D.J., Milkereit, B., and Campbell, G., 2012. Seismic methods in mineral exploration and mine planning: A general overview of past and present case histories and a look into the future: *Geophysics*, 77. https://doi.org/10.1190/geo2012-0028.1

Malehmir, A., Dahlin, P., Lundberg, E., Juhlin, C., Sjöström, H., and Högdahl, K., 2011. Reflection seismic investigations in the Dannemora area, central Sweden: Insights into the geometry of polyphase deformation zones and magnetite-skarn deposits: *Journal of Geophysical Research*, 116. https://doi.org/10.1029/2011JB008643

Malehmir, A., Tryggvason, A., Juhlin, C., Rodriguez-Tablante, J., Weihed, P., 2006. Seismic imaging and potential field modelling to delineate structures hosting VHMS deposits in the Skellefte Ore District, northern Sweden. Tectonophysics 426, 319–334. https://doi.org/10.1016/j.tecto.2006.08.006.

Marcello A., Pretti S., Salvadori I., 1978. Carta Metallogenica della Sardegna in scala 1:250.000. Ente Minerario Sardo – Servizio Geologico d'Italia, Roma.

Marino A., 1997. Il giacimento a fluorite e galena di Silius (Cagliari). C. Marini (Ed.): Le materie prime minerali sardi, problemi e prospettive, CUEC, Cagliari 258-268

Mameli, P., Mongelli, G., Oggiano, G., Dinelli, E., 2007. Geological, geochemical and mineralogical features of some bauxite deposits from Nurra (Western Sardinia, Italy): insights on conditions of formation and parental affinity. Int. J. Earth Sci. 96, 887–902. https://doi.org/10.1007/s00531-006-0142-2

Massonne, H.-J., Schreyer, W., 1987. Phengite geobarometry based on the limiting assemblage with K-feldspar, phlogopite, and quartz. Contrib. Mineral. Petrol. 96, 212–224. https://doi.org/10.1007/BF00375235

McCuaig, T.C., Hronsky, J.M.A., 2014. The Mineral System Concept: The Key to Exploration Targeting, in: Kelley, K.D., Golden, H.C. (Eds.), Building Exploration Capability for the 21st Century. Society of Economic Geologists, p. 0. https://doi.org/10.5382/SP.18.08

Meinert, L.D., Dipple, G.M., Nicolescu, S., 2005. World Skarn Deposits, in: One Hundredth Anniversary Volume. Society of Economic Geologists. https://doi.org/10.5382/AV100.11

Minzoni N., 1975. La serie delle formazioni paleozoiche a Sud del Gennargentu. Boll. Soc. Geol. It., 94: 347-365, Roma.

Mondillo, N., Boni, M., Balassone, G., Spoleto, S., Stellato, F., Marino, A., Santoro, L., Spratt, J., 2016. Rare earth elements (REE)—Minerals in the Silius fluorite vein system (Sardinia, Italy). Ore Geol. Rev. 74, 211–224. https://doi.org/10.1016/j.oregeorev.2015.11.016

Monier, G., Robert, J.-L., 1986. Evolution of the Miscibility Gap Between Muscovite and Biotite Solid Solutions with Increasing Lithium Content: An Experimental Study in the System K2O-Li2O-MgO-FeO-Al2O3-SiO2-H2O-HF at 600°C, 2 kbar P H2O: Comparison with Natural Lithium Micas. Mineral. Mag. 50, 641–651. https://doi.org/10.1180/minmag.1986.050.358.09

Montel, J.-M., Devidal, J.-L., Avignant, D., 2002. X-ray diffraction study of brabantite–monazite solid solutions. Chem. Geol., Chemistry and Physics of Accessory Minerals: Crystallisation, Transformation and Geochronoligical Applications 191, 89–104. https://doi.org/10.1016/S0009-2541(02)00150-X

Moroni, M., Naitza, S., Ruggieri, G., Aquino, A., Costagliola, P., De Giudici, G., Caruso, S., Ferrari, E., Fiorentini, M.L., Lattanzi, P., 2019. The Pb-Zn-Ag vein system at Montevecchio-Ingurtosu, southwestern Sardinia, Italy: A summary of previous knowledge and new mineralogical, fluid inclusion, and isotopic data. Ore Geol. Rev. 115, 103194. https://doi.org/10.1016/j.oregeorev.2019.103194

Mulas A., Cocco F., Naitza S., 2025. Rilevamento geologico strutturale dell'area mineraria di Santa Lucia (Fluminimaggiore, Sardegna SW). [Master's Thesis] University of Cagliari, Cagliari.

Naitza, S., Casini, L., Cocco, F., Deidda, M.L., Funedda, A., Loi, A., Oggiano, G., Secchi, F., 2024. Post-Collisional Tectonomagmatic Evolution, Crustal Reworking and Ore Genesis along a Section of the Southern Variscan Belt: The Variscan Mineral System of Sardinia (Italy). Minerals 14, 65. https://doi.org/10.3390/min14010065

Naitza, S., Conte, A.M., Cuccuru, S., Oggiano, G., Secchi, F., Tecce, F., 2017. A Late Variscan tin province associated to the ilmenite-series granites of the Sardinian Batholith (Italy): The Sn and Mo mineralisation around the Monte Linas ferroan granite. Ore Geol. Rev. 80, 1259–1278. https://doi.org/10.1016/j.oregeorev.2016.09.013

Natale P., 1969. Il giacimento di Silius nel Gerrei. Boll Ass. Miner. Subalpina 6, 1–35

Naud G., 1979. Les shales de Rios Canoni, formation-repère fossilifère dans l'Ordovicien supérieur de Sardaigne orientale. Conséquences stratigraphiques et structurales. Bill. Soc. Géol. France, 21: 155-159, Paris.

Nykänen, V., Groves, D.I., Ojala, V.J., Eilu, P., Gardoll, S.J., 2008. Reconnaissance-scale conceptual fuzzy-logic prospectivity modelling for iron oxide copper – gold deposits in the northern Fennoscandian Shield, Finland. Aust. J. Earth Sci. 55, 25–38.

Nykänen, V., Lahti, I., Niiranen, T., Korhonen, K., 2015. Receiver operating characteristics (ROC) as validation tool for prospectivity models — A magmatic Ni–Cu case study from the Central Lapland Greenstone Belt, Northern Finland. Ore Geol. Rev. 71, 853–860. https://doi.org/10.1016/j.oregeorev.2014.09.007

Oggiano, G., Gaggero, L., Funedda, A., Buzzi, L., & Tiepolo, M., 2009. Multiple early Paleozoic volcanic events at the northern Gondwana margin: U–Pb age evidence from the Southern Variscan branch (Sardinia, Italy). Gondwana Research, 17(1), 44-58. https://doi.org/10.1016/j.gr.2009.06.001

Oggiano, G., Casini, L., Mameli, P., Rossi, P., 2007. Long lived dextral strike-slip tectonics in the southern Variscan Belt: evidence from two syn-kynematic intrusions in north Sardinia. Geol. Fr. 2, 142.

Oggiano, G., Mameli, P., 2006. Diamictite and oolitic ironstones, a sedimentary association at Ordovician-Silurian transition in the north Gondwana margin: New evidence from the inner nappe of Sardinia Variscides (Italy). https://doi.org/10.1016/j.gr.2005.11.009

Oriolo, S., Schulz, B., Hueck, M., Oyhantçabal, P., Heidelbach, F., Sosa, G., van den Kerkhof, A., Wemmer, K., Fossen, H., Druguet, E., Walter, J., Cavalcante, C., Siegesmund, S., 2022. The petrologic and petrochronologic record of progressive vs polyphase deformation: Opening the analytical toolbox. Earth-Sci. Rev. 234, 104235. https://doi.org/10.1016/j.earscirev.2022.104235

Padalino, G., S, P., D, T., S, T., I, U., M, V., P, Z., 1972. Carsismi e Mineralizzazioni. Carsismi E Miner.

Paton, C., Woodhead, J.D., Hellstrom, J.C., Hergt, J.M., Greig, A., and Maas, R., 2010, Improved laser ablation U-Pb zircon geochronology through robust downhole fractionation correction: Geochemistry, Geophysics, Geosystems, v. 11, doi:10.1029/2009GC002618.

Paton, C., Hellstrom, J., Paul, B., Woodhead, J., and Hergt, J., 2011, Iolite: Freeware for the visualisation and processing of mass spectrometric data: Journal of Analytical Atomic Spectrometry, v. 26, p. 2508–2518, doi:10.1039/c1ja10172b.

Peccerillo, A., 2017. Sardinia, in: Peccerillo, A. (Ed.), Cenozoic Volcanism in the Tyrrhenian Sea Region. Springer International Publishing, Cham, pp. 313–338. https://doi.org/10.1007/978-3-319-42491-0_11

Pedregosa, F., Pedregosa, F., Varoquaux, G., Varoquaux, G., Org, N., Gramfort, A., Gramfort, A., Michel, V., Michel, V., Fr, L., Thirion, B., Thirion, B., Grisel, O., Grisel, O., Blondel, M., Prettenhofer, P., Prettenhofer, P., Weiss, R., Dubourg, V., Dubourg, V., Vanderplas, J., Passos, A., Tp, A., Cournapeau, D., 2011. Scikit-learn: Machine Learning in Python. Mach. Learn. PYTHON.

Petteruti Lieberknecht, A.M., Fedele, L., D Amelio, F., Lustrino, M., Melluso, L., Morra, V., 2003. Plio-Pleistocenic igneous activity in Sardinia (Italy). Presented at the EGS - AGU - EUG Joint Assembly, p. 7260.

Pillola, G.L., Leone, F., Loi, A., 2002. The Cambrian and Early Ordovician of SW Sardinia (Italy).

Pillola, G.L., Leone, F., Loi, A., 1995. The Lower Cambrian Nebida Group of Sardinia.

Pirajno F., 2009. Hydrothermal Processes and Mineral Systems. Springer.

Pistis, M., Loi, A., Dabard, M.-P., 2016. Influence of relative sea-level variations on the genesis of palaeoplacers, the examples of Sarrabus (Sardinia, Italy) and the Armorican Massif (western France). Comptes Rendus Geosci. 348, 150–157. https://doi.org/10.1016/j.crte.2015.09.006

Pohl, W.L., 2022. Metallogenic models as the key to successful exploration — a review and trends. Miner. Econ. 35, 373–408. https://doi.org/10.1007/s13563-022-00325-3

Porwal, A., Carranza, E.J.M., Hale, M., 2003. Artificial Neural Networks for Mineral-Potential Mapping: A Case Study from Aravalli Province, Western India. Nat. Resour. Res. 12, 155–171. https://doi.org/10.1023/A:1025171803637

Redaa, A., Farkaš, J., Gilbert, S., Collins, A.S., Wade, B., Löhr, S., Zack, T., and Garbe-Schönberg, D., 2021, Assessment of elemental fractionation and matrix effects during: In situ Rb-Sr dating of phlogopite by LA-ICP-MS/MS: Implications for the accuracy and precision of mineral ages: Journal of Analytical Atomic Spectrometry, v. 36, p. 322–344, doi:10.1039/d0ja00299b.

Roy, B., Clowes, R.M., 2000. Seismic and potential-field imaging of the Guichon Creek batholith, British Columbia, Canada, to delineate structures hosting porphyry copper deposits. Geophysics. https://doi.org/10.1190/1.1444831.

Rösel, D., Zack, T., 2022. LA-ICP-MS/MS Single-Spot Rb-Sr Dating. Geostand. Geoanalytical Res. 46, 143–168. https://doi.org/10.1111/ggr.12414

Santoro, L., Boni, M., Putzolu, F., Mondillo, N., 2023. Base-metal sulphides and barite in the Palaeozoic of SW Sardinia: from tectonically deformed SedEx and Irish-type deposits to post-Variscan hydrothermal karst and vein ores., in: Irish-Type Zn-Pb Deposits around the World. Presented at the Irish-type Zn-Pb deposits around the world, Irish Association for Economic Geology, pp. 425–442. https://doi.org/10.61153/UCNC9869

Sass-Gustkiewicz, M., Dzulynski, S., Ridge, J.D., 1982. The emplacement of zinc-lead sulfide ores in the Upper Silesian District; a contribution to the understanding of mississippi valley-type deposits. Econ. Geol. 77, 392–412. https://doi.org/10.2113/gsecongeo.77.2.392

Scano, I., 2023. Vein intersection zones and host rock composition as controlling factors in polymetallic ore shoots genesis: insights from the Southern Arburèse five-element (Ni-Co-As-Bi-Ag) vein system (SW Sardinia). Rendiconti Online Della Soc. Geol. Ital. 61, 17–26. https://doi.org/10.3301/ROL.2023.42

Scano, I., Attardi, A., Cocco, F., Fancello, D., Murroni, A., Zara, F., Naitza, S., 2023. Ni-Co-As-Bi minerals in the Silius vein system, (SE Sardinia, Italy): The polymetallic evolution of a word-class fluorspar deposit. SGA 2023, Proceedings Volume 3, 96-99

Secchi, F., Casini, L., Cifelli, F., Naitza, S., Carta, E., Oggiano, G., 2022. Syntectonic magmatism and reactivation of collisional structures during late-Variscan shearing (SW Sardinia, Italy). Int. J. Earth Sci. 111, 1469–1490. https://doi.org/10.1007/s00531-022-02193-2

Sedda L., Attardi A., De Giudici G., Natiza S., 2025. A new geodatabase of mining waste dumps in Sardinia (Italy): a tool for the identification and potential valorisation of Critical and Strategic Raw Materials (CRM and SRM). Abstract Book - Geosciences and the Challenges of the 21st Century. Italian Geological Society, 714. doi.org/10.3301/ABSGI.2025.03

Simmons, S.F., White, N.C., John, D.A., 2005. Geological Characteristics of Epithermal Precious and Base Metal Deposits, in: Hedenquist, J.W., Thompson, J.F.H., Goldfarb, R.J., Richards, J.P. (Eds.), One Hundredth Anniversary Volume. Society of Economic Geologists, p. 0. https://doi.org/10.5382/AV100.16

Smith, M.P., Henderson, P., Campbell, L.S., 2000. Fractionation of the REE during hydrothermal processes: constraints from the Bayan Obo Fe-REE-Nb deposit, Inner Mongolia, China. Geochim. Cosmochim. Acta 64, 3141–3160. https://doi.org/10.1016/S0016-7037(00)00416-6

Stille H., 1939. Bemerkungen betreffend die "Sardische Faltung" und den Ausdruck "ophiolitisch", Zeitsch. Deutsch. Geol. Gest., 91, 771-773.

Tocco S., Marcello A., Mazzella A., Naitza S., Pretti S., Valera P., Valera R., 2008. La Carta Metallogenica e delle Georisorse della Sardegna in Scala 1:250.000. Rend. Online Soc. Geol. It., 3.

Velde, B., 1965. Experimental determination of muscovite polymorph stabilities. Am. Mineral. 50, 436–449.

Vermeesch, P., 2018. IsoplotR: A free and open toolbox for geochronology. Geosci. Front., SPECIAL ISSUE: Frontiers in geoscience:A tribute to Prof. Xuanxue Mo 9, 1479–1493. https://doi.org/10.1016/j.gsf.2018.04.001

von Raumer, J.F., Stampfli, G.M., Arenas, R., Sánchez Martínez, S., 2015. Ediacaran to Cambrian oceanic rocks of the Gondwana margin and their tectonic interpretation. Int. J. Earth Sci. 104, 1107–1121. https://doi.org/10.1007/s00531-015-1142-x

Williams-Jones, A.E., Migdisov, A.A., Samson, I.M., 2012. Hydrothermal Mobilisation of the Rare Earth Elements – a Tale of "Ceria" and "Yttria." Elements 8, 355–360. https://doi.org/10.2113/gselements.8.5.355

Wu, G., Chen, G., Wang, D., Cheng, Q., Zhang, Z., Yang, J., Xie, S., 2014. Identifying mineral prospectivity using seismic and potential field data in the Hongniangyu district, Inner Mongolia, China. Ore Geology Reviews, Volume 119, April 2020, 103317. 10.1016/j.oregeorev.2020.103317

Youden, W.J., 1950. Index for rating diagnostic tests. Cancer 3, 32–35. https://doi.org/10.1002/1097-0142(1950)3:1%253C32::aid-cncr2820030106%253E3.0.co;2-3

Zack, T., and Hogmalm, K.J., 2016, Laser ablation Rb/Sr dating by online chemical separation of Rb and Sr in an oxygen-filled reaction cell: Chemical Geology, v. 437, p. 120–133, doi:10.1016/j.chemgeo.2016.05.027.

Zadeh, L.A., 1965. Fuzzy sets. Inf. Control 8, 338–353. https://doi.org/10.1016/S0019-9958(65)90241-X

Zara F., Attardi A, Scano I., Naitza S., 2022. Studio sulla mineralizzazione idrotermale a fluorite, barite, REE e solfuri di Pb, Zn e Cu della Miniera di Silius, Distretto del Gerrei (Sardegna Sud-Orientale). [Master's Thesis] University of Cagliari, Cagliari.

Zhang, L., Yi, J., 2010. Management methods of spatial data based on PostGIS, in: 2010 Second Pacific-Asia Conference on Circuits, Communications and System. Presented at the 2010 Second Pacific-Asia Conference on Circuits, Communications and System, pp. 410–413. https://doi.org/10.1109/PACCS.2010.5626962

Zimmermann, H.-J., Zysno, P., 1980. Latent connectives in human decision making. Fuzzy Sets Syst. 4, 37–51. https://doi.org/10.1016/0165-0114(80)90062-7

Acknowledgements

I thank my colleagues and friends from UniCa for the technical and moral support. Lorenzo Sedda with whom I shared part of the PhD project. Costantino Pala with whom I share the path and the PhD difficulties. A big thank to Francesca Zara, Daniele Cossu, Alberto Mulas and Fabrizio Cocco for the field work together. My partner Andrea, who supported me morally during the last year.

I am grateful to Prof. Jarek Majka for hosting me at Uppsala University, and the collaboration on the Oschiri greisen deposit together with PhD Chris Barnes and PhD Riccardo Callegari, who run the geochemical analyses and helped me on the dating process.

This thesis was produced while attending the PhD programme in Earth and Environmental Sciences and Technologies at the University of Cagliari, Cycle XXXVIII, with the support of a scholarship financed by NRRP, funded by the European Union - NextGenerationEU - Mission 4 "Education and Research", Component 2 “From Research to Business” – Investment 3.1 “Fund to create an integrated system of research and innovation infrastructures”.

Finanziato dall'Unione europea NextGenerationEU | Ministero dell'Università e della Ricerca | Italiadomani Piano Nazionale di Ripresa e Resilienza | Università degli Studi di Cagliari